

Università degli Studi di Milano-Bicocca
Dipartimento di Biotecnologie e Bioscienze
Dottorato di ricerca in Tecnologie Convergenti per i Sistemi
Biomolecolari
XXXIV Ciclo



**Monolayers and three-dimensional cultures to investigate
metabolic reprogramming in breast and bladder cancer**

Gloria Campioni

Matr. 848844

Tutor: Prof. Marco Vanoni

Anno Accademico 2020-2021

ABSTRACT

Metabolic reprogramming has been observed in many types of cancer, and it is considered a hallmark of this heterogeneous multifactorial disease. Understanding the mechanisms leading to metabolic rewiring and how these activities promote the activation of cancer's malignant properties can help exploit metabolic alterations for therapeutic benefit. In solid tumors, cancer cells interact with the complex habitat of the tumor microenvironment (TME), which can modulate cancer cells' metabolism and their sensitivity or resistance to drug treatment. Three-dimensional (3D) models, such as spheroids, organoids, and organ-on-chips, are changing the paradigm of preclinical cancer research as they more closely resemble the complex tissue environment and architecture found in tumors *in vivo* than bidimensional (2D) cell cultures. Therefore, 3D models could potentially improve the robustness and reliability of preclinical research data, reducing the need for animal testing and favoring their transition to clinical practice.

Breast cancer is the most common cancer and the leading cause of cancer death for women worldwide. The therapeutic strategy for mammary carcinoma is guided by the histopathological and molecular classification, based on the expression of biomarkers such as hormone receptors (estrogen, ER, and progesterone, PR, receptors) and the human epidermal growth factor receptor-2 (HER2). Triple negative breast cancer is the most aggressive subtype and still lacks a targeted therapy.

Bladder cancer is the 6th most common malignancy in men worldwide and one of the most expensive cancers to manage. Even though most patients are diagnosed with non-muscle invasive bladder cancer, recurrences are frequent (50–70%), sometimes including progression to invasive tumors, which drastically reduce survival expectations.

In this thesis, we performed a metabolic characterization of luminal (MCF7) and triple negative (MDA-MB-231 and SUM159PT) breast cancer cell lines and compared their different response to metabolic perturbations through the evaluation of cell

proliferation (in 2D) and spheroid formation ability. The main results of this work suggest that nutritional deprivations and pharmacological treatments targeting energetic metabolism have a more significant impact on the proliferation of cells growing in 2D than on spheroid formation (3D). Moreover, the perturbation of glucose metabolism by glucose deprivation and 2-deoxy-glucose treatment showed the most potent effect on the spheroid formation process, severely reducing spheroid vitality and morphology, especially on the highly glycolytic MDA-MB-231 cell line.

Furthermore, we developed a reliable and reproducible workflow for the metabolic analysis of three-dimensional cultures by Seahorse XFe96 technology, an extracellular flux analyzer that simultaneously measures the Oxygen Consumption Rate (OCR) and the Extracellular Acidification Rate (ECAR) of living cells. The optimization of the spheroid formation protocol enabled the production of spheroids highly regular in shape and homogenous in size, dramatically reducing variability in the OCR and ECAR measurements among the experimental technical replicates, both under basal and drug treatment conditions. Furthermore, the normalization on a per-cell basis allowed us to directly compare these metabolic parameters between spheroids of different sizes and between 2D and 3D cultures, revealing that metabolic differences among the studied spheroids are mostly related to the cell line rather than to the size of the spheroid.

Finally, we characterized energy metabolism and cellular properties associated with spreading and tumor progression of RT112 and 5637, two cell lines from Grade 2 human bladder cancer. Although the two cell lines displayed distinct metabolic and invasive properties, both exhibited sizable respiration, and the metformin treatment gave a global downregulation of the proliferation, migration, and the ability to form spheroids.

Altogether, the findings of this thesis open new research perspectives for identifying novel potential therapeutic targets against cancer, getting closer toward the understanding of cancer metabolic plasticity that can be exploited for developing efficient therapeutic strategies for the treatment of oncologic patients.

RIASSUNTO

La riprogrammazione metabolica è stata osservata in molti tipi di cancro ed è considerata un tratto distintivo di questa malattia eterogenea multifattoriale. Comprendere i meccanismi che portano al riarrangiamento metabolico e come queste attività promuovono l'attivazione di proprietà maligne nel cancro può aiutare a sfruttare le alterazioni metaboliche a beneficio terapeutico. Nei tumori solidi le cellule tumorali interagiscono con il complesso habitat del microambiente tumorale (TME) che può modulare il metabolismo delle cellule tumorali e la loro sensibilità o resistenza al trattamento farmacologico. I modelli tridimensionali (3D), come gli sferoidi, gli organoidi e gli organ-on-chip stanno cambiando il paradigma della ricerca preclinica sul cancro poiché rappresentano più fedelmente la complessità dell'ambiente e dell'architettura tissutale che si trova nei tumori in vivo rispetto alle colture cellulari bidimensionali (2D). Perciò l'utilizzo dei modelli 3D potrebbe potenzialmente migliorare la robustezza e l'affidabilità dei dati della ricerca preclinica riducendo la necessità di test sugli animali e favorendone la traslazione alla pratica clinica.

Il cancro al seno è il tumore più comune e la principale causa di morte legata al cancro nelle donne in tutto il mondo. La strategia terapeutica per il carcinoma mammario è guidata dalla classificazione istopatologica e molecolare, basata sull'espressione di biomarcatori come i recettori ormonali (recettore per gli estrogeni, ER, e recettore per il progesterone, PR) e il recettore per il fattore di crescita epidermico umano 2 (HER2). Il cancro al seno triplo negativo è il sottotipo più aggressivo e per il quale manca ancora una terapia mirata.

Il cancro alla vescica è il sesto tumore maligno più comune al mondo negli uomini e uno dei tumori più costosi da gestire. Anche se la maggior parte dei tumori viene diagnosticato come cancro alla vescica non-muscolo invasivo, le recidive sono frequenti (50-70%) e possono includere la progressione a tumori invasivi, che riducono drasticamente le aspettative di sopravvivenza.

In questa tesi, abbiamo eseguito una caratterizzazione metabolica di linee cellulari di carcinoma mammario luminale (MCF7) e triplo negativo (SUM159PT e MDA-MB-231) e abbiamo confrontato la loro diversa risposta alle perturbazioni metaboliche attraverso la valutazione della proliferazione cellulare (in 2D) e della capacità di formare sferoidi. I principali risultati di questo capitolo suggeriscono che le deprivazioni nutrizionali e i trattamenti farmacologici contro il metabolismo energetico hanno un impatto maggiore sulla proliferazione delle cellule che crescono in 2D rispetto alla formazione di sferoidi (3D). Inoltre, la perturbazione del metabolismo del glucosio tramite deprivazione di glucosio e trattamento con 2-deossiglucosio ha mostrato l'effetto più forte sul processo di formazione degli sferoidi, riducendo gravemente la vitalità e la morfologia degli sferoidi, specialmente sulla linea cellulare altamente glicolitica MDA-MB-231.

Inoltre, abbiamo sviluppato un flusso di lavoro affidabile e riproducibile per l'analisi metabolica di colture tridimensionali mediante la tecnologia Seahorse XFe96, un analizzatore di flusso extracellulare che misura simultaneamente il tasso di consumo di ossigeno (OCR) e il tasso di acidificazione extracellulare (ECAR) delle cellule viventi. L'ottimizzazione del protocollo di formazione degli sferoidi ha consentito di produrre sferoidi di forma altamente regolare e di dimensioni omogenee, riducendo drasticamente la variabilità nelle misurazioni di OCR ed ECAR tra i replicati tecnici sperimentali, sia in condizioni basali che di trattamento farmacologico. La normalizzazione per cellula ci ha permesso di confrontare direttamente questi parametri metabolici tra sferoidi di diverse dimensioni e tra colture 2D e 3D, rivelando che le differenze metaboliche tra gli sferoidi studiati sono per lo più legate alla linea cellulare piuttosto che alla dimensione dello sferoide.

Infine, abbiamo caratterizzato il metabolismo energetico e le proprietà cellulari associate alla diffusione e alla progressione del tumore nelle linee cellulari tumorali di Grado 2 derivanti da vescica umana, RT112 e 5637. Nonostante le due linee cellulari mostrassero proprietà metaboliche e invasive distinte, entrambe presentavano una respirazione considerevole e il trattamento con metformina ha causato una down-

regolazione globale della proliferazione, della migrazione e della capacità di formare sferoidi.

Complessivamente i risultati di questa tesi aprono nuove prospettive di ricerca per l'identificazione di nuovi potenziali bersagli terapeutici contro il cancro, avvicinandosi alla comprensione della plasticità metabolica del cancro che può essere sfruttata per sviluppare strategie terapeutiche efficienti per il trattamento di pazienti oncologici.

Index

| | |
|--|----|
| INTRODUCTION | 11 |
| 1.1 Cancer: an overview | 11 |
| 1.2 Targeting cancer metabolism | 15 |
| 1.2.1 Glucose metabolism | 16 |
| 1.2.2 Glutamine metabolism | 18 |
| 1.2.3 Fatty acids metabolism | 20 |
| 1.2.4 Oxidative phosphorylation | 20 |
| 1.2.5 Redox homeostasis and ROS detoxification | 22 |
| 1.3 Cancer stem cells metabolism | 23 |
| 1.4 The tumor microenvironment | 24 |
| 1.5 <i>In vitro</i> models of the tumor microenvironment | 27 |
| 1.5.1 3D cancer models | 27 |
| 1.5.2 Homotypic and heterotypic spheroids | 30 |
| 1.6 Breast cancer | 33 |
| 1.6.1 Breast anatomy | 33 |
| 1.6.2 Carcinogenesis and risk factors | 34 |
| 1.6.3 Epidemiology | 38 |
| 1.6.4 Classification and staging | 39 |
| 1.6.5 Diagnosis and therapy | 44 |
| 1.6.6 Breast cancer metabolism | 46 |
| 1.7 Bladder cancer | 48 |
| 1.7.1 Bladder anatomy | 48 |
| 1.7.2 Classification, grading and staging | 49 |
| 1.7.3 Epidemiology and risk factors | 53 |
| 1.7.4 Carcinogenesis | 54 |
| 1.7.5 Diagnosis and therapy | 54 |
| 1.7.6 Bladder cancer metabolism | 57 |
| AIM OF THE THESIS | 59 |

| | |
|--|-----|
| CHAPTER 1: UNRAVELLING METABOLIC DIFFERENCES BETWEEN LUMINAL AND TRIPLE NEGATIVE CELL LINES IN 2D AND 3D BREAST CANCER MODELS | 61 |
| 2.1 Abstract | 61 |
| 2.2 Introduction | 62 |
| 2.3 Materials and methods..... | 65 |
| 2.3.1 Cell lines and culture media composition | 65 |
| 2.3.2 Production of three-dimensional cultures | 67 |
| 2.3.3 Nutritional deprivation and drug treatment assay in 2D cultures | 68 |
| 2.3.4 Spheroid formation assays under metabolic perturbation | 70 |
| 2.3.5 High-content analysis of 2D and 3D cultures | 71 |
| 2.3.6 Evaluation of metabolic parameters by Seahorse XFe96 analyzer | 72 |
| 2.3.7 Statistical analysis..... | 76 |
| 2.4 Results | 77 |
| 2.4.1 Cell size and growth profile in adhesion (2D)..... | 77 |
| 2.4.2 Characterization of the metabolic phenotype in 2D: assessment of basal respiration and glycolysis | 77 |
| 2.4.3 Analysis of mitochondrial functionality in 2D..... | 79 |
| 2.4.4 Metabolic perturbation assays in 2D: nutritional deprivation and pharmacological treatment..... | 82 |
| 2.4.5 Propensity to form spheroids (3D) | 87 |
| 2.4.6 Spheroid formation assays under metabolic perturbation by nutritional deprivation or pharmacological treatment | 89 |
| 2.4.7 Preliminary metabolic characterization of homotypic and heterotypic three-dimensional (3D) cultures: analysis of basal and perturbed respiration and acidification rate..... | 96 |
| 2.5 Discussion | 101 |
| CHAPTER 2: AN OPTIMIZED WORKFLOW FOR ANALYSIS OF METABOLIC FLUXES IN CANCER SPHEROIDS USING SEAHORSE TECHNOLOGY | 108 |
| CHAPTER 3: PROFILING AND TARGETING OF ENERGY AND REDOX METABOLISM OF GRADE II BLADDER CANCER CELLS WITH DIFFERENT INVASIVENESS PROPERTIES | 138 |
| GENERAL DISCUSSION | 173 |
| REFERENCES | 179 |

| | |
|------------------------------|-----|
| CONTRIBUTIONS | 200 |
| ACKNOWLEDGEMENT | 201 |

INTRODUCTION

1.1 Cancer: an overview

Cancer is the second leading cause of death worldwide (behind only cardiovascular diseases), according to a scientific study conducted among 22 groups of diseases and injuries in 2019 [1]. The Global Cancer Statistics 2020 estimated 19.3 million new cases and almost 10 million cancer deaths (+20.6% since 2010) worldwide in 2020. Female breast cancer has surpassed lung cancer as the most commonly diagnosed cancer, with an estimated 2.3 million new cases (11.7%), while lung cancer remains the first leading cause of cancer-related death (18%) in 2020 [2].

The challenge in finding a common effective strategy to treat cancer is in part due to the large heterogeneity across tumors: there are more than 100 types of cancer according to the National Cancer Institute (NCI), and cancer subtypes have been discovered for many of them. In order to consider these variations, there is increasing interest in the concept of personalized medicine, which is based on the stratification of patients into different molecularly defined groups and then using different treatments and/or interventions for each group [3]. This inter-tumor heterogeneity is classically recognized through different morphology traits, expression subtypes, or classes of genomic copy number patterns, among other differences. The genetic mutations that contribute to defining cancer subgroups, are usually those responsible for cancer initiation and progression and tend to affect two main types of genes: proto-oncogenes and tumor suppressor genes. Proto-oncogenes encode for proteins that function to stimulate cell division, inhibit cell differentiation, and halt cell death, such as *RAS*, *PI3K*, *ERBB*, *EGFR*, *RAF*, and *MYC* [4]. Tumor suppressor genes encode for proteins that regulate the cell cycle, apoptosis, and DNA repair mechanisms. The loss-of-function mutations in genes like *TP53*, *RB*, *PTEN*, *BRCA*, and *APC* can contribute to neoplastic transformation [5]. A useful tool to be exploited to better comprehend the complexity

of inter-tumor heterogeneity is multi-omics analysis, which can serve as a scaffold to identify a set of biomarkers that can be used for patients' stratification in clinics [3].

Further complicating this scenario is the observation of intratumor heterogeneity, characterized by histopathological sectors of different morphology or staining behavior within a tumor, more recently defined as the molecular level by the genetic differences observed in tumor subpopulations even among individual malignant cells [6–8]. Intratumor heterogeneity has been explained using different plausible models of tumor progression, including the clonal evolution model [9] and the cancer stem cell model [10–12].

The clonal evolution model suggests that tumors evolve by the expansion of one (monoclonal) or multiple (polyclonal) subpopulations to form the tumor mass. These subpopulations of cells can survive – if the acquired mutations are advantageous for tumor progression – or become extinct – if not – as in Darwinian selection. On the contrary, the cancer stem cells (CSCs) model states that cells within the tumor are hierarchically organized in much the same manner as normal tissues; cancer stem cells are rare precursors cells with self-renewal properties, that can give rise to different subpopulations. The extreme biological heterogeneity caused by the CSCs can lead to a lack of consistency in treatment planning, causing therapeutic resistance and the onset of relapses and metastasis [13,14].

To get closer to finding the best cancer treatment, inter- and intra-tumor heterogeneity should always be considered, but the main issue remains to understand what all these cancer types have in common and what distinguishes them from normal cells. For this purpose, Hanahan and Weinberg in 2000 stated that the vast catalogue of cancer cell genotypes is a manifestation of six essential alterations in cell physiology that collectively dictate malignant growth: self-sufficiency in growth signals, insensitivity to growth-inhibitory (antigrowth) signals, evasion of programmed cell death (apoptosis), limitless replicative potential, sustained angiogenesis, and tissue invasion and metastasis [15]. Later, in 2011, the same authors suggested that two additional

hallmarks of cancer are involved in the pathogenesis of some and perhaps all cancers: the ability of cancer cells to evade immunological destruction, and the capability to modify or reprogram, cellular metabolism in order to support neoplastic proliferation most effectively [16]. This latter characteristic of cancer cells is the central theme of this thesis, which has been studied in different models of breast and bladder cancer. Metabolic rewiring is essential for cancer cells because they need to satisfy the enhanced energy demand, generate the metabolic precursors for cell biosynthesis in order to expand and maintain the redox balance in the cell [17]. Cancer cell metabolic reprogramming is the combined result of signals deriving from intrinsic factors, such as oncogenic alterations (e.g. *KRAS*, *MYC*, *PTEN*) and epigenetic modulations, as well as extrinsic factors mediated by the tumor microenvironment (TME) [18]. The environment in which cancer cells establish can be hostile, especially during tumor initiation, and it can impose many challenges for the cancer cells: physical pressure, oxidative stress, nutrient deprivation and competition, hypoxia, and immune surveillance. Metabolic plasticity gives cancer cells the advantage to survive and adapt to these harsh environmental stresses. Interactions among the intrinsic metabolic network and the extrinsic signals from the TME drive cancer cells to exhibit varying metabolic requirements and properties [19], such as the ability to modify their metabolic pathways (e.g., aerobic glycolysis), to enhance the external metabolites uptake, and to maximize the efficiency of metabolic enzyme activities [20] (**Figure 0.1**). On the other hand, once cancer cells have passed the restriction point of the primary overall anti-tumorigenic environment they must survive, they become able to reprogram the cells in their microenvironment (e.g. Cancer-Associated Fibroblasts, Tumor-Associated Macrophages), or even recruit cell types to aid their progression (these aspects are discussed more in detail in paragraph 1.4)[18,19,21].

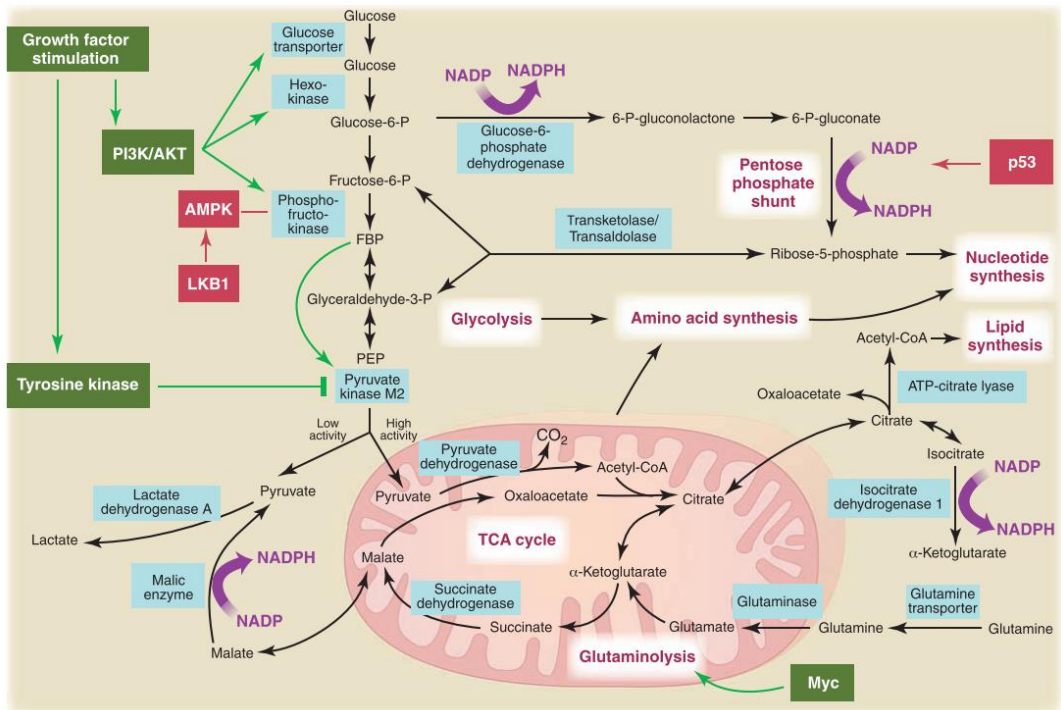


Figure 0.1. Metabolic pathways active in proliferating cells are directly controlled by signaling pathways involving known oncogenes and tumor suppressor genes. This schematic shows the interconnection of glycolysis, oxidative phosphorylation, the pentose phosphate pathway, and glutamine metabolism in proliferating cells (Heiden et al. [22]).

Among the intrinsic factors driving cancer metabolic reprogramming, oncogenes and tumor suppressor genes play an essential role. For instance, oncogenic mutations of *c-MYC*, *KRAS*, and *YAP* have been reported to upregulate glucose transporter (GLUT1) expression [23–27]. The oncogenic hyperactivation of the phosphoinositide 3-kinase (PI3K)/AKT pathway, along with mTOR, controls the uptake and utilization of multiple nutrients, including glucose, amino acids, nucleotides, and lipids [18,28]. It was demonstrated that its activation upregulates the activity of the glycolytic enzyme hexokinase (HK2) by increasing mitochondria-associated hexokinase activity [29]. In various cancer cell lines, HIF-1a induces the activation of lactate dehydrogenase in hypoxic tumor microenvironments, propelling the pyruvate to lactate conversion [30]. In cancer cells, hyperactive PI3K/AKT and oncogenic *c-MYC* upregulate pentose

phosphate pathway (PPP) influx [31,32], which is involved both in nucleotide biosynthesis and in redox homeostasis through NADPH production.

Cancer is a complex disease in which both genetic defects and microenvironmental components contribute to the development, progression, and metastasization of disease, representing major hurdles in the identification of more effective and safer treatment regimens for patients. *In vitro* tumor models have provided important tools for cancer research and serve as low-cost screening platforms for drug therapies. However, classical bidimensional (2D) monocultures are a very simplistic model that does not fully consider the complexity of the neoplastic disease. Models such as cell co-cultures, three-dimensional (3D) cultures (like spheroids), and patient-derived tumor organoids closely resemble tumor cytoarchitecture and also have the advantage of mimicking tumor behavior, which is heavily dependent on environmental signals, cell-cell interactions, and the extracellular matrix [33].

In the following paragraphs, the topics of metabolic alterations in cancer and complex *in vitro* cancer models are deepening, with a particular focus on mammary carcinoma and bladder cancer.

1.2 Targeting cancer metabolism

The aberrant metabolism of proliferating cancer cells presents potential opportunities from a therapeutic perspective, and there has been a growing interest in studying the best way to target cancer metabolism [34,35]. Antimetabolites such as antifolate compounds (folic acid, methotrexate, aminopterin), and purines and pyrimidines analogues (6-mercaptopurine, 5-fluorouracil, capecitabine) are standards in many modern chemotherapy regimens that increase patient survival and, in some cases, help cure the disease [36]. However, targeting general proliferative metabolism may not offer an adequate therapeutic window since many non-malignant cells, including those in bone marrow, intestinal crypts, and hair follicles, are rapidly proliferating. Therefore, prominent side effects of antimetabolite chemotherapy are caused by the destruction

of normal rapidly proliferating cells. Therefore, finding non-toxic alternative metabolic therapeutic targets against cancer cells is urgent. The main metabolic pathways that have been considered attractive for this purpose are glucose, glutamine, and fatty acid pathways.

1.2.1 Glucose metabolism

Otto Warburg in the 1920s observed a phenomenon that became the foundation for the field of cancer metabolism. According to normal cellular respiration, glucose is converted to pyruvate, which then enters the tricarboxylic acid (TCA) cycle to undergo oxidative phosphorylation (OXPHOS) in the presence of oxygen, and there should be minimal lactate production. However, in his studies, Warburg observed an increased glucose uptake and increased lactic acid production in tumor cells as compared to normal cells, even in the presence of oxygen [37]. This phenomenon, the metabolism of glucose to lactate despite the presence of adequate oxygen, is called the **Warburg effect** or **aerobic glycolysis** [38,39]. Despite glycolysis produces at least 16-18 times less ATP per glucose molecule than the TCA cycle followed by OXPHOS, in the Warburg effect, the flux of glucose to lactate is up to 100 times faster than through the TCA cycle, resulting in similar amounts of ATP production over the same time [40]. Tumor cells need not only ATP but also anabolic metabolism to accumulate a large amount of biomass to sustain their growth. The Warburg effect via multiple glycolytic intermediates provides a carbon source that contributes to the nucleotide, fatty acid, and amino acid synthesis pathways (**Figure 0.2**). One ubiquitous application of the Warburg effect is the use of positron-emission tomography (PET) imaging in oncology, which has become indispensable in the detection of tumors and the monitoring of the response of existing cancer to therapeutic intervention. PET is an exploitation of the high rate of glycolysis in cancer cells as it uses a radiolabeled glucose analogue, [¹⁸F]fluoro-2-deoxy-d-glucose (FDG), which accumulates in tumor cells due to their rapid uptake of glucose [41].

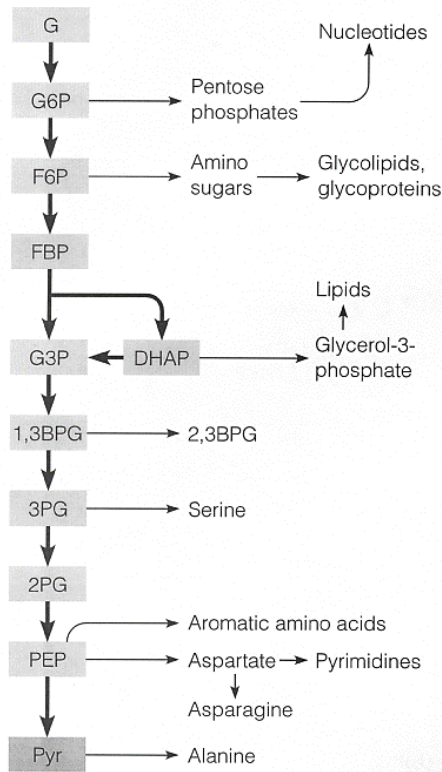


Figure 0.2. Major alternative fates of glycolytic intermediates in biosynthetic pathways (Figure from Mathews and van Holde: *Biochemistry*).

However, despite the Warburg effect was observed in many cancer types, more recent studies observed that subpopulations of cancer cells under hypoxia conditions still express genes related to mitochondrial function maintaining their tumorigenicity [42]. Moreover, considering intra-tumor heterogeneity, subpopulations of cancer cells can exhibit different metabolic phenotypes: indeed, it was observed that cancer stem cells have a lower glucose uptake and prefer OXPHOS rather than glycolysis to fulfil energy requirements [43].

Targeting glucose metabolism has been explored as a promising strategy. For example, using glucose analogues such as 2-Deoxy-Glucose (2DG), which binds and inhibits the first glycolytic enzyme hexokinase (HK2), can mimic a glucose deprivation condition, causing a decrease of glycolysis, and eventually induction of ROS-mediated apoptosis in multiple cancer types [44,45]. Drugs inhibiting Lactate dehydrogenase (LDH) enzymatic

activity, with the aim to block the regeneration of NAD⁺ (crucial in supporting the Warburg effect), have demonstrated anticancer effect in many cases. For instance, 1-(phenylseleno)-4-(trifluoromethyl) benzene (PSTMB) induces apoptosis in lung cancer, breast cancer, colon cancer, and melanoma cells via LDH inhibition [46]. Moreover, the combination of metformin with MCT-1 inhibitor AZD3965 (MCT-1 is the transporter responsible for lactate secretion in the TME) blocks lactate-mediated tumor progression and has significant anticancer effects [47].

It was demonstrated that a potent drug targeting glucose metabolism, Glutor, induces cell death of monolayer and spheroid-cultured cancer cells, by inhibiting glucose transporters GLUT-1/-3. Moreover, a synergic effect in cancer cell growth inhibition was observed by combining Glutor and glutaminase inhibitor CB-839 [48].

1.2.2 Glutamine metabolism

In addition to glucose, proliferating cancer cells also rely on glutamine as a major source of energy and building blocks. Glutamine is one of the most abundant non-essential amino acids in the bloodstream and it contributes not only carbon but also reduced nitrogen for the *de novo* biosynthesis of purine and pyrimidine nucleotides, other non-essential amino acids and it is a precursor for protein and glutathione biosynthesis [49](**Figure 0.3**).

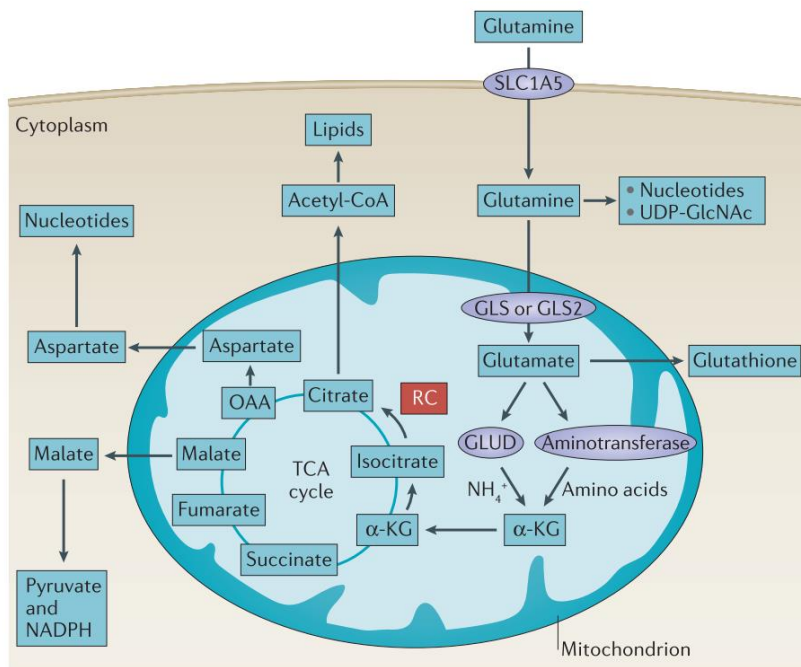


Figure 0.3. Main metabolic pathways of glutamine (Altman et al.[50]).

Many tumor cells manifest ‘glutamine addiction’, meaning that they are reliant on exogenous glutamine so the depletion of this amino acid can lead to cancer cell death [51]. It was found that cancer cells rely on the reductive carboxylation of glutamine-derived citrate to produce acetyl-CoA – necessary for lipids biosynthesis - and other TCA cycle intermediates, useful as cellular building blocks. Cells can become dependent upon glutaminolysis (the glutamine conversion to glutamate) as a result of genetic alterations affecting oxidative mitochondrial function [52]. A recent computational study demonstrated that enhanced glutamine-dependent lactate production can promote cancer cell growth even when glutamine is the exclusive carbon source; this phenomenon is called the ‘WarburQ effect’ [53].

Blocking nutrient uptake or performing nutritional starvation is a powerful strategy for inhibiting specific metabolic pathways. The inhibition of glutamine transporter ASCT2 with V-9302 was demonstrated to have anticancer effects in various cancer cell lines [54]. Similarly, by inhibiting glutaminase (GLS), the enzyme which catalyzes glutamine

conversion to glutamate, through the treatment with CB-839 and BPTES it is possible to obtain cytotoxic effects in triple-negative breast cancer [55].

A recent study revealed that combined treatment with the glutaminase inhibitor CB-839 and the PI3K/aldolase inhibitor NVP-BKM120 more consistently reduces cell growth of tumor xenografts, in particular with effects on redox homeostasis and nucleic acid metabolism [56].

1.2.3 Fatty acids metabolism

The advent of advanced technology for the study of lipidomic in the last decade suggested that glycolysis and glutaminolysis are not the only pathways involved in cancer metabolic plasticity. Indeed, also reprogramming of cellular lipid metabolism contributes directly to malignant transformation and progression [57]. To support enhanced growth, cancer cells need phospholipids to form plasma and organelle membranes for daughter cells, that can be supplied through *de novo* lipid synthesis. Moreover, the upregulation of mitochondrial β -oxidation can support tumor cell energetics and redox homeostasis [58]. It was discovered, therefore, that lipid metabolism has become implicated in a variety of oncogenic processes, including metastatic colonization, drug resistance, and cell differentiation [59–61].

Inhibitor agents directed against lipogenic enzymes such as fatty acids synthase (FASN), ATP citrate lyase (ACLY), and Acetyl-CoA carboxylase (ACC) have been the subject of numerous studies, and their efficacy as anticancer therapies have been proven in various preclinical models of carcinogenesis [62,63]. Recently was found that by combining pro-apoptotic agents with Carnitine palmitoyltransferase I inhibitors (e.g., etomoxir or ranolazine) it is possible to obtain beneficial anti-cancer effects in prostate cancer and human leukaemia [64,65].

1.2.4 Oxidative phosphorylation

When Otto Warburg observed aerobic glycolysis in cancer cells, he also suggested that this behavior was usually connected with damage in mitochondria [39]. In contrast to

Warburg's theory, more recent studies found that mitochondria are usually intact in cancer cells and that some types of cancers rely on OXPHOS for bioenergetics. Therefore, mitochondrial OXPHOS inhibition is a possible target for drug development [66]. For instance, mitochondrial respiration can be targeted using Oligomycin an ATP synthase inhibitor whose effect is to reduce mitochondrial ATP production. Oligomycin significantly decreases migration (70%) and invasiveness (25%) of triple-negative breast cancer cell lines *in vitro* [67] and reduces mammosphere formation more potently in a luminal breast cancer cell line than in triple-negative subtype [68].

Another important drug targeting OXPHOS is the type 2 diabetes drug metformin. Low glucose concentrations were demonstrated to sensitize the triple-negative MDA-MB-231 breast cancer cells to the anti-proliferative effect of metformin. This drug not only demonstrated preclinical anticancer activity *in vitro* [69] and *in vivo* but also biomarker evidence of antiproliferative effects in clinical trials [70,71]. By targeting OXPHOS, metformin is particularly cytotoxic to CSCs [72,73], cells with reduced glucose utilization [74,75], and cells with mutations in OXPHOS complex I [34]. However, the mechanistic effect of this drug is still controversial and seems to be pleiotropic [76–78]: Wang et al. show that pharmacological metformin concentration improves mitochondrial respiration by increasing mitochondrial fission through AMPK-Mff signaling; in contrast, supra-pharmacological metformin concentrations reduce mitochondrial respiration through decreasing adenine nucleotide levels [79]. Other findings suggest that by inhibiting mitochondria complex I, metformin induces OXPHOS inhibition-mediated energy stress that activates AMPK. The activation of the AMPK pathway leads to the inhibition of GLUT1 expression and the anabolic metabolism, including fatty acid synthesis [76]. Moreover, metabolic plasticity can compensate for metabolic restriction by upregulating other metabolic pathways to avoid stress responses. This issue can be overcome by combining metformin with intermittent fasting, a clinically feasible approach to reduce glucose availability, obtaining a synergistic anti-neoplastic effect [80].

1.2.5 Redox homeostasis and ROS detoxification

Reactive oxygen species (ROS) are by-products generated during the OXPHOS or by redox enzymes and metal catalyzed oxidations. The control of ROS levels is essential for cell survival because these molecules can cause direct damage to the cell membrane, proteins, lipids, and nucleic acids (e.g., DNA double-strand breaks), leading to cell death [81].

Compared to healthy cells, cancer cells have aberrant ROS homeostatic characteristics; in many types of tumors, cancer cells show higher ROS levels supporting their growth, proliferation, metastasis, and survival [82]. High ROS production in cancer cells can be driven by hypoxia [83] and by oncogenic *K-RAS* which produces a constitutively active RAS protein [84].

However, the increased production of ROS in many tumor cells occurs in parallel with increased antioxidant activity, such as the glutathione – glutathione-S-transferase system [85]. Indeed, although in normal cells it is crucial for the removal and detoxification of reactive oxygen species, elevated glutathione (GSH) levels in tumor cells are associated with tumor progression and increased resistance to chemotherapeutic drugs [86]. As a consequence, recent therapies have been developed to target the GSH antioxidant system in tumors in order to lower the therapeutic resistance. An example of this strategy is represented by the inhibition of cysteine/glutamate antiporter protein SLC7A11: cysteine, indeed, is a precursor for GSH biosynthesis and the blocking of its entrance in the cell can lead to GSH depletion and cell death through ferroptosis. This effect can be reached by treating cells with the drug erastin, which exhibits efficient anti-tumor properties without affecting their normal cell counterparts. Additionally, depletion of glutathione induced by erastin leads to significantly higher cisplatin's cytotoxicity and reduced tumor resistance to this chemotherapy [87].

1.3 Cancer stem cells metabolism

Cancer stem cells (CSCs) are a subpopulation of cells within tumors, owing to the stem cell characteristics of self-renewal, quiescence, differentiation, and the ability to recapitulate the parental tumor when transplanted into a host. CSCs are correlated with the poor clinical outcome due to their contribution to chemotherapy resistance and metastasis [88].

Different reports about CSCs metabolism revealed contrasting results [14]: several studies performed on many tumor types suggest that CSCs are more glycolytic than other differentiated cancer cells [89–91], while many others demonstrate that they have a preference for mitochondrial oxidative metabolism [92–94]. A possible explanation of this discrepancy in literature is that cancer stem cells can adapt their metabolism to microenvironmental changes by conveniently shifting energy production from one pathway to another, or by acquiring intermediate metabolic phenotypes[95]. The observation of a particular phenotype instead of another can be due to the different conditions (e.g., glucose and oxygen concentration) in which experiments have been performed. Moreover, the metabolic phenotype of CSCs appears to be heterogeneous with distinct metabolic programs activated in different subpopulations of cancer cells [96]. These results suggest that the combinatory treatments blocking glycolysis and mitochondrial respiration at the same time may represent a good strategy to eradicate CSC heterogeneity than focusing exclusively on one of these pathways alone [97].

Currently, metabolic therapy against cancer presents several challenges for its efficient application in the clinic. The understanding of cancer metabolic heterogeneity and plasticity is still not completed. Moreover, the mechanisms underlying metabolic rewiring are revealed not to be the same in all cancer types: they can vary based on the tissue of origin, the tumor microenvironment, the phase of cancer progression (e.g.,

primary vs metastatic tumor) and the genetic and epigenetic alterations. Another important challenge is the difficulty to translate the preclinical studies to the clinical ones, that mostly outcome as unsuccessful. Finally, the intrinsic ability of cancer cells, especially CSCs, to switch their metabolic phenotype in response to external stimuli, can lead to cancer cells adaptation and therapeutic resistance to targeted metabolic drugs. Although these potential obstacles can be tough to overcome, the importance of studying metabolism in cancer is evident; in many cases, a promising strategy was demonstrated opting for combinatory therapies in order to increase drug efficacy and reduce cancer resistance to them [98]. Moreover, the emerging power of multi-omics approaches and the development of integrated experimental and computational tools, able to dissect metabolic features at cellular and subcellular resolution, provide unprecedented opportunities for understanding design principles of metabolic (dis)regulation and for the development of precision therapies in multifactorial diseases, such as cancer [99].

1.4 The tumor microenvironment

Tumors are not only composed of heterogeneous populations of cancer cells, but also non-malignant cells and non-cellular elements, such as extracellular matrix (ECM) and soluble factors secreted by the different cell types [100]. This dynamic environment composed of cancer cells, nonneoplastic host-tissue cells, stromal cells, blood and lymphatic vessels, and ECM, is defines as the **tumor microenvironment (TME)** [101] (**Figure 0.4**). As well as in normal organs and tissue the parenchymal cells are supported by connective tissue, the tumor stroma plays an important role in the sustainment of cancer cells. The tumor stroma is composed of abundant extracellular matrix and multiple support cells such as fibroblasts, endothelial cells, immune cells, and mesenchymal stem cells. In solid tumors, non-malignant cells can be recruited locally (tissue-resident) and systemically and comprise mainly fibroblasts, endothelial cells (EC), and innate and adaptive immune cells [102]. Cancer cells as well as fibroblasts,

macrophages, and various lymphocytes secrete cytokines that can accumulate in the tumor microenvironment and mediate communication between the various cell types in the tumor [103]. The tumor-derived cytokines, such as transforming growth factor β and tumor necrosis factor α , are also capable of modifying the protein expression pattern, metabolism, and acid-base regulatory function of fibroblasts, which become **Cancer-Associated Fibroblasts (CAFs)**, and macrophages [104–106]. Moreover, direct cell–cell contacts between cancer cells and stromal cells may play a role, for instance, in metastasis and immune cell infiltration [104]. Among the infiltrated immune cells, **Tumor-Associated Macrophages (TAMs)** represent the most abundant in the TME [106]. Studies have demonstrated that the predominant population of TAMs manifest a M2-like phenotype, characterized by an immunosuppressor state and promotion of pro-tumoral progression (as opposed to M1-like pro-inflammatory phenotype) [107]. Mesenchymal stromal cells (MSC), adipocytes and other bone marrow-derived cells have also been reported [108]. Cancer associated fibroblasts (CAFs) are believed to support the growth and invasion of cancer cells through multiple mechanisms, including metabolic crosstalk [105,109]. For instance, stromal fibroblasts that are deficient in Caveolin 1 (Cav-1) display enhanced catabolism and produce metabolites (lactate, glutamine and ketones) that are used by neighboring cancer cells to fuel oxidative energy production: this behavior is called *reverse Warburg effect* [110]. Moreover, there is evidence that CAFs can perform mitochondrial transfer toward cancer cells [111,112]. CAFs can also recruit immune cells through the release of growth factors and cytokines, causing the secretion of extracellular matrix remodeling factors by immune cells [19,106].

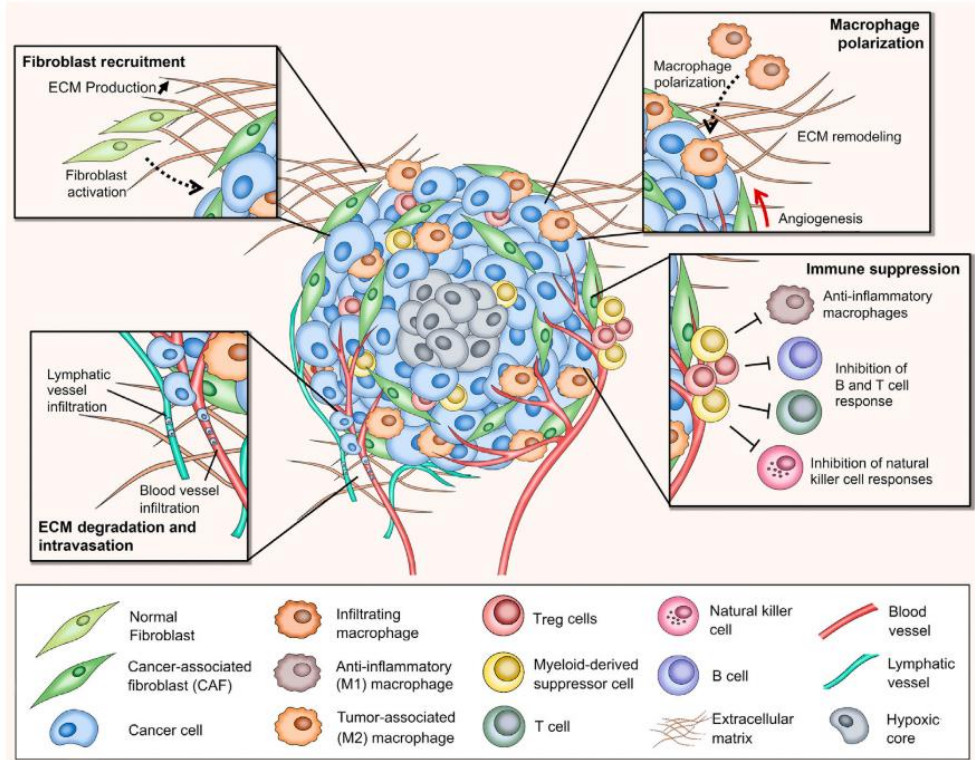


Figure 0.4. Schematic representation of the tumor microenvironment (TME) describing the different elements interacting with cancer cells, such as fibroblasts, immune system cells, extracellular matrix, blood, and lymphatic vessels (Rodriguez et al., 2021 [101]).

The composition of the tumor microenvironment is dynamic, with blood flow and metabolism varying both spatially and temporally during tumor expansion. The acidic tumor microenvironment generated by the metabolic waste products, such as CO_2 from the TCA cycle and H^+ from glycolysis, exported from the cancer cells and CAFs, represents one mechanism by which cancer cells modify the composition and function of the stroma [104].

The role of the TME in tumorigenesis, tumor progression, invasion and metastasis has been acknowledged over recent decades and is today unquestionable [113]. Moreover, the TME has been increasingly implicated in the modulation of drug response and resistance [102,114]. Therefore, the use of therapeutic agents targeting TME-mediated signaling or TME composition has been proposed, such as the drugs that inhibit matrix

metalloproteinase (MMP) activity [115], disrupt angiogenesis [116] or immunomodulators (e.g., immune checkpoint inhibitors) [117].

1.5 *In vitro* models of the tumor microenvironment

As in many other fields of medical research, the process of drug discovery in cancer research needs preclinical studies on *in vitro* cell cultures. The most common model of cancer *in vitro* is represented by two-dimensional (2D) cultures, because of their cost-effectiveness, simplicity to handle, rapidness of growth and high reproducibility. However, 2D cultures present many limitations, mainly due to their inaccurate representation of cancer tissue, leading to a vast gap between *in vitro* and *in vivo* animal studies that can easily fail due to this hurdle. On the other hand, three-dimensional (3D) cultures, such as spheroids and organoids, have the potential to provide alternative ways to reproduce *in vitro* organs and tissues more accurately in order to bridge the gap between conventional 2D culture models and *in vivo* animal models [33]. Moreover, 3D cultures can be exploited to better recapitulate the tumor microenvironment which comprehends the cell-cell interactions with the involvement of the extracellular matrix. Another way to get closer to model tumors *in vitro* is to grow more than one cell type in the same culture, using co-cultures: by adding elements of the TME it is possible to study the interactions between different cell types, to study the influence of stroma cell on cancer cells and vice-versa. Therefore, these models can represent *in vitro* a much greater similarity with the disease than conventional 2D models, with the outcome of becoming more and more complicated, and consequently needing more advanced instrumental equipment for their study [118,119].

1.5.1 3D cancer models

The aim of studying 3D models in the field of anti-cancer drug discovery is to have a better resemblance of tumor-specific architecture than 2D culture models and to mimic the tumor pathophysiological microenvironment. In 3D cultures, cancer cells should ideally represent many of the characteristics of their *in vivo* counterparts such as proliferation, differentiation, motility and metabolic heterogeneity [33]. **Table 0.1**

compares 2D and 3D cell cultures, explaining the main advantages and disadvantages of both methods.

Table 0.1. Description of the main characteristics of 2D and 3D cell culture models, highlighting pros and cons. The items reported in the table have been compiled using the reviews Jensen et al 2020, Langhans et al 2018 and Costas et al 2016 [120–122] as main sources.

| Characteristic | 2D cell culture | 3D cell culture |
|--|--|--|
| Cell growth direction and shape | Cells grow in monolayer, expanding in two directions, and their shape is flat and elongated | Cells preserve their natural round shape and expand in three directions forming multiple layers |
| Cell exposure to nutrients and oxygen | All cells in the culture are exposed to the same amount of nutrients, growth factors and oxygen | A gradient of nutrients, growth factors and oxygen are created inside the culture; the cells in the outer layers are more largely exposed to these molecules than the ones in the core |
| Homogeneity/ Heterogeneity | The cells are homogeneous in terms of proliferative status, cell cycle phase and death cells distribution inside the culture | An intrinsic heterogeneity is created in the culture: the cells in the outer layers are more proliferative, while an enrichment in quiescent and necrotic cells occurs moving to the central core of the culture |
| Cancer stem cells (CSCs) | CSCs are usually less present | An enrichment of CSCs may occur |
| Cell-cell interactions and cell-ECM interactions | Interactions between cells are less common and ECM is usually poorly developed | Cell-cell communications are common, and the ECM is more developed |
| Drug resistance | Cells often have little resistance to drugs making it appear as though drugs administered to the cells were a successful treatment | Cells are often more resistant to drug treatments, giving a more accurate representation of treatment success or failure |
| Expression levels | Gene and protein expression is often vastly different compared to <i>in vivo</i> models | Gene and protein expression levels are usually more similar to those found from cells <i>in vivo</i> |
| Cost and times | For large-scale studies, are more cost-effective than 3D cultures and can give results in a shorter amount of time | They are typically more expensive and require a larger amount of time for results, but they are still less expensive and |

| | | |
|--|--|---|
| | | time-consuming than <i>in vivo</i> models |
| Technical reproducibility and handling | They are easier to handle and present high reproducibility; results are simpler to interpret | Experimental reproducibility is lower and data interpretation can be more difficult |

According to a recent review [101], 3D culture models can be distinguished into four main groups: cell-based models, cell-ECM based models, microfluidic based models and organoids.

Cell-based 3D models include well-organized cellular aggregates called tumor spheroids. Spheroids can be developed applying different approaches including the use of bioreactors (e.g., suspension/spinner flasks), the liquid overlay technique and the hanging drop technique. The liquid overlay culture is probably the simplest of all 3D cell culture techniques and can be obtained by covering the surface for cell culture with inert substrates (agar, agarose or Matrigel) or using ultra-low attachment plates that are coated with a layer of hydrophilic polymer on the surface that prevents cell attachment and promotes cell aggregation [123]. This technique is cost-effective and enables the formation of highly reproducible spheroids without the requirement of any specific equipment, and can also be applied for heterotypic spheroids [124,125].

Cell-ECM based 3D models aim to mimic the interactions between cancer cells and the extracellular matrix by growing cells inside or upon a scaffold. An ideal scaffold should provide an appropriate environment for cell adhesion, proliferation/differentiation, and migration. For this purpose, cancer cells can be cultured within biomaterials, including decellularized native tissues, or in 3D scaffolds based on ceramics or synthetic and/or natural polymers. Hydrogels are particularly suitable for this purpose since they can be manipulated to modulate chemical-physical and mechanical properties to closely mimic the TME [126,127]. Natural biomaterials for scaffold-based 3D models that can be obtained from tissues and cells include collagen, fibrin, alginate, and chitosan that can be sourced from tissues and cells [128]. Other examples of scaffold mimicking ECM are

decellularized-ECM [129] and Matrigel, a mouse-derived *ex vivo* basement membrane substitute [130].

Another approach emerging in this field is 3D bioprinting: this technique refers to the construction of customized 3D structures under computational control using biocompatible materials to create a scaffold for 3D cellular models [127].

The **microfluidic based** 3D models are formed of platforms called *organ-on-chip* devices, consisting of a network of microfluidic channels that allow the continuous perfusion of cells seeded inside. The main advantage of microfluidics is the ability to design complex 3D culture systems in which various parameters can be modified and controlled independently, such as chemical gradients, cellular localization into separate compartments, and the orientation of tissue interfaces [131]. These models also enable the modelling of vascular system, useful for studies about intra- and extravasation of cancer cells, to understand the mechanisms leading to the metastasization [132].

Moving to more complex and heterogeneous models, **organoids** represent organotypic structures generated by the proliferation and self-organization of a progenitor cell source and can closely mimic the 3D structure and architecture of the tissue from which they were derived [101]. Tumor organoids can be obtained from induced pluripotent stem cells (iPSCs) or patient/mouse-derived tumor xenografts (PDX). PDXs are generated by transplanting freshly derived patient material subcutaneously or orthotopically into immunodeficient mice. Currently, large collections of patient-derived tumors and matching healthy organoids are generated and collected in biobanks [130,133,134].

1.5.2 Homotypic and heterotypic spheroids

Within a properly formed spheroid structure, various proliferating cellular statuses are established: the external layers are typically composed of actively proliferating cells, the intermediate zone is composed of quiescent and senescent cells, while the central core is mainly composed of apoptotic and necrotic cells [135,136]. This spatial organization, which well reproduces the situation of tumor mass *in vivo*, is due to the presence of

gradients of nutrients and oxygen. Indeed, the cells forming the outer layers of the spheroids are exposed to sufficient amounts of nutrients and oxygen and can easily expulse metabolic wastes; on the contrary, the cells at the center of the spheroid experiment a lack of nutrient and growth factors, metabolic waste accumulation (e.g., lactic acid, causing lower pH) and hypoxic conditions [33,121,137]. Cells within 3D spheroids deposit ECM constituents such as collagen (e.g., collagen IV), laminin, fibronectin, proteoglycans, tenascin and other components [138]. Moreover, spheroids ECM-cell interactions (mediated by $\alpha 5$ - and $\beta 1$ - integrin) and cell-cell interactions (mediated by E-cadherins and enforced by desmosomes and dermal junctions [139,140]) lead to increased interstitial fluid pressure, responsible for the impaired penetration of pharmaceuticals by convection [141]. The limited penetration of drugs into the tumor tissue is usually an underestimated aspect of the phenomenon of drug resistance that should be taken into consideration in preclinical modelling for drug screening [142] (**Figure 0.5**). It was observed that cancer cell resistance to drugs can be linked to the hypoxic condition of spheroids' environment, since some chemotherapeutic compounds (e.g., 5-fluorouracil, cisplatin, doxorubicin, and irinotecan) need oxygen to induce an effective anticancer effect through the formation of reactive oxygen species (ROS) that damage cell's membrane and DNA [81,143]. The gradient of oxygen that occurs inside the spheroids is also responsible for the metabolic heterogeneity of this cancer model: the cells in the external region of the spheroid typically have enough oxygen to perform mitochondrial respiration, while cells of the inner region exhibit a more glycolytic metabolism with lactate accumulation due to the lack of oxygen.

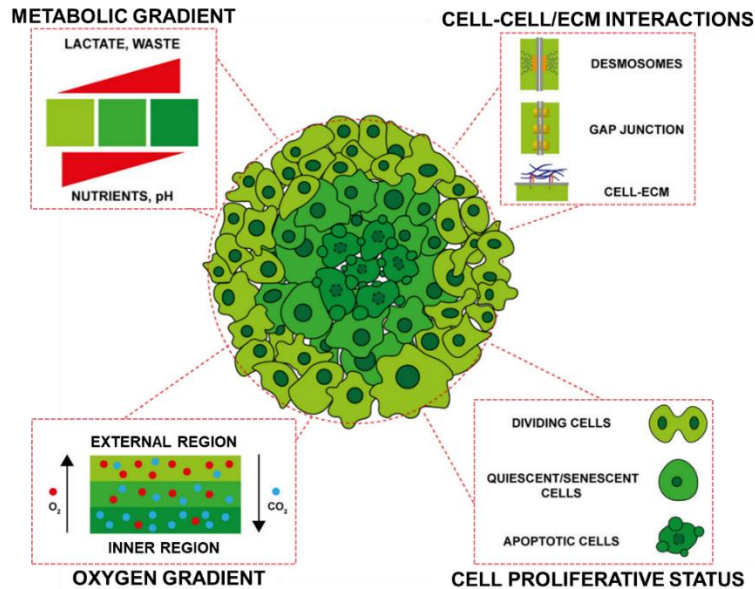


Figure 0.5. Tumor spheroid schematic structure (adapted from Zanoni et al., 2020 [33]).

It was reported that CSCs enriched spheroids can be produced from cancer cell lines through exogenous forced expression of specific sets of transcription factors (e.g., OCT-4, c-Myc), by cell sorting cancer cells expressing CSCs markers or by applying specific culture conditions (e.g., repetitive cycles of hypoxia and reoxygenation, special cell culture media without serum and supplemented with growth factors) [144].

Generally, the term '**homotypic spheroids**' refers to spheroids composed of a single cell type, while those constituted by multiple cell types are called **heterotypic spheroids**. Since fibroblasts represent one of the most abundant populations of stromal cells in the TME, contributing to tumor initiation, progression, metastasis, and response to therapy [145], heterotypic spheroids composed of tumor cells and normal fibroblasts or CAFs (which can represent 40% – 60% of the many tumor's cellular composition, including breast cancer [18]), are widely used in drug discovery studies. Therefore, it was observed that co-culturing with fibroblasts increases the proliferation of several types of cancer cells, such as lung, breast, and pancreatic tumor cells. Moreover, fibroblasts can influence the response to therapeutic agents in heterotypic spheroids *in vitro* [146,147].

1.6 Breast cancer

1.6.1 Breast anatomy

The breasts are accessory sexual organs of the female reproductive system whose structure reflects its special function: the production and secretion of milk for lactation (breastfeeding) after the birth of a child. The external features of the breast include a **nipple** surrounded by a pigmented **areola**. The areolar region is characterized by small, raised areolar glands that secrete lubricating fluid during lactation to protect the nipple from chafing. Breast milk is produced by the **mammary glands**, which are modified sweat glands. The milk itself exits the breast through the nipple via 15 to 20 **lactiferous ducts** that open on the surface of the nipple. These lactiferous ducts each extend to a lactiferous **sinus** that connects to a glandular **lobe** within the breast itself that contains groups of milk-secreting cells in clusters called **alveoli**. The clusters can change in size depending on the amount of milk in the alveolar lumen. Once the milk is made in the alveoli, stimulated myoepithelial cells that surround the alveoli contract to push the milk to the lactiferous sinuses. The lobes themselves are surrounded by adipose (fat) tissue. Supporting the breasts are multiple bands of connective tissue called **suspensory ligaments** that connect the breast tissue to the dermis of the overlying skin (**Figure 0.6**) [148]

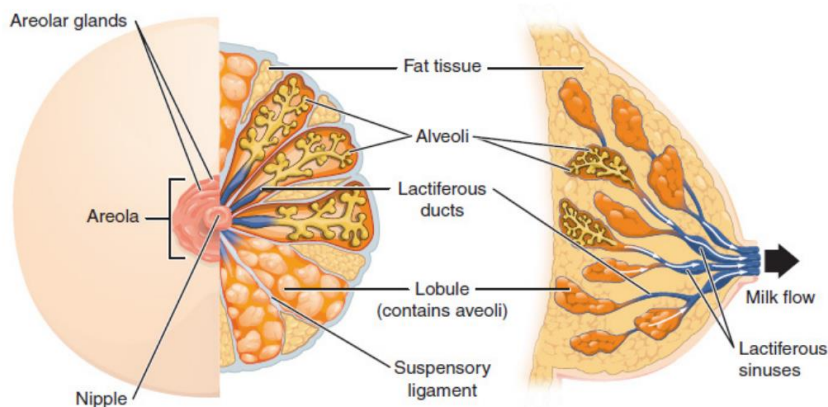


Figure 0.6. Breast anatomy: front view (left) and side view (right). (*Anatomy and Physiology Volume 3* [148]).

The vascularization of the breast is carried out by branches of the axillary artery and the internal thoracic artery. Lymph from the breast lobules, nipple and areola areas collect into the subareolar lymphatic plexus. From here, around 75% of lymph drains into the pectoral lymph nodes, and then into the **axillary lymph nodes**.

Anatomically, the adult breast sits atop the pectoralis muscle, which is atop the ribcage. The breast tissue extends horizontally from the edge of the sternum out to the midaxillary line. The breast tissue is encircled by a thin layer of connective tissue called fascia. The deep layer of this fascia sits immediately atop the pectoralis muscle, and the superficial layer sits just under the skin [149].

In women, the breast develops approximately around the age of 12-13 years and its complete maturation occurs after pregnancy and breastfeeding. The non-pregnant and non-lactating female breast is primarily composed of adipose and collagenous tissue, while mammary glands represent a minor portion of breast volume. During the normal hormonal fluctuations in the menstrual cycle, breast tissue responds to changing levels of estrogen and progesterone, which can lead to swelling and breast tenderness in some individuals, especially during the secretory phase. If pregnancy occurs, the increase in hormones leads to further development of the mammary tissue and enlargement of the breasts. During menopause, when the regular activity of the ovaries is lacking, the phenomena of senile regression prevails [150].

The male breast structure is nearly identical to the female breast, except that the male breast tissue lacks the specialized lobules since there is no physiologic need for milk production by males [149].

1.6.2 Carcinogenesis and risk factors

Breast carcinogenesis is a multistep, multipath, and multiyear disease of progressive genetic and associated tissue damage [151]. It occurs in the epithelial tissue of the mammary gland, in particular in the mammary ducts or lobules. The initiation of breast

cancer is due to transforming (genetic and epigenetic) events in a single cell [152]. The majority of invasive breast cancers are thought to develop from simple hyperplasia without atypical cells to benign lesions such as atypical ductal hyperplasia (ADH), atypical lobular hyperplasia (ALH), ductal carcinoma *in situ* (DCIS) and lobular carcinoma *in situ* (LCIS). These benign lesions are characterized by relative loss of growth control, but they lack the ability to invade and metastasize and, in this sense, are pre-malignant [153]. Subsequent tumor progression is driven by the accumulation of additional genetic changes combined with clonal expansion and selection, that lead to the acquisition of more malignancy features such as invasiveness and metastasis [151] (**Figure 0.7**).

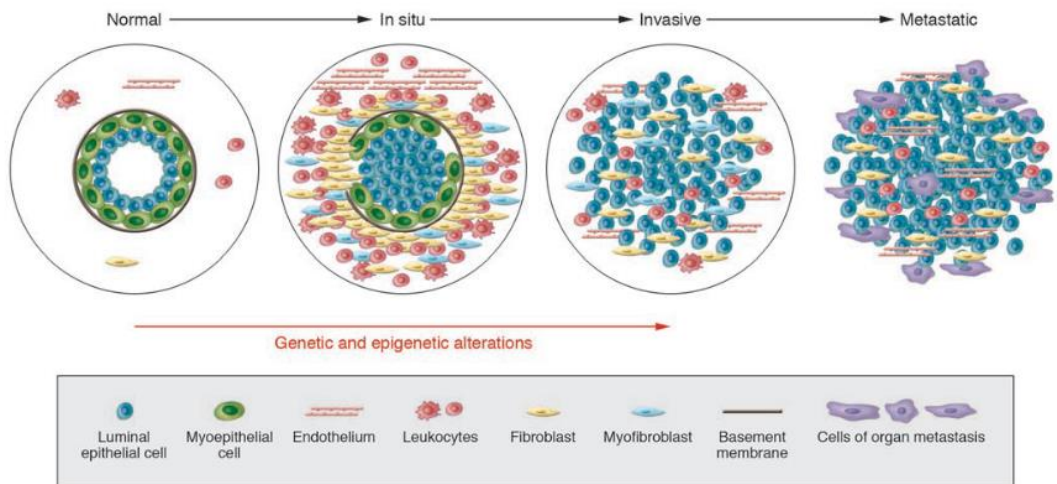


Figure 0.7. Hypothetical model of breast cancer progression: from normal tissue, to *in situ* carcinoma, to invasive and finally metastatic tumor. The figure shows a schematic section of a mammary duct. (Polyak, 2007 [152]).

The reduction of modifiable risk factors is currently the preventive therapy for several kinds of cancer, including breast cancer. Identifying the individual risk and the modifiable factors is a preventive strategy to limit the development and progression of breast cancer [151]. Unless genetic alterations are thought to be at the basis of carcinogenesis, it was estimated that less than 10% of breast cancers can be attributed to an inherited genetic mutation [154]. This type of cancer is more commonly associated

with environmental, reproductive, and lifestyle factors, some of which are potentially modifiable. The main risks factors for breast cancer can be declined in the following categories:

a) **Hormonally mediated risk factors:** Estrogen's carcinogenetic effects have been proposed as two pathways: (1) the activation of estrogen receptor (ER) alters gene expression, increasing proliferation and therefore the probability of mutations; (2) The oxidative metabolism of estrogen into quinone metabolites can lead to the formation of depurination DNA adducts or create ROS, causing oxidative damage to DNA [155]. Despite the stimulating effects of estrogen on hormone receptor-positive tumors being observed in the majority of breast cancers, more recent studies failed to show these associations and sometimes contradict prior assumptions [154]. Some examples of hormone-related risks factors are listed below [151]:

- **Age at menarche and age at menopause:** early age at menarche and late age at menopause are known to increase women's risk of developing breast cancer, but this effect might not be acting merely by lengthening women's total number of reproductive years [156];
- **Oophorectomy:** Bilateral surgical resection of ovaries reduces breast cancer risk, likely because of reductions in levels of circulating ovarian hormones [157];
- **Pregnancy:** parity and early age at first full-term pregnancy are associated with reduction of breast cancer risk [158]. The older a woman is when she has her first full-term pregnancy, the higher her risk of breast cancer;
- **Breastfeeding:** the longer women breastfeed, the more they are protected against breast cancer [159];
- **Oral contraceptives:** the use of oral contraceptives is associated with an increased breast cancer risk, but it depends on the formulation. Any association was found for low-dose estrogen contraceptives [160];

- **Hormone replacement therapy:** long-term use of combined hormone replacement therapy containing estrogen plus progestogen given to relieve the climacteric symptoms of menopause is associated with an increased risk of breast cancer [161];

b) Demographic and lifestyle factors

- **Height, obesity, Body Mass Index (BMI):** increasing height or elevated BMI are associated with an increased risk of breast cancer in postmenopausal women, however, obesity is associated with poor prognosis in women diagnosed with early-stage breast cancer [162];
- **Diet:** based on an extensive review of the literature, the association of dietary fiber, vegetables and fruits, soy and soy products, meat, fish, milk and dairy products, folate, vitamin D, calcium, selenium glycemic index, dietary patterns with breast cancer was classified as “Limited evidence—no conclusion”. Moreover, the association for total fat and breast cancer was classified as “Limited—suggestive” for postmenopausal but not for premenopausal women [163];
- **Physical activity:** physical activity probably protects against breast cancer post-menopause, and there is limited evidence suggesting that it protects against this cancer diagnosed pre-menopause [163];
- **Alcohol and tobacco:** there is substantial evidence that alcohol consumption increases breast cancer risk, but weak association was found between smoking and breast cancer risk [164];
- **Radiations:** it was documented that exposure to radiations, especially during adolescence, increases breast cancer risk [165].

c) Genetic factors: individual risk for breast cancer is increased in individuals carrying a mutation in a predisposing gene and others with several affected relatives with early age of disease onset in whom no specific mutation has been identified [166]. The most frequent hereditary mutations associated with enhanced breast cancer risk can be divided in high-penetrance genes (e.g., BRCA1, BRCA2, TP53, CDH1,

PTEN, and STK11) and moderate-penetrance genes (e.g., ATM, CHEK2, PALB2, NF1, BARD1, BRIP1, MRE11A, NBN, RAD50, RAD51C, and RAD51D)[151]. Approximately 25-28% of germline mutations responsible for breast cancer development are due to BRCA1 and BRCA2 mutations, that encode for proteins involved in DNA double-strand break repair by homologous recombination. The risk in BRCA1 and BRCA2 mutation carriers of developing breast cancer by the age of 70 is 45–87%[167]. It was reported that 78% of tumors arising in BRCA1 carriers are estrogen receptor (ER)-negative, while only 23% of tumors arising in BRCA2 mutation carriers are ER-negative. Furthermore, Human Epidermal Growth Factor 2 (HER2)-overexpression was only observed in approximate 10% of the tumors from mutation carriers. Consequently, 69% of the BRCA1 tumors are triple-negative, which is true for only 16% of the BRCA2 tumors [168].

1.6.3 Epidemiology

Breast cancer was the first most diagnosed cancer worldwide in 2020, surpassing lung cancer, accounting for 2,261,419 new cases, that represent 11.7% of global cancer incidence in both sexes [2]. In female, mammary carcinoma not only represents the first cause of cancer diagnosis but also the first cancer-related death, with 24.5% of incidence and 15.5% of mortality. It was estimated that approximately 13% of women (1 in 8) will be diagnosed with invasive breast cancer in their lifetime [169]; this probability is lower in women younger than 40 years, increases with age but lowers after menopause, with a pick between 55 and 64 years [154].

Although breast cancer is usually considered a female disease, since its insurgence is prevalent in women, actually approximately 1% of breast cancer occurs in males, and the lifetime risk of being diagnosed with breast cancer as a male is 1 in 1000 [154].

Many studies have found that breast cancer incidence and mortality vary by geographical region, age groups and ethnicity. The highest incidence values are reported in high-income and high-middle income countries, which include North-America, Australia/New Zealand and Europe, whereas breast cancer mortality registers

the highest ranges in low-income and low-middle income countries such as Africa and Oceania regions [170,171]. For what concerns the age, it was estimated that 82% of breast cancers are diagnosed among women aged over 50 years, with the median age of diagnosis around 62 years. There is a slight difference among ethnicity, indeed white women have a median age of diagnosis for breast cancer of 63 years, while in black women this parameter is 60 years. Similarly, for mortality the 90% of breast cancer deaths occur in over 50 years age group. The median age at breast cancer death is 68 years overall, 70 years for white women, and 63 years for black women [172].

A recent study revealed that the incidence of breast cancer has increased not only in woman older than 50 years but also in women under 50 years across the globe from 1998 to 2012 [173]. Therefore, since breast cancer incidence is increasing also in younger people, the global augmented risk for mammary carcinoma cannot fully explained by aging of population. Other risks factor associated with this cancer disease might be linked to changes in lifestyle, such as delayed and reduced childbirth [170,173]. According to Rojas et al. [154], less than 10% of breast cancers can be attributed to an inherited genetic mutation, while it is more commonly associated with environmental, reproductive, and lifestyle factors, some of which are potentially modifiable.

1.6.4 Classification and staging

Increased understanding of the intrinsic heterogeneity of breast cancer subtypes is essential to define a correct diagnosis, to predict the behavior of the tumor and so to define the prognosis and chose the most suitable treatment. The two main questions that breast cancer classification wants to answer are: (1) how 'bad' the tumor is (typing and grading)? and (2) how extensive the tumor (staging)? The response to the first question is based on the histologic subtypes and grade, which are detailed in the WHO tumor classification [174,175]. The stage of the tumor is based on the TNM staging, which is based on tumor size (T), nodal status (N) and distant metastasis (M).

The various types of breast cancer classification follow different schemes criteria and serving a different purpose. The major categories are the histopathological type, the

molecular subtypes, grade of the tumor, the stage of the tumor, and the expression of proteins and genes.

The **histological classification** of breast cancers is based on the pathologic growth pattern and divides them into two main groups: *in situ* carcinoma and invasive carcinoma. There are over 20 different histologic types of invasive breast cancers, while the *in situ* carcinoma have fewer subtypes. The main types and subtypes of breast cancer based on histological classification are listed below [176]:

- ***In situ* (pre-invasive) carcinoma:** cancer cells are limited to basement membrane; it accounts for 25% of cases. It is further classified in:
 - **Ductal carcinoma *in situ* (DCIS):** represents 80% of *in situ* carcinomas, sub-classified in Comedo, Cribiform, Micropapillary, Papillary and Solid.
 - **Lobular carcinoma *in situ* (LCIS):** represents 20% of *in situ* carcinomas.
- **Invasive (infiltrating) carcinoma:** it accounts for 75% of cases and it is characterized by cancer cell extension beyond basement membrane. They include:
 - **Infiltrating ductal carcinoma (IDC):** subclassified in well-differentiated, moderately-differentiated and poorly-differentiated basing on nuclear polymorphism, glandular/tubule formation and mitotic rate. They represent 70-80% of invasive lesions.
 - **Infiltrating lobular carcinoma (ILC):** it accounts for 10% of invasive lesions.
 - **Ductal/lobular carcinoma**
 - **Mucinous (colloid) carcinoma**
 - **Tubular carcinoma**
 - **Medullary carcinoma**
 - **Papillary carcinoma**

The classification based on **grading** encompasses microscopic assessment of histologic differentiation in the form of tubule formation, nuclear pleomorphism, and proliferation as indicated by mitotic index. The grade assignment is given by the

summation score of each parameter, that are evaluated with a numerical scoring system of 1 to 3 [174].

The **molecular classification** of breast cancer subtypes is based on the expression of specific molecular markers. The intrinsic subtypes are based on a 50-gene expression signature (PAM50). The surrogate intrinsic subtypes are typically used clinically and are based on histology and immunohistochemistry expression of key proteins: estrogen receptor (ER), progesterone receptor (PR), human epidermal growth factor receptor 2 (HER2) and the proliferation marker Ki67. Global gene expression profiling studies classified breast cancers into 5 subtypes by hierarchical clustering (**Table 0.2** and **Figure 0.8**).

Table 0.2. Breast cancer molecular classification and main characteristics [177]

| INTRINSIC SUBTYPES | SURROGATE INTRINSIC SUBTYPES |
|--|--|
| <p>Basal like</p> <ul style="list-style-type: none"> • TP53 mutations • Genetic instability • BRCA mutations • Medullary-like histology • Poorly differentiated | <p>Triple-negative (TNBC)</p> <ul style="list-style-type: none"> • ER⁻ PR⁻ HER2⁻ • High grade • High Ki67 index • Poor prognosis • Metaplastic, adenoid cystic, medullary-like and secretory |
| <p>Claudin-low</p> <ul style="list-style-type: none"> • Largely triple-negative • Metaplastic <p>[Normal-like subtype was an artefact: the expression of normal breast components is due to low tumor cellularity]</p> | |
| <p>HER2-enriched</p> <ul style="list-style-type: none"> • HER2 amplification • GRB7 amplification • PIK3CA mutation • TOPO2 and/or MYC amplification • Pleiomorphic lobular and micropapillary histology | <p>HER2-enriched (non-luminal)</p> <ul style="list-style-type: none"> • ER⁻, PR⁻, HER2⁺ • High grade • High Ki67 index • Aggressive but responds to targeted therapy • Intermediate prognosis • No special type of histology |
| <p>Luminal B</p> <ul style="list-style-type: none"> • PI3KCA mutations (40%) • ESR1 mutations (30–40%) • ERBB2 and ERBB3 mutations • Micropapillary and atypical lobular histology | <p>Luminal B-like HER2⁺</p> <ul style="list-style-type: none"> • ER⁺ but lower ER and PR expression than luminal A-like • HER2⁺ • Higher grade • High Ki67 index • Responds to targeted therapy |

| | |
|--|---|
| | <ul style="list-style-type: none"> • Intermediate prognosis • Pleiomorphic histology |
| | <p>Luminal B-like HER2⁻</p> <p>Same as Luminal B-like HER2⁺ but:</p> <ul style="list-style-type: none"> • HER2⁻ • Micropapillary and lobular pleiomorphic histology |
| <p>Luminal A</p> <ul style="list-style-type: none"> • Activation of <i>ESR1</i>, <i>GATA3</i>, <i>FOXA1</i>, <i>XBP1</i> • Tubular cribriform and classic lobular histology | <p>Luminal A-like</p> <ul style="list-style-type: none"> • Strongly ER⁺ and PR⁺ • HER2⁻ • Low proliferation rates • Low grade • Low Ki67 index • Good prognosis • Tubular cribriform and classic lobular histology |

According to a cross-sectional study including 320,124 women diagnosed with breast cancer from 2010 to 2016, the breast cancer molecular subtypes are distributed as follows [178]:

- 72.6% luminal A
- 11.2% luminal B
- 4.8% HER2-enriched
- 11.3% triple-negative

A more simplified molecular classification that divides breast cancers only in 3 groups, i.e., luminal (hormone responsive: ER+PR+HER-/+), HER2+ (ER-PR-HER2+), and TNBC (ER-PR-HER2-), can be found in literature.

The TNM staging system is applied for the classification of many types of tumors, with little variations. For breast cancer, the TNM system describes the tumor as follows [179]:

- **Tumor (T).** The size and location of the tumor.
 - **TX:** Primary tumor cannot be assessed
 - **T0:** No sign of a primary tumor in the breast

- **Tis:** Carcinoma *in situ*
- **T1:** The tumor size is ≤ 20 mm. It includes 4 more subgroups basing on tumor size.
- **T2:** The tumor size is > 20 mm but ≤ 50 mm
- **T3:** The tumor is > 50 mm
- **T4:** The tumor has grown into the chest wall and/or into the skin or an inflammatory breast cancer is present. It includes 4 subgroups basing on the inflammatory state.
- **Lymph Node (N).** The size and location of lymph nodes where cancer has spread.
 - **NX:** The lymph nodes cannot be assessed
 - **N0:** No sign of cancer in the lymph nodes, or tiny clusters of cancer cells ≤ 0.2 mm in the lymph nodes
 - **N1:** Cancer has spread to 1 to 3 lymph nodes (axillary, near the breastbone or sentinel), with dimensions ≤ 2 mm. It includes 4 subgroups.
 - **N2:** Cancer has spread to more than 3 lymph nodes and its dimension is > 2 mm. it includes 2 subgroups.
 - **N3:** Cancer spread to the lymph node is more severe (more lymph nodes involved, more distant to the primary tumor site, > 2 mm). It includes 4 subgroups.
- **Metastasis (M).** Cancer has spread to other parts of the body.
 - **M0:** There is no sign that cancer has spread to other parts of the body.
 - **M1:** Cancer has spread to other parts of the body, most often the bones (67%), lungs (37%), liver (41%), or brain (13%) [177].

Breast cancers that are diagnosed as metastatic at first presentation (*de novo*) account for 25–28% of metastatic breast cancers [180]. The intrinsic molecular classification of breast cancer influences the profile (timing, sites) of metastatic disease: Luminal A tumors tend to relapse late (after 5 years of first presentation) and have a tropism for bone and lymph nodes (as do luminal B, HER2-negative tumors). TNBCs are prone to early recurrences (within 2–3 years of first presentation) and tend to form visceral (lung)

and brain metastases. Since the era of anti-HER2 targeted therapy, HER2-positive breast cancers show better prognosis, but they escape therapy through brain metastasis [181].

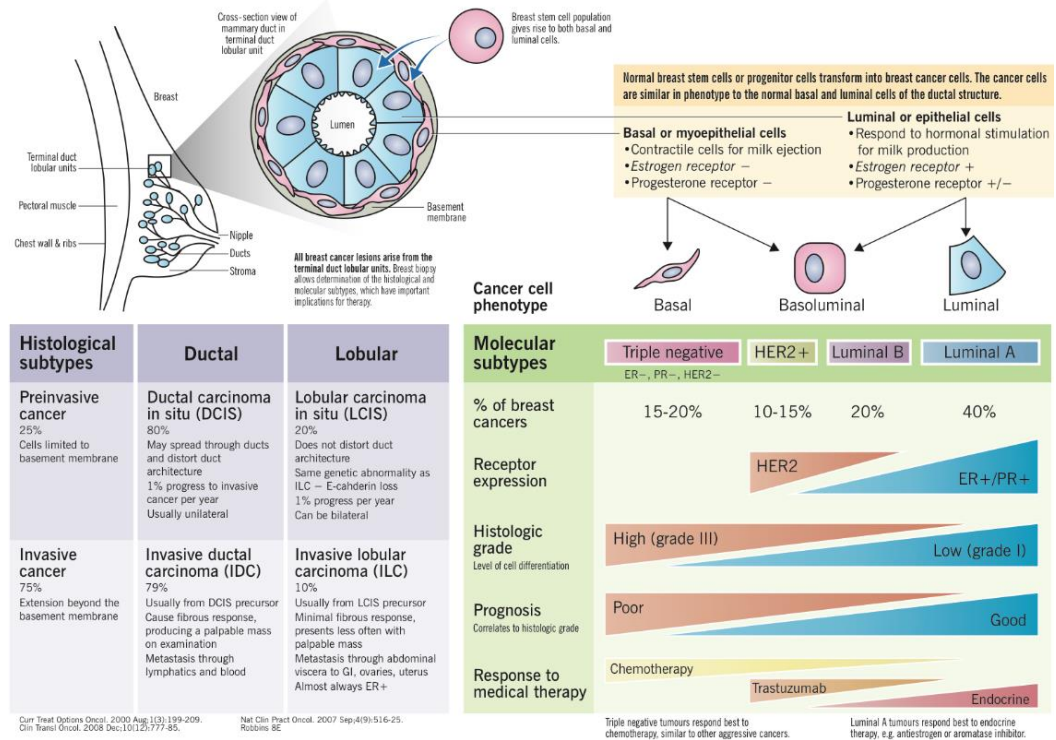


Figure 0.8. Schematic representation of the main histologic and molecular subtypes of breast cancer and main characteristics (Wong and Rebelo [182]).

1.6.5 Diagnosis and therapy

Breast cancer can be diagnosed starting from a clinical breast exam, in which the doctor feels the breast and ascertains if something unusual is present. If something suspicious is detected, more accurate examinations can be performed, such as ultrasound exam, mammogram, and mammography (X-ray of the breast). In case these exams confirm the suspect of a tumor, a fine-needle aspiration (FNA) biopsy (i.e., removal of tissue or fluid, using a thin needle) or, if the latter is not sufficient for accurate diagnosis, a more invasive core biopsy (i.e., removal of tissue using a wide needle) or an excisional biopsy can be performed (i.e., removal of an entire lump of tissue) [179].

The breast biopsy is then subjected to a histologic exam for a more accurate diagnosis, in order to define the histological subtype, the molecular subtype, and the grading of the tumor. When a breast cancer has been diagnosed, to investigate the staging of the tumor and, more specifically if lymph nodes invasion or metastasis are present, a Magnetic Resonance Imaging (MRI) scan, a Computed Tomography (CT) scan, or a Positron Emission Tomography (PET) are performed. Moreover, genomic testing can be performed to identify the genetic mutations of the tumor for a more accurate classification and diagnosis.

A correct diagnosis is essential to predict the prognosis and guide the most effective therapy.

For non-metastatic breast cancer, the main goals of therapy are eradicating tumor from the breast and regional lymph nodes and preventing metastatic recurrence. A diagram of early breast cancer therapy approach based on molecular subtype is presented in **Figure 0.9**. The first line therapy for many breast cancers is the surgical remotion with or without local adjuvant radiotherapy (i.e., adjuvant therapy is administered post-surgery, to remove eventually cancer cells not removed with surgery), and **chemotherapy** as adjuvant or neo-adjuvant (before surgery, to reduce the tumor size). The principal chemotherapeutic drugs are Adriamycin, cyclophosphamide, paclitaxel, and docetaxel. For hormone responsive breast cancers (luminal ER+PR+) and HER2+ subtypes but not for triple-negative breast cancers, a targeted therapy is available. For hormone responsive tumors, **endocrine therapy** targets ER signaling by inhibiting the production of hormones (aromatase inhibitors and gonadotropin-releasing hormone agonist (GnRH) agonists) or by interfering with the binding between estradiol and estrogen receptor (e.g., Tamoxifen and raloxifene are partial nonsteroidal estrogen agonists). Patients with ERBB2-amplified (HER2+) benefit from ERBB2-targeted therapy, including monoclonal **anti-HER2 antibodies** (such as trastuzumab and pertuzumab) and small-molecule tyrosine kinase inhibitors (such as lapatinib and neratinib) [183].

Currently, metastatic breast cancer remains incurable in virtually all affected patients. The same basic categories of systemic therapy are used in metastatic breast cancer as in neoadjuvant/adjuvant approaches. Local therapy modalities (surgery and radiation) are typically used for palliation only in metastatic disease [183].

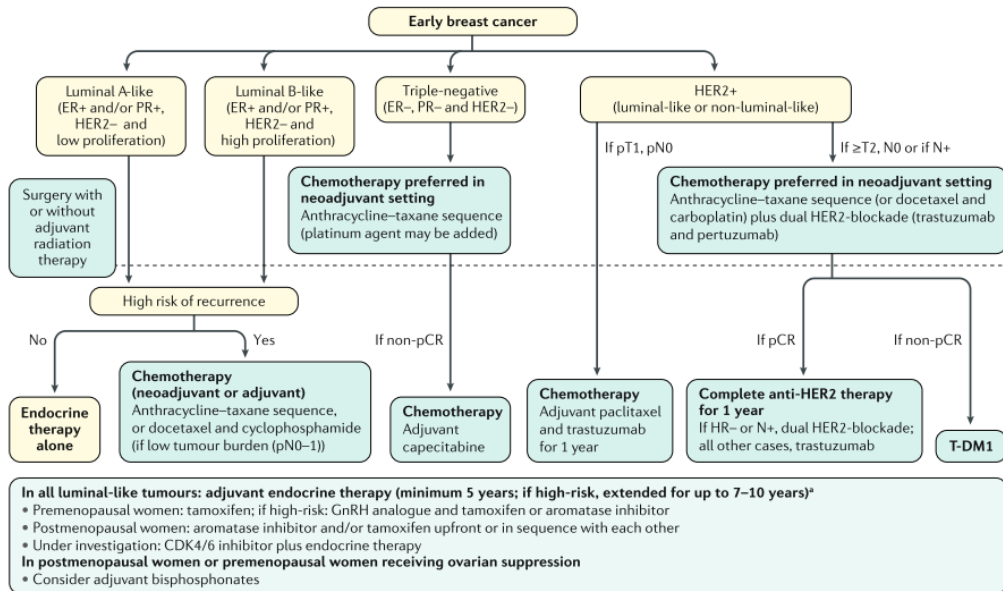


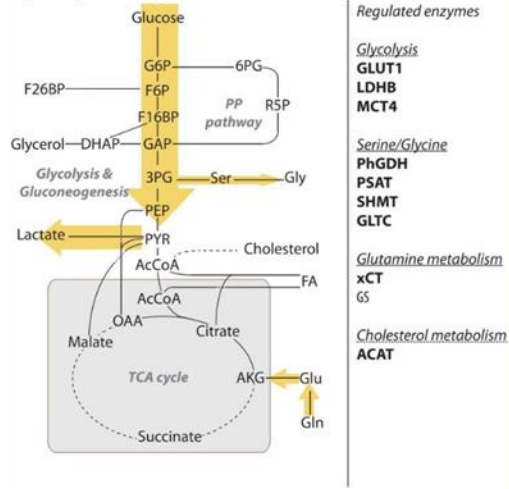
Figure 0.9. Flowchart of the main therapies for early-diagnosed breast cancers based on tumor burden or subtype. GnRH: gonadotropin-releasing hormone; HR: hormone receptor; PR: progesterone receptor; N: node status; T: tumor grade; T-DM: ado-trastuzumab emtansine; pCR: pathological complete response (Harbeck et al [177]).

1.6.6 Breast cancer metabolism

Breast cancer metabolism is characterized by wide heterogeneity since it changes dependently to the molecular subtype. Many triple-negative breast cancers display a classical Warburg metabolism with high glucose uptake and increased lactate secretion even in the presence of oxygen. *In vivo* measurements of glucose uptake rates using ^{18}F FDG-PET demonstrated that the highly glycolytic phenotype of triple-negative breast cancers is not an artifact from cell culture conditions [184]. The same study also revealed a strong correlation between increased glucose uptake and the proliferation index (through *Ki-67* nuclear staining), highlighting the evidence that this metabolic trait

of triple-negative breast cancers is linked with tumor aggressiveness. In line with the increased glucose uptake, several studies have shown an increased expression of glucose and lactate transporters (MCT), as well as lactate dehydrogenase, which interconverts pyruvate and lactate [185]. Moreover, it was observed that the activation of OXPHOS metabolism in TNBCs led to decreased metastasis and reduced tumor growth [186]. This activation was triggered by increasing the activity of complex I of the respiratory chain, which results in an increased NAD⁺/NADH ratio which decreases mTORC1 activity and subsequently leads to autophagy [187]. These data suggest that the combination of decreased oxidative phosphorylation with increased glycolysis allows fast proliferation in certain types of triple-negative breast cancers. Triple-negative breast cancers have been shown to display an increased uptake of glutamine and cholesterol, while the *de novo* synthesis of these metabolites was decreased [188,189]. Contrary to triple-negative breast cancer, estrogen receptor positive breast cancers have a high glutamine synthetase activity and increased glutamine secretion, indicating a less glutamine-dependent phenotype [189]. In contrast to triple-negative breast cancers, many estrogen receptor positive breast cancers display the so-called *reverse Warburg effect*: the phenomenon, whereby cancer associated fibroblasts (CAFs) take in glucose and release lactate and pyruvate to cancer cells. The cancer cells use the secreted lactate and pyruvate to fuel their TCA cycle [60]. Thus, in this complex interaction, the CAFs display a glycolytic metabolism, while the cancer cells rely on oxidative metabolism [190]. The interactions of cancer cells with the stroma in the TME is often bilateral: cancer cells promote the metabolic reprogramming of stromal cells (fibroblasts become CAFs) and CAFs interact with cancer cells in the reverse Warburg effect [110,191]. **Figure 0.10** schematically represents the main active metabolic pathways in TNBC (A) an ER+ (B) breast cancer subtypes.

A) Triple-negative breast cancer



B) Estrogen-receptor positive breast cancer

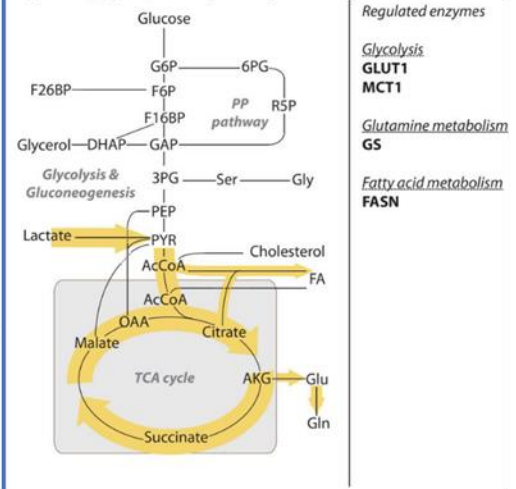


Figure 0.10. Schematic representation of (A) Triple-negative breast cancer and (B) Estrogen-receptor positive breast cancer metabolism (Elia et al.[192]).

1.7 Bladder cancer

1.7.1 Bladder anatomy

The bladder is a hollow muscular organ that functions as a temporary storage reservoir for urine. In sectional view, the mucosa lining the urinary bladder is usually thrown into folds, or rugae, that disappear as the bladder stretches and fills with urine. The triangular area bounded by the ureteral openings and the entrance to the urethra constitutes the trigone of the urinary bladder. The trigone acts as a funnel that channels urine into the urethra when the urinary bladder contracts [150](**Figure 0.11**). The wall of the bladder contains a mucosa of transitional epithelium, a submucosa, and muscularis layers. The muscularis layer consists of three layers: inner and outer longitudinal smooth muscle layers, with a layer of circular muscle sandwiched between. Collectively, these layers form the powerful detrusor muscle of the urinary bladder. Contraction of this muscle compresses the urinary bladder and expels its contents into the urethra. A layer of serosa covers the superior surface of the urinary bladder [150].

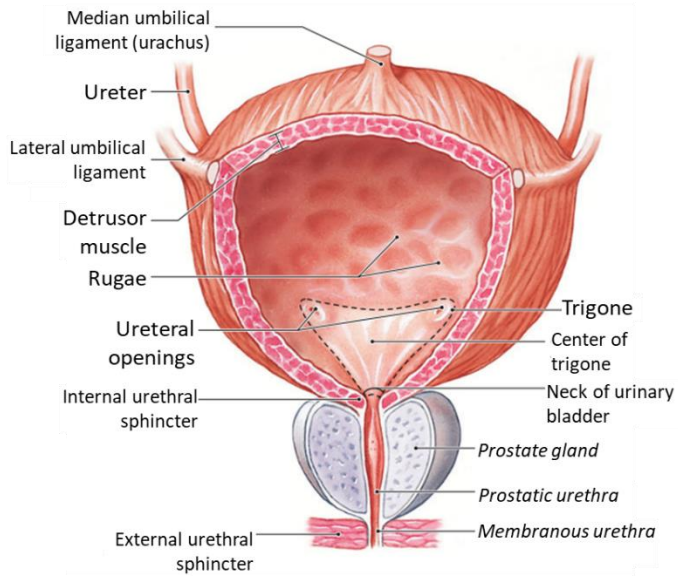


Figure 0.11. Schematic representation of a male bladder section [150].

1.7.2 Classification, grading and staging

The first classification of bladder cancer was proposed by Mostofi et al. in 1973 [193]. In this study, the histological typing of urinary bladder tumors was based on the degree of anaplasia of tumor cells, defined as increased cellularity, nuclear crowding, disturbance of cellular polarity, failure of differentiation from the base to the surface, polymorphism, irregularity in cell size, variations of shape and chromatin pattern in nuclei, displaced or abnormal mitotic figures, and giant cells. The scale had three grades: **grade 1** was defined as tumors with the lowest degree of anaplasia (well-differentiated), whether **grade 3** had the most severe degree of anaplasia (poorly differentiated) and **grade 2** is an intermediate condition (moderately differentiated). In 1998 WHO and the International Society of Urological Pathology (ISUP) introduced the term “papillary urothelial neoplasm of low malignant potential” (**PUN-LMP**) and the previous classification was reviewed and corrected with: PUNLMP (low malignancy potential), low-grade urothelial carcinoma, and high-grade carcinoma [194]. **Low-grade** urothelial carcinoma rarely invades the muscular wall of the bladder or spreads to other parts of

the body. Patients rarely die from low-grade bladder cancer. On the contrary, **high-grade** has a strong tendency to invade the muscular wall of the bladder and spread to other parts of the body. High-grade bladder cancer is treated more aggressively than low-grade bladder cancer and is much more likely to result in death [195]. Later, in 2004 another review by the WHO led to the publication of a new histological classification that provides different patient stratification between the grades of the older 1973 classification. This 2004 grading scale has been again updated in 2016 by WHO [196].

Bladder cancer is also divided into muscle-invasive and non-muscle invasive disease, based on invasion of the muscularis propria (also referred to as the detrusor muscle), which is the thick muscle deep in the bladder wall:

- **Muscle-invasive** bladder cancer (**MIBC**) is much more likely to spread to other parts of the body and is generally treated by either removing the bladder or treating the bladder with radiation and chemotherapy. As noted above, high-grade cancers are much more likely to be muscle-invasive than low-grade cancers.
- **Non-muscle invasive** bladder cancer (**NMIBC**) can often be treated by removing the tumor(s) via a transurethral approach. Sometimes chemotherapy or other treatments are introduced into the bladder with a catheter to help fight the cancer [195].

From 2017, the updated **TNM** classification is the most recommended system for the classification of the depth of tumor invasion (**staging**) and along with the 2004/2016 WHO grading system (which is used for histological classification) are the latest and most accurate guidelines at the time being. The current TNM staging classification of urothelial bladder cancer is reported in the following bulleted list [197]:

- **Tumor (T)**. The location of the primary tumor.
 - **TX**: Primary tumor cannot be assessed
 - **T0**: No sign of a primary tumor
 - **Ta**: Non-invasive papillary carcinoma
 - **Tis**: Carcinoma *in situ* ('flat tumor')

- **T1:** Tumor invades subepithelial connective tissue
- **T2:** Tumor invades muscle
 - **T2a:** tumor invades superficial muscle (inner half)
 - **T2b:** tumor invades deep muscle (outer half)
- **T3:** Tumor invades perivesical tissue
 - **T3a:** microscopically
 - **T3b:** macroscopically (extravesical mass)
- **T4:** Tumor invades any of the following: prostate stroma, seminal vesicles, uterus, vagina, pelvic wall, abdominal wall.
 - **T4a:** tumor invades prostate stroma, seminal vesicles, uterus, or vagina
 - **T4b:** tumor invades pelvic wall or abdominal wall
- **Lymph Node (N).** The location of lymph nodes where cancer has spread.
 - **NX:** regional lymph nodes cannot be assessed
 - **N0:** no sign of cancer spread in the lymph nodes
 - **N1:** metastasis in a single lymph node in the true pelvis (hypogastric, obturator, external iliac, or presacral).
 - **N2:** metastasis in multiple regional lymph nodes in the true pelvis (hypogastric, obturator, external iliac, or presacral)
 - **N3:** metastasis in common iliac lymph node(s).
- **Metastasis (M).** Cancer has spread to other parts of the body.
 - **M0:** There is no sign of distant metastasis.
 - **M1:** there is sign of one or more distant metastasis
 - **M1a:** tumor has spread to non-local lymph nodes
 - **M1b:** tumor has spread to other distant metastatic sites

Additional letters can be added to the TNM staging system, and they are reported before the letter T in lowercase: the letter *m* (multiple) indicates the presence of more than one primary tumor, the letter *c* means that the tumor was staged clinically, while the letter *p* means that the tumor was staged pathologically.

Figure 0.12 shows a schematic representation of the main types, grades, and stages of bladder cancer.

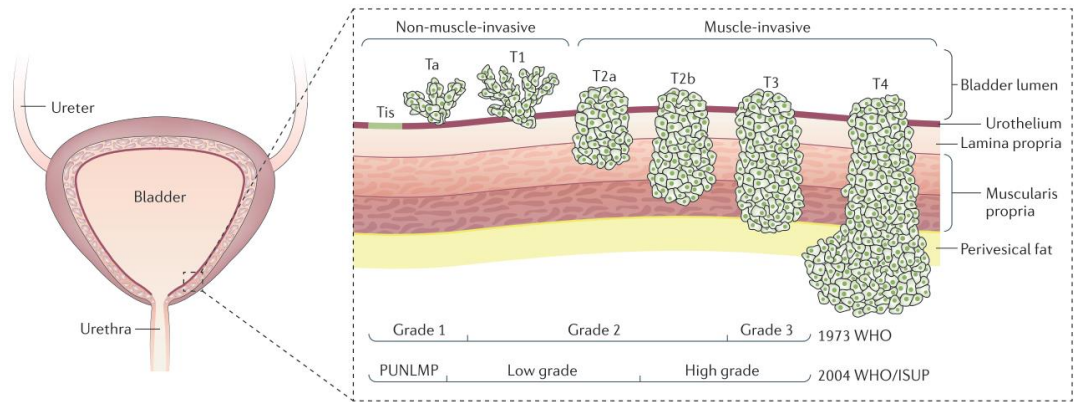


Figure 0.12. Types, grades and stages of bladder cancer (Sanli et al.[198]).

Heterogeneity in the clinical outcomes of patients suggests that biologically relevant subtypes might exist within and between NMBIC and MIBC. Transcriptional profiles currently provide the best-defined **molecular subtypes**. The initial Lund study of tumors of all grades and stages defined the following five subtypes: urobasal A, genomically unstable, (immune cell) infiltrated, squamous cell carcinoma-like and urobasal B [199]. These subtype assignments did not absolutely correlate with tumor grade and stage. Subsequently, three major transcriptional profiling studies focused on MIBC and one focused on NMIBC. To date, these classifications have used different nomenclatures [198]. **Figure 0.13** represent the overlapping between different nomenclatures of bladder cancer molecular subtypes.

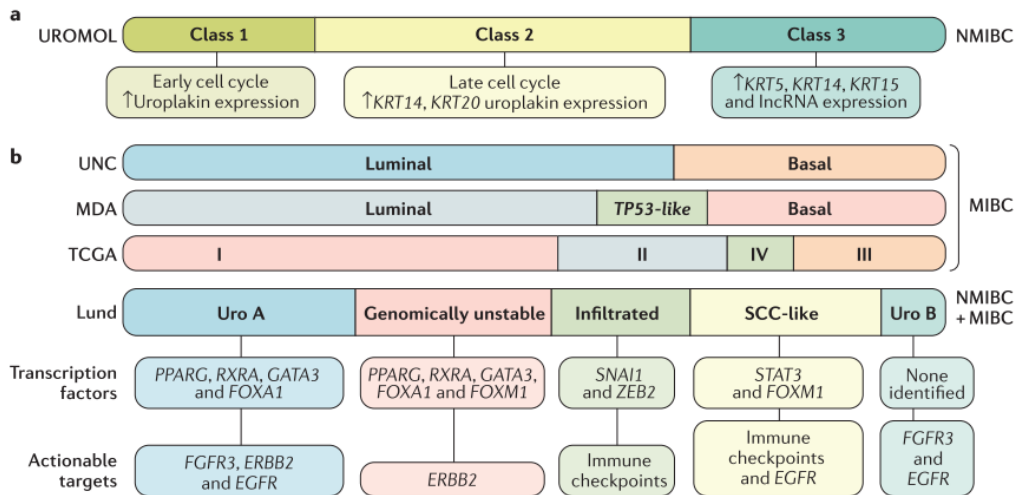


Figure 0.13. Molecular subtypes of bladder cancer: **a)** Data from the UROMOL study[200]. **b)** Nomenclature and overlap of bladder cancer, expression subtypes defined by the University of North Carolina (UNC)[201], MD Anderson Cancer Center (MDA)[202], The Cancer Genome Atlas Network (TCGA), and Lund University (Lund) [199] project (Sanli et al. [198]).

1.7.3 Epidemiology and risk factors

Bladder cancer is the 10th most diagnosed cancer worldwide considering both sexes, and the 6th most common cancer in men. GLOBOCAN2020 estimates 573,278 new cases (3% of all sites of cancer) of bladder cancer worldwide in 2020, and 212,536 cancer of bladder cancer related deaths (2.1% of total cancer cases). The incidence of bladder cancer is higher in men than in women: 77% of bladder cancer incidence and 75% of bladder cancer related deaths occur in males [2]. Bladder cancer incidence is also influenced by geographical factors, with the highest frequency of cases in Southern Europe (Greece, Spain, and Italy), Western Europe (Belgium and the Netherlands), and Northern America, although the highest global rates are in Hungary among women [203]. The observed geographic patterns of bladder cancer incidence worldwide appear to reflect the prevalence of tobacco smoking, although infection with *Schistosoma haematobium*, and other risk factors such as occupational exposures to aromatic amines and other chemicals affecting workers in the painting, rubber, or aluminum industries and arsenic contamination in drinking water are major causes in selected

populations [203]. Other risk factor to develop bladder cancer are the family history of bladder cancer and the presence of genetic mutations in HRAS, Rb1, PTEN/MMAC1, NAT2, and GSTM1 [195].

1.7.4 Carcinogenesis

Bladder cancer generally originates from the epithelium (urothelium) that covers the inner surface of the bladder, and urothelial carcinomas represent the most common type of bladder cancer [198]. Pathological and clinical information from mouse models and human samples indicate that urothelial carcinoma develops via two distinct pathways, giving rise to papillary non-muscle invasive bladder cancers (NMIBCs) and non-papillary (solid) muscle-invasive bladder cancer (MIBCs). In humans, the predicted precursors of NMIBC are flat or papillary urothelial hyperplastic lesions. Two common alterations in NMIBC, deletion of chromosome 9 and a point mutation in FGFR3 (which encodes fibroblast growth factor receptor 3), are also evident in these hyperplastic precursors [204]. It has been documented a high risk of development of MIBC in patients with dysplasia or carcinoma *in situ*, and these lesions share features with high-grade and invasive bladder cancers. These features facilitate cell proliferation and include mutations in TP53 and stabilized TP53 expression [205]. Moreover, upregulated expression of CK20 and HER2, and reduced expression of PTEN with concomitant upregulation of the PI3K pathway are shared features [206].

1.7.5 Diagnosis and therapy

The presence of blood in urine (hematuria) can be a sign of bladder cancer; it could change the color of urine ranging from pink to dark red or even orange. Sometimes there are not chromatic changes, but blood presence could be also found via urinalysis (urine testing) [207]. Bladder cancer may also cause the necessity to urinate more often or giving a sense of burning or even pain during micturition, even thou these symptoms are more likely to be caused by a urinary tract infection, bladder stones, an overactive bladder, or an enlarged prostate (in men) [207].

There are different approaches to detect bladder cancer. If some of suspicious signs of bladder cancer are present, the doctor might do a digital rectal exam (DRE), during which a gloved, lubricated finger is put into the rectum, or, for female patients, a pelvic exam can be performed. During these exams, the doctor can sometimes feel a bladder tumor, determine its size, and feel if and how far it has spread. If some anomalies are detected, the urologist can prescribe **urine tests** such as urinalysis (to check the presence of blood in urine), a urine cytology (to check the presence of cancer or pre-cancer cells in urine), a urine culture (to check the presence of urinary tract infections), or a urine tumor marker tests (to detect the presence of cancer biomarkers in urine) [207].

Evaluation of patients suspected of having bladder cancer is performed using **cystoscopy**, which is an endoscopic procedure performed with a flexible scope and with local anesthesia. Any abnormal finding, such as reddish flat, papillary, or solid lesions, requires histological evaluation because benign conditions, such as inflammatory diseases, can mimic bladder cancer. Histology can be obtained by Transurethral Resection of Bladder Tumor (**TURBT**), an endoscopic procedure that enables a thorough visualization of the bladder and appropriate resection with an attempt to include muscle for accurate staging [198]. TURBT is performed by passing a resectoscope through the urethra. Small tumors can be resected *en bloc* with the electrified wire loop of the resectoscope, whereas larger tumors are resected in multiple fractions. TURBT has not only a diagnostic role but also a therapeutic one and can be a sufficient and potentially curative therapy depending on the pathological features of the tumor.

Other specific approaches for bladder cancer diagnoses can be imaging tests such as Intravenous pyelogram (IVP, an X-ray of all of the urinary system taken after injecting an intravenous dye), Retrograde pyelogram, Computed tomography (CT), Magnetic resonance imaging (MRI), ultrasound, chest x-ray (to detect eventual lung metastasis), and bone scan (to detect eventual bone metastasis) [208].

Stratification of patients into low-, intermediate-, and high-risk groups is essential for deciding appropriate use of adjuvant intravesical chemotherapy or bacillus Calmette-

Guérin (BCG) instillations. Surgical removal of the bladder should be considered in case of BCG-unresponsive tumors or in NMIBCs with the highest risk of progression. Although TURB by itself can eradicate a Ta-T1 tumor completely, these tumors commonly recur and can progress to MIBC. It is therefore necessary to consider adjuvant therapy in all patients. Immediate single instillation (SI) has been shown to act by destroying circulating tumor cells after TURB, and by an ablative effect on residual tumor cells at the resection site and on small, overlooked tumors. An SI with mitomycin C (MMC), epirubicin, or pirarubicin has shown a beneficial effect. The need for further adjuvant intravesical therapy depends on prognosis. In low-risk patients an SI reduces the risk of recurrence and is considered the standard and complete treatment. For other patients, however, an SI remains an incomplete treatment because of the considerable likelihood of recurrence and/or progression[197]. A complete diagram showing the treatment approach to eradicate NMIBC after TURBT is represented in **Figure 0.14**.

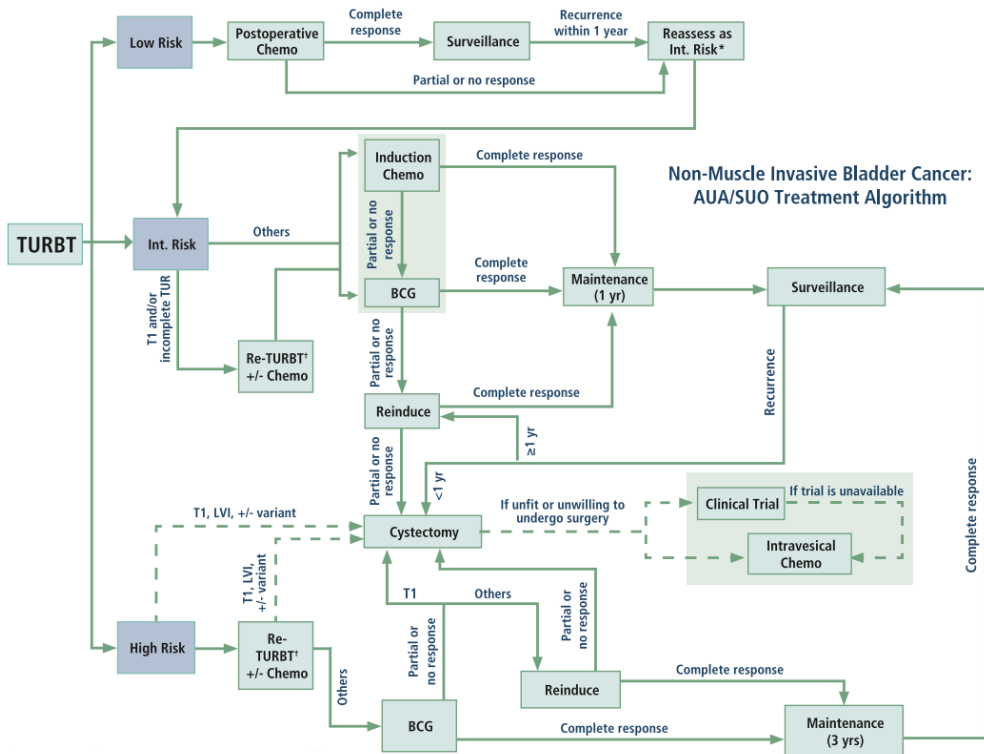


Figure 0.14. AUA/SUO treatment algorithm for Non-muscle invasive bladder cancer (Chang et al. [209]).

1.7.6 Bladder cancer metabolism

Unlike other tumor types such as breast, melanoma, colorectal cancer, lung adenocarcinoma, no effective molecular targets for therapy and no biomarkers with a predictive value have yet been identified in bladder cancer. However, different molecularly targeted agents against EGFR (epidermal growth factor receptor), FGFR (Fibroblast Growth Factor Receptor), mTORc1 (mammalian target of rapamycin complex 1), PDGFR (Platelet-derived Growth Factor Receptor), VEGFR (Vascular Endothelial Growth Factor Receptor) and many others are under evaluation [210].

In the previous paragraphs was widely discussed about the importance of metabolic rewiring in cancer and in finding new therapeutic targets in this field. Recently, a complex analysis that integrated data of metabolic alterations (involving amino acid, nucleotides, lipids and glycolysis pathways) from targeted mass-spectrometry with transcriptome data, identified a molecular signature of 30 metabolic genes, whose the up-regulation was associated with tumor progression and poor prognosis [211].

Consistently, another study highlighted that bladder cancer progression is associated with alterations in cells glycolytic profile, namely the switch from glucose to pyruvate consumption in the more aggressive stage [212]. The first steps of glycolysis are linked to the Pentose Phosphate Pathway (PPP), which plays an important role in oxygen-independent glucose conversion to ribose for nucleic acid synthesis and generation of reduced NADPH required for synthesis reactions in tumor cells. It was demonstrated that Zoledronic acid inhibits the prenylation of small guanosine-5'-triphosphate (GTP)-binding proteins, such as Ras, and thus inhibit Ras signaling *in vitro*. Mutations in the RAS oncogenes (HRAS, KRAS, NRAS) have been found in 13% of bladder tumors and occurred in all stages and grades [213]. Zoledronic acid can inhibit cell proliferation and the pentose phosphate pathway (PPP) in bladder cancer cells [214]. Another metabolic pathway that seems to be crucial for bladder cancer is fatty acids biosynthesis. High levels of fatty acids synthase (FASN) expression were observed in 59% of non-muscle-invasive BTCC tissue specimens, and FASN expression was

associated with histologic grade and recurrence. Moreover, FASN inhibitors caused the increased apoptosis and decreased proliferation of bladder cancer cells [215].

The importance of Warburg effect and other glucose metabolism alterations in bladder cancer have been reported [210]. However, unlike numerous inhibitors of glucose uptake and glycolysis are currently available, very few have been tested in bladder cancer patients, and to date there is no evidence of a clinical benefit that supports their use in clinical practice. On the other hand, a recent study demonstrated the ability of metformin to reduce, although with different efficiency, cell proliferation, sphere formation and migration in grade 2 bladder cancer cell lines, suggesting that OXPHOS targeting could be an effective strategy to reduce the invasiveness of this subtype of bladder cancer [69].

References can be found after 'General Discussion' → [REFERENCES](#)

AIM OF THE THESIS

Cancer research has seen a renewed interest in understanding metabolic reprogramming. Abnormal cancer metabolism, such as aerobic glycolysis and increased anabolic pathways, has important roles in tumorigenesis, metastasis, drug resistance, and cancer stem cells. Thus, understanding the mechanism underlying these processes can lead to the identification of promising novel anticancer approaches. Since the tumor microenvironment (TME) has emerged to play an important role in metabolic rewiring, a detailed understanding of this process requires the development of models that can closely resemble the complexity of cancer cytoarchitecture and TME, such as three-dimensional (3D) models. Among 3D models, spheroids derived from cancer cell lines resemble the tumor scenario as they are composed of several specialized areas and layers where cells have different phenotypic, functional, and metabolic behaviors. Indeed, within a spheroid, nutrient and oxygen gradients concur to create a physiological cellular heterogeneity in which proliferative cells stay in the outer layers, and quiescent or necrotic cells stay within the central core of the spheroid. Therefore, the use of 3D models for the study of cancer metabolic reprogramming can potentially improve the reliability of preclinical research data favoring their application to find alternative clinical approaches.

This thesis lays in the context of the shared scientific interest to dissect metabolic reprogramming occurring in different types of cancer cells with the aim to contribute to getting closer to finding novel therapeutic strategies against cancer.

Considering this main objective as a guiding thread, this thesis can be divided into three specific aims:

1. To unravel metabolic differences between luminal e triple negative breast cancer cell lines through the development and characterization of 2D and 3D models. Indeed, breast cancer is the most diagnosed cancer in women and the first cause of cancer-related deaths. Moreover, triple negative breast cancer is the most aggressive subtype and still lacking a targeted therapy. Exploring the

metabolic rewiring characterizing different subtypes of breast cancer using high-content imaging analysis on 3D cancer spheroids could help us to identify potential metabolic vulnerabilities that can be targeted for anticancer therapy.

2. To develop a reliable and reproducible workflow optimized for the analysis of metabolic fluxes in three-dimensional cultures using Seahorse technology. Despite the employment of this Seahorse technology on monolayers cultures is widespread in the field of cancer research, its application on three-dimensional cultures is still poorly optimized. The optimized workflow will be helpful in the high-resolution metabolic characterization of three-dimensional cultures, their comparison with monolayer cultures, and may aid in the design and interpretation of (multi)drug protocols.
3. To characterize the energetic and redox metabolism of grade 2 bladder cancer cell lines exhibiting different invasiveness properties for the identification of metabolic vulnerabilities to be exploited for targeted therapy. Grade 2 bladder cancer represents a therapeutic window that strongly requires post-surgical resection pharmacological treatments that help to eliminate residual tumor cells and prevent the formation of tumor relapse. As the molecular and metabolic characterization of these cancers and derived cellular and animal models increase, we will be able to design ever more effective single and combinatorial anti-cancer regimens based on the detected metabolic fragilities.

CHAPTER 1: UNRAVELLING METABOLIC DIFFERENCES BETWEEN LUMINAL AND TRIPLE NEGATIVE CELL LINES IN 2D AND 3D BREAST CANCER MODELS

Gloria Campioni^{1,2,†}, Valentina Pasquale^{1,2,†}, Giacomo Ducci^{1,2}, Lilia Alberghina^{1,2}, Elena Sacco^{1,2} and Marco Vanoni^{1,2*}

¹Department of Biotechnology and Bioscience, University of Milano-Bicocca, Milan 20126, Italy

²SYSBIO-ISBE.IT, Centre of Systems Biology, Milan 20126, Italy

[†] These authors equally contributed to this work

*Corresponding author: marco.vanoni@unimib.it

(Manuscript in preparation)

2.1 Abstract

Breast cancer (BC) is the first cause of cancer-related death in women, a pathology characterized by a high degree of heterogeneity, needing a tailored approach to improve treatment responses. Three major histological subtypes guide the clinical approach: luminal (ER and PR-positive); human epidermal growth factor receptor 2-positive (HER2); triple-negative breast cancer (TNBC, not expressing any of these markers). TNBC is the most heterogeneous histological subtype and the most prone to relapses, metastases, and chemoresistance. It still lacks any targeted therapy.

Metabolic rewiring in cancer cells is fundamental to maintain their transformed state and survive in the tumor milieu. Its study represents an opportunity to find new clinical approaches, using bi- and three-dimensional cancer models.

We studied the metabolic profile of three immortalized BC cell lines cultured in 2D: SUM159PT, MDA-MB-231 (both TNBC), and MCF7 (luminal). Using Agilent Seahorse XFe96 technology, that measures bioenergetic parameters in real-time on living cells, we observe that the three cell lines present strong glucose dependency for

mitochondrial respiration. Moreover, glutamine deprivation and glucose metabolism inhibition (induced by 2DG treatment or its depletion) significantly reduce cell proliferation. The mitochondrial ATP synthesis inhibition by oligomycin strongly decreases proliferation of MCF7 and SUM159PT, consistently with their higher production of ATP by respiration.

In vitro three-dimensional models (3D), such as spheroids derived from immortalized cell lines, can recapitulate the complexity and heterogeneity of the pathology. Glucose perturbation severely reduces spheroid vitality and morphology of the highly glycolytic MDA-MB-231 cell line. Glutamine deprivation slightly affects spheroid roundness or vitality. Consistently with their lower oxidative metabolism in 3D, oligomycin does not exhibit strong inhibitory effect on the formation of MDA-MB-231 and MCF7 spheroids. These results suggest that nutritional and pharmacological perturbations of energetic metabolism have a greater impact on proliferation of cells growing in 2D than on spheroid formation (3D). Since 3D structures present a rewired metabolic profile compared to the same cell lines grown in 2D, we propose in future to evaluate the effects of the different metabolic pathways' inhibition in pre-formed spheroids and in more complex 3D cancer systems.

2.2 Introduction

In 2020 breast cancer has represented the 11.7% of global cancer incidence considering both sexes, becoming the first most diagnosed cancer worldwide. In female, mammary carcinoma is also the first cause of cancer death, with a mortality rate of 15.5%[2]. Breast cancer can be classified into molecular subtypes basing on the expression of estrogen (ER) and progesterone (PR) receptors, and human epidermal growth factor receptor-2 (HER2)[176]. Nowadays, hormone receptor positive (ER+PR+) and HER2-positive (HER2+) breast cancer subtypes have a relatively low mortality rate thanks to the availability of targeted treatment strategies, such as monoclonal antibodies or endocrine therapy. On the contrary, triple negative breast cancers (TNBCs, ER-PR-HER2-) have been studied more intensely for their higher mortality

rate, which is due to frequent metastasization[216] and the lack of specific therapeutic approaches [217][192][218]. Since metabolic rewiring has been recognized as one of the most important mechanisms that cancer cells can use to sustain their enhanced growth rate[16], exploiting this intrinsic characteristic of cancer to develop novel therapeutic strategies can be a useful approach, above all against those tumors that still lack a targeted therapy[34][35][36].

Breast cancer is a heterogeneous disease on multiple aspects, including metabolic phenotyping[192][219]. TNBCs show a classic Warburg metabolism: high glucose uptake and lactate production even in the presence of oxygen[39][220]. Their glycolytic phenotype is related to increased proliferation, which implies that glycolysis is important for fueling the energy, redox or biosynthetic needs of fast-growing tumors[192]. On the other hand, ER+ mammary tumors exhibit different metabolic phenotypes: cells classified in the histological luminal B subtype manifest a sustained proliferative rate and, rarely, a reverse Warburg metabolism, while luminal A tumors have a slower proliferation which is greatly addicted to oxidative phosphorylation[185]. Moreover, many estrogen receptor positive breast cancers are able to reprogram the surrounding fibroblasts into CAF (Cancer Associated Fibroblasts) displaying the so-called reverse Warburg effect: CAFs metabolism is induced by cancer cells toward aerobic glycolysis, which leads to the release of lactate and pyruvate that are uptaken and used by the cancer cell for the TCA cycle and oxidative phosphorylation [190][110]. To better comprehend the metabolic heterogeneity of breast cancer subtypes and find alternative metabolic targets for therapy against them, the optimization of reproducible, reliable, and representative models is required. Currently, adherent mammalian cells growing on two-dimensional (2D) platforms are still the most used in research to obtain information on cellular responses to treatments because they are easy to handle, cost-effective, and reproducible. However, these models do not allow to accurately reproduce the three-dimensional (3D) environment in which cancer cells reside *in vivo* and can provide misleading results regarding the responses of cancer cells to drugs [221]. In general,

standard preclinical screening procedures for therapeutic agents include the following steps: (1) 2D cell culture system testing, (2) animal model testing, and finally (3) clinical studies. As the phases progress, the percentage of efficient agents decreases dramatically. Less than 5% of anticancer agents and cancer therapies have passed clinical trials and have approved for marketing by regulatory pharmaceutical agencies [222]. One possible cause of the failure to identify effective compounds is that the pharmacological responses of 2D cell culture systems do not consistently reflect the outcome of clinical studies [223]. The main limitation of traditional 2D culture is their inability to mimic the tumor architecture and microenvironment *in vivo*. Indeed, there are many characteristics in which 2D-grown cells differ compared to cells *in vivo*: morphological characteristics, proliferation and differentiation potentials, cell-cell interactions, cell-extracellular matrix interaction, and signal transduction systems [224]. These needs have inspired the development of 3D cell culture systems to overcome the inconsistency between *in vitro* cell-based testing and clinical studies. For these reasons, the experiments performed on 2D cultures allow preliminary and more generic studies of the disease, which subsequently must be further investigated on more complex and representative models of the pathology.

In this work the metabolic phenotype of three breast cancer cell lines grown in adhesion (2D cultures) was correlated with their ability to form spheroids (3D cultures). For this purpose, we compared one hormone receptor positive metastatic cell line, MCF7, with two triple-negative breast cancer cell lines, MDA-MB-231 (metastatic) and SUM159PT (primary tumor). The metabolic profile of 2D and 3D cultures was studied through the measurement of bioenergetic parameters by mean of Agilent Seahorse XFe96 analyzer and through proliferation (3D) and spheroid formation (3D) assays under nutritional deprivation or pharmacological treatments perturbing glucose, glutamine, fatty acids metabolism and oxidative phosphorylation. The aim of this study is to improve the comprehension of the metabolic phenotype that characterizes aggressive breast tumors in order to obtain information for the development of novel personalized therapeutic strategies.

2.3 Materials and methods

2.3.1 Cell lines and culture media composition

Three breast cancer cell lines has been studied in this work, whose main characteristics are reported in **Table 3**: MCF7, MDA-MB-231 and SUM159PT. MCF7 cell line was a generous gift from Dr. Luca Magnani (Imperial College London), while MDA-MB-231 and SUM159PT cell lines were a generous gift from Dr. Lanfrancone (European Institute of Oncology).

Table 3. Main characteristics of the BC cell lines studied in this work: tumor site, molecular classification, histology, and main mutations.

| Cell line | Tumor site | Molecular classification | Histology | Genetic alterations |
|-------------------|------------------------------|---------------------------|----------------------|---|
| MCF7 | Metastasis, pleural effusion | Luminal A (ER+ PR+ HER2-) | Adenocarcinoma | <ul style="list-style-type: none"> • <i>PIK3CA</i>^{E545K} heterozygous (low AKT activation); • <i>CDKN2A</i> homozygous deletion |
| MDA-MB-231 | Metastasis, pleural effusion | TNBC (ER- PR- HER2-) | Adenocarcinoma | <ul style="list-style-type: none"> • <i>BRAF</i>^{G464V} heterozygous • <i>CDKN2A</i> homozygous deletion • <i>KRAS</i>^{G13D} heterozygous • <i>NF</i>^{E231} homozygous • <i>TP53</i>^{R280K} homozygous |
| SUM159PT | Primary tumor (localized) | TNBC (ER- PR- HER2-) | Anaplastic carcinoma | <ul style="list-style-type: none"> • <i>TP53</i>^{V157R} heterozygous • <i>BRCA1</i>^{Q356R} homozygous • <i>HRAS</i>^{G12D} heterozygous • <i>PIK3CA</i>^{H1047L} heterozygous |

MCF7 cell line was cultured in Dulbecco's Modified Eagle Medium (DMEM, 11960-044, Gibco™-Thermo Fisher Scientific) supplemented with 10% fetal bovine serum (FBS, Gibco-ThermoFisher, Waltham, MA, USA), 4 mM glutamine, 1 mM Na-Pyruvate, and

10 nM β -estradiol (E2758, Merck Life Science), 100 U/mL penicillin and 100 mg/mL streptomycin.

MDA-MB-231 cell line was grown in RPMI-1640 medium (R0883-Merck Life Science, Darmstadt, Germany) supplemented with 10% fetal bovine serum (FBS, Gibco-ThermoFisher, Waltham, MA, USA), 4 mM glutamine, 1 mM Na-Pyruvate, 100 U/mL penicillin, and 100 mg/mL streptomycin.

SUM159PT cells were cultured in Ham's F-12 medium (11765-054, Gibco™-Thermo Fisher Scientific) supplemented with 10% fetal bovine serum (FBS, Gibco-ThermoFisher, Waltham, MA, USA), 2 mM glutamine, 5 μ g/ml insulin (I9278, Merck Life Science), 1 μ g/ml Hydrocortisone (H0888-1G, Merck Life Science) and 10 mM HEPES, 100 U/mL penicillin, and 100 mg/mL streptomycin.

To generate heterotypic spheroids, primary human normal mammary fibroblasts were used. Primary Human Normal Mammary Fibroblasts HMF8 were obtained in collaboration with Gade Laboratory for Pathology, Department of Clinical Medicine, Faculty of Medicine and Dentistry, University of Bergen, Bergen, Norway. Fibroblasts were isolated from a female donor. Cells were minced into small pieces in a tissue-treated 6 well plate, allowed to adhere, and cultured in FAD medium, which is a 1:1 mixture of Dulbecco's modified Eagle's medium (DMEM, 11960-044, Gibco™-Thermo Fisher Scientific) and Ham's F12 (11765-054, Gibco™-Thermo Fisher Scientific), supplemented with 10% fetal bovine serum (FBS, Gibco-ThermoFisher, Waltham, MA, USA), 0.4 μ g/mL hydrocortisone (H0888-1G, Merck Life Science), 50 μ g/mL Ascorbic acid (A4544, Merck Life Science), 0.05X Insulin-Transferrin-Selenium (41400-0045, Gibco™-Thermo Fisher Scientific), 2 mM glutamine and 100 U/mL penicillin and 100 mg/mL streptomycin. The outgrowth of cells with fibroblast morphology was subsequently propagated on plastic surfaces in a 1:1 FAD medium and DMEM medium.

All the cell lines were cultured at 37 °C in a humidified atmosphere of 5% CO₂. Cells were passaged when they reached sub-confluence (typically twice a week) using trypsin-ethylene-diamine-tetraacetic acid (EDTA).

The experiments on monolayer cultures were performed **2D experimental medium**, composed of DMEM w/o phenol red (Gibco™-Thermo Fisher Scientific), 10% FBS, 10 mM glucose, 2 mM glutamine. The 2D experimental medium was supplied with 10 nM β-estradiol for MCF7 cell line and with 5 μg/mL insulin and 1 μg/mL hydrocortisone for SUM159PT cell line. These additives were added to the experimental medium of these cell lines to maintain their proliferative status similar to the condition in which they normally grow. The concentration of 2 mM glutamine was chosen (even though MDA-MB-231 and MCF7 cell lines normally grow in 4 mM glutamine) to compare the metabolism of all three cell lines in the same conditions of nutrient supply.

Spheroid formation was performed in 3D experimental medium DMEM w/o phenol red (Gibco™-Thermo Fisher Scientific), 1% BSA, 10 mM glucose, 2 mM glutamine, 10 μg/mL Insulin (I9278, Merck Life Science), 0.5 μg/mL Hydrocortisone (H0888-1G, Merck Life Science), 20 ng/mL EGF (EGF Human Recombinant, Peprotech, London, UK) 100 ng/mL Cholera Toxin (C8052, Merck Life Science), 1 mM Na-Pyruvate, 100 U/mL penicillin and 100 mg/mL streptomycin. The 3D experimental medium was supplied with 10 nM β-estradiol for MCF7 spheroids.

2.3.2 Production of three-dimensional cultures

To assess the propensity of the cells to form three-dimensional structures, the BC cell lines were plated on 12-well plates not-treated for tissue culture, in 3D experimental medium at density 100,000 – 150,000 cells/well.

To obtain three-dimensional cultures, the monolayers cultures were detached using trypsin-EDTA as usual and resuspended in 3D experimental medium. The cells were counted using trypan-blue exclusion technique, and then seeded in 96-well plates at the desired density (from 5,000 cells/well to 20,000 cells/well). After that, the plate

centrifugation was performed at 325 g for 30 minutes. Two different supports were employed for spheroid formation:

- Poly-Hema coated (ET3196, EuroClone) U-Bottom 96-well plates. For Poly-Hema coating, the Poly-Hema powder was dissolved in ethanol at concentration 20 mg/mL, the solution was dispensed in the wells to cover the surface to be coated and then it was left to evaporate overnight. This approach was used to obtain spheroids for metabolic analysis by Seahorse XFe96 (Agilent) analyzer.
- CellCarrier Ultra-low-attachment (ULA) 96-well CellCarrier-ULA 96-well U-Bottom plates (PerkinElmer) were used for the spheroid formation assays, enabling high resolution analysis using Operetta CLS™.

For heterotypic spheroids' formation, HMF8 and BC cell lines were grown in adhesion and harvested separately. After cell counting, the cells were properly diluted 1:1 and seeded in U-bottom CellCarrier Spheroid ULA 96-well Microplates (Perkin-Elmer) at the density of 2×10^5 cells/ml (5,000 cells BC + 5,000 cells HMF8/well) in 100 μ L/well of 3D experimental medium.

2.3.3 Nutritional deprivation and drug treatment assay in 2D cultures

Cell proliferation was evaluated after 72h of growth by imaging acquisition and analysis for cell counting by mean of Operetta CLS™ and the associated analysis software Harmony (PerkinElmer). The assays were performed in nutritional deprivation conditions or in the presence of pharmacological treatment with drugs targeting metabolic pathways, at different concentrations. The 2D experimental medium was completed without adding glucose (for glucose deprivation) or glutamine (for glutamine deprivation) or with the addition of the following drugs:

- 2-deoxy-D-glucose (2-DG, D6134-1G, Sigma) at concentrations 0.625mM - 1.25mM - 2.5mM - 5mM - 10mM - 20mM;
- Oligomycin (75351, Sigma) at concentrations 0.0625 μ M - 0.125 μ M - 0.25 μ M - 0.5 μ M - 1.5 μ M;

- BPTES (SML0601-5MG, Sigma) at concentrations 0.5 μ M - 2. μ M - 5 μ M - 10 μ M - 20 μ M;
- Etomoxir (Merck E1905-5MG) at concentrations 5 μ M - 25 μ M - 50 μ M - 100 μ M - 200 μ M.

The cells were detached using trypsin-EDTA as usual, counted, and resuspended in complete 2D experimental medium. The cells were seeded in CellCarrier-96 Ultra Microplates 96-well plates (PerkinElmer) at 5,000 cells/cm² (SUM159PT), 10,000 cells/cm² (MCF7) or 15,000 cells/cm² (MDA-MB-231) seeding density. At time 0 (24 hours after seeding) the cells were gently washed with D-PBS w/ Ca²⁺ and Mg²⁺, and the specific medium for pharmacological treatment or nutritional deprivation was added. Each condition was tested at least in triplicate, in at least two independent experiments.

At time 0h some wells subjected to nuclear staining with Hoechst 33342 (0.5 μ g/mL), and fluorescence images were acquired by Operetta CLSTM. The dye was diluted in D-PBS at 10X concentration and then directly added to the 2D experimental medium in the wells (dilution 1:10); no washing steps were performed to avoid any possible detachment of the cells before or after the staining. At time 24h and time 48h, brightfield images of each well were acquired using the same instrument. Finally, at time 72h, the cells were stained with Hoechst and fluorescence images were taken by Operetta CLSTM. The analysis of the number of cells was performed using Harmony software.

To evaluate the effect of metabolic drugs on cell proliferation, the amount of DMSO correspondent to the highest concentration of Oligomycin or BPTES (the only two drugs dissolved in a toxic vehicle among those tested) was added to the control condition. The anti-proliferative effect, evaluated 72 hours after treatment, was calculated with the following formula:

$$\text{Antiproliferative effect \%} = 1 - \frac{n^{\circ} \text{ treated cells}}{n^{\circ} \text{ control or vehicle cells}} \times 100$$

2.3.4 Spheroid formation assays under metabolic perturbation

To perform the Spheroid formation assay, the day before seeding the cells for the experiment, the cells grown in monolayer culture were stained with CellTracker™ Green CMFDA dye (C7025, Gibco-ThermoFisher, Waltham, MA, USA). Cells were washed with D-PBS w/ Ca^{2+} and Mg^{2+} , then 10 μM CellTracker™ Green CMFDA dye diluted in DMEM w/o phenol red was added and incubated for 30 minutes at 37 °C and 5% CO_2 . The dye was removed, cells were washed with D-PBS w/ Ca^{2+} and Mg^{2+} and put in the incubator with their own maintenance medium until the next day. On the day of seeding, cells were detached with trypsin-EDTA as usual and centrifuged at 290 g for 7 minutes. The pellet was resuspended in the 3D experimental medium w/o glucose and glutamine and cell counting was performed using a Burker chamber. Whereupon the cells were seeded in U-bottom CellCarrier Spheroid ULA 96-well Microplates (PerkinElmer), previously half filled with 3D experimental medium for drug treatment or nutritional deprivation (50 μL /well). The control condition and the conditions with drugs were supplemented with double amount of glucose and glutamine, while the nutritional perturbation conditions only one of the two nutrients was added at double concentration. The drug treatments were added at 2X concentration, too. Before seeding, 10 $\mu\text{g}/\text{mL}$ Propidium Iodide (PI) was added to the cell suspension (the final concentration of PI after seeding was 5 $\mu\text{g}/\text{mL}$). The final density of cell suspension for spheroid formation assay under metabolic perturbation was 1×10^4 cells/well in 100 μL /well. After seeding, the U-bottom CellCarrier Spheroid ULA 96-well Microplates was centrifuged at 340 g for 30 min to foster cell aggregation. The plates were incubated for 3 days (72h) at 37 °C in a humidified atmosphere of 5% CO_2 during spheroid formation.

Two concentrations of each drug were tested in spheroid formation assay under metabolic perturbations: 1.25mM - 10mM 2-DG, 62.5nM – 3 μM Oligomycin, 2.5 μM – 20 μM BPTES, 25 μM – 200 μM Etomoxir.

Fluorescence and brightfield images of spheroid formation were acquired from T0 to T72 by Operetta CLS™. The morphological and physiological analysis were performed after 72h of treatment by Harmony™ software.

2.3.5 High-content analysis of 2D and 3D cultures

The high-throughput microplate confocal microscope for High-Content Analysis Operetta CLS™ was employed for the acquisition of brightfield and fluorescence images in the nutritional deprivation and pharmacological treatment assays in 2D and 3D (spheroid formation assay). The integrated Harmony™ software, was used for the images analysis. More precisely, Operetta CLS- Harmony system was applied for cell counting in adhesion dose-response experiments, for the normalization of Seahorse data (in 2D and in 3D), and the evaluation of spheroid morphological and physiological traits in the spheroid formation assays.

The efficiency of spheroid formation was evaluated through two parameters:

- The ratio between the sum of intensities of Propidium Iodide positive pixels (calculated on maximum intensity projection) and the footprint area of Cell Tracker Green positive pixels. This parameter, indicated as ***PI intensity/CT area***, was chosen as an index of spheroid mortality (*Figure 15*).
- The ***Roundness*** measured on CT area, indicating spheroid perimeter regularity and compactness. Its value varies from 0 to 1, where 1 is the roundness value of a fully filled perfect circle (*Figure 16*).

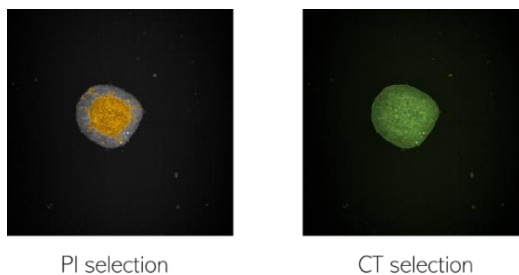


Figure 15 Exemplificative images of Propidium Iodide selection (used to calculate PI intensity) and Cell Tracker Green selection. In the maximum intensity projection, each pixel of the intensity image is set to the maximum intensity found in the corresponding pixels in the image stack.

Formula:
$$\sqrt{4\pi} \times \frac{\sqrt{1.0 \times S - (d/2.0)}}{d - 0.1}$$

S = object area
d = border area (\propto circumference)





| | Perfect circle | Elongated object | Object with irregular borders | Not fully-filled object |
|-----------------------|--|--|--|--|
| Demo shape |  |  |  |  |
| Width to length ratio | 1.0 | 0.33 | 0.59 | 1.0 |
| Roundness | 1.0 | 0.77 | 0.78 | 0.23 |

Figure 16 Formula of roundness calculated by Harmony software (above) and examples of roundness and width to length ratio values associated to objects with different shapes (below).

2.3.6 Evaluation of metabolic parameters by Seahorse XFe96 analyzer

Seahorse assays on 2D cultures were performed according to the manufacturer's instructions. were seeded in Seahorse XF plates at a density of 2×10^4 cells/well (MDA-MB-231 and MCF7 cell lines) or 5×10^4 cells/well (SUM159PT cell line) and cultured for 24h. The next day medium was replaced with Seahorse XF DMEM Medium, pH 7.4 supplemented with 10 mM D-Glucose and 2 mM L-Glutamine and cell cultures were allowed to equilibrate for 1h at 37 °C in a no-CO₂ incubator. At the end of the Seahorse measurements, Hoechst 33342 was added to each well at the final working

concentration of 1 µg/mL and after 15 min incubation nuclei/well were imaged and counted by Operetta CLS™ software Harmony, and directly used to normalize the Seahorse parameters per cell number.

For Mito stress test the following drug concentrations have been used: 1µM Oligomycin, 0.25µM FCCP (MDA-MB-231) or 0.5µM FCCP (MCF7) or 1µM SUM159PT, 0.5µM Rotenone/Antimycin A. The concentration of FCCP for each cell line was chosen after a dose-response curve (the lowest concentration with the highest response was chosen).

For ATP rate assay and Mito Fuel flex test we used the drugs concentration indicated in the manufacturer's protocol.

Seahorse assays on 3D cultures were performed in agreement to manufacturer's instructions. More in detail, the day before the assay, all wells of XFe96 Spheroid Microplate were coated with the adhesive agent Collagen type I solution (3867, Merck Life Science) diluted in H₂O at a concentration of 10 µg/cm². On the day of the assay, the wells were rinsed with sterile H₂O and left to air dry before use. Seahorse XF DMEM Medium, pH 7.4 was supplemented with 10 mM D-Glucose and 2 mM L-Glutamine and dispensed 175 µL/well in the Collagen-coated XFe96 Spheroid Microplate before transferring the spheroids in the wells.

The spheroids analyzed for Seahorse assays were freshly prepared 72h before the day of assay, as described in the section 2.3.2; the cells were stained with Cell tracker dye the day before seeding to obtain fluorescent spheroids (useful for normalization purposes, as indicated below). The medium used for spheroid formation in the U-bottom microplates was half replaced with a complete Seahorse Assay medium to mitigate buffer presence in the final assay medium. The spheroids were gently transferred in the wells XFe96 Spheroid Microplate. The position of each spheroid was verified by microscope observation and eventually corrected to have one spheroid at the center of each well. After that, the XFe96 Spheroid Microplate was centrifuged at 340 g for 15 minutes, low brake, to foster spheroids' adhesion on the collagen coating. Before the assay started, brightfield and confocal fluorescence images of each well

were acquired by Operetta CLS to compare the position of each spheroid before and after the assay and to verify if any shift occurred.

The sensor cartridge hydration and loading were performed according to manufacturer's instructions.

For Mito stress test the following drug concentrations have been used: 2 μ M Oligomycin, 2 μ M FCCP, 0.5 μ M Rotenone/Antimycin A. For Mito Fuel flex test, we used the drugs concentration indicated in the manufacturer's protocol.

For normalization, the area of each spheroid was determined by selecting the area of Cell tracker fluorescence using the images acquired by Operetta CLS (PerkinElmer) immediately after the Seahorse assay. A comparison between images acquired before and after the assay was performed to exclude from the analysis the spheroids that had eventually moved from the central position during the Seahorse assay due to mixing steps before each XF measurement. The conversion from spheroid area to cell number was obtained indirectly, thanks to the construction of a standard curve for each cell line that relates the area of the spheroid to the cell number (data not shown). These data were obtained in a parallel experiment in which different cell densities were used for spheroid formation and, after 72h, the spheroids of different dimensions were collected and trypsinized in bulk to determine the average number of live cells for each category of spheroid.

Seahorse XF assays parameters calculation:

ATP rate assay: the sequential injections of oligomycin and rotenone/antimycin A enable the calculation of total ATP production rate, which is the sum between mitochondrial ATP production rate (mitoATP) and glycolytic ATP production rate (glycoATP). The following formulas are applied by Seahorse analysis software (Wave) to calculate these parameters:

$$\text{Total ATP rate} = \text{mitoATP} + \text{glycoATP}$$

$$\text{mitoATP} = (\text{OCR}_{\text{Basal}} - \text{OCR}_{\text{Oligo}}) \times 2 \times \text{P/O}$$

$$\text{glycoATP} = \text{ECAR}_{\text{basal}} \times \text{BF} \times \text{Vol}_{\text{XFmc}} \times \text{Kvol} - (\text{OCR}_{\text{basal}} - \text{OCR}_{\text{Rot/Ant}}) \times \text{CCF}$$

Where OCR_{basal} is the 3rd OCR value before any injection, OCR_{oligo} is the lowest value of OCR after oligomycin injection, P/O is a constant value equal to 2.75, BF is buffer factor and represents the buffering capacity of the system (in this case its value is 2.5), Vol_{xFmc} is the volume of the microchamber (whose value is 2.28), $Kvol$ is a constant equal to 1.6, $OCR_{Rot/Ant}$ is the lowest OCR value after rotenone/antimycinA injection, and CCF represents the CO₂ contribution factor and has the value of 0.61.

Mito stress test: the sequential injection of oligomycin, FCCP and Rot/Ant enables the calculation of a series of parameters, whose formulas are listed below.

$$\text{Basal respiration} = OCR_{Basal} - OCR_{Rot/Ant}$$

$$\text{Maximal respiration} = OCR_{FCCP} - OCR_{Rot/Ant}$$

$$\text{Spare respiratory capacity} = OCR_{FCCP} - OCR_{Basal}$$

Where OCR_{FCCP} is the highest value of OCR after FCCP injection. The other parameters are explained above.

Mito fuel flex test: the sequential injection of a target drug followed by the injection of the other two drugs inhibitors (or vice-versa) enables the calculation of three parameters linked to glucose, glutamine and fatty acids utilization as respiratory fuels, whose formulas are listed below. The target drugs are: UK5099, which inhibits the utilization of glucose for OXPHOS by blocking the mitochondrial pyruvate transporter MPC, BPTES, which inhibits the utilization of glutamine for OXPHOS by blocking the enzyme glutaminase, and Etomoxir, that inhibits the utilization of fatty acids for OXPHOS by blocking carnitine palmitoil transferase. These drugs are injected alone as target inhibitor or in combination with one of the other inhibitors.

$$\text{Dependency}\% = \frac{OCR_{Basal} - OCR_{target\ inhibitor}}{OCR_{Basal} - OCR_{all\ inhibitors}} \times 100$$

$$\text{Capacity}\% = \left(1 - \frac{OCR_{Basal} - OCR_{other\ 2\ inhibitors}}{OCR_{Basal} - OCR_{all\ inhibitors}}\right) \times 100$$

$$\text{Flexibility}\% = \text{Capacity} - \text{Dependency}$$

The OCR and ECAR values obtained from Seahorse XF analysis have been normalized as reported previously [69][225]. Briefly, the Seahorse assays performed on 2D cultures were normalized on cell number: nuclei were stained with Hoechst 33342 at the end of the assay, images of each well were acquired by mean of Operetta CLS, and Harmony software was employed for the analysis of the images to determine the number of cells per well. The Seahorse assays performed on 3D cultures were normalized on the number of cells per spheroid determined indirectly: a standard curve was previously constructed to correlate the area of the spheroids with the number of live cells for each cell line. Then, the equations of these curves were applied to quantify each spheroid's number of cells in the Seahorse microplate from the measurement of their area (obtained using Operetta CLS and Harmony software).

2.3.7 Statistical analysis

All statistical analyses were performed using the GraphPad Prism and IBM SPSS Statistics 27 software. The significance of the observed variations was analyzed using the following statistical tests, evaluating the most appropriate to use: comparison of means with 2way ANOVA Test, one-way ANOVA test for repeated measures, or with non-parametric tests such as the Kruskal-Wallis test. A p -value < 0.05 was considered statistically significant.

Every experimental condition was tested at least in triplicate and each experiment was performed at least twice using different biological replicates, except for the experiments with heterotypic spheroids (only one biological replicate).

2.4 Results

2.4.1 Cell size and growth profile in adhesion (2D)

In order to compare BC cell lines, we started with the analysis of their growth profile under standard conditions (i.e., not subjected to any treatment, **Figure 17A**) and their size (**Figure 17B**). The data presented in **Figure 17A** suggest that SUM159PT cells are the fastest to grow, followed by the MCF7 and then the MDA-MB-231 which are the slowest. Although reproducible, these differences are not statistically significant. On the other hand, the difference in cell size is significant (**Figure 17B**). MDA-MB-231 cells are 3.4 times bigger than the other two cell lines, whose size is extremely similar. Cell size was measured by selecting the perimeter of the cells carried out on images acquired with the phase contrast optical microscope and processed with the LCmicro software.

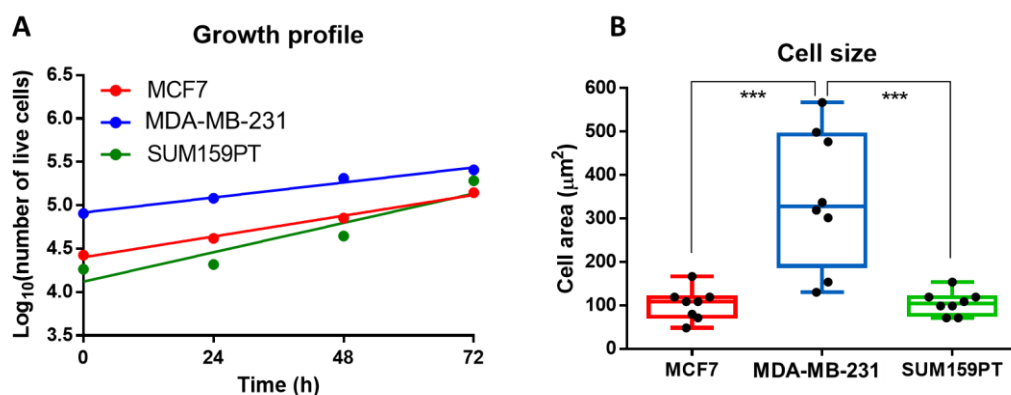


Figure 17. (A) Growth kinetics at 72 hours, vital count performed with Trypan Blue (comparison of slopes calculated with linear regression $p = 0.3524$). (B) Box and whiskers plot of mean cell size obtained by optical phase contrast microscopy (MCF7 vs MDA-MB-231 $p < 0.001$; MCF7 vs SUM159PT $p > 0.99$; MDA-MB-231 vs SUM159PT $p < 0.001$). Comparison of means with 1way Anova test. The data reported in the graphs derive from three independent experiments.

2.4.2 Characterization of the metabolic phenotype in 2D: assessment of basal respiration and glycolysis

The Oxygen Consumption Rate (OCR), a parameter related to mitochondrial respiration, and the Extracellular Acidification Rate (ECAR), largely related to glycolysis, were measured using Seahorse XFe96 analyzer and normalized on cell

number, to compare the bioenergetic parameters between the different cell lines. Observing the basal metabolic parameters of the three BC lines, it emerged that MCF7 cell line is the most aerobic, characterized way by a statistically significant higher basal OCR and lower ECAR than the other two cell lines. MDA-MB-231 cell line was the most glycolytic among the three BC cell lines, with the lowest OCR value and the highest ECAR recorded. SUM159PT cell line presented an intermediate metabolic phenotype between the two previously mentioned, since it is characterized by a lower oxygen consumption rate than MCF7 (but higher compared to MDA-MB-231) and a lower medium acidification rate than MDA-MB-231 (but higher than MCF7) (*Figure 18*).

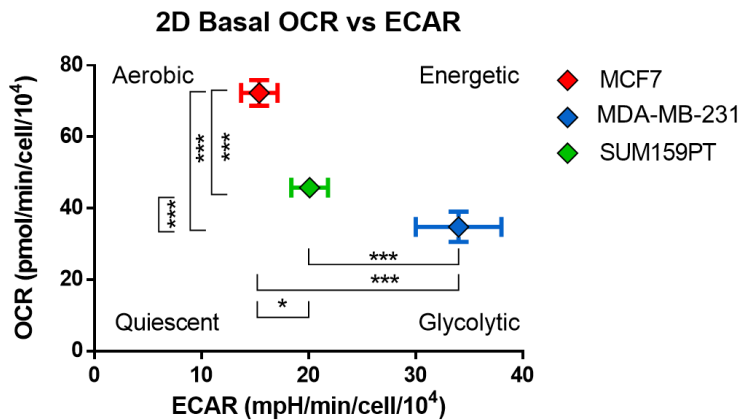


Figure 18. Basal metabolic parameters of BC lines grown in adhesion (2D). Statistically significant differences between cell lines are expressed as * = $p < 0.05$; *** = $p < 0.001$ applying the comparison of means with 2way Anova test. The data reported in the graph derive from two independent experiments.

Total ATP production rate and its distribution between glycolysis production (glycoATP) and mitochondrial respiration production (mitoATP) were obtained with ATP Rate Assay (*Figure 19*). Consistent with the data presented above, MCF7 cells exhibit a half rate of ATP production by glycolysis compared to the other two cell lines and the highest production of ATP by respiration. On the other hand, MDA-MB-231 and SUM159PT cells exhibit a similar behavior, with a comparable amount of total ATP production, principally linked to glycolytic activity (*Figure 19*).

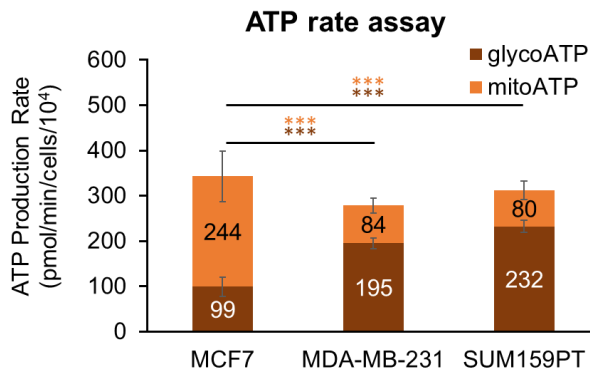


Figure 19. Histogram of total ATP production rate, mitoATP and glycoATP production rate of BC cell lines grown in adhesion (2D). Mitochondrial ATP production rate (mitoATP) is shown in orange, the rate of ATP production by glycolysis (glycoATP) is indicated in brown. The statistically significant differences between the cell lines are indicated as *** = $p < 0.001$, in orange for mitoATP and in brown for glycoATP. The comparison of means with the 2way Anova test was used for the statistics. The data reported in the graph derive from three independent experiments.

2.4.3 Analysis of mitochondrial functionality in 2D

Mito Stress Test allows to analyze respiratory function of cells through the sequential injection of drugs that modulate mitochondrial respiration. The results (**Figure 20A, B**) indicate that MCF7 cells not only have the greatest basal respiration, but also the greatest maximal respiration ($p < 0.001$; 2way Anova test), calculated as reported in the paragraph 2.3.6. This cell line also presents the greatest spare respiratory capacity, highlighting their potential to better respond to an increased demand of energy or to a stressful condition. MDA-MB-231 cell line shows the lowest values of basal and maximal respiration and, therefore, of spare respiratory capacity. SUM159PT cell line presents an intermediate situation between the other two lines. The data were analyzed by comparing the means with the 2way Anova test, pointing out that the differences found between the tumor cell lines regarding basal and maximal respiration and spare respiratory capacity are highly statistically significant ($p < 0.001$).

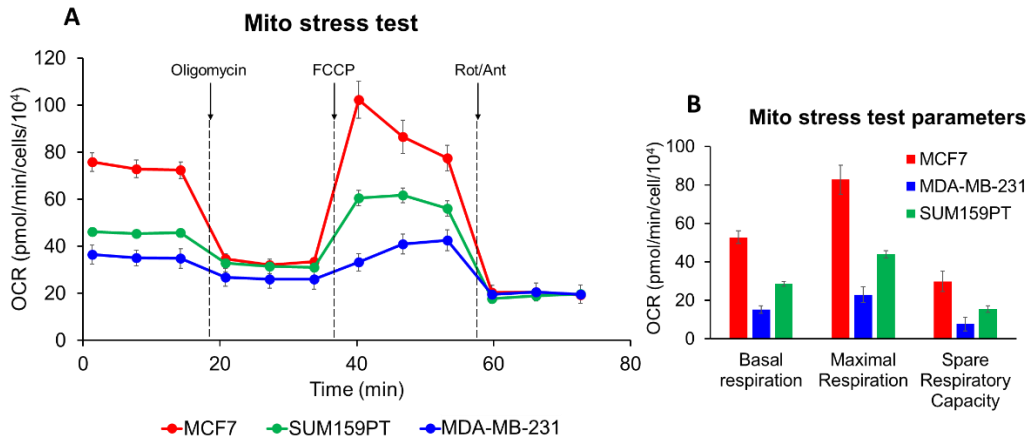


Figure 20 (A) Mito stress test OCR profile of BC cell lines grown in adhesion (2D). The arrows indicate the time point at which the drugs were injected (1 μ M Oligomycin, 0.25-1 μ M FCCP, 0.5 μ M Rotenone/Antimycin A). (B) Mito stress test parameters of calculated as reported in Materials and Methods (paragraph 2.3.6): Basal respiration, Maximal respiration, and Spare respiratory capacity. The differences between BC cell lines are all statistically significant ($p < 0.001$, not reported in the graph), calculated applying the comparison of means with 2way Anova test. The data reported in the graphs derive from two independent experiments.

Mito Fuel Flex Test enables the measurement of the total mitochondrial oxidation capacity of three nutrients, i.e., glucose, glutamine, and fatty acids, that is represented by the sum of two parameters: the dependency and flexibility. Dependency indicates the measurement of cells' reliance on a particular fuel pathway to maintain baseline respiration. Flexibility measures the ability of cells to increase oxidation of a particular fuel to compensate for inhibition of alternative fuel pathway(s).

The analysis shows that MCF7 cell line is much more dependent on glucose than the glutamine and fatty acids for oxidative phosphorylation ($p < 0.001$; 2way Anova test) and it has the flexibility to enhance its oxidation even in the absence of the other two nutrients (Figure 21). However, despite MCF7 cell line does not show any dependency on glutamine, it is able to use it as an alternative substrate in the absence of glucose and fatty acids. Likewise, its dependency on fatty acids is limited, while the flexibility in using them is greater.

MDA-MB-231 cell line is dependent on all three metabolic substrates, with a significantly higher dependency on glucose than on other nutrients ($p < 0.001$). Furthermore, this cancer cell line is much less flexible than MCF7 cell line ($p < 0.001$) to all the mitochondrial fuels, highlighting the need to have all the nutrients available for respiration (Figure 21).

Finally, the respiration of the SUM159PT line is more dependent on glucose than the other two nutrients but compared to the other BC cell lines it remains the least dependent on this substrate ($p < 0.01$). Furthermore, it shows to be very flexible in using glutamine and fatty acids, similarly to MCF7 ($p > 0.05$), but not glucose ($p < 0.001$). Only the MDA-MB-231 cell line does not seem to be able to increase the oxidation of a substrate to compensate for the inhibition of the other pathways in accordance with the data of Mito stress test (Figure 21).

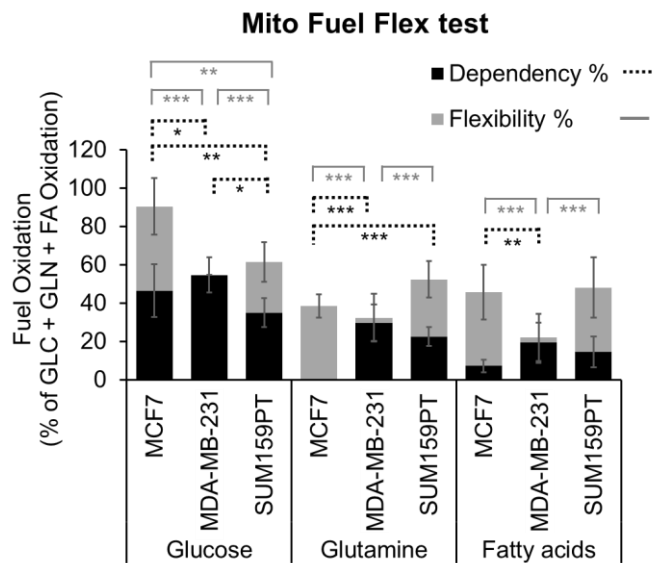


Figure 21 Histogram showing dependency and flexibility to use glucose (GLC), glutamine (GLN) and fatty acids (FA) for OXPHOS measured in the three BC lines grown in adhesion (2D). Statistically significant differences are expressed as * = $p < 0.05$; ** = $p < 0.01$; *** = $p < 0.001$ applying the comparison of means with the 2way Anova test. The data reported in the graph derive from two independent experiments.

2.4.4 Metabolic perturbation assays in 2D: nutritional deprivation and pharmacological treatment

To evaluate the impact of glucose, glutamine, fatty acids and mitochondrial respiration in supporting BC cells growth, proliferation assays were performed under nutritional deprivation or pharmacological treatments. The effects of these metabolic perturbations were tested on cell proliferation grown in adhesion (2D) after 72h of treatment.

The proliferation of all three BC cell lines is significantly reduced under glucose deprivation and 2-deoxyglucose (2DG) treatment compared to the control condition (**Figure 22A, B**). 2DG is a structural analogue of glucose which differs from the latter by replacing the hydrogen at second carbon atom with a hydroxyl group; once in the cell, it is phosphorylated by the hexokinase to 2-deoxy-D-glucose-6-phosphate (2DG-6-P), which cannot be further metabolized by glucose-6-phosphate dehydrogenase or phosphoisomerase. Therefore, once formed, it accumulates in the cell and its high intracellular levels cause the allosteric and competitive inhibition of the hexokinase which results in the inhibition of glucose metabolism.

The data show that the primary tumor line SUM159PT is the most sensitive to both glucose deprivation and pharmacological inhibition of glycolysis by 2DG, with a maximal inhibitory effect of 2DG around 80% and an EC_{50} under the lowest dose of 2DG tested ($EC_{50} = 0.3312$ mM). MCF7 cell line is the least sensitive to both nutritional deprivation and drug treatment against glucose metabolism, with a maximal 2DG inhibitory effect of 65% reached at 10mM and an $EC_{50} = 2.479$ mM. MDA-MB-231 cell line displays an intermediate inhibitory effect of both nutritional deprivation and pharmacological treatment compared to the other two BC lines (max inhibitory effect of 2DG around 70% and $EC_{50} = 2.104$ mM).

The anti-proliferative effect of glucose deprivation and the EC_{50} of 2DG treatment fit a linear regression with a $R^2 = 0.9954$, suggesting that these two metabolic perturbations have comparable effects on the BC cell lines. As expected, the relation

between them is inversely proportional: the higher the EC₅₀ of the drug treatment, the lower the anti-proliferative effect of glucose deprivation (**Figure 22C**).

Summarily, there is a significant dependence on the carbohydrate metabolic axis by the three BC cell lines, which well correlates with the data obtained by Agilent Seahorse XFe96 technology in the previously described assays.

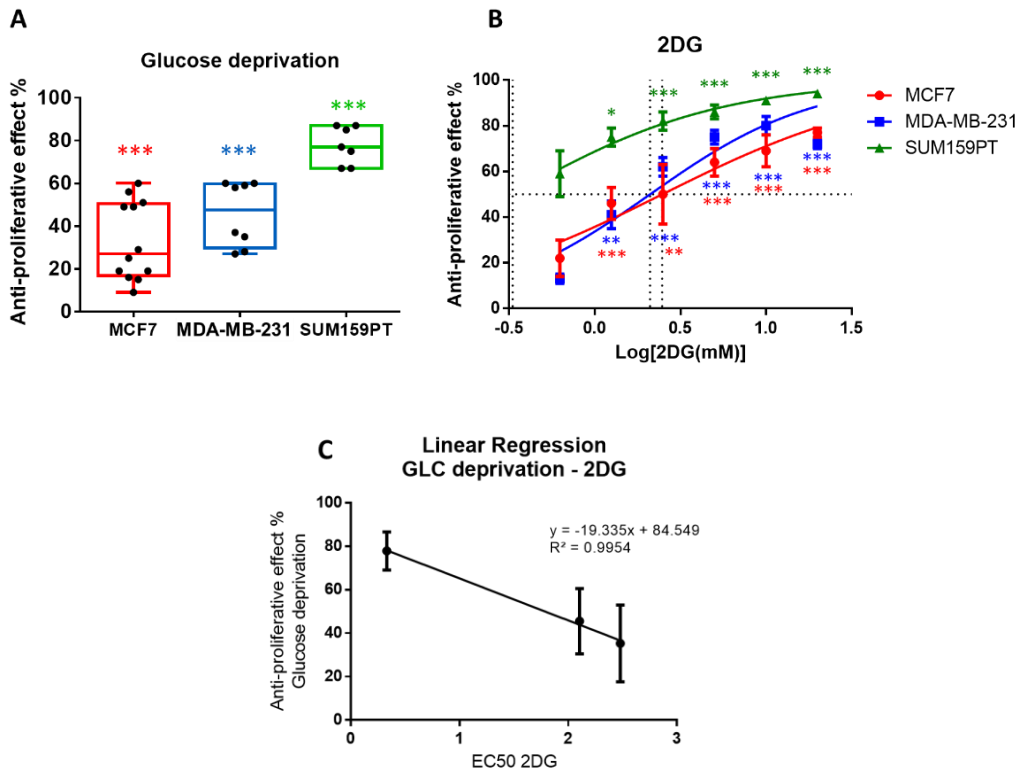


Figure 22 (A) Anti-proliferative effect % of glucose deprivation and (B) 2DG treatment tested at concentrations 0.625mM - 1.25mM - 2.5mM - 5mM - 10mM - 20mM (expressed as Log[concentration]) compared to the control condition and related statistical significance of BC cell lines grown in adhesion (2D) The anti-proliferative effect was calculated at 72 hours as $[1 - (n^{\circ} \text{ treated cells} / n^{\circ} \text{ control cells})]\%$. The count was performed with Hoechst staining and Operetta-Harmony acquisition and analysis. (C) Linear regression between the anti-proliferative effect of glucose deprivation and the EC₅₀ of 2DG treatment obtained from the curves reported in panel (B). Statistical significance calculated with 2way Anova is expressed as * = $p < 0.05$; ** = $p < 0.01$; *** = $p < 0.001$. The data reported in the graphs derive from three independent experiments.

Glutamine deprivation has a significant impact on all BC cell lines growth too, with a slightly greater effect on SUM159PT (**Figure 23A, B**). To evaluate the effect of BPTES, a

glutaminase inhibitor that is solubilized in DMSO, the appropriate vehicle concentration was added to the control condition. SUM159PT cells are the most sensitive to BPTES treatment since the lowest concentration tested, followed by MDA-MB-231. Only MCF7 cell line shows minimal sensitivity to treatment at all drug concentrations tested (unfortunately the low effect of this drug treatment cannot be completely attributed to BPTES because MCF7 proliferation revealed to be strongly inhibited by DMSO vehicle). Combining the results of nutritional and pharmacological perturbations, it emerges that SUM159PT cell line shows the greatest consistency between deprivation and BPTES treatment ($p > 0.05$; non-parametric Kruskal-Wallis test) with a maximal inhibitory effect of the drug above 80%, while MDA-MB-231 cell line and, especially, MCF7 cell line are much less sensitive to the drug effect than glutamine deprivation.

The anti-proliferative effect of glutamine deprivation and the EC_{50} of BPTES treatment do not fit a linear regression ($R^2 = 0.3663$), suggesting that these two metabolic perturbations do not have comparable effects on all the BC cell lines. This could be partially due to the cytotoxic effect of DMSO (the vehicle used to resuspend BPTES powder) on MCF7 and on the other hand the discordant data of MDA-MB-231 cell line which shows a high anti-proliferative effect of glutamine deprivation but a relatively low effect of BPTES (higher EC_{50} values compared to the other two cell lines). We

propose to further investigate this aspect studying the effect of other inhibitors of glutamine metabolism.

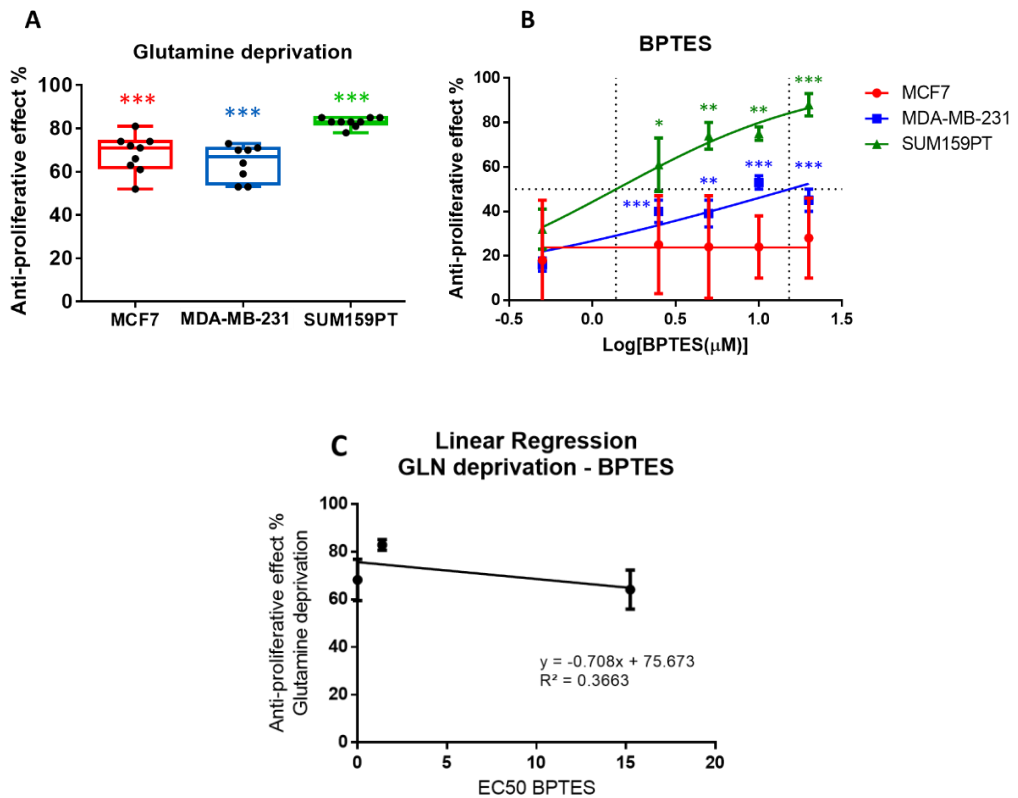


Figure 23 (A) Anti-proliferative effect % of glutamine deprivation and (B) BPTES treatment tested at concentrations 0.5 μ M - 2.5 μ M - 5 μ M - 10 μ M - 20 μ M (expressed as Log[concentration]) compared to the control condition and related statistical significance of BC cell lines grown in adhesion (2D) The anti-proliferative effect was calculated at 72 hours as $[1 - (n^\circ \text{ treated cells} / n^\circ \text{ control cells})] \%$. The count was performed with Hoechst staining and Operetta-Harmony acquisition and analysis. (C) Linear regression between the anti-proliferative effect of glutamine deprivation and the EC50 of BPTES treatment obtained from the curves reported in panel (B). Statistical significance calculated with 2way Anova is expressed as * = $p < 0.05$; ** = $p < 0.01$; *** = $p < 0.001$. The data reported in the graphs derive from three independent experiments.

At this point, the inhibition of the fatty acids metabolic axis was tested using the drug Etomoxir, carnitine palmitoyl-transferase 1A (CPT1A) inhibitor, which blocks the transport of fatty acids from the cytoplasm to the mitochondrion.

The results in **Figure 24** show that MDA-MB-231 cell line is the most sensitive to the treatment with Etomoxir, whose significant effect is evident at concentration 50 μ M ($p = 0.014$, Kruskal-Wallis non-parametric test). This data correlate with those obtained from Mito fuel flex test, which records the dependency of MDA-MB-231 cell line on all metabolic substrates and an absence of flexibility. On the other hand, MCF7 cell line shows to be affected by the drug treatment only at the highest concentration tested, 200 μ M ($p = 0.006$; Kruskal-Wallis non-parametric test). However, this result has a poor biological value due to a possible pleiotropic effect of high-dose Etomoxir. Finally, SUM159PT cell line is not significantly affected by this treatment (at all concentrations used $p > 0.05$; non-parametric Kruskal-Wallis test).

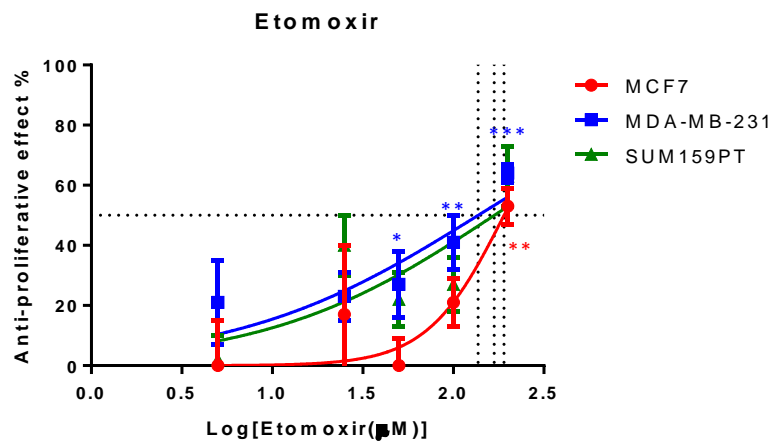


Figure 24 Anti-proliferative effect % of Etomoxir treatment tested at concentrations 5 μ M – 25 μ M – 50 μ M – 100 μ M – 200 μ M (expressed as Log[concentration]) compared to the control condition and related statistical significance of BC cell lines grown in adhesion (2D) The anti-proliferative effect was calculated at 72 hours as $[1 - (n^\circ \text{ treated cells} / n^\circ \text{ control cells})]\%$. The count was performed with Hoechst staining and Operetta-Harmony acquisition and analysis. Statistical significance calculated with 2way Anova is expressed as * = $p < 0.05$; ** = $p < 0.01$; *** = $p < 0.001$. The data reported in the graphs derive from three independent experiments.

The last drug tested was Oligomycin, an ATP-synthase inhibitor blocking the mitochondrial production of ATP.

Oligomycin treatment (*Figure 25*) have a significant impact on cell proliferation of all three BC cell lines even at the lowest concentration tested, with a greater effect on SUM159PT cell line, followed by MCF7 cell line and lastly, albeit significant, on MDA-MB-231 cell line. These data are consistent with those obtained by the Seahorse assays demonstrating that MDA-MB-231 cell line has a less functional respiratory machinery.

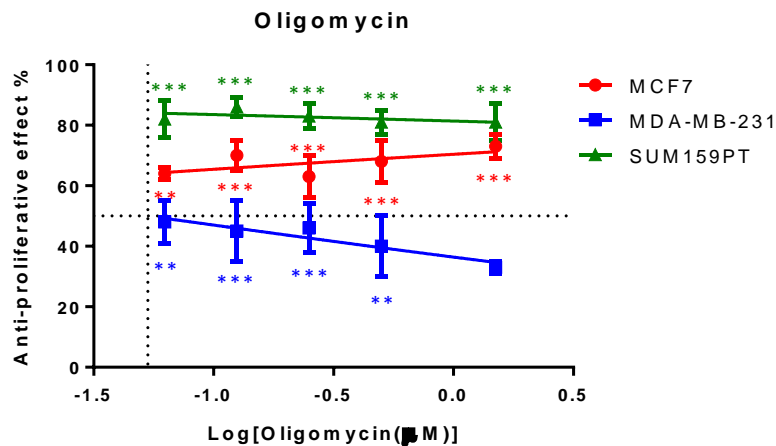


Figure 25 Anti-proliferative effect % of Oligomycin treatment tested at concentrations 0.0625μM - 0.125μM - 0.25μM - 0.5μM - 1.5μM (expressed as Log[concentration]) compared to the control condition and related statistical significance of BC cell lines grown in adhesion (2D) The anti-proliferative effect was calculated at 72 hours as $[1 - (n^{\circ} \text{ treated cells} / n^{\circ} \text{ control cells})] \%$. The count was performed with Hoechst staining and Operetta-Harmony acquisition and analysis. Statistical significance calculated with 2way ANOVA is expressed as ** = $p < 0.01$; *** = $p < 0.001$. The data reported in the graphs derive from three independent experiments.

2.4.5 Propensity to form spheroids (3D)

The propensity of BC cell lines to form spheroids was studied by seeding the cells 12-wells plates not-treated for tissue culture (suspension plates) in 3D experimental medium as described in paragraph 2.3.2. The images in *Figure 26* were obtained using a phase contrast microscope (Olympus CKX41). The images show that the MCF7 cell line does not adhere to the untreated plates and starts spontaneously forming small spheroids after 24 hours of seeding; in the following days of culture the major

observation is that these small spheroids tend to merge together, forming much larger structures with irregular shapes.

Similarly, MDA-MB-231 cell line does not adhere to untreated plates but immediately tends to form aggregates in suspension. These aggregates become more compact over time, forming irregular spheroids.

On the contrary, SUM159PT cell line adheres loosely to untreated plates; the spheroids are formed starting from the attached cells that migrate and aggregate one to each other, following a slower process compared to the other two cell lines. During the following days the spheroids grow in size and detach from the support. SUM159PT cell line forms spheroids with smaller dimensions but more regular shapes compared to MCF7 and MDA-MB-231 cell lines.

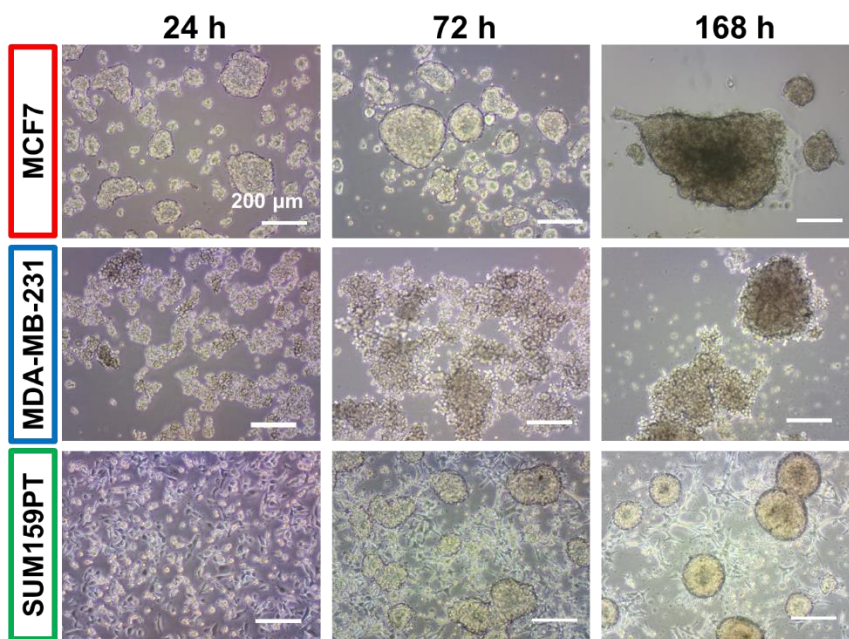


Figure 26 Phase contrast microscope images of spontaneous spheroid formation of BC cell lines at 24h (1 day), 72h (3 days), and 168h (7 days) after seeding.

In conclusion, all BC cell lines can form spheroids that progressively merge together.

The following study is the application an optimized protocol of spheroid formation to

evaluate the ability of BC cells to form three-dimensional structures under the effects of pharmacological treatments and metabolic perturbations.

2.4.6 Spheroid formation assays under metabolic perturbation by nutritional deprivation or pharmacological treatment

For studying the effect of pharmacological treatments with metabolic drugs and nutritional perturbations on the spheroid formation capacity of the three BC cell lines, a more standardized protocol was applied for spheroid formation. The protocol described in material and methods (paragraph *Errore. L'origine riferimento non è stata trovata.*) consists in seeding a specific number of cells per well (10,000 cells/well) on U-bottom Ultra-low attachment 96-well plates, followed by plate centrifugation. This method enables to obtain one single spheroid per well, with much higher reproducibility in terms of regularity and morphology (i.e., shape and size). Each condition was evaluated through imaging analysis performed on the three-dimensional structures at 72 hours after seeding in presence or absence of the metabolic perturbation.

Under glucose deprivation, MCF7 spheroids show an intensification of PI fluorescence (**Figure 27**), indicating a greater mortality induced by this metabolic perturbation that seems to be colocalized with the anoxic core (**Figure 27A**). The treatment with 2DG, especially at the highest drug concentration, favors the formation of spheroids showing a partial delocalization of dead cells, detected by PI staining; since the area of PI detection is larger, the intensity of its fluorescence does not increase. The spheroids also show substantially negligible effects on compactness and on the perimeter regularity (detected with Cell Tracker Green, indicated by roundness values), suggesting that even in the absence of glucose, MCF7 cells are able to form spheroids morphologically similar to those of control condition.

MDA-MB-231 spheroids are the most impacted by glucose deprivation and 2DG treatment, which have lead to an increase in PI fluorescence in a dose-dependent manner (**Figure 27B**), indicating an overall increase in cell mortality. In addition, a

decrease in compactness also emerges from the detection in brightfield (*Figure 27A*) and from roundness values (*Figure 27B*): the spheroids are visibly more fragmented, lacking perimeter regularity. The glucose perturbation through both nutritional deprivation and pharmacological treatment, seems having impacted and therefore prevented spheroid formation of this cell line.

In SUM159PT spheroids treated with 2DG we can observe both a loss of compactness of the necrotic core with a consequent increase in the PI area distribution and a loss of the perimeter regularity of the three-dimensional structure, in particular at the highest concentration of 2DG used (*Figure 27A-B*). Under glucose deprivation we also can observe a shrinkage of the spheroids, characterized by lower roundness and higher mortality (identified by an increased PI intensity, *Figure 27B*), demonstrating that glucose may have an important role in the spheroid formation process of SUM159PT cell line.

Therefore, these data suggest that glucose deprivation and the treatment with 2DG have a particular impact on spheroid formation of MDA-MB-231 cells; in MCF7 and

SUM159PT cell lines the greatest effect on the spheroid formation is mainly found under the higher concentration of drug treatment.

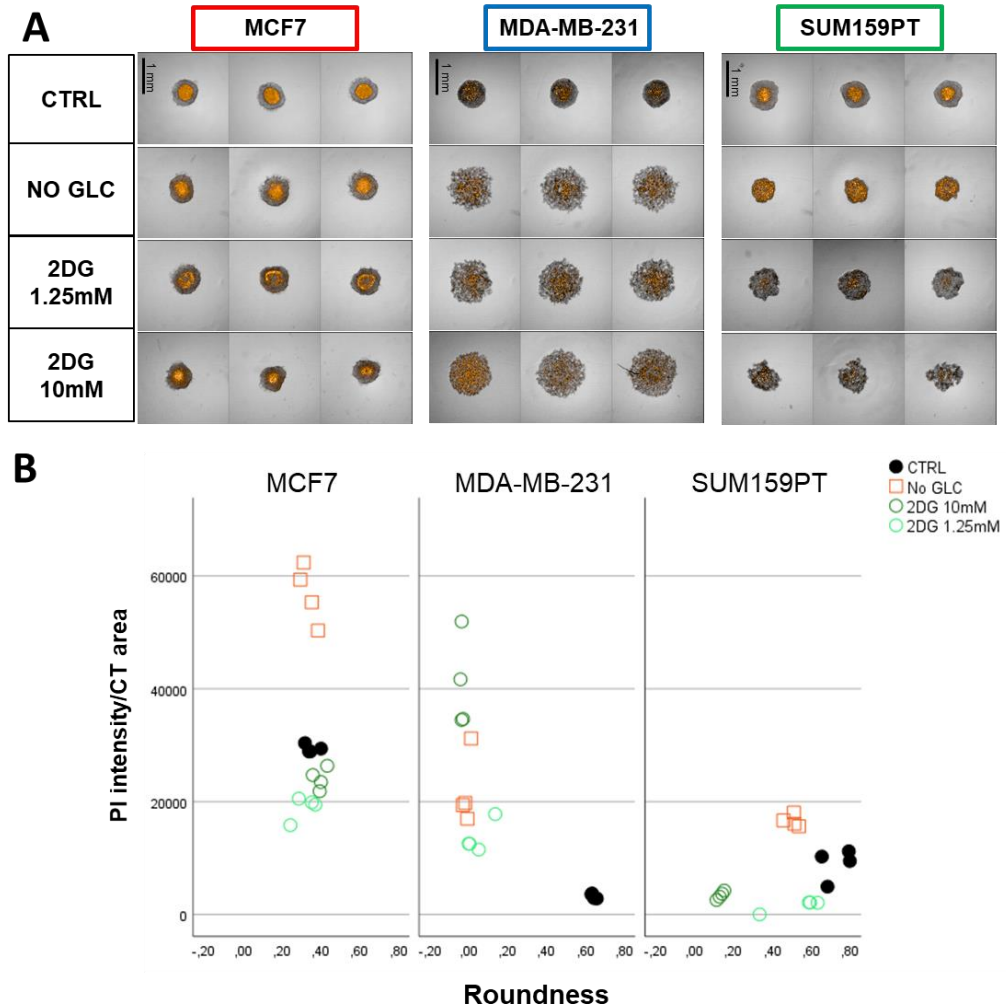


Figure 27 (A) Images of spheroid formation assay of the three BC cell lines in triplicate at 72 hours; comparison between control and glucose deprivation or treatment with 2DG at different concentrations (1.25mM - 10mM). The images show the merge of brightfield and Propidium iodide (PI) fluorescence for a qualitative evaluation. Scale bar = 1 mm. **(B)** Scatter dot plot relating roundness (parameter measuring the compactness and perimeter regularity) and intensity detected by the fluorescence of Propidium iodide normalized on the total area of the spheroid measured as a selection of the CellTracker Green fluorescence (measure of the quantity and distribution of cell mortality). The data reported in the graph derive from one experiment with four technical replicates for each condition.

Under glutamine deprivation we can notice a lowering of PI detection in MCF7 spheroids that can be explained by a spreading of PI signal within the spheroid, correlated to an initial loss of the levels of organization of the three-dimensional structure. Qualitatively similar but quantitatively milder effects of the reduced ability to form spheroids can be observed under BPTES treatment (*Figure 28A-B*). On the other hand, in MDA-MB-231 spheroids, any significative change seems to occur under treatment with BPTES, while a slight reduction of perimeter regularity/roundness can be observed under glutamine deprivation (*Figure 28B*). Glutamine deprivation seem to cause a loss of perimeter regularity and an increased dispersion of PI signal in SUM159PT spheroids, while the treatment with BPTES seem to produce just a modest shrinkage of these 3D structures (*Figure 28A-B*).

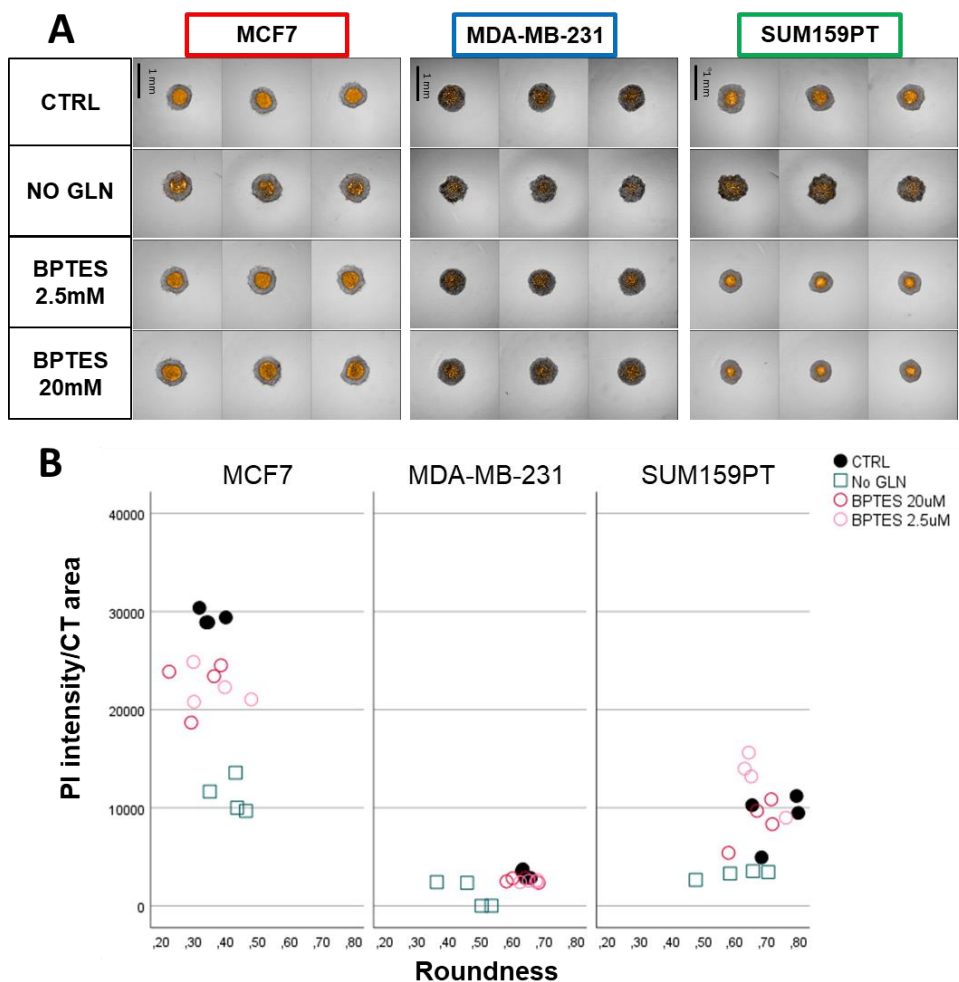


Figure 28 (A) Images of spheroid formation assay of the three BC cell lines in triplicate at 72 hours; comparison between control and glutamine deprivation or treatment with BPTES at different concentrations (2.5 μ M - 20 μ M). The images show the merge of brightfield and Propidium Iodide (PI) fluorescence for a qualitative evaluation. Scale barr = 1 mm. **(B)** Scatter dot plot relating roundness (parameter measuring the compactness and perimeter regularity) and intensity detected by the fluorescence of Propidium Iodide normalized on the total area of the spheroid measured as a selection of the CellTracker Green fluorescence (measure of the quantity and distribution of cell mortality). The data reported in the graph derive from one experiment with four technical replicates for each condition.

On the contrary, the treatment with Etomoxir does not produce any significant variations in any of the lines examined; the spheroids form without undergoing any

impact due to the presence of the drug, not even at the highest concentration tested (Figure 29A-B).

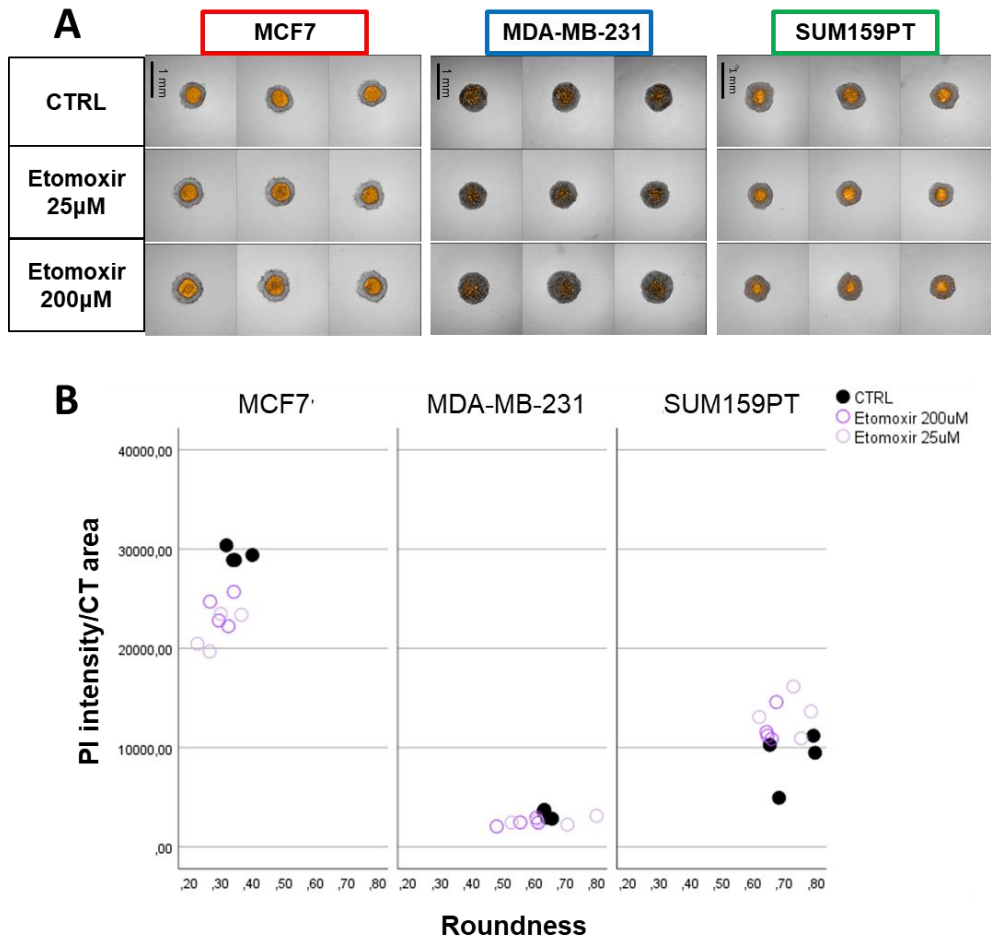


Figure 29 (A) Images of spheroid formation assay of the three BC cell lines in triplicate at 72 hours; comparison between control and treatment with Etomoxir at different concentrations (25µM - 200µM). The images show the merge of brightfield and Propidium iodide (PI) fluorescence for a qualitative evaluation. Scale barr = 1 mm. (B) Scatter dot plot relating roundness (parameter measuring the compactness and perimeter regularity) and intensity detected by the fluorescence of Propidium iodide normalized on the total area of the spheroid measured as a selection of the CellTracker Green fluorescence (measure of the quantity and distribution of cell mortality). The data reported in the graph derive from one experiment with four technical replicates for each condition.

Oligomycin does not seem to have a substantial impact on the spheroid formation process of MCF7 and MDA-MB-231 cell lines. The only significant effect of this drug can be observed in SUM159PT spheroids, which show an increased intensity of PI signal, together with a larger area of the necrotic central core and a decreased perimeter regularity (*Figure 30*).

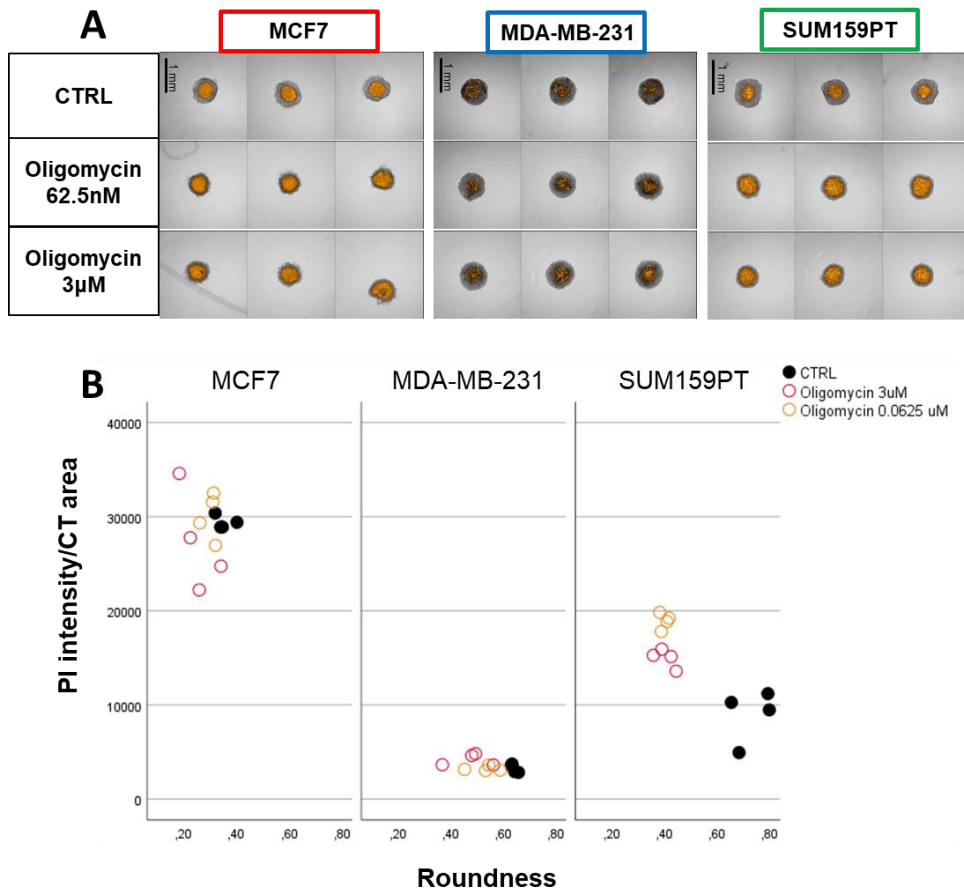


Figure 30 (A) Images of spheroid formation assay of the three BC cell lines in triplicate at 72 hours; comparison between control and treatment with Oligomycin at different concentrations (62.5nM - 3µM). The images show the merge of brightfield and Propidium Iodide (PI) fluorescence for a qualitative evaluation. Scale barr = 1 mm. (B) Graphs relating PI intensity/CT area and roundness of the spheroids under respiratory metabolism perturbation, for a quantitative evaluation. Scatter dot plot relating roundness (parameter measuring the compactness and perimeter regularity) and intensity detected by the fluorescence of Propidium Iodide normalized on the total area of the spheroid measured as a selection of the CellTracker Green fluorescence (measure of the quantity and distribution of cell mortality). The data reported in the graph derive from one experiment with four technical replicates for each condition.

2.4.7 Preliminary metabolic characterization of homotypic and heterotypic three-dimensional (3D) cultures: analysis of basal and perturbed respiration and acidification rate

In order to compare the bioenergetic parameters of spheroids formed from BC cell lines, OCR and ECAR parameters are normalized on the number of cells per spheroid, calculated indirectly from spheroid area (for further details see paragraph 2.3.6 in Materials and Methods section). The measurement of the area of each spheroid was obtained from the analysis of Cell Tracker fluorescence by mean of Operetta CLS™ and Harmony software.

The basal oxygen consumption rates of the spheroids are similar to those observed in 2D (*Figure 31*): MCF7 cell line remains the most aerobic among the BC cell lines, MDA-MB-231 cell line the one that less exploits mitochondrial respiration in basal conditions, while SUM159PT cell line shows an intermediate OCR (*Figure 31*). Contrarily to the data registered in the corresponding 2D cultures, MCF7 and SUM159PT spheroids exhibit higher extracellular acidification rates than MDA-MB-231 spheroids. Altogether these data show that MCF7 spheroids are the most energetic among the BC cell lines, MDA-MB-231 spheroids are the most quiescent ones, while SUM159PT

spheroids have an intermediate metabolism: more energetic than MDA-MB-231 spheroids but less than MCF7 ones.

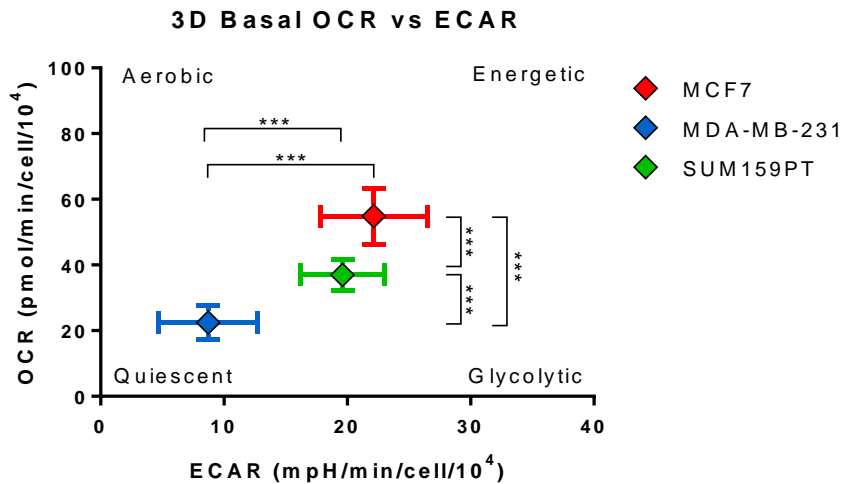


Figure 31 Basal metabolic parameters of BC lines grown as spheroids for 72h (3D). Statistically significant differences between cell lines are expressed as *= $p < 0.05$; **= $p < 0.01$; ***= $p < 0.001$ applying the comparison of means with 2way Anova test. The data reported in the graph derive from two independent experiments.

These data are better highlighted by the Mito Stress Test (**Figure 32A, B**), demonstrating that the MCF7 spheroids also have the highest value of maximal respiration and spare respiratory capacity, suggesting their greater ability to respond to an increased demand for energy than the other two cell lines. Moreover, MDA-MB-231 spheroids seem to have an enhanced response to FCCP that the adhesion counterpart: this indicates that, even though they are the most quiescent among BC spheroids, they are more flexible to increase mitochondrial respiration to respond to stressful conditions.

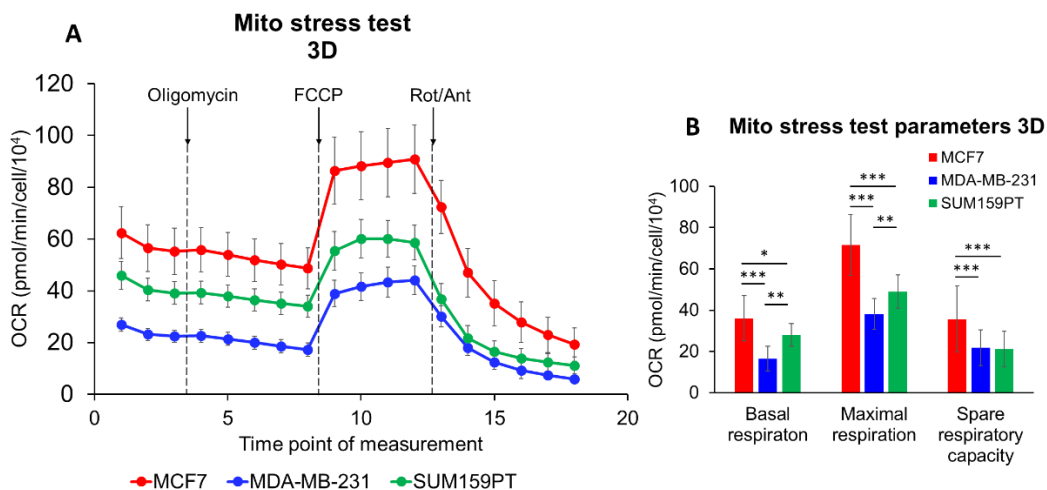


Figure 32 (A) Mito stress test OCR profile of BC cell lines grown as spheroids for 72h (3D). The arrows indicate the time point at which the drugs were injected (2 μ M Oligomycin, 2 μ M FCCP, 0.5 μ M Rotenone/Antimycin A). (B) Mito stress test parameters of calculated as reported in Materials and Methods (paragraph 2.3.6): Basal respiration, Maximal respiration, and Spare respiratory capacity. Statistically significant differences between cell lines are expressed as * = $p < 0.05$; *** = $p < 0.001$ applying the comparison of means with 2way Anova test. The data reported in the graphs derive from two independent experiments.

A preliminary characterization of heterotypic spheroids formed by MCF7 cell line and HMF8 primary human normal mammary fibroblasts was performed to investigate the metabolic interactions occurring between breast cancer cells and components of the TME. In **Figure 33**, the images of the heterotypic spheroids analyzed by Seahorse technology are represented: the breast cancer cell line MCF7 (stained with Cell Tracker red CMPTX) seems to localize in the outer layers of the heterotypic spheroid and to co-localize with primary fibroblasts HMF8 (stained with Cell Tracker Green CMFDA) in the center of the 3D structure. This distribution between cancer cells and fibroblasts was already observed in similar models [226,227].

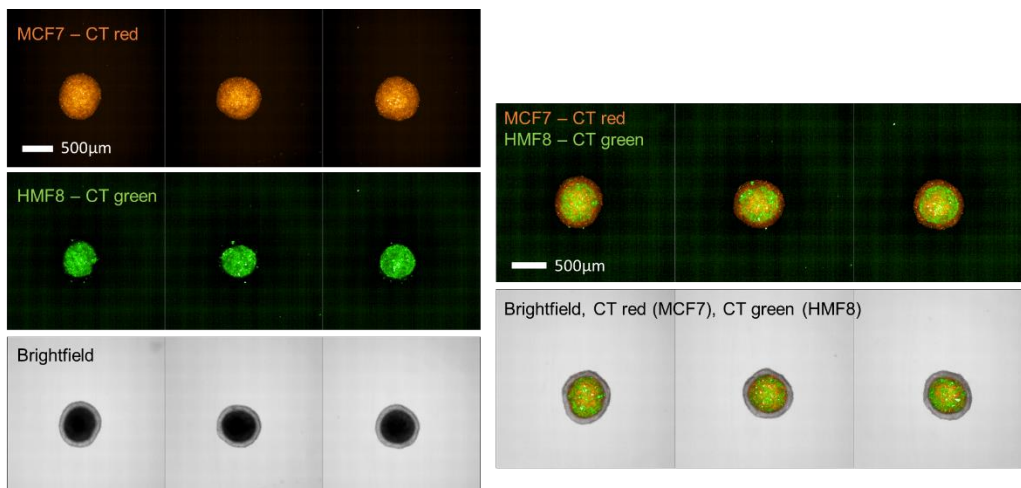


Figure 33 Heterotypic spheroids obtained by the co-culture between 5,000 cells of MCF7 cell line (CellTracker™ Red CMPTX) and 5,000 cells of fibroblasts HMF8 (CellTracker™ Green CMFDA). Images represent CT red maximum intensity projection (left-top), CT green maximum intensity projection (left-middle), brightfield (left-bottom) and merges of CT green + CT red maximum intensity projections (right-top) and merge of all channels (right-bottom) acquired by Operetta CLS™ 72h after seeding.

The results of basal and stressed energy map (**Figure 34A**) demonstrate that MCF7 and HMF8 spheroids present a similar use of glycolysis but the BC cell line has a 1.7 times greater oxygen consumption rate than fibroblasts in basal condition. On the other hand, the heterotypic spheroids are more energetic than both homotypic spheroids, with a 60% higher extracellular acidification rate than HMF8 (but similar to MCF7's ECAR) and a 120% and 30% greater use of oxidative phosphorylation than HMF8 and MCF7, respectively. Under stressful conditions (induced by the treatment with 2µM FCCP), all the spheroids simultaneously enhance glycolysis and mitochondrial respiration. In particular, HMF8 spheroids present the highest metabolic potential (**Figure 34B**), showing the greatest ability to enhance both glycolysis (+3.1 times) and mitochondrial respiration (+2.2 times), while MCF7 spheroids and heterotypic spheroids show an increase of both parameters around 1.5-1.6 times. The energetic phenotype reached by heterotypic culture is not significantly different from that of HMF8 spheroids but significantly higher than MCF7 spheroids (statistical analysis is reported in **Table 4**).

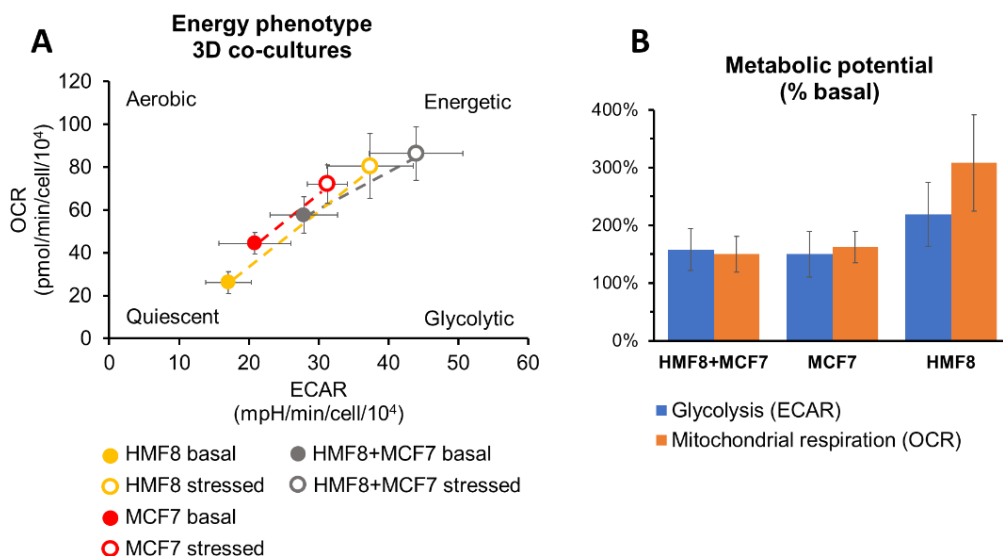


Figure 34 (A) Energy phenotype of homotypic MCF7 and HMF8 and heterotypic HMF8+MCF7 spheroids under basal and stressed conditions induced by the injection of 2 μ M FCCP. (B) Metabolic potential of the same cultures calculated as the ratio between basal and stressed OCR and ECAR%. The data reported in the graph derive from one experiment with MCF7 N=14, HMF8 N=13, HMF8+MCF7 N=28 technical replicates.

Table 4 Table of statistical comparison between basal and stressed ECAR and OCR values of the data presented in **Figure 34A**. Statistically significant differences between cell lines are expressed as *= p < 0.05; **= p < 0.01; ***= p < 0.001 applying the comparison of means with 2way Anova test.

| | | BASAL | STRESSED |
|------|-------------------|-------|----------|
| ECAR | HMF8+MCF7 vs MCF7 | NS | *** |
| | HMF8+MCF7 vs HMF8 | ** | NS |
| | MCF7 vs HMF8 | NS | NS |
| OCR | HMF8+MCF7 vs MCF7 | *** | *** |
| | HMF8+MCF7 vs HMF8 | *** | NS |
| | MCF7 vs HMF8 | *** | NS |

These data suggest that the 3D co-culture stimulates a more energetic basal metabolism than the 3D mono-cultures and reaches a greater energetic state under stressful condition compared to the homotypic breast cancer spheroids.

It should be underlined that the Seahorse analysis on whole spheroids give information about the average metabolic state of all the cells in the spheroid, and the measured parameters (OCR and ECAR) can be partially influenced by the non-homogeneous diffusion of oxygen and protons in the extracellular medium. This kind of analysis does not allow to discern the metabolic states of the single cells which compose the inner or the outer layers of the spheroid under study. Despite these limitations of Seahorse analysis, we believe that it is a valid technology to start exploring the global metabolic characteristics of three-dimensional cultures.

2.5 Discussion

It is known that tumor cells, in order to maintain their transformed state, support the high proliferative rate and survive in the tumor microenvironment, tend to remodel their metabolic network [22]. Starting from this assumption, we focused on the study of the cancer metabolic phenotype - which could represent, therefore, a real opportunity to find new therapeutic approaches - in three breast cancer cell lines: a hormone-sensitive cell line, MCF7, and two triple-negative cell lines, MDA-MB-231 and SUM159PT. For this purpose, we started by characterizing the metabolic and nutritional profiles of the three BC cell lines that grown in adhesion (2D), then moved to the qualitative and the preliminary quantitative analysis of the three-dimensional models, that are more representative of the pathology *in vivo*. The media compositions of the three BC cell lines had been previously optimized in order to evaluate the effects of deprivations and pharmacological treatments in the best possible growth conditions. The spheroids were obtained using U-bottom Ultra-Low Attachment plates which facilitate the generation of uniform spheroids and their high throughput analysis by brightfield and fluorescence microscopy.

The three BC cell lines cultured in 2D exhibit distinct metabolic profiles. As expected, the hormone receptors positive cell line MCF7 is the most respiratory, so that the production of ATP largely (over 70%) due to respiration. MCF7 cells use almost

exclusively glucose as a respiratory substrate, and they have a high ability to increase respiration in conditions of nutritional stress, demonstrating to be flexible in the use of glutamine and fatty acids for respiration in the absence of glucose. Since MCF7 cells do not use this amino acid as a respiratory substrate, this effect probably depends on the use of glutamine for the synthesis of "building blocks" necessary for proliferation [228]. Consistently with its low glycolytic rate and high flexibility in fuels oxidation, glucose deprivation and the inhibition of its metabolism by 2DG have a minor impact on MCF7 cell proliferation than the other two cell lines. As expected, the inhibition of mitochondrial respiration by oligomycin reduces MCF7 cell proliferation much more than observed in MDA-MB-231 cells.

Consistently with its molecular subtype (TNBC) [217,220,229], MDA-MB-231 cell line is the most glycolytic, with a respiratory contribution to the ATP production rate that does not exceed 30%. The main substrate of oxidative phosphorylation in this cell line is glucose, but these cells have no flexibility in responding to increased energy demand or to switch metabolic substrate oxidation under stressful condition. Consistently with the limited role of mitochondria in the ATP production, the cell proliferation inhibition induced by oligomycin is significantly lower than in the other two cell lines. The inhibitory effect on proliferation induced by glutamine deprivation is lower than that observed in MCF7 and SUM159PT cells.

SUM159PT cell line shows a glycolytic basal metabolism similar to MDA-MB-231 cell line but with a higher flexibility to respond to stressful conditions enhancing mitochondrial respiration. Mitochondrial respiration of SUM159PT cell line is more dependent on glucose than on glutamine or fatty acids. Consistently with its molecular subtype (TNBC)[220], the results of glucose deprivation and 2DG treatment assays demonstrates that SUM159PT cell line is the most sensitive to glucose perturbation (which have an impact on proliferation of about 80%).

In all cell lines, the inhibition of fatty acid oxidation by Etomoxir has limited effects on cell proliferation, which appear only at drug concentrations above 200 μ M,

concentrations at which notable off-target effects they have been reported [230]. For this reason, the effects of Etomoxir will not be considered further in this discussion.

The results obtained in this work indicate that - in general - the impact of metabolic perturbations is greater on monolayer cell proliferation than on spheroid formation capacity of the BC cell lines. The nutritional or pharmacological perturbation of glucose metabolism is the one that has the most evident impact on the spheroid formation of all three BC cell lines, especially on cell MDA-MB-231 line, which is the most strongly glycolytic. Oligomycin, unlike the results obtained in 2D, appears to have just slight effects on the spheroids' formation of SUM159PT cell line which presents a reduction in compactness and increased mortality. The comparative metabolic profile of pre-formed spheroids partially differs from 2D cultures: in particular, MDA-MB-231 cell line becomes more quiescent in 3D and MCF7 spheroids are less dependent on respiration and slightly more glycolytic than its 2D counterpart. Therefore, the lower effect of oligomycin on MCF7 and MDA-MB-231 lines, could partially reflect a metabolic rearrangement that would occurring in 3D cultures [231].

Literature data show that, in the transition from two- to three-dimensional structure, other cancer cell lines undergo a reduction in glucose uptake, lactate secretion, cellular respiration and ATP synthesis in response to hypoxia. This could suggest, in addition to a reduced proliferation of cells aggregated into spheroids, a down-regulation of respiration and, therefore, an adaptation of cellular metabolism may occur in order to better survive to non-permissive conditions [232]. In fact, it is known that tumors can undergo selection in response to therapies, generating chemoresistance and/or metastases, towards genetic and metabolic reprogramming with a worse prognosis [233].

Therefore, it will be of great interest to follow the time-dependent evolution of the metabolic rearrangement occurring in spheroids by means of expression analysis of the main molecular actors using immuno-histochemical or transcriptional analysis. To consolidate the assays presented in this work, it will be necessary to validate the

metabolic differences between adhesion cells and pre-formed spheroids through other metabolic assays such Mito fuel flex test to study the dependency and flexibility in the use of nutrients on pre-formed spheroids, and to test the effect of drugs targeting specific metabolic pathways in inducing cell death and disruption of spheroids.

The layers of cell within the spheroids create gradients of oxygen, nutrients and metabolites and barriers that influence the transport of drugs and signaling, which have an important role in the study of pathologies [135]. To observe these phenomena on living cells, there are a wide variety of fluorescent probes that can be employed through confocal microscopy [119]. However, in using confocal microscopy, the loss of fluorescent signal must be considered moving to the innermost part of the spheroid. In 3D renderings in the absence of treatments that makes the cellular matrix more accessible to light, the spheroids appear as a bowl with a light signal around the edges and a muted signal inside. Therefore, the quantifications presented in the results of spheroid formation assays represent a – albeit useful - approximation, linked to the impossibility of reconstructing the complete three-dimensional structure in our analysis conditions. Indeed, the Roundness is calculated on the circumference of the two-dimensional projection of the spheroid and not on the sphericity and intensity of the PI is related to the area and not to the volume since this is not entirely detectable. The morphometric and functional study of the spheroids requires more complex experimental techniques (such as the fixation and / or clarification of the sample, which inevitably limits the spectrum of usable vital probes), and computational techniques. Taken together, these techniques allow to observe the spheroid in its entirety, to quantify the number of cells and their morphology, thus providing a more complex and more representative picture, which will be the subject of subsequent studies.

Moreover, it should be underlined that the Seahorse analysis on whole spheroids give information about the average metabolic state of all the cells in the spheroid, and the measured parameters (OCR and ECAR) can be partially influenced by the non-

homogeneous diffusion of oxygen and protons in the extracellular medium. This kind of analysis does not allow to discern the metabolic states of the single cells which compose the inner or the outer layers of the spheroid under study. Despite these limitations of Seahorse analysis, we believe that it is a valid technology to start exploring the global metabolic characteristics of three-dimensional cultures. As future perspective we propose to integrate the metabolic data obtained by mean of Seahorse technology with more sophisticated novel techniques enabling the metabolic analysis at single-cell level on tumor spheroids [234].

In conclusion, the breast cancer cell lines examined exhibit different metabolic profiles as 2D models and can spontaneously form spheroids in untreated and cell-repellent plates. This capacity is differentially modulated by nutritional and pharmacological perturbations, with an important role for glucose metabolism. Indeed, by analyzing the transition of cells from the adhesion status to the suspension and aggregation status in three-dimensional structures, it is possible to notice different responses to pharmacological treatments suggesting that changes are taking place at metabolic level. These alterations manifest as a greater resistance to equivalent concentrations of drugs to those tested in 2D; indeed, only modest morphological alterations or mortality occur during spheroid formation under metabolic perturbations compared to the control condition. Accordingly, the data obtained by Seahorse assays on pre-formed spheroids show that the basal metabolism of BC cell lines has undergone a partial rearrangement compared to the 2D counterparts. The detected effects depend both on the initial metabolic state of the individual BC cell lines and on their flexibility to remodel their metabolism. In the future we propose to translate the here described methods developed for the study of the metabolism of three-dimensional models onto more complex cancer models. In particular, we are planning to deepen the effect of metabolic perturbations on pre-formed breast cancer spheroids, on patient derived breast organoids and on heterotypic spheroids. About the latter, a preliminary study on basal and stressed metabolic phenotype is reported in this work, but more in-depth analysis are required to dissect the heterotypic interactions between different cell

types of the TME, as well as the effects of these interactions on the response to therapies [235,236].

References can be found after 'General Discussion' → [REFERENCES](#)






CHAPTER 2: AN OPTIMIZED WORKFLOW FOR ANALYSIS OF METABOLIC FLUXES IN CANCER SPHEROIDS USING SEAHORSE TECHNOLOGY

doi: [10.3390/cells11050866](https://doi.org/10.3390/cells11050866)

PDF of the published manuscript follows

Article

An Optimized Workflow for the Analysis of Metabolic Fluxes in Cancer Spheroids Using Seahorse Technology

Gloria Campioni ^{1,2}, Valentina Pasquale ^{1,2}, Stefano Busti ^{1,2}, Giacomo Ducci ^{1,2}, Elena Sacco ^{1,2}
and Marco Vanoni ^{1,2,*}

¹ Department of Biotechnology and Biosciences, University of Milano-Bicocca, 20126 Milan, Italy; g.campioni@campus.unimib.it (G.C.); valentina.pasquale@unimib.it (V.P.); stefano.busti1@unimib.it (S.B.); g.ducci@campus.unimib.it (G.D.); elena.sacco@unimib.it (E.S.)
² SYSBIO (Centre of Systems Biology), ISBE (Infrastructure Systems Biology Europe), 20126 Milan, Italy
* Correspondence: marco.vanoni@unimib.it; Tel.: +39-02-6448-3525

Abstract: Three-dimensional cancer models, such as spheroids, are increasingly being used to study cancer metabolism because they can better recapitulate the molecular and physiological aspects of the tumor architecture than conventional monolayer cultures. Although Agilent Seahorse XFe96 (Agilent Technologies, Santa Clara, CA, United States) is a valuable technology for studying metabolic alterations occurring in cancer cells, its application to three-dimensional cultures is still poorly optimized. We present a reliable and reproducible workflow for the Seahorse metabolic analysis of three-dimensional cultures. An optimized protocol enables the formation of spheroids highly regular in shape and homogenous in size, reducing variability in metabolic parameters among the experimental replicates, both under basal and drug treatment conditions. High-resolution imaging allows the calculation of the number of viable cells in each spheroid, the normalization of metabolic parameters on a per-cell basis, and grouping of the spheroids as a function of their size. Multivariate statistical tests on metabolic parameters determined by the Mito Stress test on two breast cancer cell lines show that metabolic differences among the studied spheroids are mostly related to the cell line rather than to the size of the spheroid. The optimized workflow allows high-resolution metabolic characterization of three-dimensional cultures, their comparison with monolayer cultures, and may aid in the design and interpretation of (multi)drug protocols.

Keywords: cancer metabolism; 3D cultures; high-throughput quantitative live-cell confocal imaging; bioenergetics; mitochondrial respiration



Citation: Campioni, G.; Pasquale, V.; Busti, S.; Ducci, G.; Sacco, E.; Vanoni, M. An Optimized Workflow for the Analysis of Metabolic Fluxes in Cancer Spheroids Using Seahorse Technology. *Cells* **2022**, *11*, 866. <https://doi.org/10.3390/cells11050866>

Academic Editor: Alexander E. Kalyuzhny

Received: 30 January 2022
Accepted: 1 March 2022
Published: 2 March 2022

Publisher's Note: MDPI stays neutral with regard to jurisdictional claims in published maps and institutional affiliations.



Copyright: © 2022 by the authors. Licensee MDPI, Basel, Switzerland. This article is an open access article distributed under the terms and conditions of the Creative Commons Attribution (CC BY) license (<https://creativecommons.org/licenses/by/4.0/>).

1. Introduction

Metabolic alterations represent one of the hallmarks of cancer [1]. Tumor cells modify their metabolism by enhancing or suppressing conventional anabolic and catabolic pathways as a consequence of tumorigenic mutations (e.g., Ras [2], Myc [3,4]), and/or harsh conditions imposed by the tumor microenvironment [5]. Metabolic rewiring is necessary for cancer cells; they must support an enhanced proliferation rate, requiring a more rapid production of energy and building blocks than normal cells. Moreover, an abnormal vascularization of tumors is often associated with the development of microregions with heterogeneous cells and environments, characterized by high proliferative activity close to the capillaries, quiescent cells as intermediates, and necrotic areas at greater distances from the vessels [6,7].

In vitro cancer models are a fundamental step for studying neoplastic pathology before moving to animal models that are more complex, time-consuming, and cost-intensive—while still necessary [8]. The most utilized in vitro tumor models are bidimensional (2D) monolayers cultures. However, in recent years, it has become clear that these models can behave very differently to cancer in vivo, leading to several failures when moving to animal models [9]. Some of the physiological limits of 2D cultures are, for instance, the bidimensional, monolayer growth on planar surfaces, which reduces cell–cell and

cell–extracellular matrix interactions and implies an unrealistic homogeneous distribution of soluble molecules and gases for all the cells in the culture [10]. The development of three-dimensional (3D) cancer models has allowed us to get closer to filling the gap between 2D *in vitro* models and *in vivo* animal models because they can better recapitulate the physiological characteristics of cancer. Indeed, the 3D disposition of cells in these cultures causes the spontaneous formation of concentration gradients for oxygen, pH, and soluble components such as nutrients and waste metabolites, leading to a heterogeneous cell phenotype [11]. Among the variety of 3D cancer models, the most reliable to produce and maintain are tumor spheroids. It has been observed that within the spheroid structure, various stages of cells are established due to the gradient described above, including proliferating cells—which can be found mainly at the outer layers of the spheroid—quiescent cells, and even necrotic cells at the central core, due to the hypoxic and starved state to which they are subjected [12,13]. Unlike 2D cultures, the cell heterogeneity represented by 3D models is closer to that observed in cancer *in vivo*, and it is reasonable to hypothesize that they can be better models for the study of metabolic alterations in cancer.

The employment of Agilent Seahorse technologies for studying metabolism is spreading in many fields, including cancer research [14]. Agilent Seahorse Extracellular Flux (XF) (Agilent Technologies, Santa Clara, CA, United States) analyzers can measure, at the same time, the oxygen consumption rate (OCR) and the extracellular acidification rate (ECAR) of cells in a microplate. It also can monitor variations in these parameters in Real-Time mode after treatment with molecules or drugs of interest, using ad hoc assembled or pre-formulated drug combinations available in kit form. This approach allows the quantitative dissection of the contribution of central metabolic pathways and available nutrients to the fulfillment of the energy requirements of cells. For instance, the Mito stress test includes modulators of the electron transport chain to investigate their role in sustaining cell metabolism. This technology has been exploited, for instance, to perform metabolic phenotyping of cancer cells in standard conditions and under perturbed conditions [15], to discover the metabolic switches responsible for the acquisition of malignant features (e.g., metastasis) [16], to observe metabolic heterogeneity in cancer through the identification of cell subpopulations harboring different metabolic profiles (e.g., cancer stem cells) [17,18], and many other studies of cancer metabolism [19–22].

However, despite the fact that the most recent and up-to-date XF analyzer, the XFe96 model, is also projected for use in these kinds of studies in three-dimensional cultures, the application of Seahorse XF technology has not been so widely exploited in these models as in bidimensional cultures. Only a few published works have used this technology with cancer spheroids [23,24] and with pancreatic islets from human and mice tissues [25].

This paper proposes an optimized workflow for applying Seahorse XF technology to single cancer spheroids. The workflow involves the generation of a single spheroid in each well of a U-bottom Ultra-Low Attachment (ULA) 96 well plate (PerkinElmer, Waltham, MA, USA). The obtained spheroids are regular in shape (with sections close to a circle) and relatively homogeneous in size, which depends on the number of plated cells. The transfer of these spheroids to XF plates allows the determination of metabolic parameters under basal conditions or following drug perturbations, such as the Mito Stress test. High-resolution imaging allows the calculation of the number of viable cells in each spheroid, the normalization of metabolic parameters on a per-cell basis, and grouping of the spheroids as a function of their size (i.e., the number of viable cells). We tested our complete workflow on two breast cancer cell lines with different metabolic phenotypes: MCF7 and MDA-MB-231 [26–28]. Multi-variate statistical tests showed that metabolic differences among the studied spheroids were mostly related to the cell line rather than to the size of the spheroid. The hormone-responsive line MCF7 maintained good metabolic plasticity in 2D and 3D cultures, while the triple-negative MDA-MB-231 withstood metabolic stress much better in 2D than in 3D cultures. The optimized workflow will be helpful in the high-resolution metabolic characterization of 3D cultures, their comparison with monolayer cultures, and for the appropriate design and interpretation of (multi)drug protocols.

2. Materials and Methods

2.1. Materials and Cell Cultures

The breast cancer cell line MCF7 was a generous gift from Dr. Luca Magnani (Imperial College London). Breast cancer cell lines MDA-MB-231 and SUM159PT were a generous gift from Dr. Lanfrancone (European Institute of Oncology). The bladder cancer cell line RT4 was purchased from American Type Culture Collection (ATCC, Manassas, VA, USA).

The MCF7 cell line was cultured in Dulbecco's Modified Eagle Medium (DMEM, 11960-044, Gibco™-Thermo Fisher Scientific, Waltham, MA, USA) supplemented with 10% fetal bovine serum (FBS, Gibco™-ThermoFisher, Waltham, MA, USA), 4 mM glutamine, 1 mM Na-Pyruvate, and 10 nM β -estradiol (E2758, Merck Life Science, Darmstadt, Germany), 100 U/mL penicillin, and 100 mg/mL streptomycin.

The MDA-MB-231 cell line was grown in RPMI-1640 medium (R0883-Merck Life Science, Darmstadt, Germany) supplemented with 10% fetal bovine serum (FBS, Gibco™-ThermoFisher, Waltham, MA, USA), 4 mM glutamine, 1 mM Na-pyruvate, 100 U/mL penicillin, and 100 mg/mL streptomycin.

SUM159PT cells were cultured in Ham's F-12 medium (11765-054, Gibco™-Thermo Fisher Scientific, Waltham, MA, USA) supplemented with 10% fetal bovine serum (FBS, Gibco™-ThermoFisher, Waltham, MA, USA), 2 mM glutamine, 5 μ g/mL insulin (I9278, Merck Life Science, Darmstadt, Germany), 1 μ g/mL hydrocortisone (H0888-1G, Merck Life Science, Darmstadt, Germany), and 10 mM Hepes, 100 U/mL penicillin, and 100 mg/mL streptomycin.

The RT4 cell line was routinely grown in RPMI-1640 medium (R0883-Merck Life Science, Darmstadt, Germany) supplemented with 10% fetal bovine serum (FBS, Gibco™-ThermoFisher, Waltham, MA, USA), 4 mM glutamine, 100 U/mL penicillin, and 100 mg/mL streptomycin.

All the cell lines were cultured at 37 °C in a humidified atmosphere of 5% CO₂. Cells were passaged when they reached sub-confluence (typically twice a week) using trypsin-ethylene-diamine-tetraacetic acid (EDTA). The passage number of the cell lines used in the experiments ranged from 10 to 20. The cells were passed for no more than one month (8 passages) after the thawing.

2.2. Spheroid Formation Protocols

Spheroid formation was performed in 3D experimental medium DMEM w/o phenol red (Gibco™-Thermo Fisher Scientific, Waltham, MA, USA), 1% BSA, 10 mM glucose, 2 mM glutamine, 10 μ g/mL insulin (I9278, Merck Life Science), 0.5 μ g/mL hydrocortisone (H0888-1G, Merck Life Science, Darmstadt, Germany), 20 ng/mL EGF (EGF Human Recombinant, PeproTech, London, UK) 100 ng/mL cholera toxin (C8052, Merck Life Science, Darmstadt, Germany), 1 mM Na-pyruvate, 100 U/mL penicillin, and 100 mg/mL streptomycin. Spheroid formation was performed comparing two protocols: the *Multiple Spheroid Protocol* and the *Single Spheroid Protocol*.

Multiple Spheroids Protocol (Figure 1a)—the cells were detached using trypsin-EDTA, re-suspended in the 3D experimental medium, and seeded in T75 untreated flasks (cod. 658195, Greiner Bio-one Cellstar, Kremsmünster, Austria) at a density of $1.8\text{--}2.5 \times 10^5$ cells/mL in 10 mL of volume. The flasks were incubated for 3 days (72 h) at 37 °C in a humidified atmosphere of 5% CO₂ during spheroid formation. The *Multiple Spheroids Protocol* did not include cell staining with CellTracker™ Red CMPTX dye (Invitrogen, Thermo Fisher Scientific, Waltham, MA, USA) because this step was introduced later for simplifying Seahorse normalization.

Single Spheroid Protocol (Figure 1a)—spheroids were freshly prepared from the adhesion cultures three days (72 h) before each experiment. The day before seeding (day -1, Figure 1a), the cells grown in a monolayer culture were stained with CellTracker™ Red CMTPX dye (C34552, Gibco™-ThermoFisher, Waltham, MA, USA). First, cells were washed with D-PBS w/Ca and Mg; then, 5 μ M CellTracker™ Red CMTPX dye diluted in DMEM w/o phenol red was added and the cells incubated for 30 min at 37 °C and 5% CO₂. Finally,

the dye was removed, cells were washed with D-PBS w/Ca and Mg, and then put in the incubator with their own maintenance medium until the next day. On the day of seeding (day 0, Figure 1a), cells were detached with trypsin-EDTA as usual and centrifuged at $290\times g$ for 7 min. Next, the pellet was resuspended in the 3D experimental medium, and cell counting was performed using a Burkler chamber. After that, the cells were seeded in U-bottom CellCarrier Spheroid ULA 96-well Microplates (PerkinElmer, Waltham, MA, USA) at a density of $0.5\text{--}2 \times 10^4$ cells/well in 100 μL /well. After seeding, the U-bottom CellCarrier Spheroid ULA 96-well Microplates were centrifuged at $340\times g$ for 30 min to foster cell aggregation. Next, the plate was incubated for 3 days (72 h) at 37°C in a humidified atmosphere of 5% CO_2 during spheroid formation.

2.3. Imaging Analysis of 3D Models

Image acquisition was performed using the Operetta CLSTM high-content analysis system (PerkinElmer, Waltham, MA, USA) and an Olympus CKX41 (Olympus Scientific Solutions, Tokyo, Japan) phase-contrast microscope when cell culture support differed from multi-well microplates (e.g., petri dish).

Spheroid dimension (area) and roundness were measured using Harmony 4.9 software for images acquired with the Operetta CLSTM system. At least eight stack images with $5\times$ magnification for an overall height of 200 μm were acquired with confocal microscopy, and maximum projection was generated using Harmony software to perform the analyses. Area and roundness were then measured based on the selected fluorescence of the largest section of the spheroid using the 'calculate morphology properties' analysis block. Morphological analyses of images with $4\times$ magnification acquired using the phase contrast microscope Olympus CKX41, and therefore lacking a fluorescence signal, were performed using ImageJ (<https://imagej.nih.gov/ij>, U.S. National Institutes of Health, Bethesda, MD, USA), using freehand selection and applying measurements of area and circularity.

2.4. Seahorse XFe96 Assay Preparation and Running on 3D Cultures

2.4.1. XFe96 Spheroid Microplate Coating

The day before the assay, all wells of an XFe96 Spheroid Microplate were coated with the adhesive agent collagen type I solution (3867, Merck Life Science, Darmstadt, Germany), diluted in sterile H_2O at a concentration of 10 $\mu\text{g}/\text{cm}^2$ (Supplementary Materials Figure S1a). A volume of 80 μL of sterile collagen type I solution was dispensed in each well of the XFe96 Spheroid Microplate, avoiding bubble formation. The plate was incubated for 3 h at room temperature; then, the remaining solution was discarded, and the plate was left to dry overnight under the hood. The collagen-coated plate can be stored at 4°C for up to 7 days. On the day of the assay, the wells were rinsed with sterile H_2O and left to air-dry before use.

2.4.2. Spheroid Transfer onto the Assay Microplate

Seahorse XF DMEM Medium, pH 7.4 was supplemented with 10 mM D-Glucose and 2 mM L-Glutamine and dispensed 175 μL /well onto the collagen-coated XFe96 Spheroid Microplate.

Multiple Spheroid Protocol—the spheroids were harvested in a tube and gently washed once with complete Seahorse XF DMEM Medium. After centrifugation ($70\times g$, 5 min), spheroids were resuspended in complete Seahorse XF DMEM Medium. Finally, an aliquot of spheroid suspension was transferred onto a p100 Petri dish.

Single Spheroid Protocol—the medium used for spheroid formation in the U-bottom microplates was half replaced with a complete Seahorse Assay medium to mitigate the buffer presence in the final assay medium.

The Petri dish (*Multiple Spheroids Protocol*) or the U-bottom microplate (*Single Spheroid Protocol*) were placed on a black background to visualize the spheroids better. Single spheroids were picked up using a pre-cut P200 pipette tip or a glass Pasteur pipette to preserve the spheroids' integrity while retaining only a small amount of media volume (max volume

20 μL). The pipette tip was slowly removed from the pipette and moved against the bottom of an XFe96 Spheroid Microplate well. The spheroid was left to fall upon the center of the well by gravity or by gently tapping the tip. The position of the spheroid was verified by microscope observation and eventually corrected. This procedure was repeated for each well of the XFe96 Spheroid Microplate, excluding background wells. After that, the XFe96 Spheroid Microplate was centrifuged at $340\times g$ for 15 min, at low brake.

Before the assay started, brightfield and confocal fluorescence images of each well were acquired by Operetta CLS to compare the position of each spheroid before and after the assay and to verify if a shift occurred (Supplementary Materials Figure S1a).

2.4.3. Sensor Cartridge Hydration and Loading

The day before the Seahorse assay, the sensor cartridge was hydrated with 200 μL /well milliQ water overnight in a non- CO_2 37 $^\circ\text{C}$ humidified incubator.

On the day of the assay, 1 h before loading the injection ports, the milliQ water was replaced with a pre-warmed Seahorse XF Calibrant solution.

The lyophilized drugs provided in the Seahorse XF Mito Stress Test Kit (Agilent Technologies, Santa Clara, CA, United States) were rehydrated in complete Seahorse XF DMEM Medium to obtain stock solutions: 100 μM Oligomycin, 100 μM FCCP, and 50 μM Rotenone/Antimycin A. The drugs were then diluted in the complete Seahorse medium to reach a $10\times$ solution, to be loaded in the corresponding ports of the sensor cartridge: port A—Oligomycin (20 μL), port B—FCCP (22 μL), port C—Rot/Ant (25 μL). The final concentrations of the drugs were: 2 μM Oligomycin, 2 μM FCCP, and 0.5 μM Rotenone/Antimycin A.

After the Seahorse assay, the medium was carefully discarded with pipette tips from each well, avoiding removal of the spheroids, and the XFe96 Spheroid Microplate was frozen at $-80\text{ }^\circ\text{C}$ for up to four weeks for protein or DNA content quantification.

2.4.4. Normalization on Area

Multiple Spheroid Protocol—immediately after the Seahorse assay, 1 $\mu\text{g}/\text{mL}$ Hoechst 33342 (H3570, Gibco-ThermoFisher, Waltham, MA, USA) was added to each well and incubated for 15 min at 37 $^\circ\text{C}$ and 5% CO_2 . The fluorescence of nuclei was acquired by Operetta CLSTM (PerkinElmer, Waltham, MA, USA) and analyzed as a single object per well for spheroid area measurements. Harmony software was used for image analysis.

Single Spheroid Protocol—the area of each spheroid was determined by selecting the area of cell tracker red fluorescence using the images acquired by Operetta CLSTM (PerkinElmer, Waltham, MA, USA) immediately after the Seahorse assay. Comparison of images acquired before and after the assay allows verification of any spheroid movement from the central position during the Seahorse assay due to the mixing steps before each OCR and ECAR measurement.

2.4.5. Protein Content Assay for Normalization

An XFe96 Spheroid Microplate was thawed at room temperature for protein quantification, and 1N NaOH was added to each well (50 μL /well). The plate was incubated for 20 min at room temperature, and then 50 μL /well of 1N HCl was added. Protein content was determined using a Bio-rad Protein Assay (cat. Number 1-800-424-6723, Bio-rad Laboratories, Hercules, CA, USA); in a 96 well plate, 50 μL of each sample was added to 150 μL of previously diluted 1:5 H_2O Protein Assay Dye Reagent. Absorbance was read at 595 nm using a FLUOstar[®] Omega microplate reader (BMG LABTECH, Ortenberg, Germany). The protein content of each sample (including Seahorse Blanks to subtract the contribution of the collagen coating) was derived from a standard curve with Bovine Serum Albumin (BSA). A standard curve with different numbers of cells obtained from the digestion and cell count of a specific number of spheroids was read to calculate the protein content/cell (specifically for each cell line). The number of cells-per-spheroid was determined as the ratio between μg protein/spheroid and μg protein/cell.

2.4.6. DNA Content Assay Normalization

DNA content was quantified using a CyQUANT[®] Cell Proliferation Assay Kit (Invitrogen-ThermoFisher, Waltham, MA, USA), according to the producers' manual. A freeze–thaw cycle was added to the protocol to ensure the complete lysis of the spheroids. Green fluorescence was measured using a FLUOstar[®] Omega microplate reader (BMG LABTECH, Ortenberg, Germany). The DNA content of each sample was derived from a standard curve of the bacteriophage λ DNA standard provided in the kit. A standard curve with cells obtained from the digestion and cell count of a specific number of spheroids was read to calculate the DNA content/cell (specifically for each cell line). The number of cells-per-spheroid was determined by the ratio between ng DNA/spheroid and ng DNA/cell.

2.5. Spheroid Digestion and Cell Count

Spheroids were collected in groups of 8–15 spheroids/tube, diluted in D-PBS, centrifuged at $70 \times g$ for 5 min, and resuspended in 100 μ L trypsin-EDTA. Spheroids were incubated at 37 °C for 10 min. Since spheroids tend to precipitate with gravity, after 5 min of incubation with trypsin, the pellet was delicately moved to resuspend the spheroids. Spheroid digestion was facilitated mechanically by pipetting up and down ten times before trypsin neutralization with 200 μ L medium with 10% serum. Single cells were counted using the trypan blue exclusion method and a Burkler chamber.

2.6. Seahorse XFe96 Assay on 2D Cultures

Seahorse assays on 2D cultures were performed according to the manufacturer's instructions, as reported in Pasquale et al. [15]. MDA-MB-231 and MCF7 cell lines were seeded in Seahorse XF plates at a density of 2×10^4 cells per well and cultured for 24 h in standard culture medium. The next day, the medium was replaced with Seahorse XF DMEM Medium, pH 7.4, supplemented with 10 mM D-Glucose and 2 mM L-Glutamine, and cell cultures were allowed to equilibrate for 1 h at 37 °C in a no-CO₂ incubator. At the end of the Seahorse measurements, Hoechst 33342 was added to each well at a final working concentration of 1 μ g/mL, and after 15 min incubation, nuclei/well were imaged and counted by the Operetta CLS[™] software Harmony and directly used to normalize the Seahorse parameters per cell number.

For the Mito stress test, the following drug concentrations were used: 1 μ M Oligomycin, 0.25 μ M FCCP (MDA-MB-231) or 0.5 μ M FCCP (MCF7), and 0.5 μ M Rotenone/Antimycin A.

2.7. Statistical Analysis

A *p*-value < 0.05 was considered statistically significant. Coefficient of variation calculations, unpaired *t*-tests, and linear regressions were performed using GraphPad version 6 (GraphPad Software, Inc., San Diego, CA, USA).

Multivariate statistical analyses (principal component analysis (PCA) and agglomerative hierarchical cluster analysis) were performed using OriginPro 9.8 (OriginLab. Corp., Northampton, MA, USA). Data were rescaled into the [0–1] range by min–max normalization as a preliminary step.

PCA was employed to reduce the experimentally observed, possibly correlated parameters to a smaller set of independent variables (principal components, PC), which are linear combinations of original variables that still describe the variance of data, with only a minor loss of information. The cumulative proportion of the variance accounted for by the retained PC1 and PC2 variables was about 87%.

Agglomerative cluster analysis was performed by the 'average linkage' method (the distance between two clusters being defined as the average distance between the elements in the clusters). Euclidean distance was employed for measuring the distance between clusters.

3. Results

3.1. The Single Spheroid Protocol Produces Spheroids Homogeneous in Size and Shape

When using three-dimensional (3D) cultures, the size and heterogeneity of 3D structures, such as spheroids, is the first parameter that can affect the determination of metabolic

parameters. This chapter compares two protocols, herein referred to as the *Multiple Spheroids Protocol* and *Single Spheroid Protocol*, respectively.

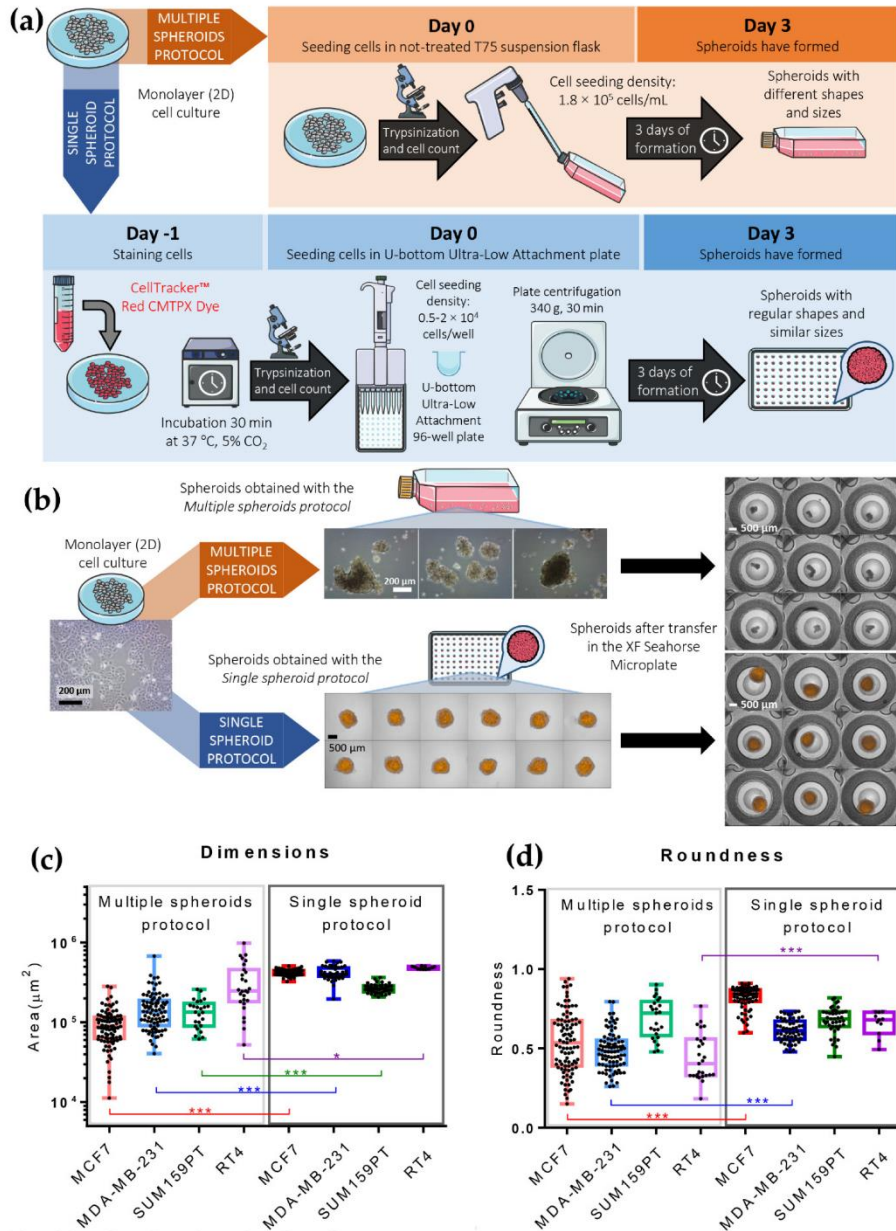


Figure 1. Spheroids from breast and bladder cancer cell lines: protocols for their generation, use in XF Seahorse bioenergetics analyses, and morphometric characterization. (a) Schematic representation

of the two protocols of spheroid formation: *Multiple Spheroids Protocol* (MSP, above) and *Single Spheroid Protocol* (SPP, below). (b) Representative pictures of MCF7-derived spheroids produced with the *Multiple Spheroids Protocol* and the *Single Spheroid Protocol* before and after transfer to the XF Seahorse microplate. Images were acquired with phase-contrast light microscopy (monolayer cell culture and *Multiple Spheroids Protocol* before transfer) and brightfield and confocal fluorescent microscopy (in orange, CellTracker™ Red CMTPX Dye) with Operetta CLS™ (*Single Spheroid Protocol* and spheroids after transfer in the XF Seahorse Microplate). (c,d) Box and whiskers plots showing single value distribution as black dots for dimension (c) and roundness (d) of spheroids obtained with *Multiple Spheroids* and *Single Spheroid Protocol* for four different cell lines: MCF7, MDA-MB-231, SUM159PT (mammary carcinoma), and RT4 (urothelial carcinoma); Statistical test: unpaired *t*-test, *** for $p < 0.001$, * for $p \leq 0.05$.

The *Multiple Spheroids Protocol* exploits the natural tendency of cancer cells to self-aggregate in 3D structures without forcing the formation of regular spheres. It requires the plating of cells suspended in 10 mL of 3D experimental medium in T75 flasks not-treated for tissue culture, at a density of $1.8\text{--}2.5 \times 10^5$ cells/mL. The spheroids form in 72 h at 37 °C in a humidified incubator, with 5% CO₂ (Figure 1a). This method—described in more detail in Section 2—is technically straightforward, does not require expensive materials or equipment, and allows the production of many spheroids in a relatively short period (72 h). On the other hand, this method does not allow easy control of the number, dimension, and shape of the formed spheroids.

The *Single Spheroid Protocol* (Figure 1a) consists of seeding the cells (optionally previously stained with CellTracker™ Red CMTPX dye) in U-bottom Ultra-Low Attachment (ULA) 96 well plates in the 3D experimental medium, at a density of $0.5\text{--}2 \times 10^4$ cells/well in 100 µL/well of medium. After the seeding, the microplates are centrifuged at $340 \times g$ for 30 min, as described in more detail in Section 2. The plate is incubated for 72 h at 37 °C in a humidified atmosphere of 5% CO₂ during spheroid formation. The use of ULA U-bottom microplates combined with plate centrifugation after plating fosters cell aggregation in a round shape, causing the formation of a single spheroid per well (Figure 1b). The dimension of the resulting spheroids—formed starting from the same cell number—is relatively homogeneous and can be regulated by varying the number of cells seeded. The *Single Spheroid Protocol* requires more steps and more sophisticated materials than the *Multiple Spheroids Protocol*.

The spheroids in the untreated T75 flasks (Figure 1b, MCF7 cell line) are morphologically heterogeneous in terms of size and shape, regardless of the cell lines used (Supplementary Materials Figure S1b left, MDA-MB-231, SUM159PT, and RT4 cell lines). In contrast, the spheroids obtained in U-bottom CellCarrier Spheroid ULA 96-well Microplates (Figure 1b, below and Supplementary Materials Figure S1b right) retain higher regularity. These differences are maintained after their transfer in the Seahorse XF Microplate (Figure 1b, right).

Figure 1c,d and Table 1 report some morphometric parameters determined on the spheroids formed by three breast cancer cell lines (MCF7, MDA-MB-231, and SUM159PT) and the RT4 bladder cancer cell line. The Area defines the measurement of the surface of the largest section of a spheroid. The Roundness defines how closely the shape of the measured object approaches that of a mathematically perfect circle (the section of a sphere); it varies between 0 and 1.

The average Area of spheroids produced with the *Single Spheroid Protocol* (plated at 10,000 cells/well) was between 30% (RT4) and 75% (MCF7) larger than the Area of spheroids produced with the *Multiple Spheroids Protocol* (Table 1, Figure 1c). Even the larger spheroids produced by the *Multiple Spheroid Protocol* were smaller than those produced by the *Single Spheroid Protocol*. The *Single Spheroid Protocol* produced spheroids homogenous in size, with a coefficient of variation (CV) between 8.6 and 17.8, while the CVs of the spheroids obtained with the *Multiple Spheroid Protocol* varied between 39.6 (for the SUM159PT cell line, which is the most prone to form regular spheroids even in untreated plates), and 67.9 (for

the bladder cancer RT4 cell line; Table 1). Spheroids produced with the *Single Spheroid Protocol* by all the cancer cell lines analyzed presented with a higher average Roundness and lower intra-spheroid variability than spheroids obtained with the *Multiple Spheroids Protocol* (Figure 1d and Table 1).

Table 1. Mean, standard deviation (SD), and Coefficient of Variation (CV) of Area and Roundness, measured on spheroids formed with the *Multiple Spheroids Protocol* and *Single Spheroid Protocol* in four cancer cell lines: MCF7, MDA-MB-231, SUM159PT, and RT4.

| Cell Line | Protocol | Area (μm^2) | | Roundness | |
|------------|---------------------------|--|--------|-------------------------------|--------|
| | | Mean \pm SD | CV (%) | Mean \pm SD | CV (%) |
| MCF7 | <i>Multiple spheroids</i> | 95,997.4 ($n = 93$) \pm 48,223.0 | 50.2 | 0.54 ($n = 93$) \pm 0.19 | 35.2 |
| | <i>Single spheroid</i> | 421,135.9 ($n = 75$) \pm 36,417.5 | 8.6 | 0.82 ($n = 75$) \pm 0.07 | 8.7 |
| MDA-MB-231 | <i>Multiple spheroids</i> | 156,971.5 ($n = 88$) \pm 94,030.3 | 59.9 | 0.49 ($n = 88$) \pm 0.12 | 24.6 |
| | <i>Single spheroid</i> | 415,612.7 ($n = 56$) \pm 73,802.6 | 17.8 | 0.61 ($n = 56$) \pm 0.07 | 11.2 |
| SUM159PT | <i>Multiple spheroids</i> | 137,404.0 ($n = 25$) \pm 54,377.4 | 39.6 | 0.69 ($n = 25$) \pm 0.12 | 18.1 |
| | <i>Single spheroid</i> | 267,606.1 ($n = 45$) \pm 34,643.6 | 12.9 | 0.67 ($n = 45$) \pm 0.08 | 12.2 |
| RT4 | <i>Multiple spheroids</i> | 333,372.0 ($n = 27$) \pm 226,341.7 | 67.9 | 0.44 ($n = 27$) \pm 0.15 | 33.1 |
| | <i>Single spheroid</i> | 483,380.8 ($n = 11$) \pm 18,691.7 | 3.9 | 0.66 ($n = 11$) \pm 0.079 | 12.0 |

These results suggest that the *Single Spheroid Protocol* developed for the formation of 3D cultures produced spheroids more regular (with sections closer to a circle) and homogeneous in terms of size and shape compared to those produced from the application of the *Multiple Spheroids Protocol*. For this reason, the *Single Spheroid Protocol* should provide more reproducible results in the Seahorse assays.

The area of the spheroids produced with the *Single Spheroid Protocol* can be modified without changing the time of spheroid formation through the seeding of different numbers of cells per well at time 0. As reported in Supplementary Materials Figure S2a,b, the area of the spheroids produced with this protocol increased with the number of seeded cells (from 5000 to 20,000 cells/well) and in a cell line-dependent manner.

3.2. The *Single Spheroid Protocol* Allows More Accurate Determination of Oxygen Consumption Rate and Extracellular Acidification Rate by Seahorse XFe96 under Basal and Drug-Perturbed Conditions

Seahorse XFe96 is an extracellular flux analyzer that simultaneously measures the Oxygen Consumption Rate (OCR) and the Extracellular Acidification Rate (ECAR) of cells or spheroids in Seahorse Microplate wells. The OCR is mainly linked to mitochondrial respiration and is only in a small part due to the activity of oxidative enzymes in the cytosol. The ECAR mainly reflects lactic fermentation, but its value is also affected by carbon dioxide released during the TCA cycle, which, combined with water, produces carbonic acid. Therefore, these parameters can provide important information on the metabolic status of the cells in basal conditions and the experimental conditions of interest.

The more regular shape and decreased size variability of spheroids obtained using the *Single Spheroid Protocol* reduced the variability in both the basal Oxygen Consumption Rate (OCR) and basal Extracellular Acidification Rate (ECAR; Figure 2a–d, Table 2).

As shown above, by modifying the number of seeded cells/well, the *Single Spheroid Protocol* modulated the number of cells-per-spheroid, and hence the dimensions of the spheroids produced. The basal OCR (Figure 3a,c) and basal ECAR (Figure 3b,c) of the spheroids were proportional to the number of cells plated to generate the spheroids, indicated in Figure 3 as 5 k (5000 cells/well) and 10 k (10,000 cells/well)—likely reflecting the number of metabolically active cells performing oxidative phosphorylation and fermentative glycolysis during the time of measurement.

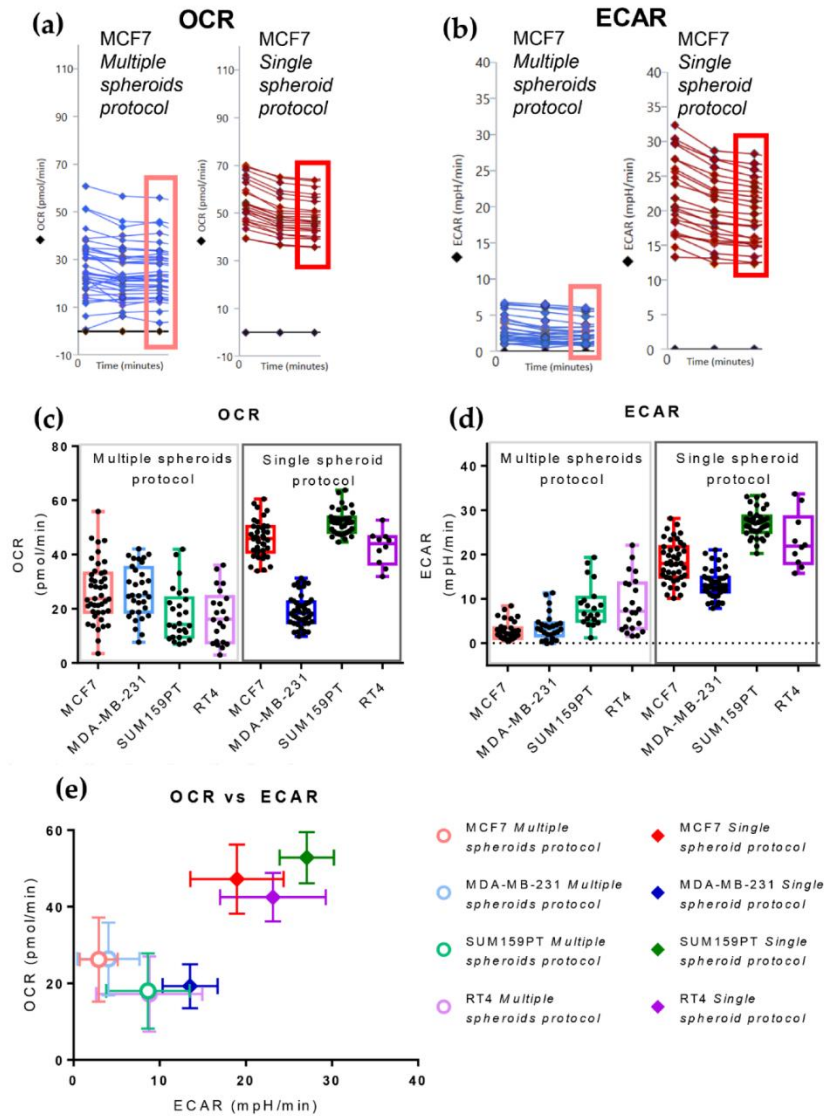


Figure 2. Comparisons of basal Oxygen Consumption Rate (OCR) and ExtraCellular Acidification Rate (ECAR) values between spheroids obtained by the *Multiple* and *Single Spheroid Protocols*. (a,b) The first three measurements of OCR (a) and ECAR (b), performed using an XF96 Seahorse Analyzer, showing the baseline profile of MCF7 spheroids obtained with the *Multiple Spheroids Protocol* (left) and *Single Spheroid Protocol* (right). Single measurements for every spheroid are reported to show distribution; the black line is for the background and corresponds to a zero value. The rectangles indicate the 3rd basal OCR and ECAR measurements used to generate the box and whisker plots presented in panels (c,d). (c,d) Box and whisker plots comparing basal OCR (c) and ECAR (d) of four cancer cell lines (mammary carcinoma: MCF7, MDA-MB-231, SUM159PT, and urothelial carcinoma:

RT4) produced by applying the *Multiple Spheroids Protocol* and the *Single Spheroid Protocol*; single value distribution is reported as black dots. (e) Correlation of OCR and ECAR values under the basal conditions of three mammary carcinoma cell lines produced with the two protocols: MCF7 (MSP $n = 43$; SSP $n = 45$), MDA-MB-231 (MSP $n = 32$; SSP $n = 45$), SUM159PT (MSP $n = 26$; SSP $n = 37$), and one urothelial carcinoma cell line: RT4 (MSP $n = 22$; SSP $n = 10$); points represent mean \pm standard deviation.

Table 2. Mean, standard deviation (SD), and the Coefficient of Variation (CV) of Basal Oxygen Consumption Rate (OCR) and Basal Extracellular Acidification Rate (ECAR) measured on spheroids formed with the *Multiple Spheroids Protocol* and *Single Spheroid Protocol* in four cancer cell lines: MCF7, MDA-MB-231, SUM159PT, and RT4.

| Cell line | Protocol | Basal OCR | | Basal ECAR | |
|------------|---------------------------|-------------------|--------|------------------|--------|
| | | Mean \pm SD | CV (%) | Mean \pm SD | CV (%) |
| MCF7 | <i>Multiple spheroids</i> | 26.20 \pm 10.99 | 41.9 | 2.68 \pm 2.05 | 76.3 |
| | <i>Single spheroid</i> | 45.76 \pm 6.68 | 14.6 | 18.33 \pm 4.58 | 25.0 |
| MDA-MB-231 | <i>Multiple spheroids</i> | 26.36 \pm 9.49 | 36.0 | 3.72 \pm 3.06 | 82.2 |
| | <i>Single spheroid</i> | 19.26 \pm 5.74 | 29.8 | 13.53 \pm 3.19 | 23.6 |
| SUM159PT | <i>Multiple spheroids</i> | 18.00 \pm 9.83 | 54.6 | 8.61 \pm 4.95 | 57.5 |
| | <i>Single spheroid</i> | 52.00 \pm 4.69 | 8.8 | 27.08 \pm 3.16 | 11.7 |
| RT4 | <i>Multiple spheroids</i> | 17.21 \pm 9.82 | 57.1 | 8.79 \pm 6.16 | 70.1 |
| | <i>Single spheroid</i> | 42.48 \pm 6.32 | 14.9 | 23.14 \pm 6.13 | 26.5 |

The *Single Spheroid Protocol* allowed a reduction in the variability in the size (Figure 1) and metabolic properties of the spheroids (Figure 2). The latter values were generally higher for spheroids formed by plating a higher cell number (Figure 3a–c). As previously mentioned, the dimensional variability of spheroids may impact the access of nutrients and oxygen to the spheroids' cells, affecting the metabolic properties of the individual spheroids. Direct determination of the actual number of viable cells in each given spheroid using imaging techniques in the XF microplate is not technically practical or even possible, due to the low resolution of the plastic and the high light-scatter of the 3D cultures that prevent a direct count of the cell nuclei inside the spheroids. Moreover, the trypsinization of the single spheroids and manual cell counting using the trypan blue exclusion technique can lead to errors in the estimation of the number of cells-per-spheroid due to the incomplete digestion of the spheroids and the loss of many cells that were alive during the assay but may be dead after the combined treatment with three drugs, as occurs in the Mito stress test.

We reasoned that the spheroid area (a non-invasive measurement that can be obtained by quantitative imaging) could be an appropriate proxy for cell number. Figure 3d shows a high correlation between the spheroid area and the number of viable cells in MCF7-derived spheroids (see Section 2). Using Figure 3d as a calibration curve, it was thus possible to calculate the number of viable cells present in the spheroids, starting from the spheroid's Area. (Figure 3e). Spheroids formed 72 h after plating contained a higher number of viable cells than those plated at time 0, suggesting that the spheroid formation process is accompanied by some cell division [29]. The number of viable cells present in the spheroids was proportional to the number of cells plated at time 0 in spheroids formed from MCF7 (Figure 3e) and MDA-MB-231 (Supplementary Material Figure S2c,d). When basal OCR and ECAR values were normalized on a per-cell basis and clustered according to the actual number of cells present in each spheroid, the difference in basal glycolytic and respiratory fluxes between spheroids of different dimensions faded out, while remaining statistically significant (Figure 3f,g).

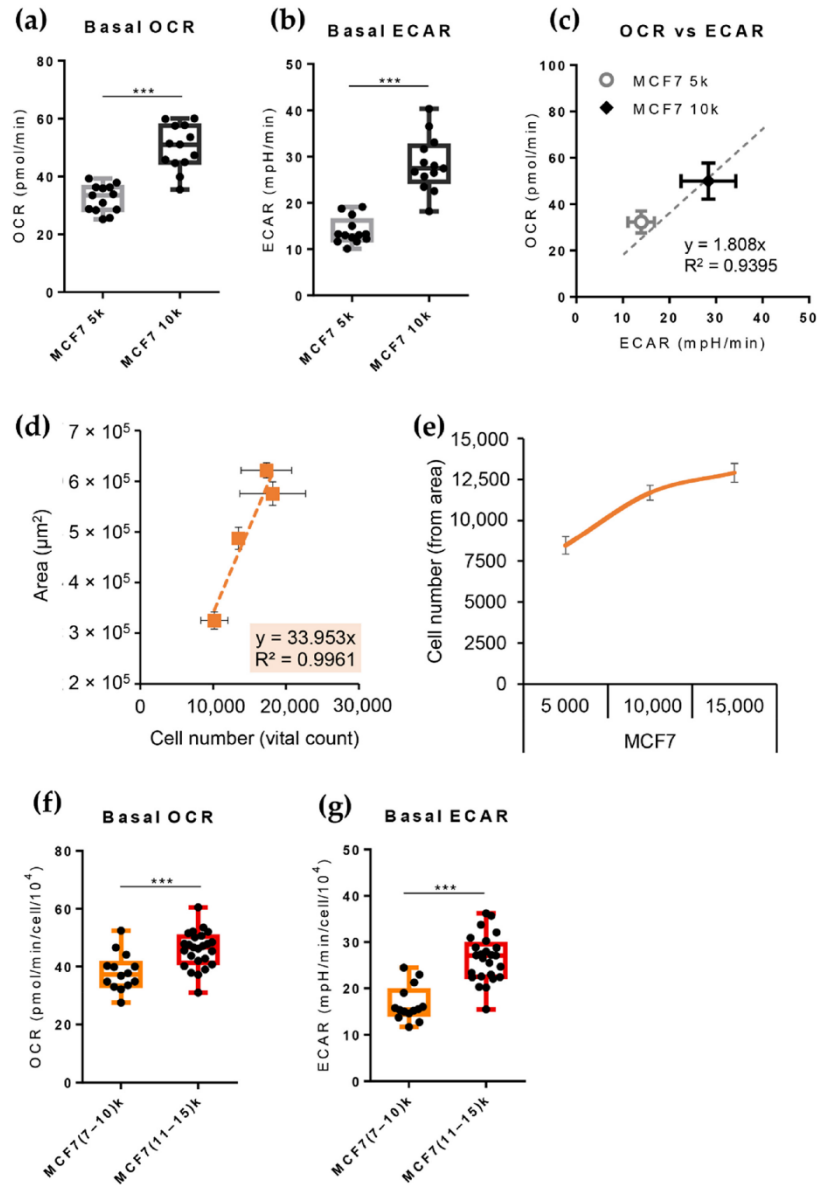


Figure 3. Basal bioenergetic analysis of spheroids obtained with the *Single Spheroid Protocol*, seeding a different number of MCF7 cells per well, and subsequent application of an area-mediated normalization approach. (a,b) Box and whisker plots of basal OCR (a) and basal ECAR (b) values of spheroids obtained seeding 5000 (5 k) cells and 10,000 (10 k) cells per well. Statistical test: unpaired *t*-test, *** $p > 0.001$. (c) Correlation of OCR and ECAR values (MCF7 5 k $n = 15$, MCF7 10 k $n = 15$); points represent mean \pm standard deviation along with regression line. Statistical test: linear regression. (d) Standard curve obtained measuring the area of groups of MCF7 spheroids produced

from 5000–10,000–15,000–20,000 cells/well and their subsequent digestion and a count of the number of viable cells after 72 h of spheroid formation (note that the number of cells-per-spheroids after 72 h of culture is different than the starting number of cells/well seeded). Points represent mean \pm standard deviation along with regression. (e) Graph representing the number of cells-per-spheroid calculated indirectly using area measurement on MCF7 spheroids tested in a Seahorse assay, grouped based on the number of cells seeded for spheroid formation (5000–10,000–15,000 cells/well). The points of the orange line depict the number of cells-per-spheroid calculated by measuring the area of each spheroid of the XF Seahorse Microplate and applying the equations derived from the standard curve in panel D. (f,g) Box and whisker plots of basal OCR (f), and basal ECAR (g) values of spheroids obtained and re-categorized according to cell number, indirectly calculated through an area-mediated normalization approach. Statistical test: unpaired *t*-test, *** $p > 0.001$.

3.3. The Single Spheroid Protocol Allows More Accurate Determination of Oxygen Consumption Rate and Extracellular Acidification Rate by Seahorse XF96 Drug-Perturbed Conditions

The Mito Stress Test enables the determination of critical parameters of mitochondrial function by measuring OCR real-time variations during the sequential injection of modulators of oxidative phosphorylation (OXPHOS) into the Seahorse microplate wells. In this assay, three drugs were loaded one after the other in the dedicated ports of the XF sensor cartridge:

1. Oligomycin: causes an OCR decrease due to ATP synthase inhibition. The difference between basal respiration and the lowest OCR value measured after oligomycin injection represents the ATP produced by the mitochondria, contributing to meeting the cell's energy needs under basal conditions (ATP linked respiration). The difference between the lowest OCR value measured after oligomycin injection and non-mitochondrial respiration (defined below) is called the proton leak and represents the remaining basal respiration not coupled to ATP production. Therefore, it can be a sign of mitochondrial damage or can be used as a mechanism to regulate mitochondrial ATP production.
2. Carbonyl cyanide-4 (trifluoromethoxy) phenylhydrazone (FCCP): disrupts the proton gradient required for ATP synthesis, uncoupling oxygen consumption from oxidative phosphorylation. It increases OCR due to the attempt of the cells to rescue the disrupted mitochondrial membrane potential through the enhancement of electron transport chain activity. This treatment allows the calculation of the Maximal respiration and Spare respiratory capacity, which reflect the capability of the cell to respond to an energetic demand, such as in a stressful condition.
3. A mixture of Rotenone and Antimycin A: these two drugs inhibit complex I and III of the electron transport chain, respectively, enabling the assessment of non-mitochondrial respiration.

Supplementary Materials Figure S3a–c report typical Mito Stress test profiles for spheroids formed with the Multiple and *Single Spheroid Protocol* (MCF7 cell line). Not only did the unperturbed, basal OCR of spheroids formed with the *Multiple Spheroids* protocol present with a more considerable variation, as reported above, but different replicates presented with qualitative variations in the Mito Stress profile. On the contrary, spheroids formed with the *Single Spheroid Protocol* presented consistent Mito Stress profiles across the wells. Moreover, as shown in Supplementary Materials Figure S4a,b, the spheroids produced with the *Multiple Spheroids* Protocol were more likely to move during the mixing steps of the assay that occur between one measurement and the subsequent one (this is reported in the Mito Stress profile as a sudden variation of OCR not related to the injection of a drug). This fact may be linked to the smaller dimensions of this group of spheroids, which makes them more sensitive to the mixing process, as they are probably lighter. Therefore, many replicates of the Multiple spheroid protocol had to be excluded from the analysis as they did not remain in a central position in the well throughout the entire assay (Supplementary Materials Figure S4a). Accordingly, compared to the Multiple Spheroids Protocol, the *Single Spheroid Protocol* drastically reduced the CV among

the replicate spheroids in each of the conditions included in a standard Mito Stress Test (Supplementary Materials Figure S4b and Table 3)—the highest variability being observed after the Rotenone/Antimycin A injection.

Table 3. Mean, standard deviation (SD), and the Coefficient of Variation (CV) of Oxygen Consumption Rate (OCR) measured during Mito Stress Test on spheroids formed with the *Multiple Spheroids Protocol* and *Single Spheroid Protocol* (10,000 cells/well) in the MCF7 cell line.

| Drug Treatment | Measurement | <i>Multiple Spheroids Protocol</i> | | <i>Single Spheroid Protocol</i> | |
|----------------------|-------------|------------------------------------|--------|---------------------------------|--------|
| | | Mean \pm SD | CV (%) | Mean \pm SD | CV (%) |
| Basal | 1 | 26.99 \pm 12.56 | 46.5 | 54.24 \pm 9.25 | 17.1 |
| | 2 | 24.64 \pm 11.13 | 45.2 | 48.90 \pm 8.53 | 17.4 |
| | 3 | 24.85 \pm 11.13 | 44.8 | 47.54 \pm 8.34 | 17.5 |
| | 4 | 21.15 \pm 9.60 | 45.4 | 47.97 \pm 8.31 | 17.3 |
| | 5 | 16.79 \pm 8.48 | 50.5 | 46.21 \pm 8.13 | 17.6 |
| Oligomycin | 6 | 14.75 \pm 7.76 | 52.6 | 44.16 \pm 7.91 | 17.9 |
| | 7 | 13.91 \pm 7.87 | 56.6 | 42.54 \pm 7.72 | 18.2 |
| | 8 | 13.82 \pm 8.06 | 58.3 | 41.01 \pm 7.60 | 18.5 |
| | 9 | 39.51 \pm 16.53 | 41.8 | 73.77 \pm 10.58 | 14.3 |
| FCCP | 10 | 35.34 \pm 15.04 | 42.6 | 75.22 \pm 10.41 | 13.8 |
| | 11 | 32.58 \pm 14.29 | 43.9 | 76.33 \pm 10.35 | 13.6 |
| | 12 | 30.55 \pm 14.48 | 47.4 | 77.31 \pm 10.28 | 13.3 |
| | 13 | 17.33 \pm 9.01 | 52.0 | 60.53 \pm 8.86 | 14.6 |
| Rotenone/Antimycin A | 14 | 12.78 \pm 6.92 | 54.1 | 38.72 \pm 9.19 | 23.7 |
| | 15 | 11.97 \pm 6.89 | 57.5 | 28.34 \pm 8.50 | 30.0 |
| | 16 | 11.47 \pm 6.35 | 55.4 | 22.11 \pm 7.55 | 34.1 |

3.4. The Cell Line of Origin Distinguishes the Metabolic Phenotype of Spheroids More Than Their Dimension

Figure 4a shows that the Seahorse Mito Stress test OCR profile of two breast cancer cell lines—MCF7 (left panels) and MDA-MB-231 (right panels)—was strongly influenced by the number of cells seeded to form spheroids (5000–10,000–15,000 cells/well). Normalization to the spheroids' Area (Figure 4b) or the viable cell number/spheroid (Figure 4c) largely compensated for the differences in basal OCR due to the different dimensions of the spheroids in both cell lines. Notably, when normalized to the viable cell number/spheroid, the Mito Stress profiles of MCF7-derived small and large spheroids were largely superimposable, while MDA-MB-231-derived spheroids showed a more marked dependence of maximal respiration obtained after FCCP treatment on the spheroid's size (Figure 4c, left and right panels, respectively).

Figure 5a,b present a global overview of the metabolic differences between spheroids formed by the MCF7 and MDA-MB-231 cell lines using principal component analysis (PCA, panels a and b) and agglomerative hierarchical clustering analysis (Panel c). Input data include metabolic parameters determined by the Mito Stress Test (see Supplementary Materials Figure S5) on individual spheroids, normalized to the number of vital cells-per-spheroids determined from the area. First, the number of viable cells present in each spheroid was obtained as described above, and spheroids were grouped according to their cell number in three color-coded classes: (07–10)k class (orange for MCF7 spheroids, cyan for MDA-MB-231 spheroids), (11–15)k class (red for MCF7 and blue (for MDA-MB-231 spheroids) and (16–22)k (black for MDA-MB-231 spheroids). MCF7 spheroids presented with no spheroids in the (16–22)k class. Seahorse parameters were then normalized according to the actual cell number of each spheroid and finally rescaled into the [0–1] range by min–max normalization.

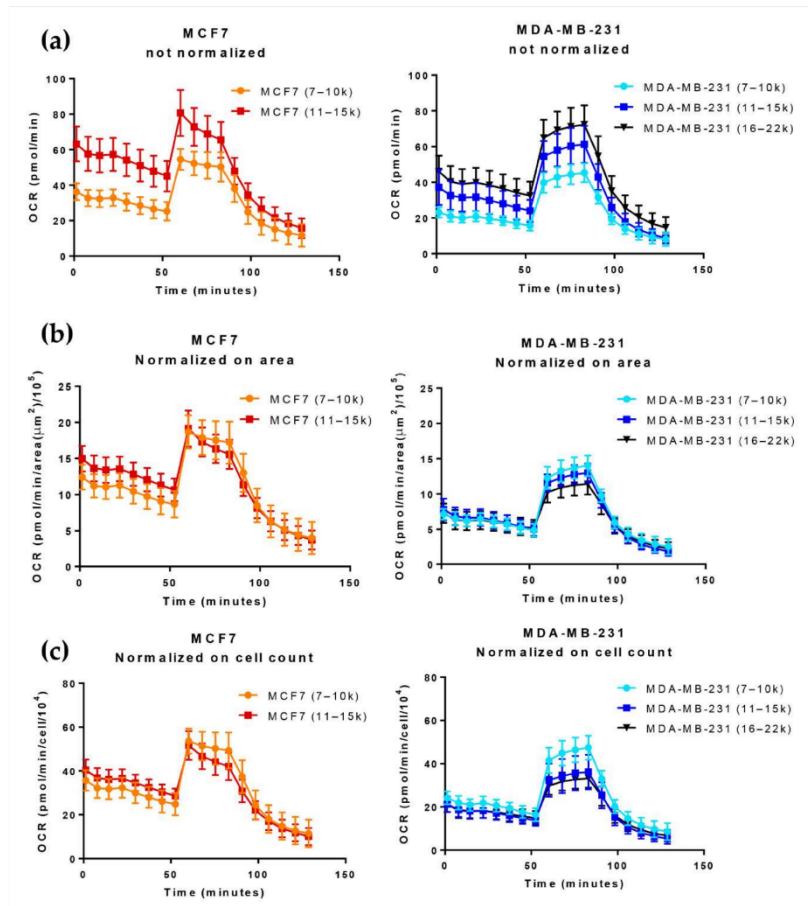


Figure 4. Comparison of the Mito Stress test OCR profile of MCF7 spheroids produced with the *Single Spheroid Protocol*, seeding a different number of MCF7 (5 k and 10 k) cells per well. Spheroids have been re-categorized in 3 groups according to cell number indirectly calculated through an area-mediated normalization approach: from 7000 to 10,000 cells/spheroid, (07–10) k; from 11,000 to 15,000 cells/spheroid, (11–15) k; from 16,000 to 22,000 cells/spheroid, (16–22) k. Points represent mean \pm standard deviation. (a) non-normalized OCR; (b) OCR normalized according to the spheroid area; (c) OCR normalized according to the number of cells in the spheroid.

PC1 accounted for 75% of the variability among the metabolic parameters of the spheroids (Figure 5a,b). With only one exception, all MCF7-derived spheroids had positive PC1 values, while the opposite held for MDA-MB-231-derived spheroids. Bigger spheroids tended to have negative PC2 values, while smaller spheroids tended to have positive PC2 values. This behavior was more apparent in MDA-MB-231- than in MCF7-derived spheroids, possibly because this line forms spheroids with a higher number of cells. Nevertheless, since PC2 only accounted for 12.5% of the total variability among spheroids, the difference in size among the spheroids only marginally accounted for the variability in their metabolic properties—at least within the size limits of the spheroids used in these experiments.

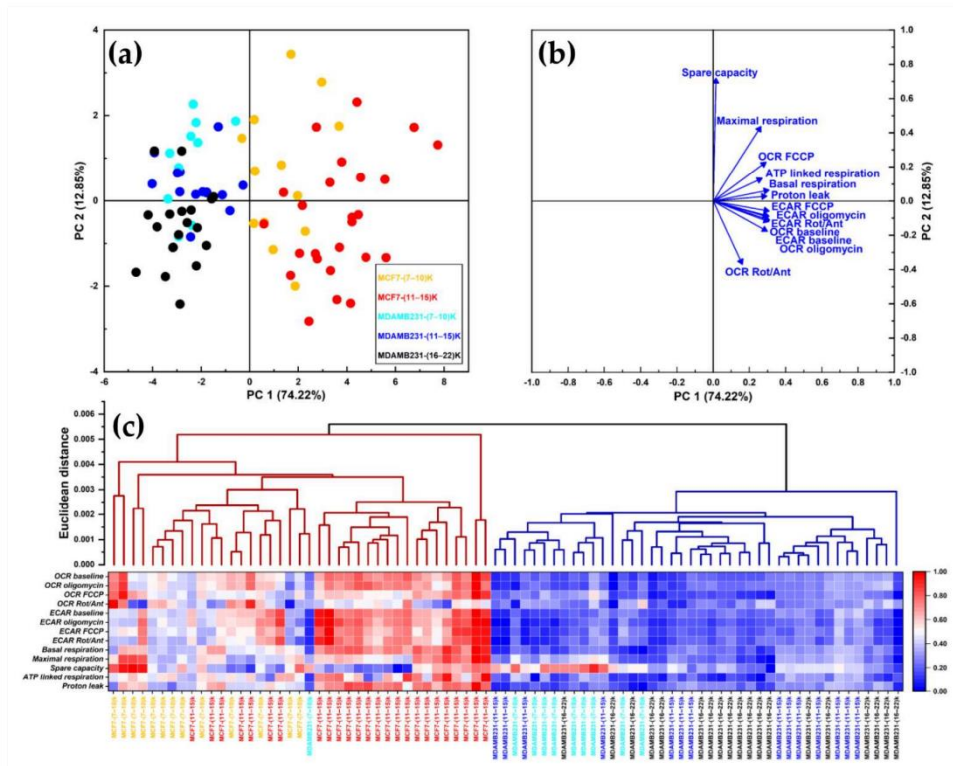


Figure 5. Multivariate statistical analysis for the metabolic parameters of MCF7 and MDA-MB-231 spheroids normalized on the number of cells in each spheroid. (a) Principal component analysis (PCA) scores plot. Data are projected onto the two-dimensional space defined by the Principal Component 1 (PC1) and Principal Component 2 (PC2), which together explain about 87% of total data variance. Each symbol represents a single spheroid, color-coded according to the cell line of origin and the cellular counts. (b) PCA Loading plot, showing the relationship between the original variables and the Principal Components. (c) Hierarchical clustering. The two clusters identified (dark red and dark blue branches) neatly separate spheroids from the two cell lines. The heatmap displays the values of metabolic parameters for each spheroid, scaled to the [0–1] range and color-coded accordingly.

Hierarchical clustering (Figure 5c) provided further evidence that metabolic differences among the studied spheroids were mostly related to the cell line rather than to the size of the spheroid. All MCF7-derived spheroids clustered in the left arm, while all MDA-MB-231-derived spheroids (except for one outlier) clustered in the right arm. Accordingly, the values of the measured metabolic parameters were mostly lower for MDA-MB-231 than for MCF7 spheroids, regardless of their respective size (see heatmap in Figure 5c). These data are consistent with the more ‘quiescent’ bioenergetic profile exhibited by the MDA-MB-231 cells (Figure 6 and paragraph below).

3.5. Growth in 3D Differentially Affects Metabolic Plasticity in MCF7 and MDA-MB-231 Cancer Cell Lines

Each cell can adjust its metabolic profile according to environmental and/or intracellular demands. Plotting the OCR vs. ECAR values under both basal, unperturbed conditions and conditions of metabolic stress provides a quick overview of the metabolic state of the

system under study. Normalizing data from spheroids on a cellular basis as described above allows the direct comparison of metabolic parameters from 2D and 3D cultures. Figure 6 compares the 2D and 3D cultures of MDA-MB-231 and MCF7 cells. Under basal conditions, monolayer cultures of MCF7 (Figure 6a, open triangles) had a more aerobic phenotype than MDA-MB-231 cells [26,28], which showed a more glycolytic metabolism (Figure 6b, open triangles). Growth in 3D drastically altered the metabolic profile of both cell lines. MCF7-derived spheroids (panel a, open circles) showed decreased respiration and increased glycolysis compared to 2D cultures; the effect on respiration was the same regardless of the size of the spheroid, while glycolysis was significantly higher in bigger spheroids. On the contrary, MDA-MB-231-derives spheroids under basal conditions were shifted towards a more quiescent metabolic state, with little if any effect on respiration and a significant reduction in glycolysis (Figure 6b, open circles).

Under stress conditions, obtained by injecting the protonophore FCCP, MCF7 cells showed increased glycolysis and respiration. The 2D cultures (Figure 6a, closed triangles) showed a more significant increase in glycolysis and respiration than the spheroids (Figure 6a, closed circles). The increase in respiratory and glycolytic fluxes following FCCP injection was more pronounced in 2D cultures than in spheroids. The stress condition had little, if any, effect on the metabolic parameters of the MDA-MB-231 2D cultures (Figure 6b, closed triangles). Surprisingly, all MDA-MB-231-derives spheroids showed a significant increase in glycolytic and respiratory flux under stress conditions (Figure 6b, closed circles), suggesting that growth in 3D increases metabolic plasticity in this cell line.

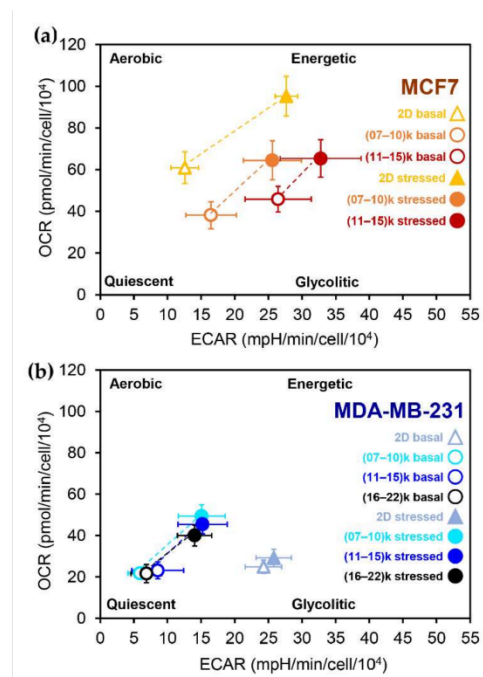


Figure 6. Comparisons of bioenergetic characterization by Seahorse analysis between the 2D and 3D cultures of the MCF7 cell line (a) and MDA-MB-231 cell line (b), possible due to cell number normalization using imaging techniques, i.e., nuclei counting using Hoechst dye in 2D cultures, area measurement for 3D cultures. Both cell lines were analyzed in three different conditions: growth in monolayer (MCF7 $n = 37$; MDA-MB-231 $n = 41$), spheroids produced with the *Single Spheroid Protocol*, and seeding different numbers of cells per well (5000–10,000–15,000). Spheroids have been

re-categorized in 3 groups according to cell number, indirectly calculated through an area-mediated normalization approach: from 7000 to 10,000 cells/spheroid, (07–10) k; from 11,000 to 15,000 cells/spheroid, (11–15) k; from 16,000 to 22,000 cells/spheroid, (16–22) k. Points represent mean \pm standard deviation. (a) Correlation of OCR and ECAR values under basal conditions and stressed (after FCCP injection) conditions of the MCF7 cell line grown in 2D and 3D; (b) Correlation of OCR and ECAR values under basal conditions and stressed (after FCCP injection) conditions of the MDA-MB-231 cell line grown in 2D and 3D.

4. Discussion

The use of spheroids and organoids is becoming increasingly popular for studying the properties of tumors and their pharmacological response [11,30–32]. In addition, these 3D structures can be valuable pre-clinical avatars in personalized medicine when produced using patient-derived cells [33–36]. Metabolism integrates information from genetic, epigenetic, and environmental signals so that each physio-pathological condition can be associated with a specific metabolic fingerprinting [37]. Seahorse is one of the most widespread and powerful technologies for dynamically characterizing the metabolism of cells and three-dimensional structures [14,15,22,38–40]. Nevertheless, appropriate optimized protocols for preparing spheroids for Seahorse analysis and interpretation of the generated data are still lacking [23–25].

This work presents an optimized workflow for producing spheroids of controlled size, regular shape, and reduced inter-spheroid variability that can be easily transferred to Seahorse plates. Since the area of the spheroids—easily determined by quantitative imaging—is proportional to the number of viable cells within the spheroid, it can be used to indirectly determine the number of viable cells that make up the spheroid—thereby obtaining a measure of its size, a highly relevant parameter for properly analyzing Seahorse-derived metabolic data of 3D structures. In fact, in the absence of vascularization, the supply of specific nutrients and oxygen [6] can become limiting for bigger spheroids, up to the point that inner cells may suffer or die [41,42]. Therefore, this normalization approach offers an easy method to correct for differences in viability among different spheroids. Furthermore, since area determination is non-invasive, spheroids can be further processed to generate alternative normalizations. Alternative normalization methods that determine the DNA or protein content produced standard curves that, with one exception, well correlated with the number of plated cells (Supplementary Materials Figure S6). However, compared to the measurement of the Area of the spheroid directly in the Seahorse microplate without further manipulation of the sample, these methods required lysis of the spheroid, pipetting from the Seahorse plate to one suitable for quantification—increasing the experimental error. As a result, they did not provide normalization as accurately as the normalization based on cell number calculated starting from the spheroid Area (Figure 4 and Supplementary Materials Figure S6a,b). Due to the ease of determination and the possibility of studying other parameters of interest, at least qualitatively, we propose using cell numbers calculated starting from the spheroid area to normalize the Seahorse parameters of 3D cultures. Moreover, as discussed later, this normalization approach allows directly comparisons of the metabolic profiles of 2D and 3D cultures.

Pharmacological perturbation of Seahorse-measured parameters provides a multi-faceted view of the metabolic profiles of cell cultures that can be used for high-resolution classification of biological samples. Using two multivariate statistical tests (PCA and agglomerative hierarchical clustering) on parameters calculated from a Mito Stress test performed on individual spheroids of different dimensions produced by MCF7 and MDA-MB-231 cells, we showed that the differences in the metabolic properties of the spheroids were mainly due to the cell line, rather than to their size. This result is not trivial since different papers suggest that the size of the spheroid may affect metabolism qualitatively, inducing rewiring of energy-producing pathways [11,13,43,44]. When the metabolic parameters were not normalized to the number of viable cells comprising each spheroid, spheroids from the two cell lines were not clearly distinguished by either PCA or hierarchi-

cal clustering (Supplementary Materials Figure S7). This fact indicates that normalization for the number of viable cells allows the highlighting of differences between the cell lines that the size of the spheroid would otherwise hide.

In the PCA plot, most metabolic parameters (except for ‘spare capacity’ and ‘OCR Rot/Ant’) were positively correlated with PC1, which separated spheroids formed by MCF7 from those formed by MDA-MB-231 cells (Figures 5b and S5b). Although PC2 only accounted for less than 13% of the total variability (Figures 5a and S5a), it distinguished MDA-MB-231-, and to a lesser extent MCF7-derived, spheroids according to size. The most significant parameter positively affecting PC2 was the spare respiratory capacity (Figures 5b and S5b), suggesting that smaller spheroids of both cell lines retained some reserve metabolic capacity to cope with stress conditions.

MCF7-derived spheroids were more glycolytic (and less respiratory) than 2D cultures (Figure 6a). Bigger spheroids were more glycolytic but did not show a reduction in respiration compared to smaller ones, consistent with the generally accepted view that the compact 3D structure of spheroids limits oxygen availability, forcing cells to increase the glycolytic flux to cope with ATP demands.

The same paradigm did not apply to MDA-MB-231 cultures. When grown in 2D, MDA-MB-231 cells were significantly more glycolytic and less respiratory than MCF7 cells and did not increase metabolism under stress conditions (Figure 6 [26–28,45]). Regardless of their size, MDA-MB-231-derived spheroids showed decreased glycolytic flux compared to 2D cultures but—unlike their 2D counterparts—showed the ability to up-regulate metabolism upon stress. So, under basal culture conditions, similarly to MCF7, MDA-MB-231 spheroids showed decreased respiration compared to 2D cultures, in keeping with a possible reduction in oxygen supply to the inner cells of the spheroids—but rather than cope with the reduced respiratory ATP production by increasing glycolysis, they entered a quiescent state, from which they could only partially exit following metabolic stress.

The number of cells per spheroid, its dimension, and its compactness may affect the diffusion gradients of oxygen and other solutes inside the spheroid [46]. In addition, production of spheroids with different protocols (e.g., the addition of matrix that increases the compactness of the spheroid, different times of spheroid formation, etc.) or subject to different treatments (e.g., nutritional deprivations and long-term pharmacological treatments) may significantly alter compactness [11,13,30]. In these cases, appropriate compactness-derived parameter(s) should be considered for normalizing Seahorse parameters and in clustering algorithms.

5. Conclusions

Accurate quantitative quality control of spheroids and normalization of data based on the number of viable cells composing the spheroids is mandatory for analyzing the metabolic phenotype of the spheroids. Our results indicate that different cell lines produce spheroids with different metabolic profiles and plasticity. As single-cell technologies [47–53] progress, it will also be possible to assess the role of cell-to-cell heterogeneity in metabolic properties and drug interactions. Extending the analysis to more cancer cell lines and primary cultures derived from different cancer types (e.g., colon, gastric, lung, skin, ovarian), to heterotypic spheroids including different cell types [54,55]—exploring a broader interval of spheroid dimensions and/or incubation times—may provide an even more complex picture. Finally, 3D structures formed from patient-derived cells [33–35] will provide an appropriate platform for designing personalized (multi)drug therapies.

Supplementary Materials: The following supporting information can be downloaded at: <https://www.mdpi.com/article/10.3390/cells11050866/s1>, Figure S1: Protocol for spheroid transfer in XF Seahorse Microplate and different outcome for spheroid culture methods; Figure S2: Impact of seeded cell number on morphology and dimension of spheroids obtained with the *Single Spheroid Protocol*; Figure S3: Comparison between *Multiple Spheroids Protocol* and *Single Spheroid Protocol* on MCF7 Mito Stress test profiles; Figure S4: Comparison of success rate in obtaining valid data with Seahorse technology between *Multiple Spheroids Protocol* and *Single Spheroid Protocol*; Figure S5: Impact

of each respiratory parameter on PCA analyses; Figure S6: Other methods for normalizing Seahorse parameters and relative application to Mito Stress test profiles; Figure S7: Multivariate statistical analysis for non-normalized metabolic parameters of MCF7 and MDA-MB-231 spheroids.

Author Contributions: Conceptualization, M.V. and E.S.; Data curation, V.P., G.C., G.D. and S.B.; Formal analysis, V.P. and S.B.; Investigation, G.C., V.P., S.B. and E.S.; Methodology, G.C., V.P., G.D. and E.S.; Project administration, M.V.; Supervision, E.S. and M.V.; Validation, S.B.; Writing—Original draft, G.C., V.P. and S.B.; Writing—Review and editing, M.V., V.P. and E.S. All authors have read and agreed to the published version of the manuscript.

Funding: This research was supported by funds from the Italian Ministry of University and Research (MIUR) through grant ‘Dipartimenti di Eccellenza 2017’ to the University of Milano-Bicocca, the ‘Research facilitation fund (Fondo per le Agevolazioni alla Ricerca–FAR)’ to E.S. and M.V., the FLAG-ERA grant ITFoC, and H2020 grants EpiPredict n. 642691 and Amplitude n. 871277 to M.V.

Institutional Review Board Statement: Not applicable.

Informed Consent Statement: Not applicable.

Data Availability Statement: All data are presented in the main text or in Supplementary Materials.

Acknowledgments: The authors would like to thank SYSBIO/ISBE.IT Center of Systems Biology and the Project of Excellence CHRONOS (CHRONical multifactorial disorders explored by NOvel integrated Strategies) for providing the advanced technologies used in this study. The authors also warmly thank Luca Magnani (Imperial College London) and Lanfrancone (European Institute of Oncology) for the generous gift of the breast cancer cell lines. We also acknowledge Lilia Alberghina for their support to our research group.

Conflicts of Interest: The authors declare no conflict of interest.

References

- Hanahan, D.; Weinberg, R.A. Hallmarks of cancer: The next generation. *Cell* **2011**, *144*, 646–674. [CrossRef] [PubMed]
- Pupo, E.; Avanzato, D.; Middonti, E.; Bussolino, F.; Lanzetti, L. KRAS-driven metabolic rewiring reveals novel actionable targets in cancer. *Front. Oncol.* **2019**, *9*, 848. [CrossRef] [PubMed]
- Dong, Y.; Tu, R.; Liu, H.; Qing, G. Regulation of cancer cell metabolism: Oncogenic MYC in the driver’s seat. *Signal Transduct. Target. Ther.* **2020**, *5*, 124. [CrossRef]
- Maya-Mendoza, A.; Ostrakova, J.; Kosar, M.; Hall, A.; Duskova, P.; Mistrik, M.; Merchut-Maya, J.M.; Hodny, Z.; Bartkova, J.; Christensen, C.; et al. Myc and Ras oncogenes engage different energy metabolism programs and evoke distinct patterns of oxidative and DNA replication stress. *Mol. Oncol.* **2015**, *9*, 601–616. [CrossRef] [PubMed]
- Lyssiotis, C.A.; Kimmelman, A.C. Metabolic Interactions in the Tumor Microenvironment. *Trends Cell Biol.* **2017**, *27*, 863–875. [CrossRef] [PubMed]
- Sutherland, R.M. Cell and environment interactions in tumor microregions: The multicell spheroid model. *Science* **1988**, *240*, 177–184. [CrossRef] [PubMed]
- Kelm, J.M.; Timmins, N.E.; Brown, C.J.; Fussenegger, M.; Nielsen, L.K. Method for generation of homogeneous multicellular tumor spheroids applicable to a wide variety of cell types. *Biotechnol. Bioeng.* **2003**, *83*, 173–180. [CrossRef]
- Langhans, S.A. Three-dimensional in vitro cell culture models in drug discovery and drug repositioning. *Front. Pharmacol.* **2018**, *9*, 6. [CrossRef]
- Unger, C.; Kramer, N.; Walzl, A.; Scherzer, M.; Hengstschläger, M.; Dolznig, H. Modeling human carcinomas: Physiologically relevant 3D models to improve anti-cancer drug development. *Adv. Drug Deliv. Rev.* **2014**, *79*, 50–67. [CrossRef]
- Jensen, C.; Teng, Y. Is It Time to Start Transitioning From 2D to 3D Cell Culture? *Front. Mol. Biosci.* **2020**, *7*, 33. [CrossRef]
- Zanoni, M.; Cortesi, M.; Zamagni, A.; Arienti, C.; Pignatta, S.; Tesei, A. Modeling neoplastic disease with spheroids and organoids. *J. Hematol. Oncol.* **2020**, *13*, 97. [CrossRef] [PubMed]
- Chaicharoenaudomrung, N.; Kunhorm, P.; Noisa, P. Three-dimensional cell culture systems as an in vitro platform for cancer and stem cell modeling. *World J. Stem Cells* **2019**, *11*, 1065–1083. [CrossRef]
- Costa, E.C.; Moreira, A.F.; de Melo-Diogo, D.; Gaspar, V.M.; Carvalho, M.P.; Correia, I.J. 3D tumor spheroids: An overview on the tools and techniques used for their analysis. *Biotechnol. Adv.* **2016**, *34*, 1427–1441. [CrossRef] [PubMed]
- Rogers, G.W.; Trockmorton, H.; Burroughs, S.E. Targeting Energy Metabolism for Cancer Therapeutic Discovery Using Agilent Seahorse XF Technology: Agilent 2019. Available online: <https://www.agilent.com/cs/library/applications/application-energy-metabolism-cancer-therapeutics-discovery-cell-analysis-5994-1017en-agilent.pdf> (accessed on 29 January 2022).
- Pasquale, V.; Ducci, G.; Campioni, G.; Ventrici, A.; Assalini, C.; Busti, S.; Vanoni, M.; Vago, R.; Sacco, E. Profiling and Targeting of Energy and Redox Metabolism in Grade 2 Bladder Cancer Cells with Different Invasiveness Properties. *Cells* **2020**, *9*, 2669. [CrossRef] [PubMed]

16. Porporato, P.E.; Payen, V.L.; Pérez-Escuredo, J.; De Saedeleer, C.J.; Danhier, P.; Copetti, T.; Dhup, S.; Tardy, M.; Vazeille, T.; Bouzin, C.; et al. A mitochondrial switch promotes tumor metastasis. *Cell Rep.* **2014**, *8*, 754–766. [[CrossRef](#)]
17. Viale, A.; Pettazzoni, P.; Lyssiotis, C.A.; Ying, H.; Sánchez, N.; Marchesini, M.; Carugo, A.; Green, T.; Seth, S.; Giuliani, V.; et al. Oncogene ablation-resistant pancreatic cancer cells depend on mitochondrial function. *Nature* **2014**, *514*, 628–632. [[CrossRef](#)]
18. Raggi, C.; Taddei, M.L.; Sacco, E.; Navari, N.; Correnti, M.; Piombanti, B.; Pastore, M.; Campani, C.; Pranzini, E.; Iorio, J.; et al. Mitochondrial oxidative metabolism contributes to a cancer stem cell phenotype in cholangiocarcinoma. *J. Hepatol.* **2021**, *74*, 1373–1385. [[CrossRef](#)]
19. Parri, M.; Ippolito, L.; Cirri, P.; Ramazzotti, M.; Chiarugi, P. Metabolic cell communication within tumour microenvironment: Models, methods and perspectives. *Curr. Opin. Biotechnol.* **2020**, *63*, 210–219. [[CrossRef](#)]
20. Damiani, C.; Gaglio, D.; Sacco, E.; Alberghina, L.; Vanoni, M. Systems metabolomics: From metabolomic snapshots to design principles. *Curr. Opin. Biotechnol.* **2020**, *63*, 190–199. [[CrossRef](#)]
21. Kam, Y.; Rogers, G.W.; Jastromb, N.; Dranka, B.P. Methods and Strategies for Normalizing XF Metabolic Data to Cellular Parameters: Agilent 2018, p. 8. Available online: https://www.agilent.com/cs/library/technicaloverviews/public/Methods_and_Strategies_for_Normalizing_Tech_Overview_022118.pdf (accessed on 29 January 2022).
22. Agilent Cell Analysis Publications Alert October 2020. Available online: <https://seahorseinfo.agilent.com/acton/media/10967/agilent-cell-analysis-publications-alert-october-2020#cancer> (accessed on 28 January 2022).
23. Jiang, L.; Shestov, A.A.; Swain, P.; Yang, C.; Parker, S.J.; Wang, Q.A.; Terada, L.S.; Adams, N.D.; McCabe, M.T.; Pietrak, B.; et al. Reductive carboxylation supports redox homeostasis during anchorage-independent growth. *Nature* **2016**, *532*, 255–258. [[CrossRef](#)]
24. Russell, S.; Wojtkowiak, J.; Neilson, A.; Gillies, R.J. Metabolic Profiling of healthy and cancerous tissues in 2D and 3D. *Sci. Rep.* **2017**, *7*, 15285. [[CrossRef](#)]
25. Taddeo, E.P.; Stiles, L.; Sereda, S.; Ritou, E.; Wolf, D.M.; Abdullah, M.; Swanson, Z.; Wilhelm, J.; Bellin, M.; McDonald, P.; et al. Individual islet respirometry reveals functional diversity within the islet population of mice and human donors. *Mol. Metab.* **2018**, *16*, 150–159. [[CrossRef](#)] [[PubMed](#)]
26. Pelicano, H.; Zhang, W.; Liu, J.; Hammoudi, N.; Dai, J.; Xu, R.H.; Pusztai, L.; Huang, P. Mitochondrial dysfunction in some triple-negative breast cancer cell lines: Role of mTOR pathway and therapeutic potential. *Breast Cancer Res.* **2014**, *16*, 434. [[CrossRef](#)] [[PubMed](#)]
27. Lanning, N.J.; Castle, J.P.; Singh, S.J.; Leon, A.N.; Tovar, E.A.; Sanghera, A.; MacKeigan, J.P.; Filipp, F.V.; Graveel, C.R. Metabolic profiling of triple-negative breast cancer cells reveals metabolic vulnerabilities. *Cancer Metab.* **2017**, *5*, 6. [[CrossRef](#)]
28. Guha, M.; Srinivasan, S.; Raman, P.; Jiang, Y.; Kaufman, B.A.; Taylor, D.; Dong, D.; Chakrabarti, R.; Picard, M.; Carstens, R.P.; et al. Aggressive triple negative breast cancers have unique molecular signature on the basis of mitochondrial genetic and functional defects. *Biochim. Biophys. Acta-Mol. Basis Dis.* **2018**, *1864*, 1060–1071. [[CrossRef](#)]
29. Durand, R.E. Multicell spheroids as a model for cell kinetic studies. *Cell Tissue Kinet.* **1990**, *23*, 141–159. [[PubMed](#)]
30. Zanoni, M.; Piccinini, F.; Arienti, C.; Zamagni, A.; Santi, S.; Polico, R.; Bevilacqua, A.; Tesei, A. 3D tumor spheroid models for in vitro therapeutic screening: A systematic approach to enhance the biological relevance of data obtained. *Sci. Rep.* **2016**, *6*, 19103. [[CrossRef](#)]
31. Nunes, A.S.; Barros, A.S.; Costa, E.C.; Moreira, A.F.; Correia, I.J. 3D tumor spheroids as in vitro models to mimic in vivo human solid tumors resistance to therapeutic drugs. *Biotechnol. Bioeng.* **2019**, *116*, 206–226. [[CrossRef](#)]
32. Mittler, F.; Obeid, P.; Rulina, A.V.; Haguet, V.; Gidrol, X.; Balakirev, M.Y. High-content monitoring of drug effects in a 3D spheroid model. *Front. Oncol.* **2017**, *7*, 293. [[CrossRef](#)]
33. Weeber, F.; Ooft, S.N.; Dijkstra, K.K.; Voest, E.E. Tumor Organoids as a Pre-clinical Cancer Model for Drug Discovery. *Cell Chem. Biol.* **2017**, *24*, 1092–1100. [[CrossRef](#)]
34. Korving, J.; Moll, J.; Voest, E.E.; Weeber, F.; de Ligt, J.; Rottenberg, S.; Bounova, G.; Boj, S.F.; Kopper, O.; Vries, R.G.J.; et al. A Living Biobank of Breast Cancer Organoids Captures Disease Heterogeneity. *Cell* **2017**, *172*, 373–386.e10.
35. Vlachogiannis, G.; Hedayat, S.; Vatsiou, A.; Jamin, Y.; Fernández-Mateos, J.; Khan, K.; Lampis, A.; Eason, K.; Huntingford, L.; Burke, R.; et al. Patient-derived organoids model treatment response of metastatic gastrointestinal cancers. *Science* **2018**, *359*, 920–926. [[CrossRef](#)] [[PubMed](#)]
36. DeRose, Y.S.; Gligorich, K.M.; Wang, G.; Georgelas, A.; Bowman, P.; Courdy, S.J.; Welm, A.L.; Welm, B.E. Patient-Derived Models of Human Breast Cancer: Protocols for In Vitro and In Vivo Applications in Tumor Biology and Translational Medicine. *Curr. Protoc. Pharmacol.* **2013**, *60*, 1–43. [[CrossRef](#)]
37. Nielsen, J. Systems Biology of Metabolism: A Driver for Developing Personalized and Precision Medicine. *Cell Metab.* **2017**, *25*, 572–579. [[CrossRef](#)] [[PubMed](#)]
38. Jones, A.E.; Sheng, L.; Acevedo, A.; Veliova, M.; Shirihai, O.S.; Stiles, L.; Divakaruni, A.S. Forces, fluxes, and fuels: Tracking mitochondrial metabolism by integrating measurements of membrane potential, respiration, and metabolites. *Am. J. Physiol.-Cell Physiol.* **2021**, *320*, C80–C91. [[CrossRef](#)] [[PubMed](#)]
39. Nolfi-Donagan, D.; Braganza, A.; Shiva, S. Mitochondrial electron transport chain: Oxidative phosphorylation, oxidant production, and methods of measurement. *Redox Biol.* **2020**, *37*, 101674. [[CrossRef](#)]
40. Wu, D.; Ma, Y.; Cao, Y.; Zhang, T. Mitochondrial toxicity of nanomaterials. *Sci. Total Environ.* **2020**, *702*, 134994. [[CrossRef](#)]
41. Freyer, J.P.; Sutherland, R.M. Selective Dissociation and Characterization of Cells from Different Regions of Multicell Tumor Spheroids. *Cancer Res.* **1980**, *40*, 3956–3965.

42. Sutherland, R.M.; Sordat, B.; Bamat, J.; Gabbert, H.; Bourrat, B.; Mueller-Klieser, W. Oxygenation and Differentiation in Multicellular Spheroids of Human Colon Carcinoma. *Cancer Res.* **1986**, *46*, 5320–5329.
43. Walenta, S.; Dotsch, J.; Bourrat-Flock, B.; Mueller-Klieser, W. Size-dependent oxygenation and energy status in multicellular tumor spheroids. *Adv. Exp. Med. Biol.* **1990**, *277*, 889–893.
44. Murphy, K.C.; Hung, B.P.; Browne-Bourne, S.; Zhou, D.; Yeung, J.; Genetos, D.C.; Leach, J.K. Measurement of oxygen tension within mesenchymal stem cell spheroids. *J. R. Soc. Interface* **2017**, *14*, 20160851. [[CrossRef](#)] [[PubMed](#)]
45. Bonanomi, M.; Salmistraro, N.; Fiscion, G.; Conte, F.; Paci, P.; Bravatà, V.; Forte, G.I.; Volpari, T.; Scorza, M.; Mastroianni, F.; et al. Transcriptomics and metabolomics integration reveals redox-dependent metabolic rewiring in breast cancer cells. *Cancers* **2021**, *13*, 5058. [[CrossRef](#)] [[PubMed](#)]
46. Leung, B.M.; Leshner-Perez, S.C.; Matsuoka, T.; Moraes, C.; Takayama, S. Media additives to promote spheroid circularity and compactness in hanging drop platform. *Biomater. Sci.* **2015**, *3*, 336–344. [[CrossRef](#)] [[PubMed](#)]
47. Damiani, C.; Maspero, D.; Di Filippo, M.; Colombo, R.; Pescini, D.; Graudenzi, A.; Westerhoff, H.V.; Alberghina, L.; Vanoni, M.; Mauri, G. Integration of single-cell RNA-seq data into population models to characterize cancer metabolism. *PLoS Comput. Biol.* **2019**, *15*, e1006733. [[CrossRef](#)]
48. Wei, D.; Xu, M.; Wang, Z.; Tong, J. The Development of Single-Cell Metabolism and Its Role in Studying Cancer Emergent Properties. *Front. Oncol.* **2022**, *11*, 814085. [[CrossRef](#)]
49. Xiao, Z.; Dai, Z.; Locasale, J.W. Metabolic landscape of the tumor microenvironment at single cell resolution. *Nat. Commun.* **2019**, *10*, 3763. [[CrossRef](#)]
50. Argüello, R.J.; Combes, A.J.; Char, R.; Gigan, J.P.; Baaziz, A.I.; Bousiquot, E.; Camosseto, V.; Samad, B.; Tsui, J.; Yan, P.; et al. SCENITH: A Flow Cytometry-Based Method to Functionally Profile Energy Metabolism with Single-Cell Resolution. *Cell Metab.* **2020**, *32*, 1063–1075.e7. [[CrossRef](#)]
51. Gómez-Cebrián, N.; Domingo-Ortí, I.; Poveda, J.L.; Vicent, M.J.; Puchades-Carrasco, L.; Pineda-Lucena, A. Multi-omic approaches to breast cancer metabolic phenotyping: Applications in diagnosis, prognosis, and the development of novel treatments. *Cancers* **2021**, *13*, 4544. [[CrossRef](#)]
52. Wu, D.; Harrison, D.L.; Szasz, T.; Yeh, C.F.; Shentu, T.P.; Meliton, A.; Huang, R.T.; Zhou, Z.; Mutlu, G.M.; Huang, J.; et al. Single-cell metabolic imaging reveals a SLC2A3-dependent glycolytic burst in motile endothelial cells. *Nat. Metab.* **2021**, *3*, 714–727. [[CrossRef](#)]
53. Harrison, D.; Wu, D.; Huang, J.; Fang, Y. Single-cell lactate production rate as a measure of glycolysis in endothelial cells. *STAR Protoc.* **2021**, *2*, 100807. [[CrossRef](#)]
54. Noel, P.; Muñoz, R.; Rogers, G.W.; Neilson, A.; Von Hoff, D.D.; Han, H. Preparation and metabolic assay of 3-dimensional spheroid co-cultures of pancreatic cancer cells and fibroblasts. *J. Vis. Exp.* **2017**, *2017*, 56081. [[CrossRef](#)] [[PubMed](#)]
55. Franchi-Mendes, T.; Eduardo, R.; Domenici, G.; Brito, C. 3D cancer models: Depicting cellular crosstalk within the tumour microenvironment. *Cancers* **2021**, *13*, 4610. [[CrossRef](#)] [[PubMed](#)]

SUPPLEMENTARY MATERIALS

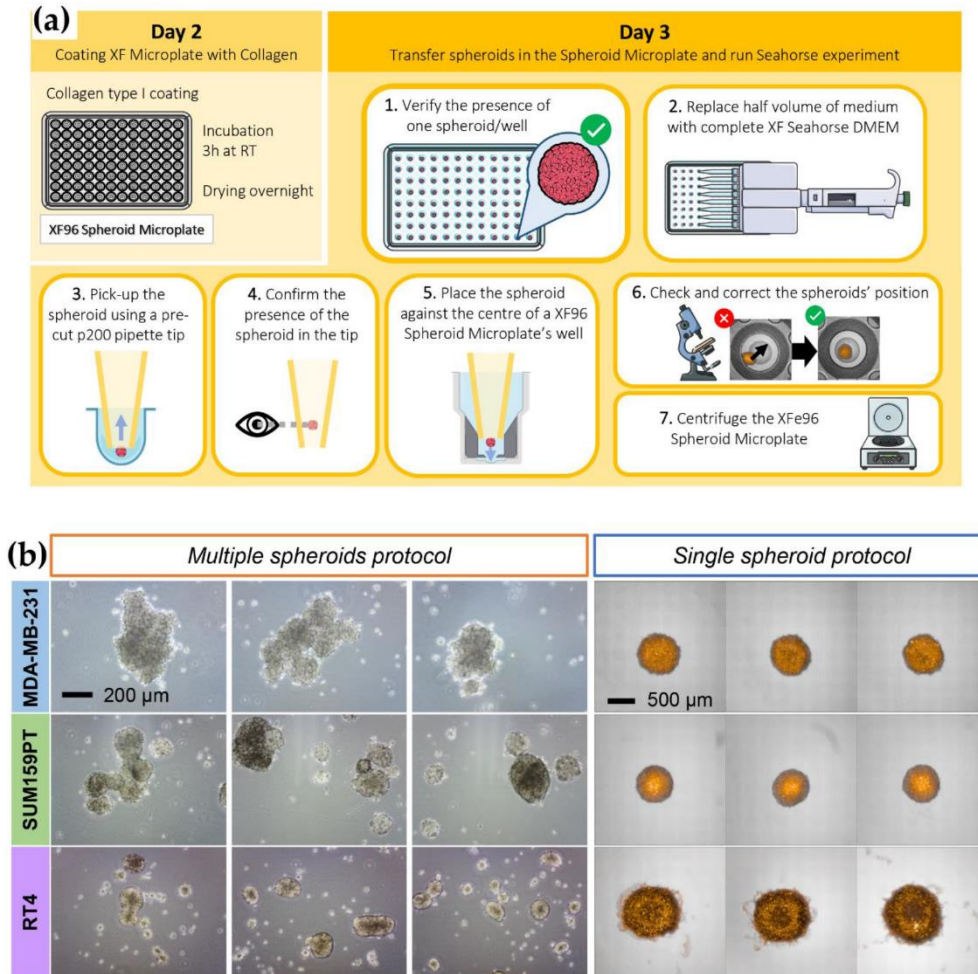


Figure S1. Protocol for spheroid transfer in XF Seahorse Microplate and different outcome for spheroid culture methods. **(a)** Schematic representation of spheroids' transfer in the XF Seahorse Microplate. **(b)** Representative pictures of MDA-MB-231 cell line, SUM159PT cell line (mammary carcinoma), and RT4 cell line (urothelial carcinoma) spheroids produced with the *Multiple spheroids protocol* (left) and the *Single spheroid protocol* (right) before their transfer in the XF Seahorse Microplate. Images were acquired in phase-contrast light microscopy (*Multiple spheroids protocol*) and brightfield and confocal fluorescent microscopy (in orange, CellTracker™ Red CMTPX Dye) with Operetta CLS™ (*Single spheroid protocol*).

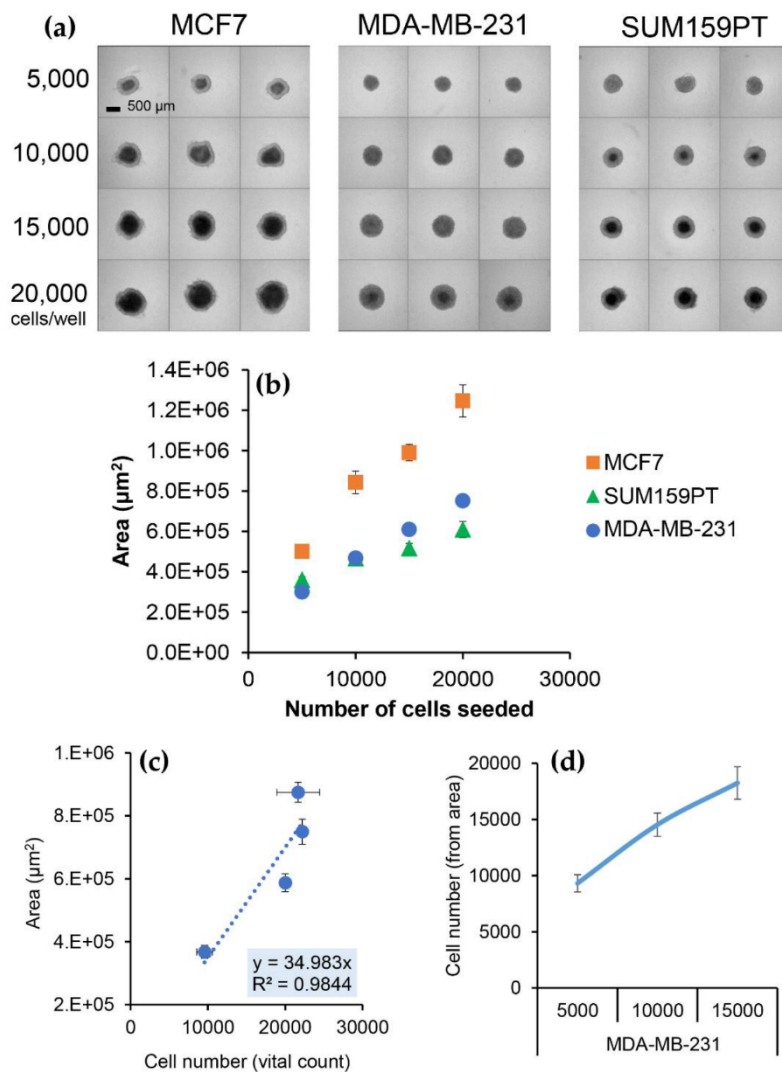


Figure S2. Impact of seeded cell number on morphology and dimension of spheroids obtained with the *Single spheroid protocol*. **(a)** Brightfield imaging with Operetta CLS™ of MCF7, MDA-MB-231, and SUM159PT spheroids produced by seeding a different number of cells/well: 5,000 cells, 10,000 cells, 15,000 cells, and 20,000 cells. **(b)** Correlation of the number of seeded cells and respective spheroid area obtained after 72 hours measured through imaging with Operetta CLS™ and analysis with Harmony software; points represent mean ± standard deviation. **(c)** Standard curve obtained measuring the area of groups of MDA-MB-231 spheroids produced from 5,000 – 10,000 – 15,000 – 20,000 cells/well and their subsequent digestion and count of the number of vital cells after 72h of spheroid formation (note that the number of cells-per-spheroids after 72h of culture is different than the starting number of cells/well seeded). Points represent mean ± standard deviation along with regression. **(d)** Graph representing the number of cells-per-spheroid indirectly calculated using area measurement on MDA-MB-231 spheroids tested in a Seahorse assay, grouped based on the number of cells seeded for spheroids formation (5,000 – 10,000 – 15,000 cells/well). The points of the blue line depict the number of cells-per-spheroid calculated by measuring the area of each spheroid of the XF Seahorse Microplate and applying the equations derived from the standard curve in panel (c).

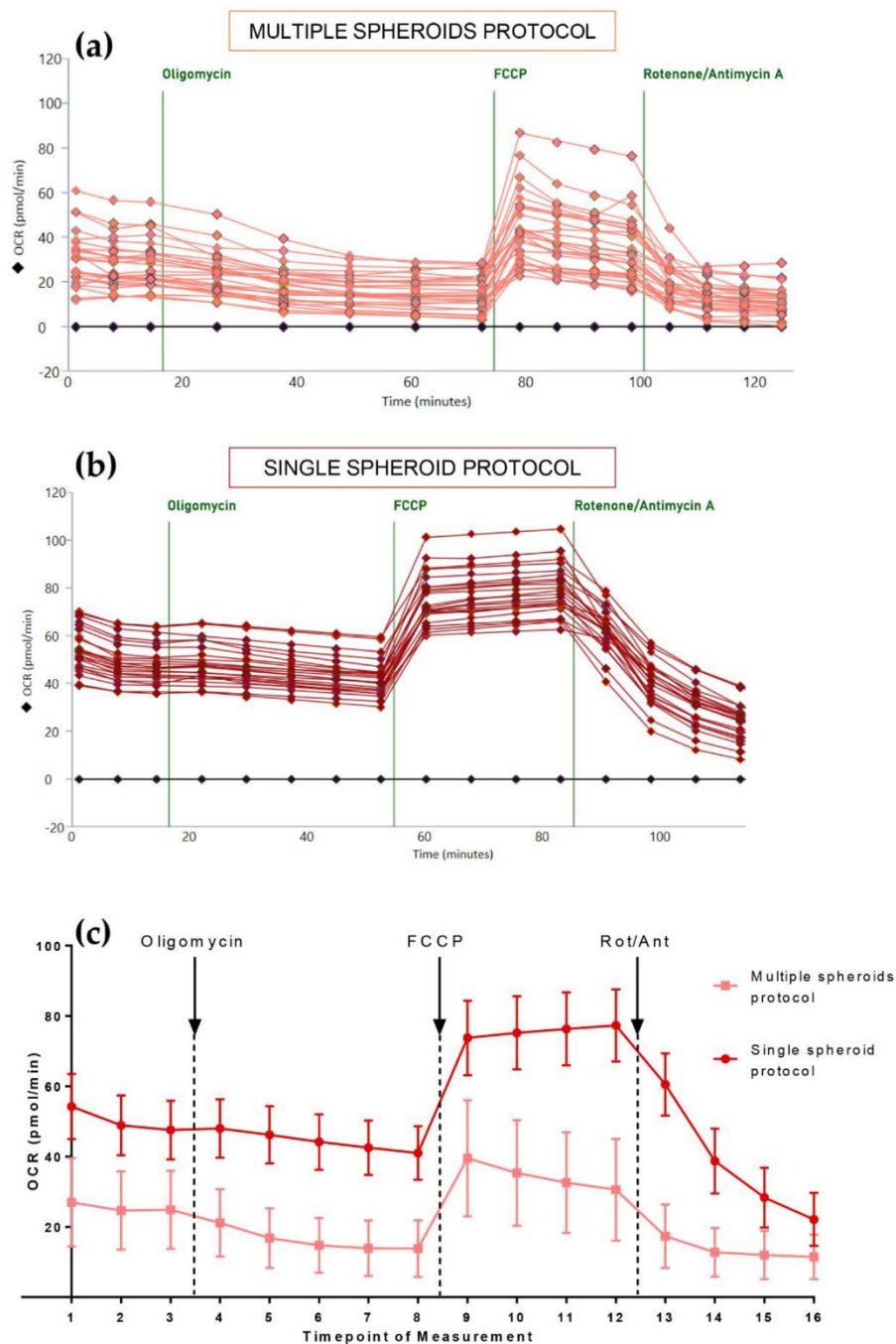


Figure S3. Comparison between *Multiple spheroids protocol* and *Single spheroid protocol* on MCF7 Mito Stress test profiles. OCR Profiles of Mito stress test produced with *Multiple spheroids protocol* (a) and *Single spheroid protocol* (b); single measurement for every spheroid is reported to show distribution, the black line is for background and corresponds to zero value. (c) The mean \pm standard deviation of OCR values is plotted for each measurement of the Mito stress test comparing the two protocols of spheroid formation.

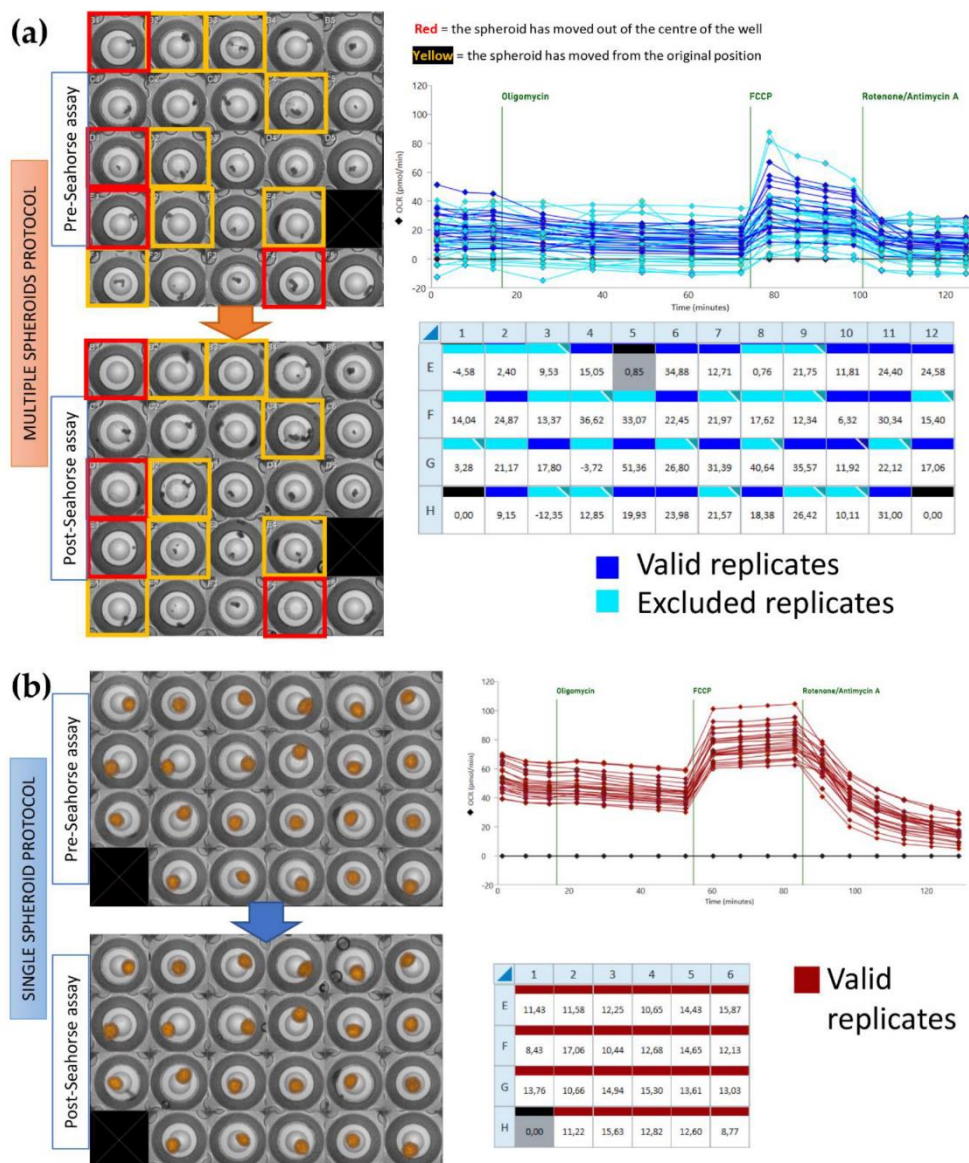


Figure S4. Comparison of success rate in obtaining valid data with Seahorse technology between *Multiple spheroids protocol* and *Single spheroid protocol*. Representation through imaging (brightfield imaging with Operetta CLS™), Mito stress test profile plot, and plate schematic depiction of the success rate in obtaining valid data analyzing 3D structure with Seahorse technology choosing between *Multiple spheroids protocol* and *Single spheroid protocol*. **(a)** The *Multiple spheroids protocol* requires a strict selection of the replicates to eliminate those spheroids that have moved during the assay. The image shows examples of replicates that have been excluded from the analysis (light blue) and examples of replicates that have been conserved for the analysis (dark blue); red and yellow squares represent changes in the sample contained in the well, respectively movement out of the center of the well or from the original position. **(b)** All the replicates can be considered valid with the *Single spheroid protocol* since none of the spheroids have moved during the assay.

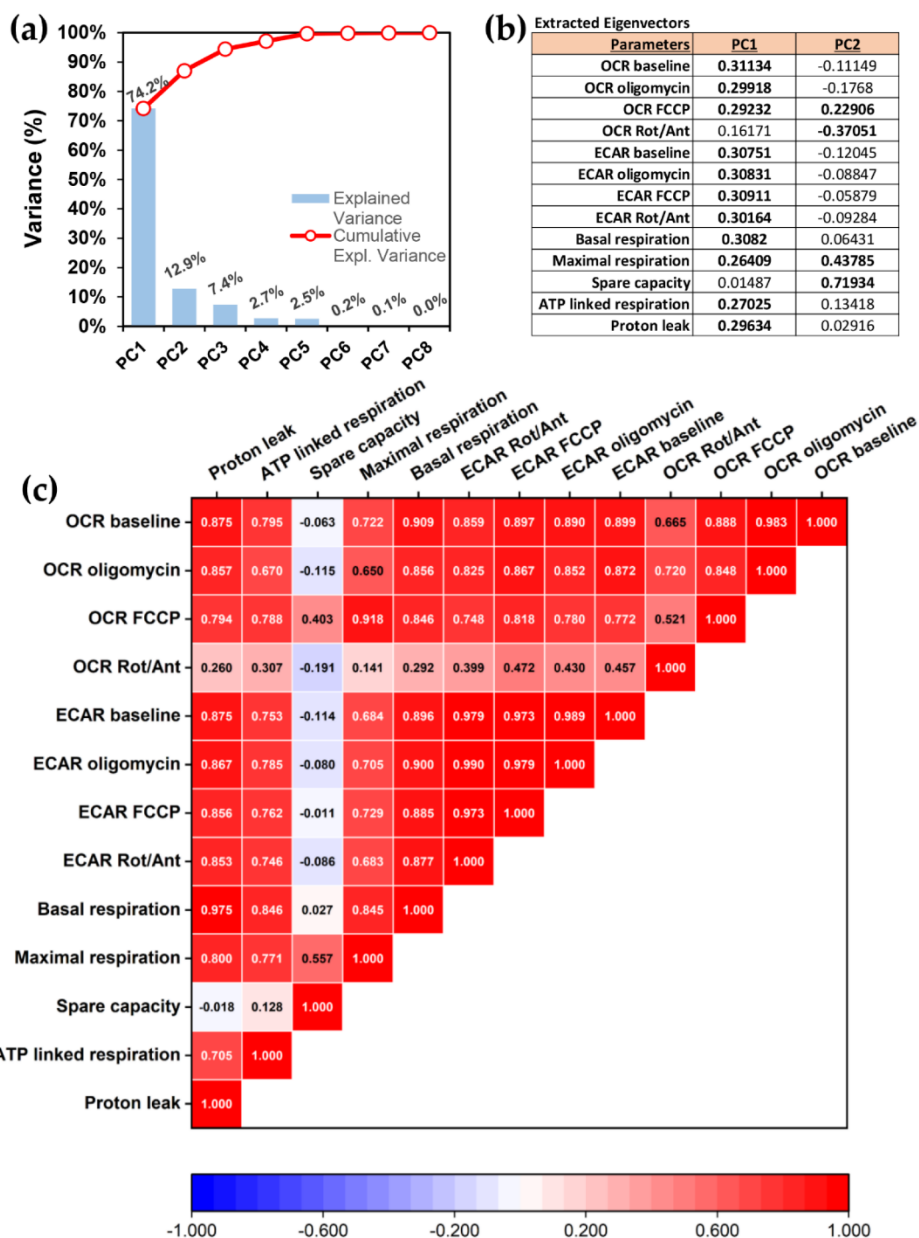


Figure S5. Impact of each respiratory parameter on PCA analyses. **(a)** PCA score plots, showing the amount of variance explained by each PCA component and the cumulative variance. **(b)** The extracted Eigenvectors define the contributes (loadings) of the original variables to the Principal Components. Values are comprised between -1 and +1. Absolute values near zero indicate that a variable contributes little to the Principal Component, whereas larger absolute values (in bold fonts) indicate significant contributions. **(c)** Correlation matrix for the original observed parameters. Values are comprised between -1 and 1, with -1 (blue) indicating a perfectly negative linear correlation between two variables, 0 (white) indicating no linear correlation, and 1 (red) indicating a perfect positive linear correlation.

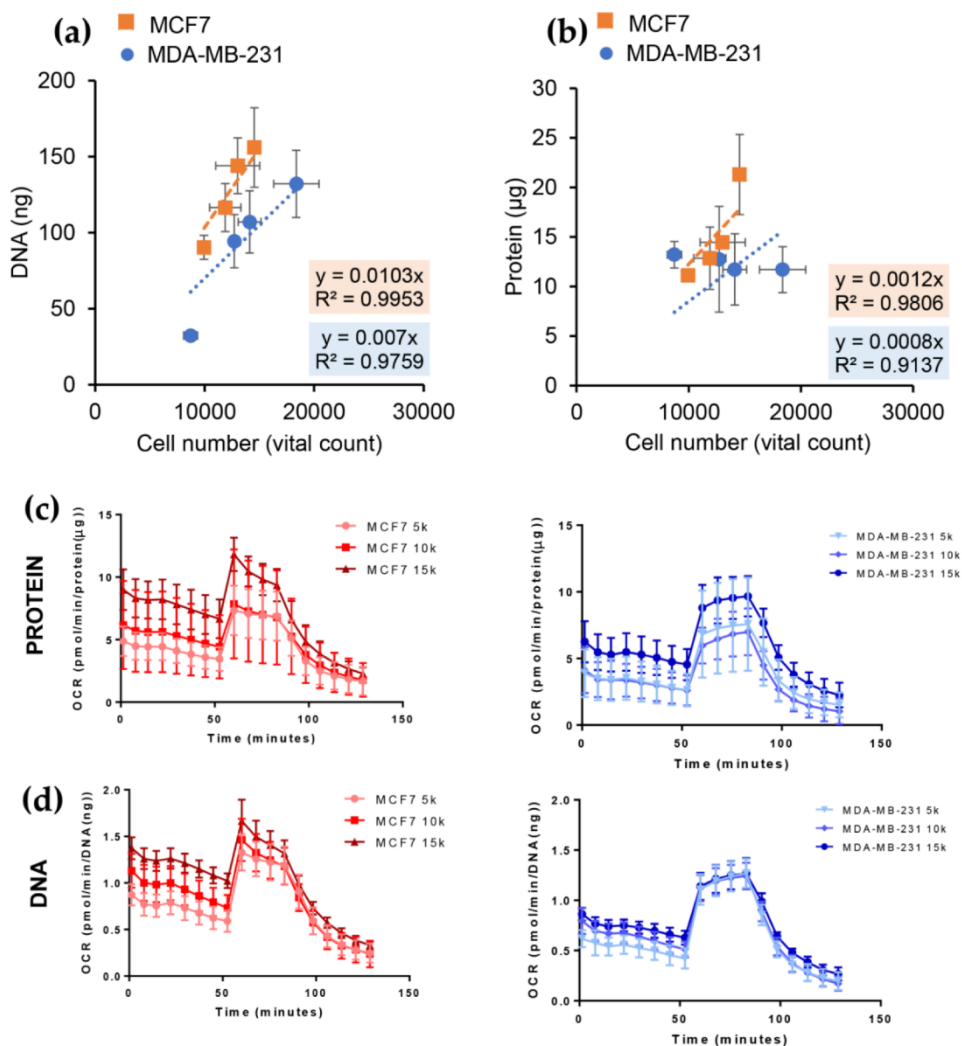


Figure S6. Other methods to normalize Seahorse parameters and relative application on Mito stress test profiles. **(a,b)** The curves show the relation between DNA **(a)** and protein **(b)** content and the number of vital cells in spheroids. The curves were obtained from the digestion and vital count of the cell number in groups of spheroids produced from 5,000 to 20,000 cells/well and the subsequent quantification of their protein and DNA content. **(c,d)** Mito stress profile was obtained testing spheroids of MCF7 and MDA-MB-231 produced by seeding a different number of cells/well (5,000 cells/well = 5k; 10,000 cells/well = 10k; and 15,000 cells/well = 15k); each point represents the OCR mean with the relative standard deviation of the indicated group of spheroids as a function of time. **(c)** OCR values normalized on the protein content of a group of spheroids directly on the XF Seahorse Microplate. **(d)** OCR values normalized on the DNA content of a group of spheroids directly on the XF Seahorse Microplate.

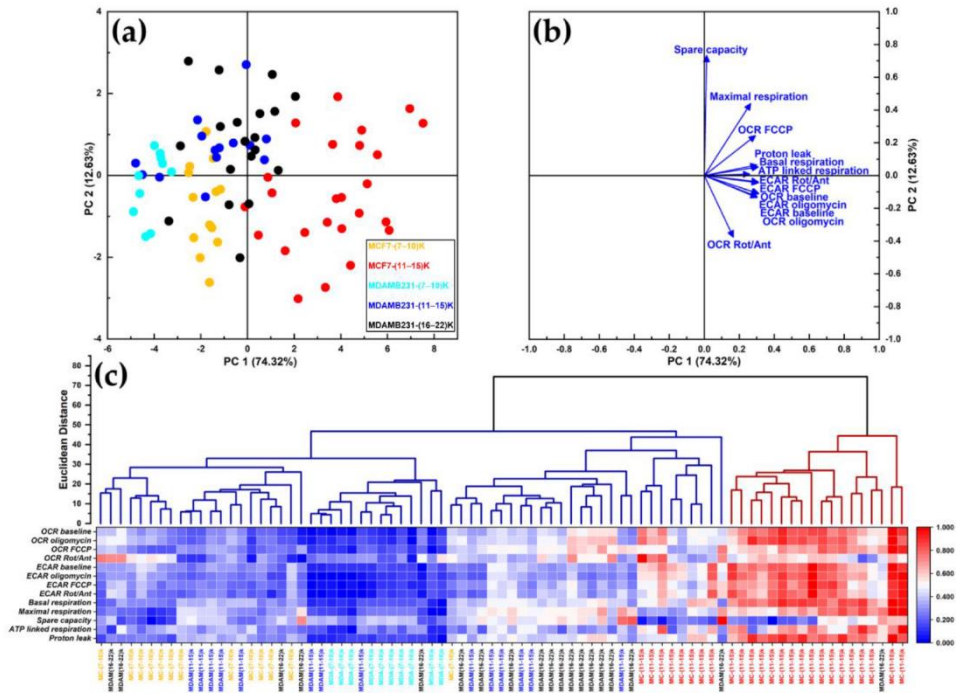


Figure S7. Multivariate statistical analysis for non-normalized metabolic parameters of MCF7 and MDA-MB-231 spheroids. **(a)** PCA scree plots, showing the amount of variance explained by each PCA component and the cumulative variance. **(b)** The extracted Eigenvectors define the contributes (loadings) of the original variables to the Principal Components. Values are comprised between -1 and +1. Absolute values near zero indicate that a variable contributes little to the Principal Component, whereas larger absolute values (in bold fonts) indicate significant contributes. **(c)** Correlation matrix for the original observed parameters. Values are comprised between -1 and 1, with -1 (blue) indicates a perfectly negative linear correlation between two variables, 0 (white) indicating no linear correlation and 1 (red) indicating a perfectly positive linear correlation.

CHAPTER 3: PROFILING AND TARGETING OF ENERGY AND REDOX METABOLISM OF
GRADE II BLADDER CANCER CELLS WITH DIFFERENT INVASIVENESS PROPERTIES

Doi: 10.3390/cells9122669

PDF of the published manuscript follows

Profiling and Targeting of Energy and Redox Metabolism in Grade 2 Bladder Cancer Cells with Different Invasiveness Properties

Valentina Pasquale ^{1,2,†}, Giacomo Ducci ^{1,2,†}, Gloria Campioni ^{1,2}, Adria Ventrici ¹, Chiara Assalini ³, Stefano Busti ^{1,2}, Marco Vanoni ^{1,2,*}, Riccardo Vago ^{3,4,*} and Elena Sacco ^{1,2,*}

¹ Department of Biotechnology and Biosciences, University of Milano-Bicocca, Piazza della Scienza 2, 20126 Milan, Italy; valentina.pasquale@unimib.it (V.P.); g.ducci@campus.unimib.it (G.D.); g.campioni@campus.unimib.it (G.C.); a.ventrici@campus.unimib.it (A.V.); stefano.busti1@unimib.it (S.B.)

² SYSBIO-ISBE-IT-Candidate National Node of Italy for ISBE, Research Infrastructure for Systems Biology Europe, 20126 Milan, Italy

³ Urological Research Institute, Division of Experimental Oncology, IRCCS San Raffaele Hospital, 20132 Milan, Italy; assalini.chiara@hsr.it

⁴ Università Vita-Salute San Raffaele, 20132 Milan, Italy

* Correspondence: marco.vanoni@unimib.it (M.V.); vago.riccardo@hsr.it (R.V.); elena.sacco@unimib.it (E.S.); Tel.: +39-02-6448-3525 (M.V.); +39-02-2643-5664 (R.V.); +39-02-6448-3379 (E.S.)

† These authors equally contributed to this work.

Received: 18 November 2020; Accepted: 8 December 2020; Published: 11 December 2020

Abstract: Bladder cancer is one of the most prevalent deadly diseases worldwide. Grade 2 tumors represent a good window of therapeutic intervention, whose optimization requires high resolution biomarker identification. Here we characterize energy metabolism and cellular properties associated with spreading and tumor progression of RT112 and 5637, two Grade 2 cancer cell lines derived from human bladder, representative of luminal-like and basal-like tumors, respectively. The two cell lines have similar proliferation rates, but only 5637 cells show efficient lateral migration. In contrast, RT112 cells are more prone to form spheroids. RT112 cells produce more ATP by glycolysis and OXPHOS, present overall higher metabolic plasticity and are less sensitive than 5637 to nutritional perturbation of cell proliferation and migration induced by treatment with 2-deoxyglucose and metformin. On the contrary, spheroid formation is less sensitive to metabolic perturbations in 5637 than RT112 cells. The ability of metformin to reduce, although with different efficiency, cell proliferation, sphere formation and migration in both cell lines, suggests that OXPHOS targeting could be an effective strategy to reduce the invasiveness of Grade 2 bladder cancer cells.

Keywords: bladder cancer; energy and redox metabolism; cellular bioenergetics; mitochondrial function; glycolysis; fatty acids oxidation; oxidative stress; 2D and 3D cultures; Seahorse Extracellular Flux Analyzer; quantitative imaging; Operetta CLS™

1. Introduction

Bladder cancer (BC) is among the most common malignancies worldwide and one of the most expensive cancers to manage [1]. Most BC patients (75–80%) are diagnosed with non-muscle invasive BC (NMIBC). Recurrences are frequent (50–70%), sometimes including progression to invasive tumors (Muscle invasive BC, MIBC), which drastically reduce survival expectations. NMIBC is usually treated by transurethral resection (TUR) to remove the tumor and obtain histological examination material. After resection, patients are introduced to a treatment regimen, which reflects

the disease's nature and potential, based on histological grade and tumor-node-metastasis stage. Therefore, a proper definition of urothelial neoplasms grading is a crucial driver to stratify tumor behavior, including progression and recurrence for optimal patient management and surveillance follow-up [2,3]. In 2004, the World Health Organization (WHO) introduced a classification, confirmed in 2016, including the concept of Low-Grade (LG) and High-Grade (HG) tumors, as well as the papillary urothelial neoplasm of low malignant potential category [4]. One critical issue in this categorization is grade heterogeneity in papillary neoplasms, a mixture of non-invasive HG and LG features that can be observed in around 25% of cases [5]. So far, molecular markers are not part of standard clinical practice, even if molecular changes in HG tumors occur at early stages before developing the corresponding morphological features [6]. In the case of borderline histology, to distinguish LG and HG tumors, other parameters such as urinary cytology, multifocality, size of the lesion, prior history, and recurrence can be considered for grading determination, but they are often not consistent. Mixed lesions represent a challenging topic and no authoritative recommendations on reporting them are available from the WHO 2016 [3].

In this context, it is crucial to identify new markers that can contribute to patients' stratification to direct them to more effective and less toxic targeted treatments, even to be combined with conventional therapies, to improve prognosis, avoid relapses, or to promote the overcoming of chemoresistance. Reprogramming of energy metabolism has emerged as a hallmark of cancer, and altered metabolic pathways can represent attractive clinical targets exploitable in new therapeutic strategies [7,8]. Cancer cells exhibit profound metabolic rearrangements, which support their enhanced growth, allowing them to proliferate and survive in conditions where normal cells do not [9,10]. Among the most common rearrangements there is the well-known Warburg effect, which consists of enhancing aerobic glycolysis at the expense of mitochondrial respiration, which leads to ferment the glycolysis-derived pyruvate to lactic acid, even under normoxic condition [11]. This metabolic rewiring allows obtaining energy, reducing power and building blocks for biosynthetic processes, faster than through alternative metabolic pathways. This type of metabolism is usually exploited by actively proliferating cells [12,13] and maximally contracted skeletal muscle cells, which must reach short-term high energy goals [14]. Although initially associated with mitochondrial defects, it is clear by now that the Warburg effect also occurs in the presence of functional mitochondria. The activation of specific signaling pathways (i.e., Hypoxia-induced HIF-1 α , PI3K-Akt-mTOR, RAS/MEK/MAPK), of specific oncogenes (i.e., RAS [15–17], Myc [18]), the inactivation of tumor suppressors (i.e., p53 [19,20]), and/or the selective pressure exerted by the microenvironment [21–24] all contribute to driving the Warburg effect. The hyperglycolytic phenotype, characterized by increased glucose uptake and glycolysis, is associated with further metabolic changes that include the extensive anaplerotic use of other nutrients, such as glutamine, for the replenishment of the TCA cycle intermediates [25–27]. Although these rearrangements can provide selective advantages to cancer cells, they also confer dependence on specific enzymatic activities and specific nutrients and open to novel therapeutic opportunities [28–30]. For example, glutamine addicted cancer cells need glutamine to survive because they depend on glutaminolysis for anaplerosis and their biosynthetic needs [27,31]. Many other metabolic targets have been identified in cancers, including urothelial bladder cancers [32,33], and are also evaluated as prognostic markers [34]. Several drugs that affect the altered metabolism are under clinical trial in the perspective of precision medicine [35–37]. Deregulations of energy metabolism can also affect reducing equivalents and impact on redox homeostasis by making cancer cells more sensitive to oxidative stress [38–40].

In this work we present a characterization of the energy and redox metabolism of two bladder cancer cell lines with a low histological grade of tumor progression (Grade 2), RT112, and 5637. Grade 2 represents a therapeutic window that strongly requires post-surgical resection pharmacological treatments that help to eliminate residual tumor cells and prevent the formation of tumor relapses. Based on gene mutation patterns and genomic changes, the two cell lines are representative of luminal like FGFR3-driven cancer (RT112), and of the basal-like TP53/RB tumor suppressor-driven cancer (5736), often used as models of non-aggressive and aggressive BCs, respectively [41,42]. Here we show that the RT112 cell line is largely less efficient in migration, but forms spheroids more

efficiently. Both cell lines produce ATP by both OXPHOS and glycolysis. However, RT112 cells are more energetic, have higher metabolic plasticity and are less sensitive than 5637 to nutritional perturbation of cell proliferation and migration. Although both cell lines, when grown under adhesion are sensitive to targeting of both OXPHOS and glycolysis, although with different efficiency, only targeting of OXPHOS significantly affects spheroid formation of both cell lines.

2. Materials and Methods

2.1. Materials and Cell Cultures

Grade 2 bladder cancer cell lines RT112 and 5637, originally established from primary urinary bladder carcinoma [43,44], were purchased from American Collection of Cell Cultures (ATCC, Manassas, VA, USA). Cell lines were routinely grown in RPMI-1640 medium (R0883-Merck Life Science, Darmstadt, Germany) supplemented with 10% fetal bovine serum (FBS, Gibco-ThermoFisher, Waltham, MA, USA), 4 mM glutamine, 100 U/mL penicillin and 100 mg/mL streptomycin, at 37 °C in a humidified atmosphere of 5% CO₂. Cells were passaged using trypsin-ethylenediaminetetraacetic acid (EDTA). Assays on adherent cells were performed in experimental medium: DMEM w/o phenol red (Gibco™-Thermo Fisher Scientific), FBS 10%, 10 mM glucose, 2 mM glutamine, 100 U/mL penicillin and 100 mg/mL streptomycin. Sphere formation was performed in 3D experimental medium DMEM w/o phenol red (Gibco™-Thermo Fisher Scientific), 1% BSA, 10 mM glucose, 2 mM glutamine, 10 µg/mL Insulin (I9278, Merck Life Science), 0.5 µg/mL Hydrocortisone (H0888-1G, Merck Life Science), 20 ng/mL EGF (EGF Human Recombinant, Peprotech, London, UK) 100 ng/mL Cholera Toxin (C8052, Merck Life Science), 100 U/mL penicillin and 100 mg/mL streptomycin).

Anti-β-Actin mouse monoclonal antibody (Catalog number A5441, Sigma-Aldrich, St. Louis, MO, USA), dilution 1:10,000; anti-vimentin mouse monoclonal antibody (Catalog number sc-32322, Santa Cruz Biotechnology, Dallas, TX, USA), dilution 1:2000; Anti-P Src (Tyr416) rabbit polyclonal antibody (Catalog number 2101, Cell Signaling Technology®, Danvers, MA, USA), dilution 1:1000; Anti-Src rabbit polyclonal antibody (Catalog number 2109, Cell Signaling Technology®), dilution 1:1000. Unless specified, all reagents were from Merck Life Science. Stocks used: 0.9 M 2-Deoxy-D-glucose (2-DG) in assay medium; 2.5 mM antimycin A in DMSO; 10 mM etomoxir in sterile water; 25 mM carbonyl cyanide *p*-trifluoromethoxyphenylhydrazone (FCCP) in DMSO; 1 M H₂O₂; 1 M metformin in assay medium; 2.5 mM oligomycin A in DMSO; 2.5 mM rotenone in DMSO; 20 mM UK5099 in DMSO.

2.2. Cell Proliferation and Viability Assays

Cell proliferation under H₂O₂ treatment was analyzed by growth kinetics: 3.8 × 10⁵ cells were plated in 6-well plates with 2 mL of standard medium and incubated at 37 °C and 5% CO₂. After 18 h medium was changed and cells were exposed to different perturbed conditions (medium containing different concentrations of H₂O₂; 0–50 mM). At different time points the viable cell number was counted using Trypan-Blue exclusion method.

Cell viability under etomoxir treatment was analyzed by an MTT assay: 5 × 10³ cells were plated in 96-well plates in 50 µL of standard medium and incubated at 37 °C and 5% CO₂. The day after 50 µL of medium supplemented with 2× serial dilutions of etomoxir or vehicle was added to the wells. 72 h after treatment, 20 µL of MTT formazan (20 mg/mL in isopropanol) was added to the culture media. After 1 h of incubation at 37 °C, the medium was gently removed and cells were suspended in 100 µL DMSO and then absorbance at 570 nm was recorded by using a Victor Multilabel Plate Reader (Perkin-Elmer, Waltham, MA, USA). The viability of cells treated with increasing concentrations of drugs was tested relative to the viability of the same cells treated with vehicle.

Cell proliferation in response to metabolic targeting was analyzed by growth kinetics: 2.1 × 10⁴ cells were plated in Cell Imaging 24-well Plates in 500 µL of experimental medium at 37 °C and 5% CO₂. After 24 h medium was changed, and cells were exposed to experimental medium containing dose-response concentrations of selected drugs (2DG 0-0.5-5-15 mM, metformin 0-1-5-10-20 mM).

Cell growth was monitored through imaging acquisitions every 24 h using Operetta CLS™ high-content analysis system in brightfield using 10× magnification. After 72 h cells were stained with Hoechst 33342 (working concentration 1 µg/mL incubated for 15 min at 37 °C and 5% CO₂) and imaging acquisitions were made using Operetta CLS™ with 10× magnification in brightfield and widefield fluorescence microscopy. Total cell count (nuclei positive for Hoechst 33342) was obtained using the Harmony software.

2.3. Wound Healing Assay

Cell migratory capacity was evaluated with wound healing assay. 10⁵ cells were plated in Cell Imaging 24-well Plates in 500 µL of experimental medium at 37 °C and 5% CO₂. As an adherent confluent monolayer formed, cells were stained using CellTracker™ Red CMTPX Dye 5 µM (C34552, stock 10 mM in DMSO, Invitrogen™-Thermo Fisher Scientific), according to the supplier's instructions, to track cell movements. Cell starvation lasting 8 h, with FBS-free experimental medium, was performed to stop cell proliferation. At the end of starvation protocol, pre-wound images of the entire well were acquired using Operetta CLS™ using 10× magnification in brightfield and widefield fluorescence microscopy to detect CellTracker. Next, a wound was made by scratching the monolayer cells with a sterile 10 µL pipette tip, and, after washing, the medium was changed to 0.1% FBS experimental medium containing dose-response concentrations of selected drugs (2DG 0-0.5-5-15 mM, metformin 0-1-5-10 mM). Wound coverage was monitored with automatized time-lapse imaging acquisition using Operetta CLS™, acquiring every entire well of the 24-well plate, both in brightfield and widefield fluorescence microscopy, using 10× magnification, every 35 min (time of acquisition of the entire plate) for 40 h with monitored temperature (37 °C) and atmosphere (5% CO₂). Evaluation of drug-dependent wound coverage was obtained using the Harmony software.

2.4. Sphere Formation Assays

Sphere formation was evaluated using different cell growth supports: 6-well plates not treated for cell adhesion, 6-well cell-repellent plates and Cell Imaging 24-well Plates coated with Poly(2-hydroxyethyl methacrylate) (Poly-HEMA, Merck Life Science). 4 × 10⁵ cells in 6-well and 1.5 × 10⁵ cells in 24-well were seeded in 3D experimental medium and sphere formation was monitored every 24 h with phase contrast microscopy and with Operetta CLS™, respectively, until the endpoint (72 h). We monitored sphere formation with imaging analysis. 4 × 10⁴ cells were seeded on CellCarrier-96 ULA Ultra Microplates 96-well (PerkinElmer) pre-stained with CellTracker™ Red CMTPX Dye 5 µM (Invitrogen™-Thermo Fisher Scientific). Assay was performed in 200 µL 3D experimental medium containing dose-response concentrations of selected drugs (2DG 0-0.5-5-15 mM, metformin 0-1-5-10-20 mM). Sphere morphology was monitored through imaging acquisitions of every complete well every 24 h, for 72 h, using Operetta CLS™, both in brightfield and widefield fluorescence microscopy with 10× magnification. We analyzed sphere formation using the Harmony software.

2.5. Metabolic Profiling by Seahorse Assays

Bioenergetic parameters of RT112 and 5637 cells under standard and nutritionally perturbed growth conditions were measured with the Seahorse Extracellular Flux XF24 and XFe96 analyzers (Agilent, Santa Clara, CA, USA; <https://www.agilent.com/en/products/cell-analysis/how-seahorse-xf-analyzers-work>). *XF Glycolysis stress test*, *Mitochondrial stress test*, and *Palmitate-BSA Fatty Acid Oxidation assay kit* protocols (Agilent) were performed using the XF24 analyzer, while *ATP rate assay* and *Mitochondrial Fuel Flex test kit* protocols (Agilent) were performed with the XFe96 analyzer, according to the manufacturer's instructions. Briefly cells were seeded in Seahorse XF plates at a density of 5 × 10⁴ (XF24) or 4 × 10⁴ (XFe96) cells per well and cultured for 24 h. The next day medium was replaced with low buffered XF assay medium (103575-100 Agilent), supplemented with 10 mM glucose, unless otherwise specified, and 2 mM glutamine and cell cultures were allowed to equilibrate for 1 h at 37 °C in a no-CO₂ incubator. Seahorse XF analysis was performed at 37 °C simultaneously measuring Oxygen Consumption Rate (OCR = pmole O₂/min) and ExtraCellular

Acidification Rate (ECAR = mpH/min). The XFe96 analyzer allows also measuring the Proton Efflux Rate (PER = pmolesH⁺/min). At the end of the analysis performed in XF24 plates, the medium was removed, cells were gently washed with PBS, suspended in JS lysis buffer and scraped after two freezing and thawing cycles. The protein content of cell lysates was measured by Bradford assay and used to normalize respiratory and glycolytic parameters. Subsequently these parameters were normalized on cell number, taking into consideration the protein content per cell. For the assays in XFe96 format, at the end of the Seahorse measurements, Hoechst 33342 was added to each well at the final working concentration of 1 µg/mL and after 15 min incubation nuclei/well were imaged and counted by Operetta CLS™ software Harmony, and directly used to normalize the Seahorse parameters per cell number. Samples were analyzed with at least 10 technical replicates. Data derive from two independent experiments.

2.5.1. XF Cell Mitochondrial Stress Test

This assay was performed to determine the mitochondrial bioenergetics. Oxygen Consumption Rate was analyzed under basal condition and after the treatment with different drugs including the ATP synthase inhibitor oligomycin A (optimal dose chosen after dose-response optimization assay: 0.125–2 µM oligomycin A), an ETC accelerator ionophore (optimal dose chosen after dose-response optimization assay: 0.25–4 µM FCCP), and an ETC inhibitors mixture (1 µM rotenone and 1 µM antimycin A). The response to the minimal dose of oligomycin A and FCCP, generating the maximal effect, accounts for non-phosphorylating mitochondrial respiration and maximal FCCP-uncoupled respiration, respectively. The response to the rotenone and antimycin A mixture accounts for non-mitochondrial oxygen consumption. Respiratory parameters were elaborated using the following formulas:

$$\text{Basal Mitochondrial Respiration (Basal-MR)} = \text{OCR}_{\text{basal}} - \text{OCR}_{\text{rot/ant}}$$

$$\text{Non-Phosphorylating Mitochondrial Respiration (oligo-NPMR)} = \text{OCR}_{\text{oligo}} - \text{OCR}_{\text{rot/ant}}$$

$$\text{FCCP-uncoupled Mitochondrial Respiration (FCCP-MR)} = \text{OCR}_{\text{FCCP}} - \text{OCR}_{\text{rot/ant}}$$

$$\text{Sare respiratory capacity} = \text{OCR}_{\text{FCCP}} - \text{OCR}_{\text{rot/ant}} / \text{OCR}_{\text{basal}} - \text{OCR}_{\text{rot/ant}}$$

$$\text{Coupling efficiency} = 1 - (\text{OCR}_{\text{oligo}} - \text{OCR}_{\text{rot/ant}}) / (\text{OCR}_{\text{basal}} - \text{OCR}_{\text{rot/ant}})$$

2.5.2. XF Glycolysis Stress Test

This assay was performed to determine the glycolytic bioenergetics. Extracellular acidification was analyzed in glucose-free-medium before and after the sequential injections of 10 mM glucose, oligomycin A (optimal dose chosen after dose-response optimization assay: 0.125–2 µM oligomycin A), and 50 mM 2-Deoxy-D-glucose (2-DG), a glycolysis inhibitor. The response to the minimum dose generating the maximal effect of oligomycin A accounts for glycolytic capacity. The response to 2-DG accounts for non-glycolytic extracellular acidification. Data were elaborated using the following formulas:

$$\text{Basal glycolysis} = \text{ECAR}_{\text{glc}} - \text{ECAR}_{\text{2-DG}}$$

$$\text{Glycolytic capacity} = \text{ECAR}_{\text{oligo}} - \text{ECAR}_{\text{2-DG}}$$

$$\text{Glycolytic reserve} = \text{ECAR}_{\text{oligo}} - \text{ECAR}_{\text{glc}}$$

2.5.3. XF ATP Rate Assay

This assay measures OXPHOS and glycolysis's contribution to ATP production. This assay was performed under standard and 2 h glucose deprivation. OCR and acidification were measured before and after sequential injection of 1.5 µM oligomycin A and 0.5 µM rotenone/antimycin A. Data were assessed with XF Wave Software (Seahorse Bioscience, Agilent).

2.5.4. XF Palmitate-BSA FAO Assay

Fatty Acid Oxidation (FAO) of RT112 and 5637 cells were analyzed using the XF Palmitate-BSA FAO Substrate, namely 1 mM palmitate, a long chain fatty acid, conjugated to 0.17 mM BSA (6:1 palmitate:BSA ratio). For the FAO assay 3.5×10^5 cells were seeded in 100 μ L of the standard medium onto Seahorse XF24-well plates and incubated at 37 °C and 5% CO₂. After 24 h, medium was replaced with substrate-limited medium (DMEM medium supplemented with 0.5 mM glucose, 1 mM glutamine, 0.5 mM carnitine and 1% FBS, 5 mM Hepes pH 7.4) and cells were incubated at 37 °C, and 5% CO₂. After 24 h (45 min before XF analysis), the medium was replaced with FAO-assay medium (KHB supplemented with 5 mM glucose, 0.5 mM glutamine, 0.5 mM carnitine and 5 mM Hepes pH 7.4) and cell cultures were allowed to equilibrate for 1 h at 37 °C in a no-CO₂ incubator. After 30 min (15 min before XF analysis) 40 μ M etomoxir or vehicle was added to appropriate wells on the microplate, and just before initiating XF analysis 220 μ M palmitate-BSA or BSA was added to appropriate wells on the microplate. In summary we tested four different conditions for each XF FAO assay:

- (1) BSA-Eto (BSA control without etomoxir) accounting for total respiration, including that one deriving from endogenous fatty acids oxidation;
- (2) BSA+Eto (BSA control with etomoxir) accounting for respiration not depending on endogenous fatty acids oxidation;
- (3) Palm:BSA-Eto (palmitate-BSA without etomoxir) accounting for total respiration, including that one deriving from exogenous fatty acids oxidation;
- (4) Palm:BSA+Eto (palmitate-BSA with etomoxir) accounting for respiration not depending on exogenous fatty acids oxidation.

2.5.5. XF Mitochondrial Fuel Flex Test

This assay was performed to measure the dependency, capacity and flexibility of cells to oxidize three critical mitochondrial fuels—glucose, glutamine and fatty acids. The assay was performed in an XF assay medium containing 10 mM glucose, 2 mM glutamine and 1 mM Na-pyruvate. Cells were exposed to BPTES (3 μ M), etomoxir (4 μ M) or UK5099 (2 μ M) in succession and OCR was measured before and after injection of each compound. Data were assessed with XF Wave Software (Seahorse Bioscience, Agilent).

2.6. Flow Cytometry

For FACS analysis 1×10^6 cells were plated in 6-well plates with 2 mL of experimental medium and incubated overnight at 37 °C and 5% CO₂. Cells were then stained with different dyes, as described below, before or after treatment with trypsin-EDTA following dye and antibody protocols and the supplier's recommendations, suspended in PBS supplemented with 0.2% BSA and acquired by CytoFlex S (Beckman Coulter, Brea, CA, USA). Data were elaborated using CytExpert 2.0 software (Beckman Coulter).

To evaluate mitochondrial membrane potential and mass cells were stained with 100 nM MitoTracker™ Red CMXRos (Invitrogen™ Thermo Fisher Scientific, 1 mM stock in DMSO) and 25 nM MitoTracker™ Green FM (Invitrogen™ Thermo Fisher Scientific, 1 mM stock in DMSO), respectively, in FBS-free medium for 20 min at 37 °C and 5% CO₂.

To evaluate mitochondrial and intracellular ROS, cells were stained with 5 μ M MitoSOX™ Red Mitochondrial Superoxide Indicator (MitoSOX, Invitrogen™ Thermo Fisher Scientific, 5 mM stock in DMSO), and 10 mM 2',7'-dichlorodihydrofluoresceine diacetate (H2DCFDA Merck Life Science, 5 mM stock in ethanol), respectively, in FBS-free medium for 30 min at 37 °C and 5% CO₂. According to fluorescence panel necessity, dead cells were excluded from analysis using viability dyes 7-aminoactinomycin D (Thermo Fisher Scientific) or LIVE/DEAD™ Fixable Green Dead Cell Stain (Thermo Fisher Scientific). Cell staining was performed according to supplier's instruction.

To evaluate stemness, cells were stained as single cell suspension with conjugated antibody CD44-APC (cod. 17-0441-82 eBioscience™, San Diego, CA, USA), CD133-PE (cod. 12-1338-42

eBioscience™), and Aldefluor, Stem Cell Identification Kit (STEMCELL Technologies™, Vancouver, BC, Canada) according to supplier's protocol. Dead cells were excluded from analysis using viability dyes 7-aminoactinomycin D.

Data were expressed as Median Fluorescence Intensity (MFI) of labeled living cells corrected for MFI of unlabeled living cells' autofluorescence.

2.7. Imaging

Analysis of mitochondrial machinery and redox status was performed by high-resolution imaging.

2.7.1. High-resolution Imaging for Quantitative Analysis

Cells (6.5×10^4) were seeded per well on Cell Imaging 24-well Plates, incubated overnight at 37 °C and 5% CO₂. The day after cells were stained with selected dye, then gently washed with phenol red-free medium and promptly analyzed in the experimental medium using Operetta CLS™, with confocal imaging set-up and 63× magnification. To evaluate mitochondrial membrane potential and mass, cells were stained with 100 nM MitoTracker™ Red CMXRos and 25 nM MitoTracker™ Green FM, respectively, for 20 min at 37 °C and 5% CO₂.

To evaluate mitochondrial ROS, intracellular ROS and lipid oxidation status, cells were stained with 3 μM MitoSOX (5 mM stock in DMSO), 10 μM H2DCFDA (20 mM stock in DMSO) and 10 μM BODIPY™ 581/591 C11 (Lipid Peroxidation Sensor, Invitrogen™ Thermo Fisher Scientific, 20 mM stock in DMSO), respectively, for 25, 10, and 30 min at 37 °C and 5% CO₂. Following imaging acquisition of selected dye, cells were stained with Hoechst 33342 (1 μg/mL incubated for 15 min at 37 °C and 5% CO₂) and further imaging acquisitions were made using Operetta CLS™ with 63× magnification with the confocal set-up. Dye quantitative analysis and total cell count (nuclei positive for Hoechst 33342) were obtained using Harmony software (as schematized in Supplementary Figure S1D–F).

To analyze mitochondrial mass, we plated 1.2×10^4 cells in CellCarrier-96 Ultra Microplates 96-well (PerkinElmer) and incubated at 37 °C and 5% CO₂ overnight. The day after, cells were transiently transfected using Lipofectamine reagent (Invitrogen, Carlsbad, CA, USA), according to the manufacturer's instruction, with 1.0 μg of pEYFP-mito vector expressing the mitochondrially targeted yellow fluorescent protein MitoYFP (Clontech, Mountain View, CA, USA). After 48 h, cells were stained with Hoechst 33342 (working concentration 1 μg/mL incubated for 15 min at 37 °C and 5% CO₂) and imaging acquisitions were made using Operetta CLS™ with 63× magnification with the confocal set-up. Quantitative analysis and total cell count (nuclei positive for Hoechst 33342) were obtained using the Harmony software.

For cell area measurements, 6.5×10^4 cells were seeded per well on Cell Imaging 24-well Plates, incubated overnight at 37 °C and 5% CO₂. The day after cells were stained using Vybrant™ DiI Cell-Labeling Solution 5 μM (V22885, stock solution 1 mM, Invitrogen™-Thermo Fisher Scientific) according to supplier's instruction, then analyzed in the experimental medium using Operetta CLS™ with confocal imaging set-up and 63× magnification. Cell area was obtained using the Harmony software.

2.7.2. High-resolution Imaging with Manually Operated Confocal Microscopy

To analyze SOX2 expression in cells grown as monolayers or spheroids, cells were seeded in different 6-well plates: 1×10^5 cells for RT112 cells and 1.2×10^5 cells for 5637 cells in tissue culture-treated plates in 2 mL 2D experimental medium and 4×10^5 cells for both RT112 and 5637 cells in not-treated and cell repellent plates in 2 mL 3D experimental medium and incubated at 37 °C and 5% CO₂. Sphere formation was monitored every 24 h with phase contrast microscopy until endpoint (72 h). Adherent cells were harvested by trypsinization and spheres were dissociated. Cells were seeded at subconfluent concentration on 13 mm microscopy slides and incubated at 37 °C, 5% CO₂ for 24 h. Cells were fixed in two passages with progressive higher concentration of paraformaldehyde at room

temperature. After washing with PBS, blocking solution (PBS 1×, 10% normal goat serum (NGS), 0.2% Triton X) was added, incubation lasted for 1 h and 30 min at room temperature. Incubation with primary antibody 1:100 in PBS 1×, NGS 10% was performed overnight at 4 °C (anti-h/mSOX2 MAB2018 Clone 245610 R&D Systems, Minneapolis, MN, USA). After washing with PBS, each slide was incubated with secondary antibody 1:1000 (anti-mouse IgG2a conjugated PE) in the same buffer for 45 min at room temperature in an obscured chamber. Cells were stained with Hoechst 33342 (0.5 µg/mL incubated for 15 min at RT and 5% CO₂) and image acquisitions were made using an A1R confocal microscope (Nikon, Tokyo, Japan) with 40× magnification.

For high resolution imaging of mitochondrial machinery, 2×10^4 cells were plated in 10 compartment CellView culture slide with glass bottom (GreinerBioOne, Kremsmünster, Austria) and incubated overnight at 37 °C and 5% CO₂. Afterward, cells were stained as previously described with MitoTracker™ Green FM and MitoTracker™ Red CMXRos and analyzed by live imaging confocal microscopy with a Nikon A1R confocal microscope for 48 h with 63× magnification.

For analysis of mitochondrial network morphology, 2.5×10^5 cells were plated in Cellview cell culture dishes with glass bottom (Greiner BioOne) and incubated at 37 °C and 5% CO₂ overnight. The day after, cells were transiently transfected using Lipofectamine reagent (Invitrogen), according to the manufacturer's instruction, with 1 µg of pEYFP-Mito vector. Forty-eight h after transfection cells were stained with Hoechst 33342 (1 µg/mL incubated for 15 min at 37 °C and 5% CO₂) and analyzed by live imaging with a Nikon A1R confocal microscope with 100× magnification.

2.8. RNA Extraction and qRT-PCR

Total RNA from bladder cancer cells was extracted using TRIzol LS Reagent (Invitrogen) according to the manufacturer's recommended protocols. The total RNA quantity was assessed using a Nanodrop spectrophotometer (ND-1000, Nanodrop, Labtech International, Uckfield, UK). Each RNA sample was then retrotranscribed with High Capacity cDNA Reverse Transcription Kit (Applied Biosystems, Foster City, CA, USA). A calibration curve was performed for each gene of interest to test primers and to determine the correct concentration of cDNA to be used for quantitative real time PCR. Reactions were run on an ABI 7000 Real Time PCR system (Applied Biosystems). Primers were purchased from Eurofins (Luxembourg). ATP5A1, ATP5B1, ALDH3A1, GAPDH, LDHA, PKM1 and PKM2 expression levels (indicated as "fold change") were analyzed in triplicate, normalized to HPRT1 and calculated according to the CT method. Primers used: ATP5A1F 5'-CATTGGTGATGGTATTGCGC-3'; ATP5A1R 5'-TCCCAAACA CGACAACCTCC-3'; ATP5B1F 5'-CCGTGAGGGCAATGATTTATAC-3'; ATP5B1R 5'-GTCAAAC CAGTCAGAGCTACC-3'; ALDH3A1-F 5'-GCAGACCTGCACAAGAATGA-3' ALDH3A1-R 5'-TGTAGAGCTCGTCTGCTGA-3'; GAPDH-F 5'-GGACTCATGACCACAGTCCA-3'; GAPDH-R 5'-CCAGTAGAGGCAGGGATGAT-3'; LDHA-F5'-AGCCCGATTCCGTTACCT-3', LDHA-R 5'-CA CCAGCAACATTCATTCCA-3'; PKM1-F5'-ACCGCAAGCTGTTTGAAGAA-3', PKM1-R 5'-TCCA TGAGGTCTGTGGAGTG-3'; PKM2-F 5'-ATCGTCCTACCAAGTCTGG-3', PKM2-F 5'-GAAG ATGCCACGGTACAGGT-3'; HPRT1-F 5'-TGCAGACTTGCTTTCCTTG-3', HPRT1-R 5'-CTGGCT TATATCCAACACTTCG-3'.

2.9. Protein Content, Western Blotting

To determine the cell size of RT112 and 5637 cells, we measured the protein content by Bradford assay (Bio-Rad, Hercules, CA, USA) on cell lysates obtained from 1×10^6 cells harvested by trypsinization, gently washed in PBS, suspended in lysis buffer (50 mM Tris-HCl pH 7.4, 5 mM EDTA, 1 mM EGTA, 10 mM 2-mercaptoethanol), and subjected to three freeze and thaw cycles. For western blotting analysis, 1×10^6 cells were seeded in p100 plates in complete medium and incubated overnight for the attachment. After 24h cells were washed with phosphate buffer saline without calcium and magnesium (PBS), scraped and lysed in lysis buffer supplemented with protease and phosphatase inhibitors. Proteins quantification was performed using BIO-RAD BCA Protein Assay Kit. Cellular lysates (10–30 µg proteins) were resuspended in Sample Buffer with β-mercaptoethanol (312.5 mM Tris-HCl pH 6.8, 10% SDS, 50% glycerol, 25% β-mercaptoethanol and 0.01% bromophenol

blue) and analyzed by SDS-PAGE. After electrophoresis, proteins were transferred to nitrocellulose membrane by electroblotting. The membrane was incubated 1 h or overnight with 5% nonfat milk in Tris Buffered Saline supplemented with Tween 20 (TBS-T): 10 mM Tris, pH 8.0, 150 mM NaCl, 0.1% Tween 20. Membranes were probed with specific antibodies for 1 h or overnight. Blots were washed with TBS-T for three times and incubated with ECL (Amersham ECL Prime Western Blotting Detection Reagent, GE Healthcare UK, Little Chalfont, UK) according to the manufacturer's protocols. Bands were analyzed with the ImageJ software.

2.10. Statistical analysis

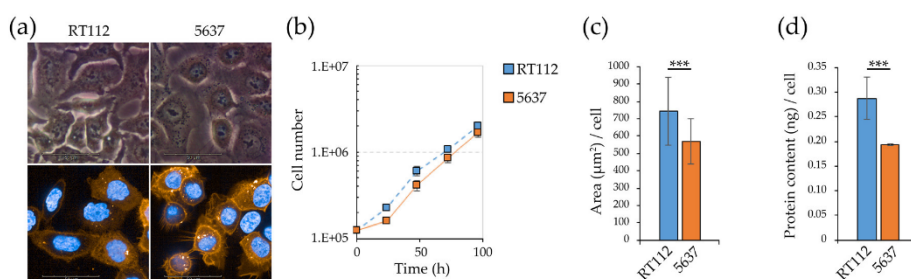
Unless specified otherwise, all experiments were carried out at least in triplicate. The number of technical replicates within each experiment is reported in the Results section. Results were expressed as means \pm standard deviation and variables were compared using unpaired Student's *t*-test or general linear model according to their distribution. A *p*-value < 0.05 was considered statistically significant. All statistical analyses were performed using GraphPad version 6 (GraphPad Software, Inc., San Diego, CA, USA) software.

3. Results

3.1. Morphofunctional Features of RT112 and 5637 Grade 2 Bladder Cancer Cells

RT112 and 5637 (Figure 1a) are bladder cancer cell lines, of the same histological Low Grade (G2). The two cell lines have a similar proliferation rate (Figure 1b), but RT112 cells are significantly larger, as shown by imaging data (average area in square micrometers, Figure 1c) and biochemical determination of the protein content/cell (Figure 1d).

A wound healing assay (Figure 1e,f, Supplementary Video 1) shows that 5637 cells present a significantly higher migration rate than RT112. Consistently, 5637—but not RT112—cells show a significant level of vimentin (Figure 1g), the main protein of intermediate filaments, a canonical marker of epithelial-mesenchymal transition (EMT) reprogramming, associated with the acquisition of migratory and invasive phenotype [45,46]. The increase in the migratory capacity of 5637 is also associated with a reduction in the Src kinase specific activity (here measured as the ratio between Y416-phosphorylated form and the total protein) (Figure 1h,i). This protein plays a key role in the process called “adhesion turnover”, consisting of the continuous formation of cellular matrix at the front pole of the cell and continue old cellular matrix disassembly at the rear [47]. The expression and activity of Src are inversely related to the migratory and metastatic capacity also in other bladder cancer cell lines [48].



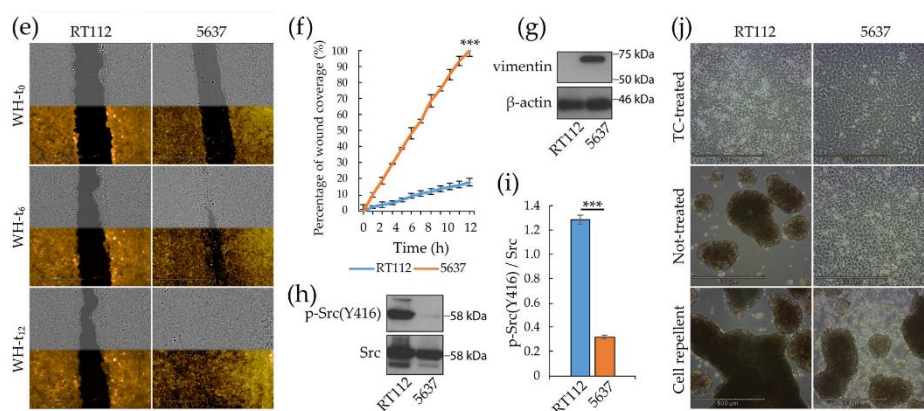


Figure 1. Morpho/functional readouts of RT112 and 5637 cells: proliferation rate, migration and spheroids formation capacity. (a) RT112 and 5637 cell morphology by phase contrast and confocal microscopy. For confocal microscopy cell membranes and nuclei were stained with fluorescent Vybrant™ DiI Cell-Labeling Solution (orange) and Hoechst 33342 (blue) dye respectively. (b) RT112 and 5637 cell growth curves in standard medium. Viable cells were counted by the Trypan-Blue exclusion method. (c) RT112 and 5637 average cell surface area measured as Vybrant™ fluorescent area using Harmony software. (d) RT112 and 5637 average protein content per cell measured by Bradford assay. (e) Representative wound healing assay images acquired by brightfield and fluorescence microscopy with Operetta CLS™ at 0 h, 6 h and 12 h after scratch (orange: CellTracker™ Red CMTPX Dye). (f) Percentage of wound coverage in wound healing assay through time (0–12 h), measured using Harmony software. (g,h) Western blot analysis for vimentin (g) and for Src and p-Src(Y416) (h) proteins in RT112 and 5637 cells. (i) p-Src(Y416)/Src ratio in RT112 and 5637 cells measured after densitometric analysis of Western Blot bands with ImageJ. (j) Spheroids formation assay in different supports: tissue culture treated (upper panels), not-treated (middle panels) and cell repellent supports (lower panels). Images were acquired in phase contrast light microscopy. Results are the mean of two (f) or three (b–d,i) experimental replicates. Statistical test: t-test and linear regression, *** for $p < 0.001$.

A significant difference in the RT112 and 5637 cell lines' adhesive properties is highlighted by the cells' different behavior when seeded on polystyrene plates not subjected to the tissue culture treatment, which makes them more hydrophilic, that we refer to as “not treated”. On these plates in serum-free medium, only RT112 cells form spheroids, while the 5637 cell line grows as a monolayer (Figure 1j). On cell repellent plates (in serum-free medium) both cell lines form spheroids. Compared to 5637, RT112 cells form a significantly higher number of spheroids (Supplementary Figure S2a,b), characterized by a significantly larger area (Supplementary Figure S2c).

Compared to RT112, monolayers of 5637 cells show higher levels of some markers of stemness, and invasiveness, typically linked to tumor malignancy [49,50], namely a higher positivity to the fluorescent dye Aldefluor™ (Figure 2a), a readout of the expression of ALDH1A1 [51,52], and in expression level of the transmembrane glycoprotein CD44 [53,54] (Figure 2b), but not of CD133 [55,56] (Figure 2c). In agreement with previous studies [57], spheroid growth in both lines is associated with increased expression and nuclear localization (activation) of the transcription factor SOX2 (Figure 2d), a member of the SRY-related HMG-box (SOX) family. SOX2 is a known marker of stemness not expressed in healthy urothelial cells and related to the presence of cancer stem cells (CSCs), also in bladder cancer [49].

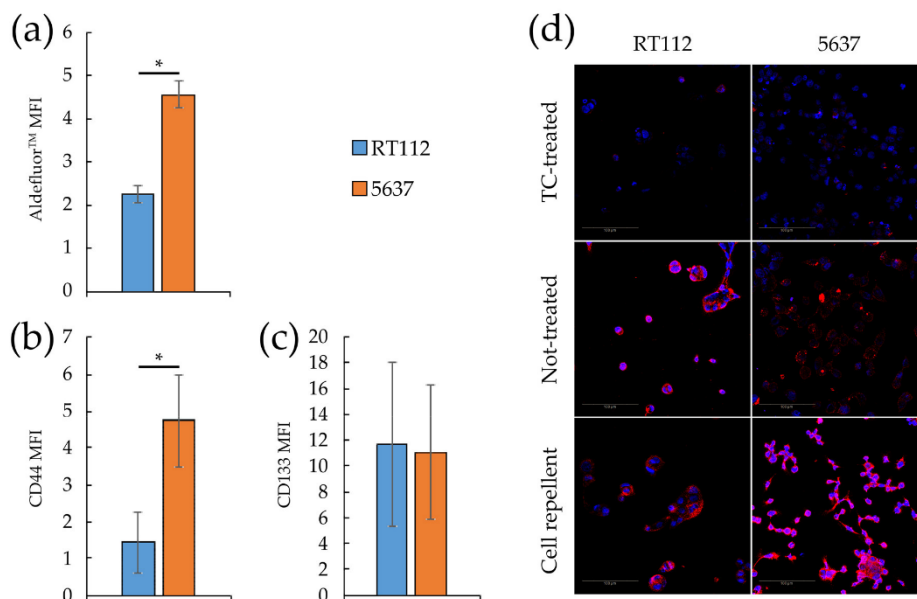


Figure 2. Stemness markers of monolayers and spheroids from RT112 and 5637 cells. (a–c) Median fluorescence intensity of Aldefluor™ (a), CD44 (b) and CD133 (c) by flow cytometry analysis on RT112 and 5637 cells grown as monolayers. Results are the mean of two (a) and three (b,c) experimental replicates. Statistical test: *t*-test, * for $p < 0.05$. (d) Representative images from confocal immunofluorescence (IF) microscopy of RT112 and 5637 cells using SOX2 Antibody (red) and Hoechst 33342 (blue) for nuclei. Cells were grown as monolayer or spheroids on different (Tissue culture-treated, Not-treated or Cell repellent) supports, before being seeded in adherent condition on chamber slides for IF.

3.2. Glycolytic and Mitochondrial Bioenergetics of RT112 and 5637 Grade 2 Bladder Cancer Cells

Metabolic rewiring is a hallmark of cancer [7,58], allowing cancer cells to meet their energy and biosynthetic needs to support enhanced cell growth and survival under nutrient-poor environmental conditions, not allowing survival or proliferation of normal cells.

The main metabolic routes contributing to the energy homeostasis are glycolysis and oxidative phosphorylation (OXPHOS), which couple the breakdown of nutrients as glucose, amino acids and fatty acids to ATP production. These two pathways also play a pivotal role in redox homeostasis since they contribute to producing the reducing power required for anabolic processes and for counteracting oxidative stress. The Seahorse Extracellular Flux Analyzer (Agilent) measures in real time the ExtraCellular Acidification Rate (ECAR) related to the excretion of lactate that in turn is strictly related to the glycolytic flux, and the Oxygen Consumption Rate (OCR), that is primarily due to mitochondrial respiration, in living cells [59]. The Seahorse XF Glycolysis Stress Test and Mitochondrial Stress Test protocols dissect the glycolytic and respiratory fluxes components into basal, maximal and reserve (spare) glycolytic or respiratory capacity through the consecutive addition of specific drugs, whose optimization is reported in Supplementary Figure S3a–c.

Seahorse analysis demonstrated that, compared to RT112, 5637 cells show a significant reduction in basal and maximal (i.e., oligomycin induced) glycolytic capacity as well as in glycolytic reserve (Figure 3a,c). Consistently, the levels of mRNAs encoding two key glycolytic enzymes are down-regulated in 5637 cells compared RT112: glyceraldehyde 3-phosphate dehydrogenase (GAPDH), responsible of the conversion of glyceraldehyde-3-phosphate to 1,3-biphosphoglycerate with the production of NADH and H^+ , and lactate dehydrogenase A (LDHA), that catalyzes fermentation of

pyruvate to lactate (Supplementary Figure S3d,e). The level of mRNAs encoding the M1 and M2 isoforms of pyruvate kinase M (PKM), that catalyzes the transfer of a phosphoryl group from phosphoenolpyruvate (PEP) to ADP generating ATP, are instead similar in both cell lines (isoform M2, associated with cancer) or higher in 5637 (isoform M1) (Supplementary Figure S3f,g). The physiological consequence of the PKM expression pattern is difficult to predict, since the sugar kinase activity of the enzyme is regulated by a complex interplay between allosteric activators and inhibitors [60,61].

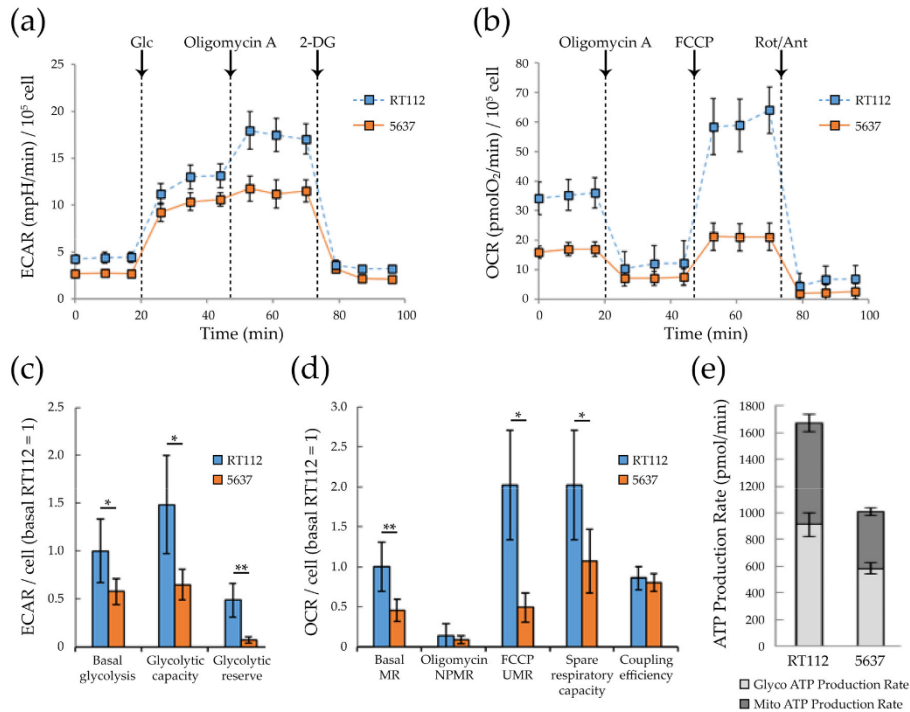


Figure 3. Glycolysis and respiratory bioenergetics of RT112 and 5637 cells. (a) Representative ExtraCellular Acidification Rate (ECAR) profile of monolayer cells subjected to XF Glycolysis Stress Test with XF24 Agilent Seahorse under sequential injections of 10 mM glucose, 0.25 μ M oligomycin A and 50 mM 2-deoxy-glucose (b) Representative Oxygen Consumption Rate (OCR) profile of monolayer cells subjected to XF Mito Stress Test with XF24 Agilent Seahorse under sequential injections of 0.25 μ M oligomycin A, 2 μ M FCCP and 1 μ M Rotenone + 1 μ M Antimycin A. ECAR and OCR values measured using XF24 Agilent Seahorse were normalized on protein content measured by Bradford assay. Data were further normalized per cell number, taking into consideration the protein content per cell (Figure 1d) (c) Glycolytic bioenergetic parameters measured from Seahorse results: basal glycolysis, glycolytic capacity and glycolytic reserve (d). Respiratory bioenergetics parameter measured from Seahorse results: basal mitochondrial respiration (MR), non-phosphorylating mitochondrial respiration (NPMPR) and FCCP-uncoupled respiration (UMR), spare respiratory capacity and coupling efficiency. (e) ATP production rates due to glycolysis or mitochondrial respiration as measured with XF Real-Time ATP rate assay using XFe96 Agilent Seahorse. Proton Efflux Rate (PER) and OCR values were normalized on cell number measured by counting Hoechst-positive nuclei with Operetta CLSTM and Harmony software. Statistical test: *t*-test, * for $p < 0.05$; ** for $p < 0.01$.

Compared to RT112, 5637 cells show a significantly reduced basal mitochondrial (MR, 2-fold reduction) and FCCP-uncoupled (UMR, 4-fold reduction) respiration (Figure 3b,d). Non-phosphorylating mitochondrial respiration (NPMR) is low and very similar in both cell lines, indicating that the enhanced basal mitochondrial respiration in RT112 is essentially devoted to ATP production. As expected, 5637 cells produce significantly less ATP than RT112 by mitochondrial respiration, and by glycolysis as well (Figure 3e).

We further analyzed mitochondrial morphology and function by confocal microscopy and high content analysis performed with Operetta CLS™. We first determined mitochondrial mass using either quantification of a transiently expressed mitochondrial-specific YFP protein (MitoYFP, Figure 4a,b) or staining with MitoTracker Green, a dye which localizes into mitochondria regardless of mitochondrial membrane potential [62] (Figure 4c,d). Quantification of both the MitoYFP-positive area/cell (Supplementary Figure S1a) and of the intensity of the MitoTracker Green signal/cell (Supplementary Figure S1b), suggests that 5637 cells have a higher mitochondrial mass compared to RT112.

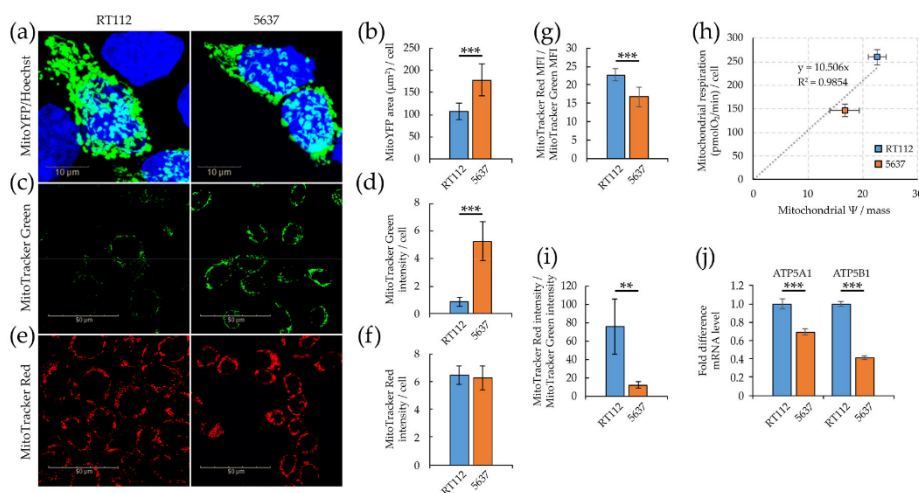


Figure 4. Mitochondrial efficiency of RT112 and 5637 cells. (a) Confocal imaging of fixed cells transiently transfected for the expression of the mitochondrial-specific MitoYFP protein (green), stained with Hoechst 33342 dye labeling nuclei (blue). (b) Mitochondrial area per cell quantified as the ratio of green (MitoYFP) fluorescent area to blue Hoechst-positive objects (nuclei) in manually selected 30–40 ROIs containing green positive cells. (c) Confocal imaging of living cells stained with mitochondrion-selective MitoTracker™ Green FM (green). (d) Mitochondrial mass per cell calculated as the ratio of MitoTracker™ green fluorescence intensity to blue Hoechst-positive objects (nuclei). (e) Confocal imaging of living cells stained with the potentiometric mitochondrion-selective MitoTracker™ Red CMXRos dye (red). (f) Mitochondrial membrane potential per cell calculated as the ratio of MitoTracker™ Red CMXRos fluorescence intensity to blue Hoechst-positive objects (nuclei). (g) Mitochondrial membrane potential per mitochondrial mass unit calculated as the ratio of the median fluorescence intensity of MitoTracker Red CMXRos per cell and the median fluorescence intensity of MitoTracker Green per cell by flow cytometry analysis. (h) Correlation between basal respiration OCR and mitochondrial membrane potential per mitochondrial mass unit measured by flow cytometry. (i) Mitochondrial membrane potential per mitochondrial mass unit calculated by quantitative imaging as the ratio of the Mitotracker Red and Green's fluorescence intensity per cell. (j) mRNA level by qRT-PCR of ATP5A1 and ATP5B1 genes normalized to the house-keeping HPRT-1 gene level. Quantitative imaging analysis was performed with Harmony software (b,d,f,i). All results are the mean of at least three experimental replicates. Statistical test: t-test, ** for $p < 0.01$; *** for $p < 0.001$.

We then investigated the mitochondrial membrane potential with MitoTracker Red, a potentiometric fluorescent red dye that accumulates into mitochondria depending on membrane potential, and mitochondrial activity [63]. MitoTracker Red intensity/cell is similar in the two cell lines (Figures 4e,f and S1c). The ratio between the MitoTracker Red and MitoTracker Green intensities determined by imaging (Figure 4i,) or the ratio between the median fluorescence intensities determined by FACS (Figure 4g) defines mitochondrial activity per unit of mitochondrial mass (*i.e.*, mitochondrial specific activity). Both measurements indicate that mitochondrial specific activity is higher in RT112 than in 5637 cells and well correlates with enhanced mitochondrial respiration measured by Seahorse flux analysis (basal OCR, Figure 3d), as reported in Figure 4h. In keeping with these data RT112 cells have higher expression level of two ATP synthase subunits, ATP5A1 and ATP5B1 (Figure 4j), and produce more ATP by mitochondrial respiration (Figure 3e).

3.3. Redox Homeostasis in RT112 and 5637 Cell Lines

Mitochondrial respiration is the primary source of cellular ROS and both cell lines under investigation are oxidative. Therefore, we analyzed mitochondrial and cytoplasmatic ROS levels by flow cytometry, and quantitative imaging (Operetta CLS™) on living cells stained with MitoSOX and 2',7'-dichlorofluorescein diacetate (H2DCFDA), respectively [64]. MitoSOX is a mitochondrion selective dye which is oxidized by superoxide but not by other reactive oxygen species (ROS) and reactive nitrogen species (RNS), while H2DCFDA is a fluorogenic dye that allow measuring hydroxyl, peroxy and other ROS species within the cell. After passive diffusion into cells, H2DCFDA is deacetylated by cellular esterases to the corresponding dichlorodihydrofluorescein derivative, whose ROS oxidation originates a fluorescent adduct, 2',7'-dichlorofluorescein (DCF), that remains trapped inside the cells. Quantitative imaging results, confirmed by flow cytometry analysis (Figure 5a–f), showed that although RT112 cells have a higher (30% more) content of mitochondrial superoxide than 5637, in keeping with their higher respiratory rate, they are characterized by a significantly lower total intracellular ROS level.

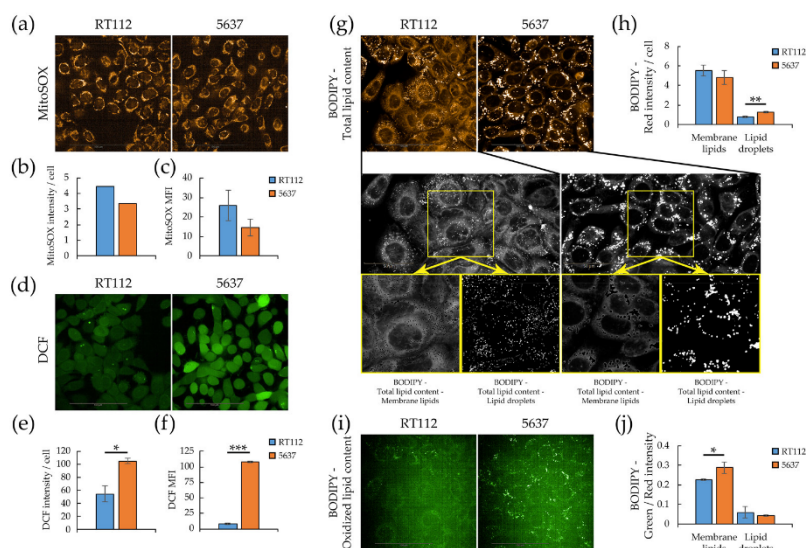


Figure 5. Redox homeostasis and lipid peroxidation in RT112 and 5637 cells. Quantitative imaging was performed with Operetta CLS™ and Harmony software (a) Confocal imaging of living cells stained with MitoSOX (orange). (b) Mitochondrial ROS level per cell calculated as the ratio of MitoSOX red fluorescence intensity to blue Hoechst-positive objects (nuclei) (c) MitoSOX median fluorescence intensity obtained by flow cytometry. (d) Confocal imaging of living cells stained with

2',7'-Dichlorofluorescein diacetate (green). (e) Total ROS level per cell calculated as the ratio of DCF green fluorescence intensity to blue Hoechst-positive objects (nuclei). (f) Total ROS level per cell obtained from DCF median fluorescence intensity obtained from flow cytometry. (g) Confocal imaging of red fluorescence of living cells stained with the Lipid Peroxidation Sensor BODIPYTM 581/591 C11 (orange, total lipid content, upper panels) and grayscale representative image as used for quantitative analysis of total lipid content (middle panels), membrane lipids and lipid droplets (lower panels). (h) Lipids per cell quantified as membrane lipids and lipid droplets measured using Harmony software. (i) Confocal imaging of green fluorescence of living cells stained with the Lipid Peroxidation Sensor BODIPYTM 581/591 C11 (green, oxidized lipid content). (j) Oxidized/total membrane lipids and lipid droplets ratio, calculated as the ratio of green to red fluorescence intensity. All results are the mean of at least three experimental replicates. Statistical test: *t*-test, * for $p < .05$; ** for $p < .01$; *** for $p < .001$.

Since high ROS concentrations lead to free radical mediated chain reactions that indiscriminately target intracellular molecules, including polyunsaturated fatty acids of lipid membranes [65], we analyzed by confocal microscopy (Operetta CLSTM) lipid peroxidation using a ratio-fluorescence assay on living cells stained with the oxidative sensitive C11-BODIPY581-591 dye [66]. This probe incorporates readily into cellular membranes and its fluorescence shifts from red to green upon oxidation. Figure 5g,i report confocal images of red and green fluorescence of RT112 and 5637 cells stained with C11-BODIPY581-591. It is possible to distinguish bright fluorescent spots corresponding to lipid droplets, and a diffuse fluorescence corresponding to membrane lipid content. The bottom part of the same panel reports an enlarged, grayscale version of the images to highlight the quantification procedure. Although 5637 and RT112 have a similar total lipid content, quantitative imaging shows that 5637 have a slightly lower membrane lipid content and a lower number of significantly larger and denser lipid droplets on a cellular basis (Figures 5h and S4a,b). In contrast, 5637 show higher oxidation of membrane lipids (diffuse green fluorescence). The two cell lines show no significant difference in lipid droplets' oxidation (Figures 5j and S4c,d). In keeping with the higher ROS and peroxidized lipids levels, 5637 cells are more sensitive to oxidative stress, namely H₂O₂ treatment (Supplementary Figure S4g).

3.4. Metabolic Plasticity in RT112 and 5637 Cell Lines

As highlighted by the Seahorse experiments described above (Figure 3b,d), RT112 cells are more energetic than 5637, having a more efficient glycolytic and mitochondrial apparatus both for the production of energy in basal conditions, and for responding to eventual energy stress (greater glycolytic reserve, and spare respiratory capacity, or nutrient perturbation). Consistently, when exposed to glucose deprivation (blocking glycolysis) the RT112 cells increase the mitochondrial respiration more effectively compared to 5637. The reduced plasticity of 5637 is appreciable in Figure 6a which reports the two lines' energy phenotype under basal (in presence or absence of glucose) and maximal conditions (oligomycin-induced glycolysis, and FCCP-uncoupled respiration).

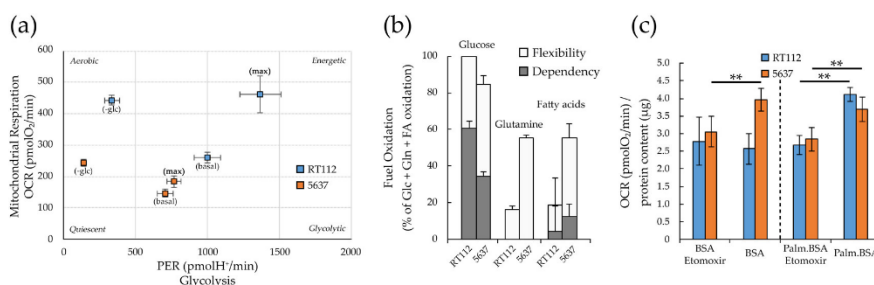


Figure 6. Glycolytic and respiratory capacity and nutrient usage in RT112 and 5637 cells. (a) PER and OCR values (attributable to glycolysis and oxidative phosphorylation respectively) in basal condition,

maximal capacity (reached with treatment with optimized concentration of oligomycin A for maximal glycolytic capacity or FCCP for maximal respiratory capacity) and under 5 h-glucose deprivation. Seahorse data were normalized on cell number measured after Hoechst 33342 staining as blue-positive objects acquired by Operetta CLS™ and counted using Harmony software. (b) The ability to oxidize three different nutrients (glucose, glutamine and fatty acids) reported as dependency and flexibility from XF Mito Fuel Flex Test performed using Agilent Seahorse XFe96 Analyzer. (c) OCR values measured in presence/absence of 5 μ M Etomoxir from XF Palmitate-BSA FAO Substrate assay using Agilent Seahorse XF24 Analyzer. OCR values were normalized on protein content measured by Bradford assay. All results are the mean of at least three experimental replicates. Statistical test: *t*-test, ** for $p < 0.01$.

To understand the two cell lines' ability and flexibility to oxidize different nutrients, we performed the Seahorse XF Mitochondrial Fuel Flex test (Figure 6b). The test showed that both cell lines strongly depend on glucose as a fuel for mitochondrial respiration, make limited use of fatty acids and no use of glutamine at all (dependency, gray bars). Both cell lines are flexible enough to increase allocation of glucose, glutamine and fatty acids for mitochondrial respiration (Flexibility, white bars).

Fatty acid oxidation into mitochondria provides twice as much ATP as carbohydrates on a dry mass basis. Indeed, energy-demanding tissues generally carried out fatty acid β -oxidation (FAO). Furthermore, several cancer cells are dependent on FAO for survival and growth, since it can eliminate potentially toxic lipids, inhibit pro-apoptotic pathways and provide metabolic intermediates for anaplerosis, besides providing ATP and NADPH, counteracting energy and oxidative stress [67].

We extended our studies dealing with energy homeostasis of RT112 and 5637 cells to FAO for these reasons. The Seahorse XF fatty acid β -oxidation (FAO) test assays the cells' capability to oxidize endogenous fatty acids and/or the long chain fatty acid palmitate, exogenously added in the culture medium. The share of respiration devoted to FAO can be calculated as the difference between the basal respiration and the residual respiration obtained after treatment with 40 μ M etomoxir, an irreversible inhibitor of carnitine palmitoyltransferase-1 (CPT1), which is a mitochondrial transporter required for FAO [68]. The FAO assay (Figure 6c) demonstrates that both cell lines can oxidize the exogenous palmitate, while only 5637 cells can also oxidize also the endogenous fatty acids.

3.5. Targeting Metabolism in RT112 and 5637 Cell Lines

The different assays reported above (Figure 5; Figure 6) indicate that both cell lines present, albeit with some differences, some kind of metabolic flexibility. Here we tested the pharmacological effect of the inhibition of glycolysis and OXPHOS on cell proliferation, migration and propensity to form spheroids. We used the non-hydrolyzable glucose analog 2-Deoxy-D-glucose (2-DG), to inhibit glycolysis, and metformin to inhibit, possibly indirectly, mitochondrial respiration [69–71].

Treatment with both 2-DG and metformin inhibits cell proliferation of both bladder cancer cell lines (Figure 7a,b). Compared to RT112, the 5637 cell line's proliferation was more sensitive to both 2-DG and metformin. This behavior could be due to the more remarkable metabolic plasticity of RT112 cells, which would improve resistance to the inhibition of any of the two energy pathways.

While metformin inhibits in a dose-dependent manner the already limited lateral migration of RT112, 2-DG does not inhibit migration of this cell line (Figure 7c). Indeed, 2-DG seems to paradoxically stimulate cell migration. Whether this is caused by the enhanced metabolic flexibility of RT112 cells or by the short timeframe of this experiment (12 h compared to the 72 h used in the cell proliferation and spheroid formation assays), remains to be seen. Treatments with both metformin and 2DG significantly reduce the migratory capacity of 5637 (Figure 7d).

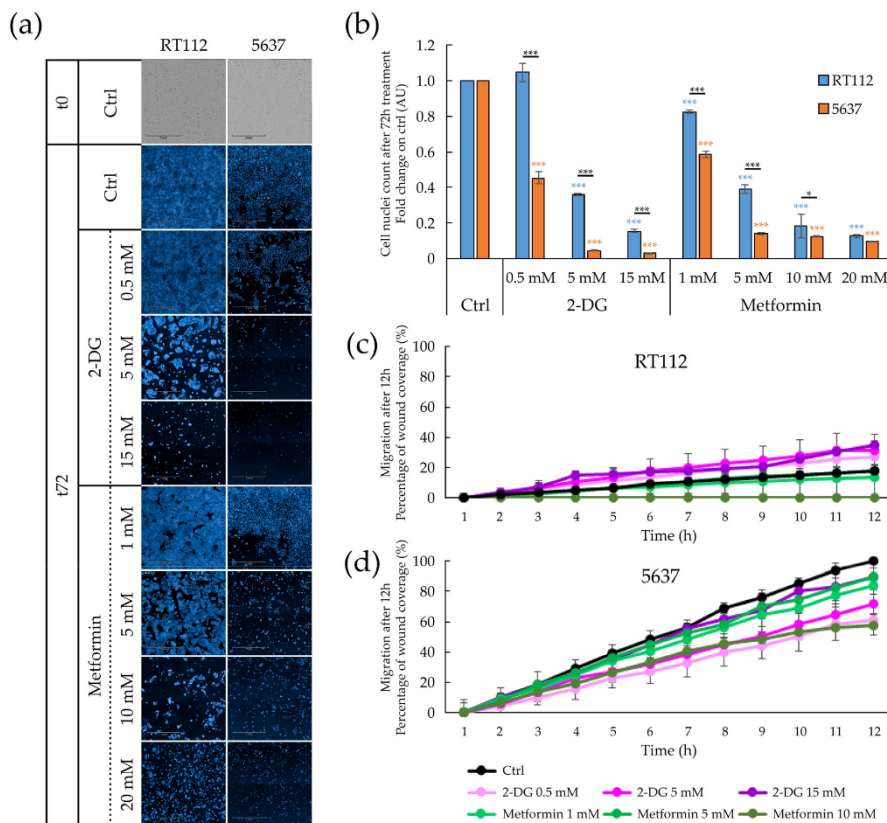


Figure 7. Effect of pharmacological treatment on proliferation and migratory capacity of RT112 and 5637 cells grown as adherent cells. **(a)** Representative images of brightfield (T0) and Hoechst 33342 stained nuclei acquired with Operetta CLS™ of adherent cells after 72 h-treatment with increasing concentration of 2-Deoxy-D-glucose (2-DG) (0, 0.5, 5, 15 mM) and metformin (0, 1, 5, 10, 20 mM). **(b)** Fold change relative to the control condition of nuclei count of cells treated for 72 h grown with 2-Deoxy-D-glucose (2-DG) and metformin treatment. Results are the mean of three experimental replicates. **(c,d)** Percentage of wound coverage in wound healing assay after 12 h-treatment condition of increasing concentration of 2-Deoxy-D-glucose (2-DG) (0, 0.5, 5, 15 mM) and metformin (0, 1, 5, 10 mM) of RT112 cells **(c)** and 5637 cells **(d)**. Results are the mean of two experimental replicates, except for 15 mM 2-DG and 10 mM metformin conditions performed in single replicate. Statistical test: t-test, * for $p < 0.05$; *** for $p < 0.001$.

Then we tested the effect of 2-DG and metformin on the ability of RT112 and 5637 to form spheroids from single cells in non-adherent conditions. Spheroid formation exploits features of cell progenitors or cancer stem cells (CSC), such as anchorage-independent growth, anoikis resistance and self-renewal [72,73]. Figure 8 and Supplementary Figure S5 show cell tracker-labeled spheroids at 0 and 72 h after seeding and during time course (24-48-72 h) respectively. Untreated spheroids (upper line) have a compact, regular, bright shape and may be surrounded by some cells, especially in the case of the 5637 cell line. The 2-DG treatment has little effect at the lowest tested concentration, while higher concentrations inhibit the development of a properly formed spheroid, originating less bright and more spread aggregates. The effect appears more potent in 5637 cells. A more substantial disruptive effect on the proper formation of spheroids is elicited by treatment with metformin, in keeping with literature data suggesting that spheroid formation is exquisitely dependent on

mitochondrial respiration [74–77]. The aggregates formed after both pharmacological perturbations by RT112 cells appear irregular than those formed by 5637 cells.

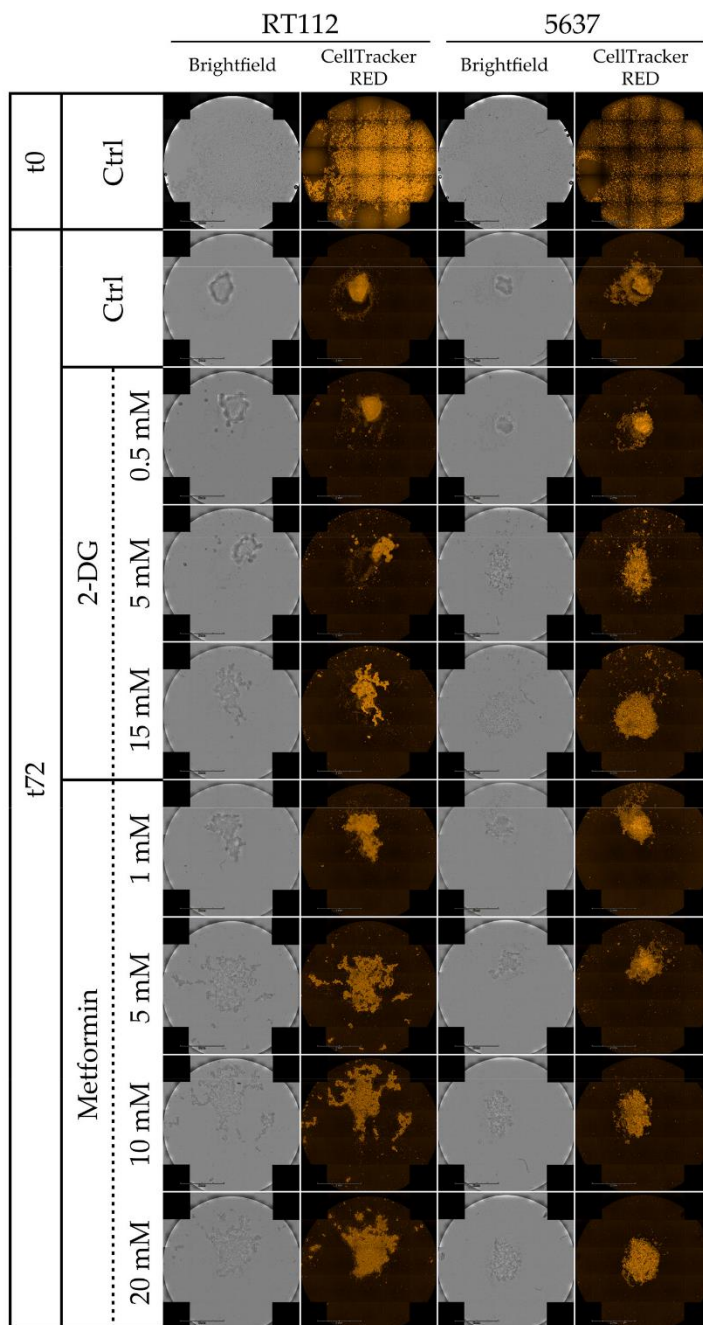


Figure 8. Spheroid formation under pharmacological treatment of RT112 and 5637 cells. Representative images from brightfield and fluorescence microscopy (orange: CellTracker™ Red CMTPX Dye) acquired with Operetta CLS™ at 0 h and 72 h of cells grown in cell repellent 96-well

plate under treatment with increasing concentration of 2-Deoxy-D-glucose (2-DG) (0, 0.5, 5, 15 mM) and metformin (0, 1, 5, 10, 20 mM).

4. Discussion

Bladder cancer ranks eleventh among the most diagnosed cancer globally. Nearly 90% of these cancers are urothelial carcinomas [78]. Early and accurate diagnostic staging and development of sensitive biomarkers are crucial for identifying the most aggressive cancers and developing appropriate therapeutic interventions. Metabolism is increasingly recognized as a driver in the development and maintenance of multifactorial diseases such as cancer [79,80]. Accordingly, detection and characterization of the metabolic footprint of bladder cancers [81,82] could be instrumental for both early diagnosis and therapy monitoring.

Fast cell growth, ability to move and to form 3D structures contribute to defining a cancer cell's aggressiveness. RT112 and 5637 cells are classified at the same histological low grade, but express molecular markers related to different aggressiveness. The two cell lines present a similar growth rate, but RT112 cells are significantly larger. RT112 form spheroids more efficiently, even on surfaces where 5637 do not form spheroids at all. Even on cell repellent plates, where both cell lines generate spheroids, RT112 form more spheroids with a larger size. In contrast, the 5637 cells migrate much faster (Figure 1 and video S1). This phenotypic trait is consistent with data that classify RT112 as luminal-like cells enriched in papillary architecture, [43,83,84], and 5637 as basal-like cells enriched for squamous differentiation, considered as models of non-aggressive and aggressive BCs, respectively [44,84,85].

Once characterized the cellular properties associated with spreading and tumor progression of RT112 and 5637, we analyzed their cellular bioenergetics, and nutrient usage in order to identify a potential fragility or dependency to be targeted with a pharmacological treatment.

Seahorse analysis showed that both cell lines can use glycolysis and respiration to produce ATP. However, the RT112 cell line is more energetic than 5637 with a higher basal respiration and glycolytic flux (Figure 6a), essentially due to a potentiated respiratory and glycolytic machinery.

Most cells exploit only a part of their total bioenergetic capacity, operating at a basal level and maintaining a reserve capacity for sudden surges in energy requirements due to stress or increased workload. Under standard growth conditions, 5637 cells use most of their glycolytic and respiratory potential, while RT112 cells have a large, unused glycolytic and respiratory reserve. Both cell lines respond to glucose deprivation by increasing respiration, possibly because glucose starvation unlocks the respiratory machinery. The increase in respiration is less striking in 5637 cells.

Mitochondria are both the source and target of reactive oxygen species (ROS), and damaged mitochondria can release more ROS [86,87]. In detail, about 1–2% O₂ uptaken by the mitochondria is reduced to superoxide anion radical and ROS as a byproduct of electron transport during oxidative phosphorylation, in particular through the activity of complex I (NADH dehydrogenase ubiquinone-ubiquinol reductase) [88] and complex III (ubiquinol cytochrome c reductase) [89]. Electron transport chain (ETC) generates ROS particularly when is slowed down by high mitochondrial membrane potential ($\Delta\psi_m$), or functions in reverse from complex II to complex I, as for ubiquinol excess produced in several mitochondrial metabolic pathways such as fatty acid β -oxidation or oxidation of α -glycerophosphate. ROS generation can also be attributed to the TCA cycle's specific dehydrogenases due to an increased NADH/NAD⁺ ratio.

Consistently with their higher respiratory rate, RT112 cells have higher levels of mitochondrial ROS. However, the total level of ROS is higher in 5637 cells. This can be due to a less efficient detoxification system, or poor supply of reducing equivalents required to maintain the antioxidant capacity of the glutathione system. The increased intracellular ROS level in 5637 cells correlates with increased lipid peroxidation. Lipid peroxidation produces highly-reactive aldehyde species, including 4-hydroxy 2-nonenal (4-HNE), considered second messengers of oxidative stress and playing a critical role in cell proliferation and survival, and thereby in cancer progression as reviewed in [90–92]. The aldehyde dehydrogenase ALDH3A1 acts as a specific scavenger for these fatty aldehydes [93,94]. RT-PCR analysis (Figure S4h) demonstrates that ALDH3A1 is not expressed in

5637, unlike RT112, indicating that the accumulation of peroxidized lipids could be associated with an ineffective detoxification system. 5637 cells are also more sensitive to H₂O₂-induced oxidative stress, suggesting a differential balance between ROS production and detoxification mechanisms in the two bladder cancer cell lines.

Metabolic plasticity is the ability to modulate the use of glycolysis and OXPHOS, to meet the energy and biosynthetic needs depending on the nutritional/environmental conditions, enabling the cancer cells to adapt to various microenvironmental conditions including hypoxia and acidosis. Although most cancer cells, according to the Warburg paradigm, internalize glucose faster and metabolize it via aerobic glycolysis to sustain active proliferation, they remain able to completely oxidize glucose, unless they display significant mitochondrial defects [95]. Indeed both glycolysis and respiration can be simultaneously turned on [9].

In addition to glucose-derived pyruvate, other nutrients provide substrates to the TCA cycle to support mitochondrial metabolism, including lactate and amino acids, i.e., glutamine, and fatty acids. Glucose appears the favorite respiratory substrate for both cell lines, although they can use glutamine and fatty acids when required. Contrary to RT112, the 5637 cell line appears able to use endogenous fatty acids. However, in keeping with the negligible contribution of fatty acids to mitochondria respiration in both cell lines (Figure 6b), *in vivo* administration of low concentrations of etomoxir [68,96,97]—that guarantee to avoid off-target effects reported at higher dosage [98] and that led to the stoppage of etomoxir clinical trials—does not significantly affect the viability of RT112 and 5637 monolayers (Supplementary Figure S4e,f).

While inhibition of either glycolysis (through treatment with the glucose analog 2-deoxyglucose (2-DG) or respiration (through metformin) results in general down-regulation of cell proliferation, cell migration and spheroid formation in both RT112 and 5637 cells, some difference is worth noting. RT112 cells are less sensitive than 5637 to the inhibitory effect of both drugs on proliferation and cell migration. 2-DG does not inhibit migration in RT112 cells. Migration results with this cell line should be taken cautiously, because of the extremely low migration rate. This overall lower sensitivity to metabolic perturbations is consistent with the more energetic phenotype of the RT112 cell line and its higher ability to cope with metabolic stress, as shown by Seahorse analysis (Figure 3). Metformin appears to inhibit spheroid formation more than 2-DG, in both cell lines. Consistently, recent data indicate that mitochondrial respiration is particularly important in metastatic/circulating cancer cells [99,100], in the development and maintenance of chemoresistance mechanisms [77], and in cancer stem cells [74,101,102], which are particularly enriched in 3D cellular structures, as spheroids.

5. Conclusions

In conclusion, our study highlights that two bladder cancer cell lines, established from primary urinary bladder carcinoma of the same histological grade, associated with different aggressiveness and prognoses, present distinct metabolic and invasive properties. Although both cell lines use both glycolysis and respiration to support energy production, RT112 cells present overall higher metabolic plasticity and a higher propensity to form 3D structures while being vastly less efficient in migration. Despite these differences, both cell lines have sizable respiration, and the metformin treatment gives a global down-regulation of the proliferation, migration, and the ability to form spheroids. This suggests that the targeted inhibition of energy metabolism may also be effective in a heterogeneous tumor context. Intriguingly, while RT112 are less sensitive than 5637 to pharmacological perturbation of cell proliferation and migration by 2-DG and metformin, they are more sensitive in the spheroid formation assay. These differences may be partially due to transcriptional rewiring and altered signaling and communication within the forming spheroid architecture. As the molecular and metabolic characterization of these cancers and derived cellular and animal [103] models increase, we will be able to design ever more effective single and combinatorial [104,105] anti-cancer regimens based on the detected metabolic fragilities. This ability appears particularly important for cancers of low histological grade, such as the Grade 2 bladder tumors, representing a critical therapeutic window for adjuvant or post-operative treatments to reduce the tumor mass or avoid the formation of relapses.

Supplementary Materials: The following are available online at www.mdpi.com/2073-4409/9/12/2669/s1: Figure S1: Quantitative imaging by Operetta CLS™ high-content analysis and the Harmony software. Figure S2: RT112 and 5637 cells spheroids formation capacity. Figure S3: Figure S3 Oligomycin and FCCP optimization for the measurement of glycolytic and respiratory bioenergetics, and mRNA levels of selected glycolytic enzymes differentially expressed in RT112 and 5637 cells. Figure S4: Figure S4. Lipid content, lipid peroxidation and redox homeostasis in RT112 and 5637 cells. Figure S5: Spheroid formation capacity of RT112 and 5637 cells under pharmacological treatment; Video S1: RT112 and 5637 cells migration time-lapse.

Author Contributions: Conceptualization, M.V. and E.S.; Data curation, V.P., G.D., G.C., A.V., C.A., R.V. and E.S.; Funding acquisition, M.V., R.V. and E.S.; Investigation, V.P., G.D., G.C., A.V., C.A., S.B. and E.S.; Writing—original draft, V.P., G.D. and E.S.; Writing—review & editing, M.V., R.V. and E.S. All authors have read and agreed to the published version of the manuscript.

Funding: This work was supported by funds from the Italian Ministry of University and Research (MIUR) through grants “Research facilitation fund (Fondo per le Agevolazioni alla Ricerca - FAR)” to ES and MV, and “Dipartimenti di Eccellenza 2017” to University of Milano Bicocca. This work has been also partially funded from the European Union’s Horizon 2020 research and innovation programme under grant agreement No 871277 to MV, and by the Italian Ministry of Health (GR-2011-02351220) to RV.

Acknowledgments: The authors would like to thank SYSBIO/ISBE.IT Center of Systems Biology and the Project of Excellence CHRONOS (CHRONical multifactorial disorders explored by NOvel integrated Strategies) for providing advanced technologies used in this study. The authors also warmly thank Silvia Nicolis for the kind gift of anti-SOX2 antibodies.

Conflicts of Interest: The authors declare no conflict of interest

References

1. Yeung, C.; Dinh, T.; Lee, J. The Health Economics of Bladder Cancer: An Updated Review of the Published Literature. *Pharm. Econ.* **2014**, *32*, 1093–1104, doi:10.1007/s40273-014-0194-2.
2. Babjuk, M.; Böhle, A.; Burger, M.; Capoun, O.; Cohen, D.; Compérat, E.; Hernández, V.; Kaasinen, E.; Palou, J.; Roupřet, M.; et al. EAU Guidelines on Non-Muscle-invasive Urothelial Carcinoma of the Bladder: Update 2016. *Eur. Urol.* **2017**, *71*, 447–461, doi:10.1016/j.eururo.2016.05.041.
3. Witjes, F.; Lebrecht, T.; Compérat, E.; Cowan, N.C.; De Santis, M.; Bruins, H.M.; Hernández, V.; Espinós, E.L.; Dunn, J.; Rouanne, M.; et al. Updated 2016 EAU Guidelines on Muscle-invasive and Metastatic Bladder Cancer. *Eur. Urol.* **2017**, *71*, 462–475, doi:10.1016/j.eururo.2016.06.020.
4. Compérat, E.M.; Burger, M.; Gontero, P.; Mostafid, H.; Palou, J.; Roupřet, M.; Van Rhijn, B.W.; Shariat, S.F.; Sylvester, R.J.; Zigeuner, R.; et al. Grading of Urothelial Carcinoma and The New “World Health Organisation Classification of Tumours of the Urinary System and Male Genital Organs 2016.” *Eur. Urol. Focus* **2019**, *5*, 457–466, doi:10.1016/j.euf.2018.01.003.
5. Cheng, L.; Neumann, R.M.; Nehra, A.; Spotts, B.E.; Weaver, A.L.; Bostwick, D.G. Cancer heterogeneity and its biologic implications in the grading of urothelial carcinoma. *Cancer* **2000**, *88*, 1663–1670, doi:10.1002/(sici)1097-0142(20000401)88:73.0.co;2-8.
6. Downes, M.R.; Weening, B.; Van Rhijn, B.W.G.; Have, C.L.; Treurniet, K.M.; Van Der Kwast, T.H. Analysis of papillary urothelial carcinomas of the bladder with grade heterogeneity: Supportive evidence for an early role of CDKN2A deletions in the FGFR3 pathway. *Histopathol* **2016**, *70*, 281–289, doi:10.1111/his.13063.
7. Hanahan, D.; Weinberg, R.A. Hallmarks of cancer: The next generation. *Cell* **2011**, *144*, 646–674.
8. Warburg, O. On the Origin of Cancer Cells. *Science* **1956**, *123*, 309–314, doi:10.1126/science.123.3191.309.
9. DeBerardinis, R.J.; Chandel, N.S. Fundamentals of cancer metabolism. *Sci. Adv.* **2016**, *2*, e1600200, doi:10.1126/sciadv.1600200.
10. Zhu, J.; Thompson, C.B. Metabolic regulation of cell growth and proliferation. *Nat. Rev. Mol. Cell Biol.* **2019**, *20*, 436–450, doi:10.1038/s41580-019-0123-5.
11. DeBerardinis, R.J.; Chandel, N.S. We need to talk about the Warburg effect. *Nat. Metab.* **2020**, *2*, 127–129, doi:10.1038/s42255-020-0172-2.
12. Wang, T.; Marquardt, C.; Foker, J. Aerobic glycolysis during lymphocyte proliferation. *Nat. Cell Biol.* **1976**, *261*, 702–705, doi:10.1038/261702a0.
13. Bauer, D.E.; Harris, M.H.; Plas, D.R.; Lum, J.J.; Hammerman, P.S.; Rathmell, J.C.; Riley, J.L.; Thompson, C.B. Cytokine stimulation of aerobic glycolysis in hematopoietic cells exceeds proliferative demand. *FASEB J.* **2004**, *18*, 1303–1305, doi:10.1096/fj.03-1001fje.

14. Peek, C.B.; Levine, D.C.; Cedernaes, J.; Taguchi, A.; Kobayashi, Y.; Tsai, S.J.; Bonar, N.A.; McNulty, M.R.; Ramsey, K.M.; Bass, J. Circadian Clock Interaction with HIF1 α Mediates Oxygenic Metabolism and Anaerobic Glycolysis in Skeletal Muscle. *Cell Metab.* **2017**, *25*, 86–92, doi:10.1016/j.cmet.2016.09.010.
15. Chiaradonna, F.; Sacco, E.; Manzoni, R.; Giorgio, M.; Vanoni, M.; Alberghina, L. Ras-dependent carbon metabolism and transformation in mouse fibroblasts. *Oncogene* **2006**, *25*, 5391–5404, doi:10.1038/sj.onc.1209528.
16. Ying, H.; Kimmelman, A.C.; Lyssiotis, C.A.; Hua, S.; Chu, G.C.; Fletcher-Sananikone, E.; Locasale, J.W.; Son, J.; Zhang, H.; Coloff, J.L.; et al. Oncogenic Kras Maintains Pancreatic Tumors through Regulation of Anabolic Glucose Metabolism. *Cell* **2012**, *149*, 656–670, doi:10.1016/j.cell.2012.01.058.
17. Damiani, C.; Colombo, R.; Gaglio, D.; Mastroianni, F.; Pescini, D.; Westerhoff, H.V.; Mauri, G.; Vanoni, M.; Alberghina, L. A metabolic core model elucidates how enhanced utilization of glucose and glutamine, with enhanced glutamine-dependent lactate production, promotes cancer cell growth: The WarburQ effect. *PLoS Comput. Biol.* **2017**, *13*, e1005758, doi:10.1371/journal.pcbi.1005758.
18. Pupo, E.; Avanzato, D.; Middonti, E.; Bussolino, F.; Lanzetti, L. KRAS-Driven Metabolic Rewiring Reveals Novel Actionable Targets in Cancer. *Front. Oncol.* **2019**, *9*, 848, doi:10.3389/fonc.2019.00848.
19. Matoba, S.; Kang, J.-G.; Patino, W.D.; Wragg, A.; Boehm, M.; Gavrilova, O.; Hurley, P.J.; Bunz, F.; Hwang, P.M. p53 Regulates Mitochondrial Respiration. *Science* **2006**, *312*, 1650–1653, doi:10.1126/science.1126863.
20. Lago, C.U.; Sung, H.J.; Ma, W.; Wang, P.Y.; Hwang, P.M. P53, aerobic metabolism, and cancer. *Antioxidants Redox Signal.* **2011**, *15*, 1739–1748.
21. Hoxhaj, G.; Manning, B.D. The PI3K–AKT network at the interface of oncogenic signalling and cancer metabolism. *Nat. Rev. Cancer* **2019**, *20*, 74–88, doi:10.1038/s41568-019-0216-7.
22. Sciacovelli, M.; Frezza, C. Oncometabolites: Unconventional triggers of oncogenic signalling cascades. *Free. Radic. Biol. Med.* **2016**, *100*, 175–181, doi:10.1016/j.freeradbiomed.2016.04.025.
23. Tommasini-Ghelfi, S.; Murnan, K.; Kouri, F.M.; Mahajan, A.S.; May, J.L.; Stegh, A.H. Cancer-associated mutation and beyond: The emerging biology of isocitrate dehydrogenases in human disease. *Sci. Adv.* **2019**, *5*, eaaw4543, doi:10.1126/sciadv.aaw4543.
24. Dang, C.V.; Lewis, B.C.; Dolde, C.; Dang, G.; Shim, H. Oncogenes in tumor metabolism, tumorigenesis, and apoptosis. *J. Bioenerg. Biomembr.* **1997**, *29*, 345–354, doi:10.1023/a:1022446730452.
25. DeBerardinis, R.J.; Mancuso, A.; Daikhin, E.; Nissim, I.; Yudkoff, M.; Wehrli, S.; Thompson, C.B. Beyond aerobic glycolysis: Transformed cells can engage in glutamine metabolism that exceeds the requirement for protein and nucleotide synthesis. *Proc. Natl. Acad. Sci. USA* **2007**, *104*, 19345–19350, doi:10.1073/pnas.0709747104.
26. Gaglio, D.; Metallo, C.M.; A Gameiro, P.; Hiller, K.; Danna, L.S.; Balestrieri, C.; Alberghina, L.; Stephanopoulos, G.; Chiaradonna, F. Oncogenic K-Ras decouples glucose and glutamine metabolism to support cancer cell growth. *Mol. Syst. Biol.* **2011**, *7*, 523, doi:10.1038/msb.2011.56.
27. Son, J.; Lyssiotis, C.A.; Ying, H.; Wang, X.; Hua, S.; Ligorio, M.; Perera, R.M.; Ferrone, C.R.; Mullarky, E.; Shyh-Chang, N.; et al. Glutamine supports pancreatic cancer growth through a KRAS-regulated metabolic pathway. *Nat. Cell Biol.* **2013**, *496*, 101–105, doi:10.1038/nature12040.
28. Rashkovan, M.; Ferrando, A. Metabolic dependencies and vulnerabilities in leukemia. *Genes Dev.* **2019**, *33*, 1460–1474, doi:10.1101/gad.326470.119.
29. Chajès, V.; Cambot, M.; Moreau, K.; Lenoir, G.M.; Joulin, V. Acetyl-CoA Carboxylase α Is Essential to Breast Cancer Cell Survival. *Cancer Res.* **2006**, *66*, 5287–5294, doi:10.1158/0008-5472.can-05-1489.
30. Wang, Z.; Liu, F.; Fan, N.; Zhou, C.; Li, D.; MacVicar, T.; Dong, Q.; Bruns, C.J.; Zhao, Y. Targeting Glutaminolysis: New Perspectives to Understand Cancer Development and Novel Strategies for Potential Target Therapies. *Front. Oncol.* **2020**, *10*, pp. 589–508, doi:10.3389/fonc.2020.589508.
31. Gaglio, D.; Soldati, C.; Vanoni, M.; Alberghina, L.; Chiaradonna, F. Glutamine Deprivation Induces Abortive S-Phase Rescued by Deoxyribonucleotides in K-Ras Transformed Fibroblasts. *PLoS ONE* **2009**, *4*, e4715, doi:10.1371/journal.pone.0004715.
32. Massari, F.; Ciccicarese, C.; Santoni, M.; Iacovelli, R.; Mazzucchelli, R.; Piva, F.; Scarpelli, M.; Berardi, R.; Tortora, G.; Lopez-Beltran, A.; et al. Metabolic phenotype of bladder cancer. *Cancer Treat. Rev.* **2016**, *45*, 46–57, doi:10.1016/j.ctrv.2016.03.005.
33. Petrella, G.; Ciufolini, G.; Vago, R.; Cicero, D.O. The Interplay between Oxidative Phosphorylation and Glycolysis as a Potential Marker of Bladder Cancer Progression. *Int. J. Mol. Sci.* **2020**, *21*, 8107, doi:10.3390/ijms21218107.

34. Loras, A.; Trassierra, M.; Sanjuan-Herráez, D.; Martínez-Bisbal, M.C.; Castell, J.V.; Quintás, G.; Ruiz-Cerdá, J.L. Bladder cancer recurrence surveillance by urine metabolomics analysis. *Sci. Rep.* **2018**, *8*, 1–10, doi:10.1038/s41598-018-27538-3.
35. Sborov, D.W.; Haverkos, B.M.; Harris, P.J. Investigational cancer drugs targeting cell metabolism in clinical development. *Expert Opin. Investig. Drugs* **2015**, *24*, 79–94, doi:10.1517/13543784.2015.960077.
36. A Pierotti, M.; Berrino, F.; Gariboldi, M.B.; Melani, C.; Mogavero, A.; Negri, T.; Pasanisi, P.; Pilotti, S. Targeting metabolism for cancer treatment and prevention: Metformin, an old drug with multi-faceted effects. *Oncogene* **2013**, *32*, 1475–1487, doi:10.1038/onc.2012.181.
37. Luengo, A.; Gui, D.Y.; Vander Heiden, M.G. Targeting Metabolism for Cancer Therapy. *Cell Chem. Biol.* **2017**, *24*, 1161–1180.
38. De Sanctis, G.; Spinelli, M.; Vanoni, M.; Sacco, E. K-Ras Activation Induces Differential Sensitivity to Sulfur Amino Acid Limitation and Deprivation and to Oxidative and Anti-Oxidative Stress in Mouse Fibroblasts. *PLoS ONE* **2016**, *11*, e0163790, doi:10.1371/journal.pone.0163790.
39. Baracca, A.; Chiaradonna, F.; Sgarbi, G.; Solaini, G.; Alberghina, L.; Lenaz, G. Mitochondrial Complex I decrease is responsible for bioenergetic dysfunction in K-ras transformed cells. *Biochim. Biophys. Acta (BBA) Bioenerg.* **2010**, *1797*, 314–323, doi:10.1016/j.bbabi.2009.11.006.
40. Weinberg, F.; Hamanaka, R.; Wheaton, W.W.; Weinberg, S.; Joseph, J.; Lopez, M.; Kalyanaraman, B.; Mutlu, G.M.; Budinger, G.R.S.; Chandel, N.S. Mitochondrial metabolism and ROS generation are essential for Kras-mediated tumorigenicity. *Proc. Natl. Acad. Sci. USA* **2010**, *107*, 8788–8793, doi:10.1073/pnas.1003428107.
41. Earl, J.; Rico, D.; De Pau, E.C.S.; Rodríguez-Santiago, B.; Méndez-Pertuz, M.; Aufer, H.; Gómez-López, G.; Grossman, H.B.; Pisano, D.G.; Schulz, W.A.; et al. The UBC-40 Urothelial Bladder Cancer cell line index: A genomic resource for functional studies. *BMC Genom.* **2015**, *16*, 1–16, doi:10.1186/s12864-015-1450-3.
42. Sjö Dahl, G.; Eriksson, P.; Patschan, O.; Marzouka, N.; Jakobsson, L.; Bernardo, C.; Lövgren, K.; Chebil, G.; Zwarthoff, E.; Liedberg, F.; et al. Molecular changes during progression from nonmuscle invasive to advanced urothelial carcinoma. *Int. J. Cancer* **2019**, *146*, 2636–2647, doi:10.1002/ijc.32737.
43. Marshall, C.J.; Franks, L.M.; Carbonell, A.W. Markers of Neoplastic Transformation in Epithelial Cell Lines Derived From Human Carcinomas. *J. Natl. Cancer Inst.* **1977**, *58*, 1743–1751, doi:10.1093/jnci/58.6.1743.
44. Fogh, J.; Fogh, J.M.; Orfeo, T. One Hundred and Twenty-Seven Cultured Human Tumor Cell Lines Producing Tumors in Nude Mice. *J. Natl. Cancer Inst.* **1977**, *59*, 221–226, doi:10.1093/jnci/59.1.221.
45. Chung, B.-M.; Rotty, J.D.; A Coulombe, P. Networking galore: Intermediate filaments and cell migration. *Curr. Opin. Cell Biol.* **2013**, *25*, 600–612, doi:10.1016/j.ccb.2013.06.008.
46. Strouhalova, K.; Přečková, M.; Gandalovičová, A.; Brábek, J.; Gregor, M.; Rösel, D. Vimentin Intermediate Filaments as Potential Target for Cancer Treatment. *Cancers* **2020**, *12*, 184, doi:10.3390/cancers12010184.
47. Webb, D.J.; Donais, K.; Whitmore, L.A.; Thomas, S.M.; Turner, C.E.; Parsons, J.T.; Horwitz, A.F. FAK–Src signalling through paxillin, ERK and MICK regulates adhesion disassembly. *Nat. Cell Biol.* **2004**, *6*, 154–161, doi:10.1038/ncb1094.
48. Thomas, S.; Overvest, J.B.; Nitz, M.D.; Williams, P.D.; Owens, C.R.; Sanchez-Carbayo, M.; Frierson, H.F.; Schwartz, M.A.; Theodorescu, D. Src and Caveolin-1 Reciprocally Regulate Metastasis via a Common Downstream Signaling Pathway in Bladder Cancer. *Cancer Res.* **2010**, *71*, 832–841, doi:10.1158/0008-5472.can-10-0730.
49. Zhang, X.; Zhao, W.; Li, Y. Stemness-related markers in cancer. *Cancer Transl. Med.* **2017**, *3*, 87–95, doi:10.4103/ctm.ctm_69_16.
50. Reya, T.; Morrison, S.J.; Clarke, M.F.; Weissman, I.L. Stem cells, cancer, and cancer stem cells. *Nature* **2001**, *414*, 105–111.
51. Toledo-Guzmán, M.E.; Hernández, M.I.; Gómez-Gallegos, Á.A.; Ortiz-Sánchez, E. ALDH as a Stem Cell Marker in Solid Tumors. *Curr. Stem Cell Res. Ther.* **2019**, *14*, doi:10.2174/1574888X13666180810120012.
52. Rodríguez-Torres, M.; Allan, A.L. Aldehyde dehydrogenase as a marker and functional mediator of metastasis in solid tumors. *Clin. Exp. Metastasis* **2016**, *33*, 97–113, doi:10.1007/s10585-015-9755-9.
53. Farid, R.M.; Sasmour, S.A.E.-M.; El-Din, Z.A.E.-K.S.; Salman, M.I.; Omran, T.I. Expression of CD133 and CD24 and their different phenotypes in urinary bladder carcinoma. *Cancer Manag. Res.* **2019**, *11*, 4677–4690, doi:10.2147/cmar.s198348.

54. Shmelkov, S.V.; Butler, J.M.; Hooper, A.T.; Hormigo, A.; Kushner, J.; Milde, T.; Clair, R.S.; Baljevic, M.; White, I.; Jin, D.K.; et al. CD133 expression is not restricted to stem cells, and both CD133+ and CD133–metastatic colon cancer cells initiate tumors. *J. Clin. Investig.* **2008**, *118*, 2111–2120, doi:10.1172/jci34401.
55. Höfner, T.; Macher-Goeppinger, S.; Klein, C.; Schillert, A.; Eisen, C.; Wagner, S.; Rigo-Watermeier, T.; Baccelli, I.; Vogel, V.; Trumpp, A.; et al. Expression and prognostic significance of cancer stem cell markers CD24 and CD44 in urothelial bladder cancer xenografts and patients undergoing radical cystectomy. *Urol. Oncol. Semin. Orig. Investig.* **2014**, *32*, 678–686, doi:10.1016/j.urolonc.2014.01.001.
56. Chan, K.S.; Espinosa, I.; Chao, M.; Wong, D.; Ailles, L.; Diehn, M.; Gill, H.; Presti, J.; Chang, H.Y.; Van De Rijn, M.; et al. Identification, molecular characterization, clinical prognosis, and therapeutic targeting of human bladder tumor-initiating cells. *Proc. Natl. Acad. Sci. USA* **2009**, *106*, 14016–14021, doi:10.1073/pnas.0906549106.
57. Wen, Y.; Hou, Y.; Huang, Z.; Cai, J.; Wang, Z. SOX2 is required to maintain cancer stem cells in ovarian cancer. *Cancer Sci.* **2017**, *108*, 719–731, doi:10.1111/cas.13186.
58. Pavlova, N.N.; Thompson, C.B. The Emerging Hallmarks of Cancer Metabolism. *Cell Metab.* **2016**, *23*, 27–47, doi:10.1016/j.cmet.2015.12.006.
59. Ferrick, D.A.; Neilson, A.; Beeson, C. Advances in measuring cellular bioenergetics using extracellular flux. *Drug Discov. Today* **2008**, *13*, 268–274, doi:10.1016/j.drudis.2007.12.008.
60. Dombrauckas, J.D.; Santarsiero, B.D.; Mesecar, A.D. Structural Basis for Tumor Pyruvate Kinase M2 Allosteric Regulation and Catalysis. *Biochemistry* **2005**, *44*, 9417–9429, doi:10.1021/bi0474923.
61. Yuan, M.; McNae, I.; Chen, Y.; Blackburn, E.A.; Wear, M.A.; Michels, P.A.; Gilmore, L.; Hupp, T.; Walkinshaw, M.D. An allostatic mechanism for M2 pyruvate kinase as an amino-acid sensor. *Biochem. J.* **2018**, *475*, 1821–1837, doi:10.1042/bcj20180171.
62. Poot, M.; Zhang, Y.Z.; Krämer, J.A.; Wells, K.S.; Jones, L.J.; Hanzel, D.K.; Lugade, A.G.; Singer, V.L.; Haugland, R.P. Analysis of mitochondrial morphology and function with novel fixable fluorescent stains. *J. Histochem. Cytochem.* **1996**, *44*, 1363–1372, doi:10.1177/44.12.8985128.
63. Mitra, K.; Lippincott-Schwartz, J. Analysis of Mitochondrial Dynamics and Functions Using Imaging Approaches. *Curr. Protoc. Cell Biol.* **2010**, *46*, 4.25.1–4.25.21, doi:10.1002/0471143030.cb0425s46.
64. Iannetti, E.F.; Prigione, A.; Smeitink, J.A.M.; Koopman, W.J.H.; Beyrath, J.; Renkema, H. Live-Imaging Readouts and Cell Models for Phenotypic Profiling of Mitochondrial Function. *Front. Genet.* **2019**, *10*, 131, doi:10.3389/fgene.2019.00131.
65. Halliwell, B.; Chirico, S. Lipid peroxidation: Its mechanism, measurement, and significance. *Am. J. Clin. Nutr.* **1993**, *57*, 715S–725S, doi:10.1093/ajcn/57.5.715s.
66. Pap, E.; Drummen, G.; Winter, V.; Kooij, T.; Rijken, P.; Wirtz, K.; Kamp, J.O.D.; Hage, W.; Post, J. Ratio-fluorescence microscopy of lipid oxidation in living cells using C11-BODIPY581/591. *FEBS Lett.* **1999**, *453*, 278–282, doi:10.1016/s0014-5793(99)00696-1.
67. Carracedo, A.; Cantley, L.C.; Pandolfi, P.P. Cancer metabolism: Fatty acid oxidation in the limelight. *Nat. Rev. Cancer* **2013**, *13*, 227–232, doi:10.1038/nrc3483.
68. Ceccarelli, S.M.; Chomienne, O.; Gubler, M.; Arduini, A. Carnitine Palmitoyltransferase (CPT) Modulators: A Medicinal Chemistry Perspective on 35 Years of Research. *J. Med. Chem.* **2011**, *54*, 3109–3152, doi:10.1021/jm100809g.
69. El-Mir, M.-Y.; Nogueira, V.; Fontaine, E.; Avéret, N.; Rigoulet, M.; Leverve, X. Dimethylbiguanide Inhibits Cell Respiration via an Indirect Effect Targeted on the Respiratory Chain Complex I. *J. Biol. Chem.* **2000**, *275*, 223–228, doi:10.1074/jbc.275.1.223.
70. Owen, M.R.; Doran, E.; Halestrap, A.P. Evidence that metformin exerts its anti-diabetic effects through inhibition of complex I of the mitochondrial respiratory chain. *Biochem. J.* **2000**, *348*, 607–614, doi:10.1042/0264-6021:3480607.
71. Vial, G.; Detaillé, D.; Guigas, B. Role of Mitochondria in the Mechanism(s) of Action of Metformin. *Front. Endocrinol.* **2019**, *10*, p. 294, doi:10.3389/fendo.2019.00294.
72. Ishiguro, T.; Ohata, H.; Sato, A.; Yamawaki, K.; Enomoto, T.; Okamoto, K. Tumor-derived spheroids: Relevance to cancer stem cells and clinical applications. *Cancer Sci.* **2017**, *108*, 283–289, doi:10.1111/cas.13155.
73. Mehta, P.; Novak, C.; Raghavan, S.; Ward, M.; Mehta, G. Self-Renewal and CSCs In Vitro Enrichment: Growth as Floating Spheres. In *Bioinformatics in MicroRNA Research*; Springer Science and Business Media LLC: Berlin, Germany, 2018; Volume 1692, pp. 61–75.

74. Sancho, P.; Barneda, D.; Heeschen, C. Hallmarks of cancer stem cell metabolism. *Br. J. Cancer* **2016**, *114*, 1305–1312, doi:10.1038/bjc.2016.152.
75. Sotgia, F.; Fiorillo, M.; Lisanti, M.P. Hallmarks of the cancer cell of origin: Comparisons with “energetic” cancer stem cells (e-CSCs). *Aging* **2019**, *11*, 1065–1068, doi:10.18632/aging.101822.
76. Fiorillo, M.; Lamb, R.; Tanowitz, H.B.; Mutti, L.; Krstic-Demonacos, M.; Cappello, A.R.; Martinez-Outschoorn, U.E.; Sotgia, F.; Lisanti, M.P. Repurposing atovaquone: Targeting mitochondrial complex III and OXPHOS to eradicate cancer stem cells. *Oncotarget* **2016**, *7*, 34084–34099, doi:10.18632/oncotarget.9122.
77. Denise, C.; Paoli, P.; Calvani, M.; Taddei, M.L.; Giannoni, E.; Kopetz, S.; Kazmi, S.M.A.; Pia, M.M.; Pettazzoni, P.; Sacco, E.; et al. 5-Fluorouracil resistant colon cancer cells are addicted to OXPHOS to survive and enhance stem-like traits. *Oncotarget* **2015**, *6*, 41706–41721, doi:10.18632/oncotarget.5991.
78. Ferlay, J.; Steliarova-Foucher, E.; Lortet-Tieulent, J.; Rosso, S.; Coebergh, J.; Comber, H.; Forman, D.; Bray, F. Cancer incidence and mortality patterns in Europe: Estimates for 40 countries in 2012. *Eur. J. Cancer* **2013**, *49*, 1374–1403, doi:10.1016/j.ejca.2012.12.027.
79. Nielsen, J. Systems Biology of Metabolism: A Driver for Developing Personalized and Precision Medicine. *Cell Metab.* **2017**, *25*, 572–579, doi:10.1016/j.cmet.2017.02.002.
80. Damiani, C.; Gaglio, D.; Sacco, E.; Alberghina, L.; Vanoni, M. Systems metabolomics: From metabolomic snapshots to design principles. *Curr. Opin. Biotechnol.* **2020**, *63*, 190–199, doi:10.1016/j.copbio.2020.02.013.
81. Tan, G.; Wang, H.; Yuan, J.; Qin, W.; Dong, X.; Wu, H.; Meng, P. Three serum metabolite signatures for diagnosing low-grade and high-grade bladder cancer. *Sci. Rep.* **2017**, *7*, srep46176, doi:10.1038/srep46176.
82. Mpanga, A.Y.; Siluk, D.; Jacyna, J.; Szerkus, O.; Wawrzyniak, R.; Markuszewski, M.; Kalisz, R.; Markuszewski, M.J. Targeted metabolomics in bladder cancer: From analytical methods development and validation towards application to clinical samples. *Anal. Chim. Acta* **2018**, *1037*, 188–199, doi:10.1016/j.aca.2018.01.055.
83. Zuiverloon, T.C.; De Jong, F.C.; Costello, J.C.; Theodorescu, D. Systematic Review: Characteristics and Preclinical Uses of Bladder Cancer Cell Lines. *Bladder Cancer* **2018**, *4*, 169–183, doi:10.3233/blc-180167.
84. Warrick, J.I.; Walter, V.; Yamashita, H.; Chung, E.; Shuman, L.; Amponsa, V.O.; Zheng, Z.; Chan, W.; Whitcomb, T.L.; Yue, F.; et al. FOXA1, GATA3 and PPAR γ Cooperate to Drive Luminal Subtype in Bladder Cancer: A Molecular Analysis of Established Human Cell Lines. *Sci. Rep.* **2016**, *6*, 38531, doi:10.1038/srep38531.
85. Rebouissou, S.; Bernard-Pierrot, I.; De Reyniès, A.; Lepage, M.-L.; Krucker, C.; Chapeaublanc, E.; Héroult, A.; Kamoun, A.; Caillault, A.; Letouzé, E.; et al. EGFR as a potential therapeutic target for a subset of muscle-invasive bladder cancers presenting a basal-like phenotype. *Sci. Transl. Med.* **2014**, *6*, 244ra91, doi:10.1126/scitranslmed.3008970.
86. Turrens, J.F. Mitochondrial formation of reactive oxygen species. *J. Physiol.* **2003**, *552*, 335–344.
87. Zorov, D.B.; Juhaszova, M.; Sollott, S.J. Mitochondrial Reactive Oxygen Species (ROS) and ROS-Induced ROS Release. *Physiol. Rev.* **2014**, *94*, 909–950, doi:10.1152/physrev.00026.2013.
88. Vinogradov, A.; Grivennikova, V.G. Oxidation of NADH and ROS production by respiratory complex I. *Biochim. et Biophys. Acta (BBA) Bioenerg.* **2016**, *1857*, 863–871, doi:10.1016/j.bbabo.2015.11.004.
89. Bleier, L.; Dröse, S. Superoxide generation by complex III: From mechanistic rationales to functional consequences. *Biochim. Biophys. Acta (BBA) Bioenerg.* **2013**, *1827*, 1320–1331, doi:10.1016/j.bbabo.2012.12.002.
90. Barrera, G.; Pizzimenti, S.; Dianzani, M.U. Lipid peroxidation: Control of cell proliferation, cell differentiation and cell death. *Mol. Asp. Med.* **2008**, *29*, 1–8, doi:10.1016/j.mam.2007.09.012.
91. Barrera, G. Oxidative Stress and Lipid Peroxidation Products in Cancer Progression and Therapy. *ISRN Oncol.* **2012**, *2012*, 1–21, doi:10.5402/2012/137289.
92. Ayala, A.; Muñoz, M.F.; Argüelles, S. Lipid Peroxidation: Production, Metabolism, and Signaling Mechanisms of Malondialdehyde and 4-Hydroxy-2-Nonenal. *Oxidative Med. Cell. Longev.* **2014**, *2014*, 1–31, doi:10.1155/2014/360438.
93. Black, W.; Chen, Y.; Matsumoto, A.; Thompson, D.C.; Lassen, N.; Pappa, A.; Vasiliou, V. Molecular mechanisms of ALDH3A1-mediated cellular protection against 4-hydroxy-2-nonenal. *Free. Radic. Biol. Med.* **2012**, *52*, 1937–1944, doi:10.1016/j.freeradbiomed.2012.02.050.
94. Singh, S.; Brocker, C.; Koppaka, V.; Chen, Y.; Jackson, B.C.; Matsumoto, A.; Thompson, D.C.; Vasiliou, V. Aldehyde dehydrogenases in cellular responses to oxidative/electrophilic stress. *Free. Radic. Biol. Med.* **2013**, *56*, 89–101, doi:10.1016/j.freeradbiomed.2012.11.010.

95. Corbet, C.; Feron, O. Cancer cell metabolism and mitochondria: Nutrient plasticity for TCA cycle fueling. *Biochim. Biophys. Acta (BBA) Bioenerg.* **2017**, *1868*, 7–15, doi:10.1016/j.bbcan.2017.01.002.
96. Bentebibel, A.; Sebastián, D.; Herrero, L.; López-Viñas, E.; Serra, D.; Asins, G.; Gómez-Puertas, P.; Hegardt, F.G. Novel Effect of C75 on Carnitine Palmitoyltransferase I Activity and Palmitate Oxidation. *Biochemistry* **2006**, *45*, 4339–4350, doi:10.1021/bi052186q.
97. Declercq, P.E.; Falck, J.R.; Kuwajima, M.; Tyminski, H.; Foster, D.W.; McGarry, J.D. Characterization of the mitochondrial carnitine palmitoyltransferase enzyme system. I. Use of inhibitors. *J. Biol. Chem.* **1987**, *262*, 9812–9821.
98. Raud, B.; Roy, D.G.; Divakaruni, A.S.; Tarasenko, T.N.; Franke, R.; Ma, F.H.; Samborska, B.; Hsieh, W.Y.; Wong, A.H.; Stüve, P.; et al. Etomoxir Actions on Regulatory and Memory T Cells Are Independent of Cpt1a-Mediated Fatty Acid Oxidation. *Cell Metab.* **2018**, *28*, 504–515.e7, doi:10.1016/j.cmet.2018.06.002.
99. LeBleu, V.S.; O’Connell, J.T.; Herrera, K.N.G.; Wikman-Kocher, H.; Pantel, K.; Haigis, M.C.; De Carvalho, F.M.; Damascena, A.; Chinen, L.T.D.; Rocha, R.M.; et al. PGC-1 α mediates mitochondrial biogenesis and oxidative phosphorylation in cancer cells to promote metastasis. *Nat. Cell Biol.* **2014**, *16*, 992–1003, doi:10.1038/ncb3039.
100. Sotgia, F.; Whitaker-Menezes, D.; Martinez-Outschoorn, U.E.; Flomenberg, N.; Birbe, R.C.; Witkiewicz, A.K.; Howell, A.; Philp, N.J.; Pestell, R.G.; Lisanti, M.P. Mitochondrial metabolism in cancer metastasis. *Cell Cycle* **2012**, *11*, 1445–1454, doi:10.4161/cc.19841.
101. Sancho, P.; Burgos-Ramos, E.; Tavera, A.; Kheir, T.B.; Jagust, P.; Schoenhals, M.; Barneda, D.; Sellers, K.; Campos-Olivas, R.; Graña, O.; et al. MYC/PGC-1 α Balance Determines the Metabolic Phenotype and Plasticity of Pancreatic Cancer Stem Cells. *Cell Metab.* **2015**, *22*, 590–605, doi:10.1016/j.cmet.2015.08.015.
102. Lagadinou, E.D.; Sach, A.; Callahan, K.; Rossi, R.M.; Neering, S.J.; Minhajuddin, M.; Ashton, J.M.; Pei, S.; Grose, V.; O’Dwyer, K.M.; et al. BCL-2 Inhibition Targets Oxidative Phosphorylation and Selectively Eradicates Quiescent Human Leukemia Stem Cells. *Cell Stem Cell* **2013**, *12*, 329–341, doi:10.1016/j.stem.2012.12.013.
103. Invrea, F.; Rovito, R.; Torchiaro, E.; Petti, C.; Isella, C.; Medico, E. Patient-derived xenografts (PDXs) as model systems for human cancer. *Curr. Opin. Biotechnol.* **2020**, *63*, 151–156, doi:10.1016/j.copbio.2020.01.003.
104. Reckzeh, E.S.; Karageorgis, G.; Schwalfenberg, M.; Ceballos, J.; Nowacki, J.; Stroet, M.C.; Binici, A.; Knauer, L.; Brand, S.; Choidas, A.; et al. Inhibition of Glucose Transporters and Glutaminase Synergistically Impairs Tumor Cell Growth. *Cell Chem. Biol.* **2019**, *26*, 1214–1228.e25, doi:10.1016/j.chembiol.2019.06.005.
105. Gaglio, D.; Bonanomi, M.; Valtorta, S.; Bharat, R.; Ripamonti, M.; Conte, F.; Fisco, G.; Righi, N.; Napodano, E.; Papa, F.; et al. Disruption of redox homeostasis for combinatorial drug efficacy in K-Ras tumors as revealed by metabolic connectivity profiling. *Cancer Metab.* **2020**, *8*, 1–15, doi:10.1186/s40170-020-00227-4.

Publisher’s Note: MDPI stays neutral with regard to jurisdictional claims in published maps and institutional affiliations.



© 2020 by the authors. Licensee MDPI, Basel, Switzerland. This article is an open access article distributed under the terms and conditions of the Creative Commons Attribution (CC BY) license (<http://creativecommons.org/licenses/by/4.0/>).

SUPPLEMENTARY MATERIALS

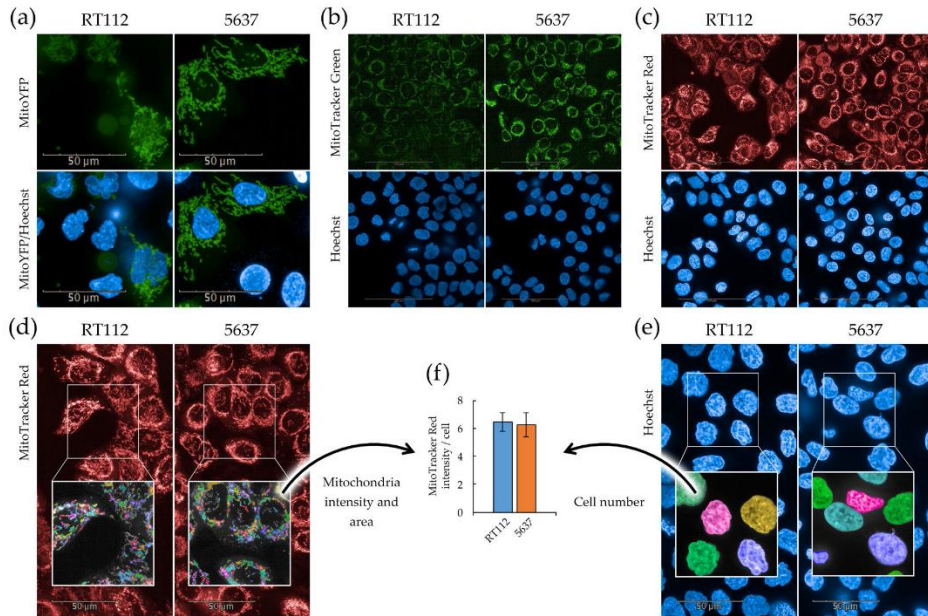


Figure S1. Quantitative imaging by Operetta CLS™ high-content analysis and Harmony software. (a) Confocal imaging using Operetta CLS™ of living transiently transfected cells expressing the mitochondrial-specific MitoYFP protein (green) and stained with Hoechst 33342 dye labelling nuclei (blue) showing only MitoYFP on upper panes and merged on lower panes. (b) Confocal imaging using Operetta CLS™ of cells stained with MitoTracker™ Green FM dye (green) labelling mitochondria and Hoechst 33342 dye (blue) labelling nuclei. (c) Confocal imaging using Operetta CLS™ of cells stained with MitoTracker™ Red CMXRos dye (red) labelling mitochondria and Hoechst 33342 dye (blue) labelling nuclei. (d) Confocal imaging using Operetta CLS™ of live cells stained with mitochondrial staining MitoTracker™ Red CMXRos with highlighted mitochondria selection based on MitoTracker™ Red CMXRos fluorescence using Harmony software as operated for imaging analysis to obtain intensity data. (e) Hoechst 33342 dye labelling nuclei (blue) and nuclei selection method based on Hoechst 33342 dye fluorescence using Harmony software as operated for imaging analysis to obtain cell count. (f) Resulting graph of analysed data representing mitochondrial membrane potential per cell, obtained from MitoTracker™ Red CMXRos fluorescence and Hoechst 33342-positive nuclei count.

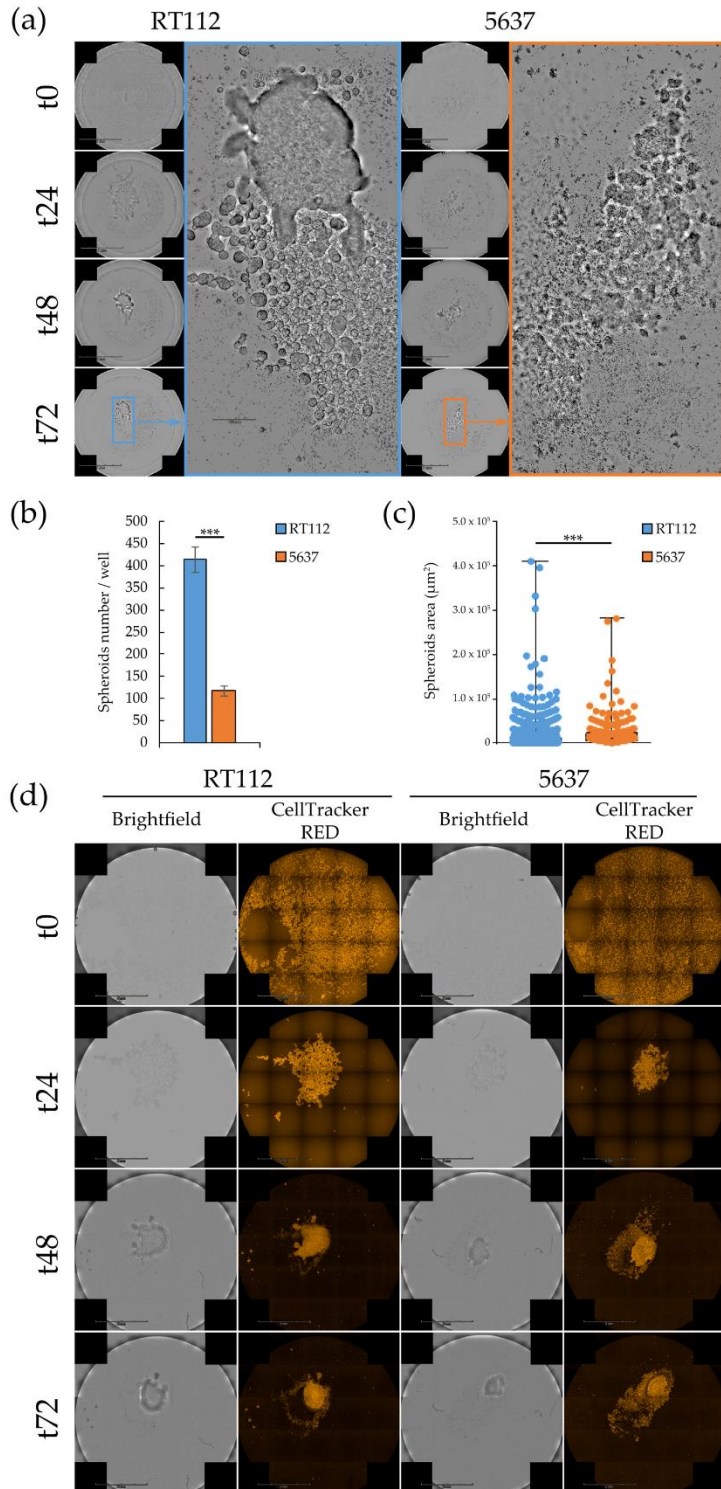


Figure S2. RT112 and 5637 cells spheroids formation capacity. (a-c) Spheroids formation through time (0 hours – 72 hours) in polyHEMA-treated 24-well plate. (a) Representative brightfield images acquired using the Operetta CLS™ are shown. (b) Number of spheroids per well obtained by manual selection using ImageJ software. (c) Whiskers plot of area of spheroids measured on manually selected ROIs using ImageJ software. (d) Spheroids formation through time (0 hours – 72 hours) in cell repellent 96-well plate. Representative images of brightfield and fluorescence confocal microscopy (orange: CellTracker™ Red CMTPX Dye) acquired using the Operetta CLS™ are shown. All results are the mean of at least three experimental replicates. Statistical test: t-test, *** for $P < .001$.

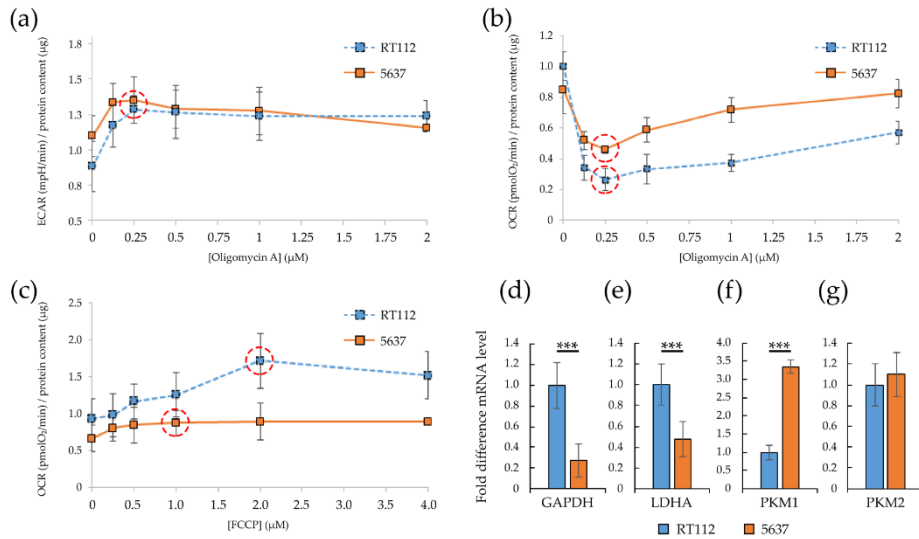


Figure S3. Oligomycin and FCCP optimization for the measurement of glycolytic and respiratory bioenergetics, and mRNA levels of selected glycolytic enzymes differentially expressed in RT112 and 5637 cells. (a-c) ECAR and OCR values detected by Seahorse XF24 Analyzer normalized on protein content measured by Bradford assay. ECAR (a) and OCR (b) values measured after injection of increasing concentrations of oligomycin A (0, 0.125, 0.25, 0.5, 1 and 2 µM). OCR (c) values measured after injection of increasing concentrations of FCCP (0, 0.25, 0.5, 1, 2 and 4 µM). (d-g) mRNA level by qRT-PCR of genes GAPDH (d), LDHA (e), PKM1 (f) and PKM2 (g) normalized to the house-keeping gene HPRT-1 level. All results are the mean of at least three experimental replicates. Statistical test: t-test, *** for $P < .001$.

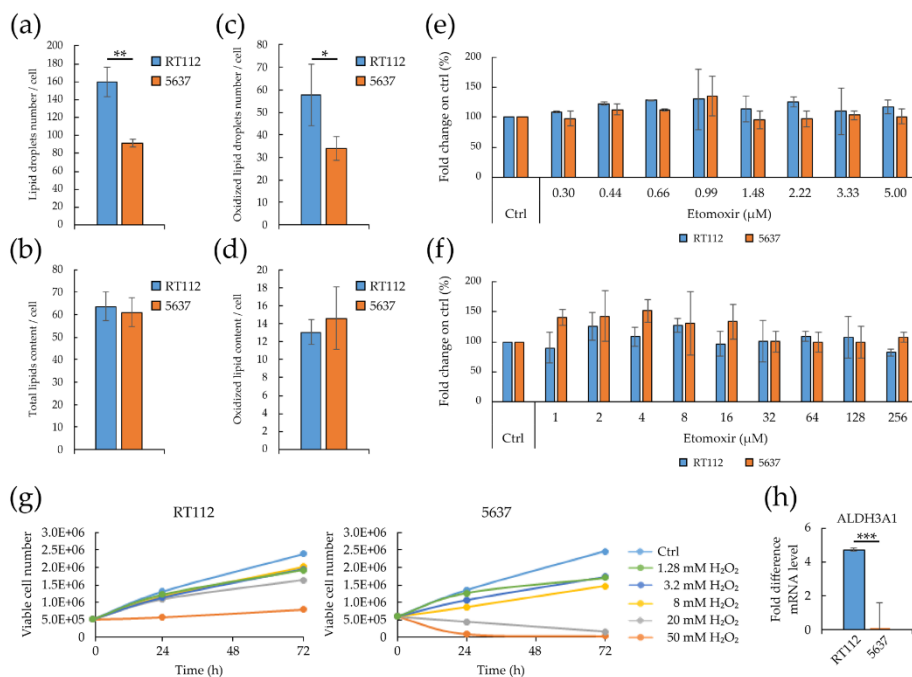


Figure S4. Lipid content, lipid peroxidation and redox homeostasis in RT112 and 5637 cells. (a) Number of lipid droplets per cell obtained using Harmony software. (b) Total lipids per cell measured using Harmony software. (c) Number of oxidized lipid droplets per cell obtained using Harmony software. (d) Total oxidized lipids per cell measured using Harmony software. (e, f) Fold change on control condition of adherent cells treated for 72h with increasing concentration of Etomoxir (e: 0.30, 0.44, 0.66, 0.99, 1.48, 2.22, 3.33, 5 μM; f: 1, 2, 4, 8, 16, 32, 64, 128, 256 μM). (g) Growth curves of RT112 and 5637 cells under treatment with increasing concentration of H₂O₂ (0, 1.28, 3.2, 8, 20, 50 mM). Viable cell number at 0, 24 and 72 hours was obtained by the Trypan Blue exclusion method. (h) qRT-PCR analysis for ALDH3A1 mRNA levels in RT112 and 5637 cells, normalized to the house-keeping gene HPRT-1 level. All results are the mean of at least three experimental replicates. Statistical test: t-test, * for $P < 0.05$; ** for $P < 0.01$; *** for $P < 0.001$.

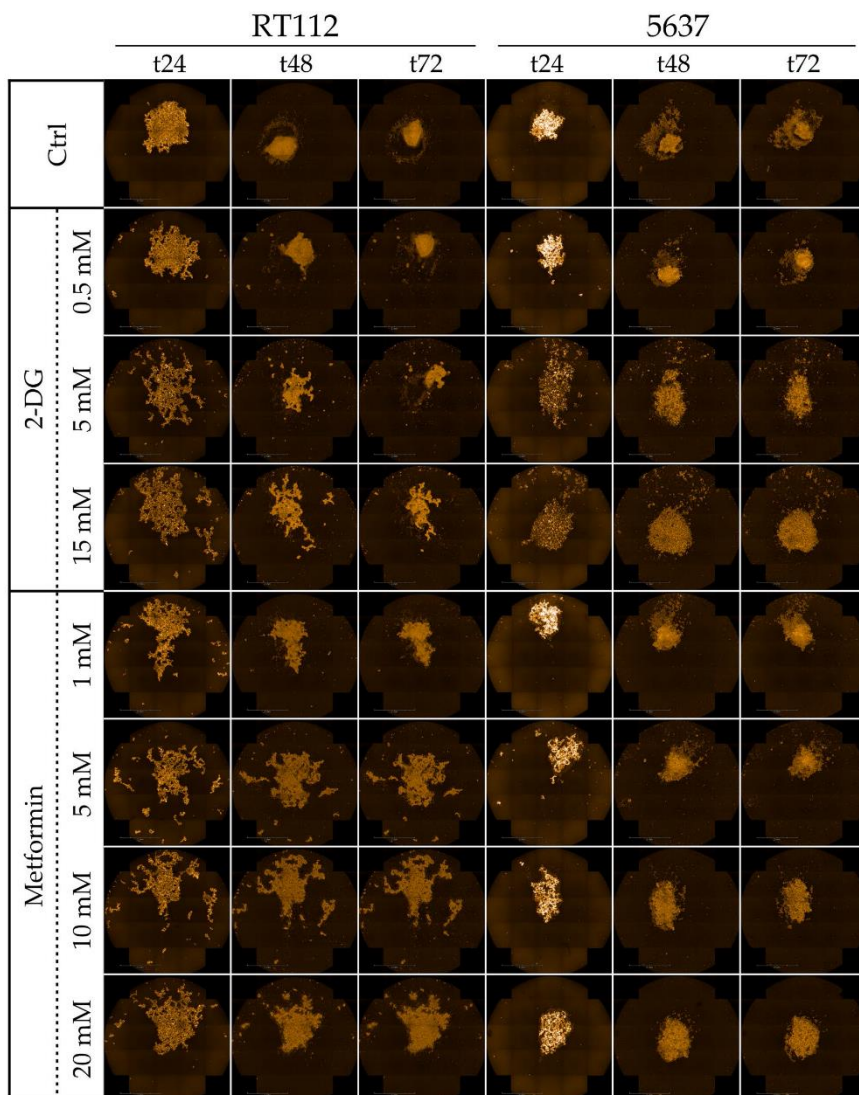


Figure S5. Spheroid formation capacity of RT112 and 5637 cells under pharmacological treatment. Representative images are shown: fluorescence microscopy (orange: CellTracker™ Red CMTPX Dye) at 24, 48 and 72 hours of cells grown in cell repellent 96-well plate treated with increasing concentration of 2-deoxy-D-glucose (2-DG) (0, 0.5, 5, 15 mM) and metformin (0, 1, 5, 10, 20 mM) acquired with Operetta CLS™.

Video S1. RT112 and 5637 cells migration time-lapse. Time-lapse movie showing RT112 (left) and 5637 (right) migration in 12 hour time-course in wound healing assay. Movie frames were obtained with Operetta CLS™ in brightfield and fluorescence microscopy (orange: CellTracker™ Red CMTPX Dye).

GENERAL DISCUSSION

Cancer is one of the major contributors to disease burden worldwide. There were 23.6 million new global cancer cases in 2019, 10.0 million cancer deaths, and 250 million disability-adjusted life years estimated to be due to cancer. Since 2010, these numbers have increased of 26.3%, 20.9% and 16.0%, respectively [1]. Moreover, the projections forecast that the global cancer burden will continue to grow for at least two decades [237]. The main causes of therapeutic failures in cancer treatment are the late stage at diagnosis, development of therapeutic resistance that can lead to spreading of metastasis, and formation of recurrence. The need to find novel therapeutic approaches is urgent, but the main challenge to achieving this goal is finding a universally efficient therapy against cancer. However, this is not considered the best approach in the era of personalized medicine. Cancer heterogeneity has been observed in many contexts, revealing the existence of numerous types and subtypes of cancer that differ for the tissue of origin and differ genetically, metabolically, pathologically, and clinically. Accordingly, exploring this biological diversity that characterizes tumors is crucial for finding new prognostic biomarkers for patients' stratification and identifying specific neoplastic disease vulnerabilities [3]. For this purpose, the aberrant metabolism of proliferating cancer cells presents potential opportunities, and there has been a growing interest in studying how best to target cancer metabolism [34].

Chapter 1 and Chapter 3 of this thesis report the metabolic characterization of three breast cancer cell lines (one hormone-responsive and two triple-negative) and two grade 2 bladder cancer cell lines. These works stress that even cancer cells derived from the same clinical cancer subtype of cancer, and so treated with similar approaches, can exhibit different invasiveness, migratory properties, metabolic plasticity, and response to pharmacological treatments nutritional perturbations.

In considering these aspects, we observed that cancer cells' phenotypes *in vitro* can vary substantially from adhesion monolayer (2D) cultures and suspension three-

dimensional (3D) cultures. Tumor spheroids are more complex *in vitro* models than 2D cultures, and they more closely resemble the pathophysiological features of clinical tumors. Indeed, although 2D culture models are still instrumental in many research fields, including high-throughput drug screening of human diseases, they present many drawbacks as tumor models. For instance, cancer cells proliferation in monolayer cultures is unnaturally fast compared to cancer growth *in vivo*, probably due to genetical modification that cell lines have acquired to adapt their survival *in vitro* and to the availability of nutrients, oxygen, and growth factors that are homogeneously distributed to all the cells of the culture [120]. On the contrary, three-dimensional models of cancer, such as spheroids, present a more realistic condition of the tumor in patients, with gene expression levels that better resemble levels found from cells *in vivo* [238,239], more similar cell-cell and cell-ECM interactions, and a different distribution in gradients of metabolites, signaling small molecules, and gases [33,135].

Similarly, drugs penetration into the cells is differently modulated between 2D and 3D cultures, and this explains parts of our observation about the lower drug sensitivity of cancer cells to metabolic perturbations during spheroids formation. Another possible explanation of this aspect is that the re-arrangement of cancer cells into 3D structures creates a selection pressure on cells, where only those cells that undergo a favorable metabolic transformation survive, leading to the selection of more resistant cells, or in other terms, the enrichment of the so-called Cancer Stem Cells, that exhibit a less proliferative but more aggressive phenotype [14].

The research illustrated in Chapter 1 and Chapter 3 has been possible thanks to the development and the optimization of the protocols for the study of 3D cultures using advanced technologies (e.g., Seahorse XFe96 analyzer and Operetta CLS™ High-content analysis system), a time-consuming but necessary process that has been partially shown in Chapter 2. The need to fine-tune these methods, which is still ongoing, was driven by the aim to apply advanced technologies available to the study of three-dimensional models avoiding misinterpretations of the data due to low

reproducibility or technical issues. For what concerns Operetta CLS™, we explored different analytic approaches trying to find the morphological and physiological parameters enabling us to describe not only qualitatively (as shown in Chapter 3) but also quantitatively (as shown in Chapter 1), the effects of pharmacological or nutritional perturbations on the spheroid formation process. Indeed, while high-resolution imaging quantifies aspects linked to energetic metabolic, migration, and proliferation relatively simply, its application to spheroids presents many hurdles. The high thickness and low transparency of three-dimensional cultures cause a light-scattering phenomenon that limits light penetration, inhibiting the complete digital reconstruction of the 3D structure in live imaging and, therefore, the correct evaluation of 3D parameters (e.g., volume, sphericity). Despite the development of many clearing techniques designed to overcome this problem [240], this approach is hard to apply on spheroid formation assays, in which the treatment can partially or fully disrupt the structures or if the process is intended to be observed in live imaging. Moreover, clearing strategies usually lead to phenomena of spheroid shrinkage or swelling so that the original morphological features of the spheroid can be lost. In Chapter 1, we applied the quantitative live imaging analysis of 3D cultures that we valuated to better correlate with the qualitative observation of spheroids formation (roundness) and variations on their vitality (P.I. intensity/C.T. area), even though it still requires to pay attention to data interpretation (in particular related to the use of the intensity of P.I. calculated on maximal intensity projection, which not always correlate proportionally with the mortality rate for instance due to dead cells disintegration that can lead to a lowering of this signal).

The optimized workflow for Seahorse analysis of three-dimensional cultures that we illustrated in Chapter 2 offers a variety of implementation aspects potentially highly usable for the study of metabolic aspects in cancer spheroids. However, it is important to underline that Seahorse technology measures metabolic parameters deriving from the oxygen consumption and extracellular acidification occurring in the medium immediately surrounding the cells of the spheroid, so it gives information about the

average metabolic state of the three-dimensional structure. Considering that in cancer spheroids the proliferative state of the cells and their access to nutrients and oxygen varies depending on their position in the spheroid itself [33,241], the metabolic phenotype of these cells is not homogeneous like in monolayer cultures. It would be interesting to discern the metabolic differences among the cells residing in different layers of the cancer spheroid, but for this kind of single-cell analysis Seahorse technology is not adequate. A possible innovative technique that can supply for a similar analysis is SCENITH (SCENITH, for Single Cell ENergetic metabolism by profiling Translation inHibition): a flow cytometry-based method for functional profiling energy metabolism with single cell resolution [234]. SCENITH is a method that allows to simultaneously establish the phenotype and extract the global metabolic profile of multiple cell types in parallel, *ex vivo*. It can be used to monitor cellular responses to a combination of multiple metabolites and inhibitors in a way comparable to other techniques, including Seahorse XF analyzer. Another possible approach to study the metabolic phenotype of cells within a spheroid is to use genetically encoded fluorescent biosensors such as Fluorescence Resonance Energy Transfer (FRET) sensors and Single Fluorescent Protein (FP) sensors [242–244]. These biosensors are proteins capable of binding particular substrates or metabolites (e.g., NAD⁺/NADH, NADP⁺/NADPH, ATP) fused with fluorescent proteins. The binding causes structural changes that alter the spectra of the fluorescent protein that can be measured using flow cytometers and fluorescence microscopes. Since this system enables to measure metabolic processes occurring in living cells (so clearing strategies are not applicable in this context), a multiphoton microscope capable to improve spatial resolution for 3D cell models would be required for the analysis at single-cell level [245].

In the short term, we propose to deepen the observed aspects regarding metabolic perturbations not only on spheroids during formation but also on pre-formed spheroids, therefore going beyond the exploration of how metabolism influences the formation of new tumor masses and see how metabolic drugs act on pre-formed masses (which best represent the clinical situation at the time of cancer diagnosis).

The development of technologies providing detailed metabolic profiles, pathway identification and flux analysis, and genome-wide and focused constraint-based metabolic models are opening the way to systems metabolomics [3]. Therefore, we will integrate our studies on cancer metabolism using a multi-omics approach, including metabolomics and population and single-cell transcriptomics [246]. The collection of these data on 3D models will be applied for the construction of constraint-based computational models able to identify potential metabolic vulnerabilities of cancer cells and predict their response to pharmacological treatments [53,99,247]. As the final step of this process, the experimental validation of computer predictions by genetic and/or chemical silencing of the selected targets will be performed. For this purpose, we started the collection of transcriptomic and metabolomic samples of a panel of six bladder cancer cell lines classified as different grades and stages, grown as monolayer (2D) and spheroids (3D). The application of this workflow to patient-derived organoids can be useful for modeling preclinical avatars for personalized medicine [3,33,133], allowing to dissect the metabolic heterogeneity of breast cancer (especially the most aggressive subtype, TNBC) [248] and bladder cancer at different pathological grades [249].

The setting up of reliable protocols for studying cancer metabolism in advanced 3D cultures shown in this thesis and their characterization using metabolomics and Raman spectroscopy will be exploited for the ongoing H2020-funded project AMPLITUDE. The project aims to apply multi-modal imaging for biomarker identification in bladder cancer to improve the accuracy of diagnosis, reduce recurrence, and increase survival of this cancer type [250,251]. This would help clinicians to choose the most appropriate therapeutic approach earlier or efficiently and non-invasively monitor the effects of applied treatment.

Cancer metabolic rewiring involves heterotypic crosstalk in the tumor microenvironment [19,101]. In particular, cancer-associated fibroblasts are believed to support the growth and invasion of cancer cells through multiple mechanisms, including the secretion of growth factors and pro-inflammatory mediators, cell-cell

interactions, and metabolic crosstalk with tumor cells [109]. Therefore, in the future, we propose to amplify our studies on heterotypic spheroids, which provide a more sophisticated model for the phenotypic and cellular heterogeneity of tumor metabolism. At the end of Chapter 1, we illustrated preliminary results about the metabolic characterization of multicellular spheroids made of breast cancer cells and normal mammary fibroblasts. The future aim of this study is to verify the protective or antagonist role of cancer-associated fibroblasts in response to drug treatments.

Therefore, through these three chapters of the thesis, we highlighted that in targeting the spheroid formation process, the effects of metabolic perturbations are less efficient than those observed on monolayer cells proliferation. For this reason, developing accurate and reliable three-dimensional models for the study of metabolic plasticity in cancer is crucial to overcome the primary limits of bi-dimensional models *in vitro*. We also observed that targeting respiratory metabolism in grade 2 bladder cancers shows promising results despite differences in invasiveness properties.

Though further investigations are needed to properly understand the full potential of these findings in the treatment of cancer patients, this thesis contributes to expanding our current understanding of cancer cell metabolism to design novel personalized therapies.

REFERENCES

1. Kocarnik, J.M.; Compton, K.; Dean, F.E.; Fu, W.; Gaw, B.L.; Harvey, J.D.; Henrikson, H.J.; Lu, D.; Pennini, A.; Xu, R.; et al. Cancer Incidence, Mortality, Years of Life Lost, Years Lived With Disability, and Disability-Adjusted Life Years for 29 Cancer Groups From 2010 to 2019. *JAMA Oncol.* **2021**, *98195*, 1–24.
2. Sung, H.; Ferlay, J.; Siegel, R.L.; Laversanne, M.; Soerjomataram, I.; Jemal, A.; Bray, F. Global Cancer Statistics 2020: GLOBOCAN Estimates of Incidence and Mortality Worldwide for 36 Cancers in 185 Countries. *CA. Cancer J. Clin.* **2021**, *71*, 209–249.
3. Nielsen, J. Systems Biology of Metabolism: A Driver for Developing Personalized and Precision Medicine. *Cell Metab.* **2017**, *25*, 572–579.
4. Thomas, R.K.; Baker, A.C.; DeBiasi, R.M.; Winckler, W.; LaFramboise, T.; Lin, W.M.; Wang, M.; Feng, W.; Zander, T.; MacConaill, L.E.; et al. High-throughput oncogene mutation profiling in human cancer. *Nat. Genet.* **2007**, *39*, 347–351.
5. Joyce, C.; Rayi, A.; Kasi, A. *Tumor-Suppressor Genes*; StatPearls Publishing, 2018;
6. Hirsch, F.R.; Ottesen, G.; Pødenphant, J.; Olsen, J. Tumor heterogeneity in lung cancer based on light microscopic features - A retrospective study of a consecutive series of 200 patients, treated surgically. *Virchows Arch. A Pathol. Anat. Histopathol.* 1983, *402*, 147–153.
7. Van Der Poel, H.G.; Oosterhof, G.O.N.; Schaafsma, H.E.; Debruyne, F.M.J.; Schalken, J.A. Intratumoral nuclear morphologic heterogeneity in prostate cancer. *Urology* **1997**, *49*, 652–657.
8. Russnes, H.G.; Navin, N.; Hicks, J.; Borresen-Dale, A.L. Insight into the heterogeneity of breast cancer through next-generation sequencing. *J. Clin. Invest.* **2011**, *121*, 3810–3818.
9. Nowell, P.C. The clonal evolution of tumor cell populations. *Science (80-.)*. **1976**, *194*, 23–28.
10. Sell, S.; Pierce, G.B. Maturation arrest of stem cell differentiation is a common pathway for the cellular origin of teratocarcinomas and epithelial cancers. *Lab. Investig.* 1994, *70*, 6–22.
11. Aguilar-Gallardo, C.; Simón, C. Cells, stem cells, and cancer stem cells. *Semin. Reprod. Med.* **2013**, *31*, 5–13.
12. Shackleton, M.; Quintana, E.; Fearon, E.R.; Morrison, S.J. *Heterogeneity in Cancer: Cancer Stem Cells versus Clonal Evolution*; Elsevier B.V., 2009; Vol. 138, pp. 822–829;.

13. Ishii, H.; Iwatsuki, M.; Ieta, K.; Ohta, D.; Haraguchi, N.; Mimori, K.; Mori, M. Cancer stem cells and chemoradiation resistance. *Cancer Sci.* **2008**, *99*, 1871–1877.
14. Peiris-Pagès, M.; Martinez-Outschoorn, U.E.; Pestell, R.G.; Sotgia, F.; Lisanti, M.P. Cancer stem cell metabolism. *Breast Cancer Res.* 2016, *18*.
15. Hanahan, D.; Weinberg, R.A. The hallmarks of cancer. *Cell* **2000**, *100*, 57–70.
16. Hanahan, D.; Weinberg, R.A. Hallmarks of cancer: The next generation. *Cell* **2011**, *144*, 646–674.
17. Vazquez, A.; Kamphorst, J.J.; Markert, E.K.; Schug, Z.T.; Tardito, S.; Gottlieb, E. Cancer metabolism at a glance. *J. Cell Sci.* **2016**, *129*, 3367–3373.
18. Dey, P.; Kimmelman, A.C.; Depinho, R.A. Metabolic codependencies in the tumor microenvironment. *Cancer Discov.* **2021**, *11*, 1067–1081.
19. Lyssiotis, C.A.; Kimmelman, A.C. Metabolic Interactions in the Tumor Microenvironment. *Trends Cell Biol.* 2017, *27*, 863–875.
20. Huaman, M.A.; Fiske, C.T.; Jones, T.F.; Warkentin, J.; Shepherd, B.E.; Maruri, F.; Sterling, T.R. the Emerging Hallmarks of Cancer Metabolism. **2015**, *143*, 951–959.
21. Kaymak, I.; Williams, K.S.; Cantor, J.R.; Jones, R.G. Immunometabolic Interplay in the Tumor Microenvironment. *Cancer Cell* 2021, *39*, 28–37.
22. Heiden, M.G.V.; Cantley, L.C.; Thompson, C.B. Understanding the warburg effect: The metabolic requirements of cell proliferation. *Science (80-)*. **2009**, *324*, 1029–1033.
23. Dong, Y.; Tu, R.; Liu, H.; Qing, G. Regulation of cancer cell metabolism: oncogenic MYC in the driver's seat. *Signal Transduct. Target. Ther.* 2020, *5*, 1–11.
24. Maya-Mendoza, A.; Ostrakova, J.; Kosar, M.; Hall, A.; Duskova, P.; Mistrik, M.; Merchut-Maya, J.M.; Hodny, Z.; Bartkova, J.; Christensen, C.; et al. Myc and Ras oncogenes engage different energy metabolism programs and evoke distinct patterns of oxidative and DNA replication stress. *Mol. Oncol.* **2015**, *9*, 601–616.
25. Cox, A.G.; Tsomides, A.; Yimlamai, D.; Hwang, K.L.; Miesfeld, J.; Galli, G.G.; Fowl, B.H.; Fort, M.; Ma, K.Y.; Sullivan, M.R.; et al. Yap regulates glucose utilization and sustains nucleotide synthesis to enable organ growth. *EMBO J.* **2018**, *37*.
26. Pupo, E.; Avanzato, D.; Middonti, E.; Bussolino, F.; Lanzetti, L. KRAS-driven metabolic rewiring reveals novel actionable targets in cancer. *Front. Oncol.* 2019, *9*, 848.

27. Ying, H.; Kimmelman, A.C.; Lyssiotis, C.A.; Hua, S.; Chu, G.C.; Fletcher-Sanankone, E.; Locasale, J.W.; Son, J.; Zhang, H.; Coloff, J.L.; et al. Oncogenic kras maintains pancreatic tumors through regulation of anabolic glucose metabolism. *Cell* **2012**, *149*, 656–670.
28. Hoxhaj, G.; Manning, B.D. The PI3K–AKT network at the interface of oncogenic signalling and cancer metabolism. *Nat. Rev. Cancer* **2020**, *20*, 74–88.
29. Gottlob, K.; Majewski, N.; Kennedy, S.; Kandel, E.; Robey, R.B.; Hay, N. Inhibition of early apoptotic events by Akt/PKB is dependent on the first committed step of glycolysis and mitochondrial hexokinase. *Genes Dev.* **2001**, *15*, 1406–1418.
30. Cui, X.; Han, Z.; He, S.; Wu, X.; Chen, T.; Shao, C.; Chen, D.; Su, N.; Chen, Y.; Wang, T.; et al. HIF1/2 α mediates hypoxia-induced LDHA expression in human pancreatic cancer cells. *Oncotarget* **2017**, *8*, 24840–24852.
31. Saha, A.; Connelly, S.; Jiang, J.; Zhuang, S.; Amador, D.T.; Phan, T.; Pilz, R.B.; Boss, G.R. Akt phosphorylation and regulation of transketolase is a nodal point for amino acid control of purine synthesis. *Mol. Cell* **2014**, *55*, 264–276.
32. Morrish, F.; Isern, N.; Sadilek, M.; Jeffrey, M.; Hockenbery, D.M. C-Myc activates multiple metabolic networks to generate substrates for cell-cycle entry. *Oncogene* **2009**, *28*, 2485–2491.
33. Zanoni, M.; Cortesi, M.; Zamagni, A.; Arienti, C.; Pignatta, S.; Tesei, A. Modeling neoplastic disease with spheroids and organoids. *J. Hematol. Oncol.* **2020**, *13*, 1–15.
34. Martinez-Outschoorn, U.E.; Peiris-Pagés, M.; Pestell, R.G.; Sotgia, F.; Lisanti, M.P. Cancer metabolism: A therapeutic perspective. *Nat. Rev. Clin. Oncol.* **2017**, *14*, 11–31.
35. Park, J.H.; Pyun, W.Y.; Park, H.W. Cancer Metabolism: Phenotype, Signaling and Therapeutic Targets. *Cells* **2020**, *9*.
36. Luengo, A.; Gui, D.Y.; Vander Heiden, M.G. Targeting Metabolism for Cancer Therapy. *Cell Chem. Biol.* **2017**, *24*, 1161–1180.
37. Otto Warburg, B.; Wind, F.; Negelein, N.; Warburg, O.; Wind, F.; Negelein, E. THE METABOLISM OF TUMORS IN THE BODY. *J. Gen. Physiol.* **1927**, *8*, 519.
38. Warburg, O. Über den Stoffwechsel der Carcinomzelle. *Naturwissenschaften* **1924**, *12*, 1131–1137.
39. Warburg, O. On the origin of cancer cells. *Science (80-.)*. **1956**, *123*, 309–314.
40. Demetrius, L.; Tuszynski, J.A. Quantum metabolism explains the allometric scaling of metabolic rates. *J. R. Soc. Interface* **2010**, *7*, 507–514.

41. Bose, S.; Le, A. Glucose Metabolism in Cancer. In *Advances in Experimental Medicine and Biology*; Adv Exp Med Biol, 2018; Vol. 1063, pp. 3–12.
42. Le, A.; Stine, Z.E.; Nguyen, C.; Afzal, J.; Sun, P.; Hamaker, M.; Siegel, N.M.; Gouw, A.M.; Kang, B. -h.; Yu, S.-H.; et al. Tumorigenicity of hypoxic respiring cancer cells revealed by a hypoxia-cell cycle dual reporter. *Proc. Natl. Acad. Sci.* **2014**, *111*, 12486–12491.
43. Gao, C.; Shen, Y.; Jin, F.; Miao, Y.; Qiu, X. Cancer stem cells in small cell lung cancer cell line H446: Higher dependency on oxidative phosphorylation and mitochondrial substrate-level phosphorylation than non-stem cancer cells. *PLoS One* **2016**, *11*.
44. Stein, M.; Lin, H.; Jeyamohan, C.; Dvorzhinski, D.; Gounder, M.; Bray, K.; Eddy, S.; Goodin, S.; White, E.; Dipaola, R.S. Targeting tumor metabolism with 2-deoxyglucose in patients with castrate-resistant prostate cancer and advanced malignancies. *Prostate* **2010**, *70*, 1388–1394.
45. Aft, R.L.; Zhang, F.W.; Gius, D. Evaluation of 2-deoxy-D-glucose as a chemotherapeutic agent: Mechanism of cell death. *Br. J. Cancer* **2002**, *87*, 805–812.
46. Kim, E.Y.; Chung, T.W.; Han, C.W.; Park, S.Y.; Park, K.H.; Jang, S.B.; Ha, K.T. A Novel Lactate Dehydrogenase Inhibitor, 1-(Phenylseleno)-4-(Trifluoromethyl) Benzene, Suppresses Tumor Growth through Apoptotic Cell Death. *Sci. Rep.* **2019**, *9*, 1–12.
47. Belouche-Babari, M.; Wantuch, S.; Galobart, T.C.; Koniordou, M.; Parkes, H.G.; Arunan, V.; Chung, Y.L.; Eykyn, T.R.; Smith, P.D.; Leach, M.O. MCT1 inhibitor AZD3965 increases mitochondrial metabolism, facilitating combination therapy and noninvasive magnetic resonance spectroscopy. *Cancer Res.* **2017**, *77*, 5913–5924.
48. Reckzeh, E.S.; Karageorgis, G.; Schwalfenberg, M.; Ceballos, J.; Nowacki, J.; Stroet, M.C.M.; Binici, A.; Knauer, L.; Brand, S.; Choidas, A.; et al. Inhibition of Glucose Transporters and Glutaminase Synergistically Impairs Tumor Cell Growth. *Cell Chem. Biol.* **2019**, *26*, 1214-1228.e25.
49. Deberardinis, R.J.; Cheng, T. Q's next: The diverse functions of glutamine in metabolism, cell biology and cancer. *Oncogene* 2010, *29*, 313–324.
50. Altman, B.J.; Stine, Z.E.; Dang, C. V. From Krebs to clinic: Glutamine metabolism to cancer therapy. *Nat. Rev. Cancer* **2016**, *16*, 619–634.
51. Petronini, P.G.; Urbani, S.; Alfieri, R.; Borghetti, A.F.; Guidotti, G.G. Cell susceptibility to apoptosis by glutamine deprivation and rescue: Survival and apoptotic death in cultured lymphoma-leukemia cell lines. *J. Cell. Physiol.* **1996**, *169*, 175–185.

52. Mullen, A.R.; Wheaton, W.W.; Jin, E.S.; Chen, P.H.; Sullivan, L.B.; Cheng, T.; Yang, Y.; Linehan, W.M.; Chandel, N.S.; Deberardinis, R.J. Reductive carboxylation supports growth in tumour cells with defective mitochondria. *Nature* **2012**, *481*, 385–388.
53. Damiani, C.; Colombo, R.; Gaglio, D.; Mastroianni, F.; Pescini, D.; Westerhoff, H.V.; Mauri, G.; Vanoni, M.; Alberghina, L. A metabolic core model elucidates how enhanced utilization of glucose and glutamine, with enhanced glutamine-dependent lactate production, promotes cancer cell growth: The WarburQ effect. *PLoS Comput. Biol.* **2017**, *13*, e1005758.
54. Schulte, M.L.; Fu, A.; Zhao, P.; Li, J.; Geng, L.; Smith, S.T.; Kondo, J.; Coffey, R.J.; Johnson, M.O.; Rathmell, J.C.; et al. Pharmacological blockade of ASCT2-dependent glutamine transport leads to antitumor efficacy in preclinical models. *Nat. Med.* **2018**, *24*, 194–202.
55. Gross, M.I.; Demo, S.D.; Dennison, J.B.; Chen, L.; Chernov-Rogan, T.; Goyal, B.; Janes, J.R.; Laidig, G.J.; Lewis, E.R.; Li, J.; et al. Antitumor activity of the glutaminase inhibitor CB-839 in triple-negative breast cancer. *Mol. Cancer Ther.* **2014**, *13*, 890–901.
56. Gaglio, D.; Bonanomi, M.; Valtorta, S.; Bharat, R.; Ripamonti, M.; Conte, F.; Fisson, G.; Righi, N.; Napodano, E.; Papa, F.; et al. Disruption of redox homeostasis for combinatorial drug efficacy in K-Ras tumors as revealed by metabolic connectivity profiling. *Cancer Metab.* **2020**, *8*, 1–15.
57. Beloribi-Djefafia, S.; Vasseur, S.; Guillaumond, F. Lipid metabolic reprogramming in cancer cells. *Oncogenesis* **2016**, *5*, e189–e189.
58. Jeon, S.M.; Chandel, N.S.; Hay, N. AMPK regulates NADPH homeostasis to promote tumour cell survival during energy stress. *Nature* **2012**, *485*, 661–665.
59. Luo, X.; Cheng, C.; Tan, Z.; Li, N.; Tang, M.; Yang, L.; Cao, Y. Emerging roles of lipid metabolism in cancer metastasis. *Mol. Cancer* **2017**, *16*.
60. Hendrich, A.; Michalak, K. Lipids as a Target for Drugs Modulating Multidrug Resistance of Cancer Cells. *Curr. Drug Targets* **2005**, *4*, 23–30.
61. Pascual, G.; Avgustinova, A.; Mejetta, S.; Martín, M.; Castellanos, A.; Attolini, C.S.O.; Berenguer, A.; Prats, N.; Toll, A.; Hueto, J.A.; et al. Targeting metastasis-initiating cells through the fatty acid receptor CD36. *Nature* **2017**, *541*, 41–45.
62. Flavin, R.; Peluso, S.; Nguyen, P.L.; Loda, M. Fatty acid synthase as a potential therapeutic target in cancer. *Futur. Oncol.* **2010**, *6*, 551–562.
63. Hatzivassiliou, G.; Zhao, F.; Bauer, D.E.; Andreadis, C.; Shaw, A.N.; Dhanak, D.; Hingorani, S.R.; Tuveson, D.A.; Thompson, C.B. ATP citrate lyase inhibition can suppress tumor cell growth. *Cancer Cell* **2005**, *8*, 311–321.

64. Samudio, I.; Harmancey, R.; Fiegl, M.; Kantarjian, H.; Konopleva, M.; Korchin, B.; Kaluarachchi, K.; Bornmann, W.; Duvvuri, S.; Taegtmeier, H.; et al. Pharmacologic inhibition of fatty acid oxidation sensitizes human leukemia cells to apoptosis induction. *J. Clin. Invest.* **2010**, *120*, 142–156.
65. Schlaepfer, I.R.; Rider, L.; Rodrigues, L.U.; Gijón, M.A.; Pac, C.T.; Romero, L.; Cimic, A.; Sirintrapun, S.J.; Glodé, L.M.; Eckel, R.H.; et al. Lipid catabolism via CPT1 as a therapeutic target for prostate cancer. *Mol. Cancer Ther.* **2014**, *13*, 2361–2371.
66. Ashton, T.M.; Gillies McKenna, W.; Kunz-Schughart, L.A.; Higgins, G.S. Oxidative phosphorylation as an emerging target in cancer therapy. *Clin. Cancer Res.* **2018**, *24*, 2482–2490.
67. Pacheco-Velázquez, S.C.; Robledo-Cadena, D.X.; Hernández-Reséndiz, I.; Gallardo-Pérez, J.C.; Moreno-Sánchez, R.; Rodríguez-Enríquez, S. Energy Metabolism Drugs Block Triple Negative Breast Metastatic Cancer Cell Phenotype. *Mol. Pharm.* **2018**, *15*, 2151–2164.
68. Lamb, R.; Harrison, H.; Hult, J.; Smith, D.L.; Lisanti, M.P.; Sotgia, F. Mitochondria as new therapeutic targets for eradicating cancer stem cells: Quantitative proteomics and functional validation via MCT1/2 inhibition. *Oncotarget* **2014**, *5*, 11029–11037.
69. Pasquale, V.; Ducci, G.; Campioni, G.; Ventrici, A.; Assalini, C.; Busti, S.; Vanoni, M.; Vago, R.; Sacco, E. Profiling and Targeting of Energy and Redox Metabolism in Grade 2 Bladder Cancer Cells with Different Invasiveness Properties. *Cells* **2020**, *9*, 1–26.
70. Kordes, S.; Pollak, M.N.; Zwinderman, A.H.; Mathôt, R.A.; Weterman, M.J.; Beeker, A.; Punt, C.J.; Richel, D.J.; Wilmink, J.W. Metformin in patients with advanced pancreatic cancer: A double-blind, randomised, placebo-controlled phase 2 trial. *Lancet Oncol.* **2015**, *16*, 839–847.
71. Hadad, S.; Iwamoto, T.; Jordan, L.; Purdie, C.; Bray, S.; Baker, L.; Jellema, G.; Deharo, S.; Hardie, D.G.; Pusztai, L.; et al. Evidence for biological effects of metformin in operable breast cancer: A pre-operative, window-of-opportunity, randomized trial. *Breast Cancer Res. Treat.* **2011**, *128*, 783–794.
72. Shi, P.; Liu, W.; Tala, T.; Wang, H.; Li, F.; Zhang, H.; Wu, Y.; Kong, Y.; Zhou, Z.; Wang, C.; et al. Metformin suppresses triple-negative breast cancer stem cells by targeting KLF5 for degradation. *Cell Discov.* **2017**, *3*.
73. Song, C.W.; Lee, H.; Dings, R.P.M.; Williams, B.; Powers, J.; Santos, T. Dos; Choi, B.H.; Park, H.J. Metformin kills and radiosensitizes cancer cells and preferentially kills cancer stem cells. *Sci. Rep.* **2012**, *2*.
74. Menendez, J.A.; Oliveras-Ferraro, C.; Cufí, S.; Corominas-Faja, B.; Joven, J.;

- Martin-Castillo, B.; Vazquez-Martin, A. Metformin is synthetically lethal with glucose withdrawal in cancer cells. *Cell Cycle* 2012, *11*, 2782–2792.
75. Wahdan-Alaswad, R.; Fan, Z.; Edgerton, S.M.; Liu, B.; Deng, X.S.; Arnadottir, S.S.; Richer, J.K.; Anderson, S.M.; Thor, A.D. Glucose promotes breast cancer aggression and reduces metformin efficacy. *Cell Cycle* **2013**, *12*, 3759–3769.
 76. Aljofan, M.; Riethmacher, D. Anticancer activity of metformin: A systematic review of the literature. *Futur. Sci. OA* 2019, *5*.
 77. Foretz, M.; Guigas, B.; Bertrand, L.; Pollak, M.; Viollet, B. Metformin: From mechanisms of action to therapies. *Cell Metab.* 2014, *20*, 953–966.
 78. S. Wahdan-Alaswad, R.; D. Thor, A. Metformin Activity against Breast Cancer: Mechanistic Differences by Molecular Subtype and Metabolic Conditions. In *Metformin [Working Title]*; IntechOpen, 2020; Vol. i, p. 13.
 79. Wang, Y.; An, H.; Liu, T.; Qin, C.; Sesaki, H.; Guo, S.; Radovick, S.; Hussain, M.; Maheshwari, A.; Wondisford, F.E.; et al. Metformin Improves Mitochondrial Respiratory Activity through Activation of AMPK. *Cell Rep.* **2019**, *29*, 1511-1523.e5.
 80. Elgendy, M.; Cirò, M.; Hosseini, A.; Weiszmann, J.; Mazzarella, L.; Ferrari, E.; Cazzoli, R.; Curigliano, G.; DeCensi, A.; Bonanni, B.; et al. Combination of Hypoglycemia and Metformin Impairs Tumor Metabolic Plasticity and Growth by Modulating the PP2A-GSK3 β -MCL-1 Axis. *Cancer Cell* **2019**, *35*, 798-815.e5.
 81. Deavall, D.G.; Martin, E.A.; Horner, J.M.; Roberts, R. Drug-induced oxidative stress and toxicity. *J. Toxicol.* 2012, *2012*, 13.
 82. Kennedy, L.; Sandhu, J.K.; Harper, M.E.; Cuperlovic-culf, M. Role of glutathione in cancer: From mechanisms to therapies. *Biomolecules* 2020, *10*, 1–27.
 83. Chandel, N.S.; Maltepe, E.; Goldwasser, E.; Mathieu, C.E.; Simon, M.C.; Schumacker, P.T. Mitochondrial reactive oxygen species trigger hypoxia-induced transcription. *Proc. Natl. Acad. Sci. U. S. A.* **1998**, *95*, 11715–11720.
 84. Weinberg, F.; Hamanaka, R.; Wheaton, W.W.; Weinberg, S.; Joseph, J.; Lopez, M.; Kalyanaraman, B.; Mutlu, G.M.; Budinger, G.R.S.; Chandel, N.S. Mitochondrial metabolism and ROS generation are essential for Kras-mediated tumorigenicity. *Proc. Natl. Acad. Sci. U. S. A.* **2010**, *107*, 8788–8793.
 85. Gamcsik, M.P.; Kasibhatla, M.S.; Teeter, S.D.; Colvin, O.M. Glutathione levels in human tumors. *Biomarkers* 2012, *17*, 671–691.
 86. Traverso, N.; Ricciarelli, R.; Nitti, M.; Marengo, B.; Furfaro, A.L.; Pronzato, M.A.; Marinari, U.M.; Domenicotti, C. Role of glutathione in cancer progression and chemoresistance. *Oxid. Med. Cell. Longev.* 2013, *2013*.
 87. Sato, M.; Kusumi, R.; Hamashima, S.; Kobayashi, S.; Sasaki, S.; Komiyama, Y.;

- Izumikawa, T.; Conrad, M.; Bannai, S.; Sato, H. The ferroptosis inducer erastin irreversibly inhibits system xc- and synergizes with cisplatin to increase cisplatin's cytotoxicity in cancer cells. *Sci. Rep.* **2018**, *8*, 968.
88. Desai, A.; Yan, Y.; Gerson, S.L. Concise Reviews: Cancer Stem Cell Targeted Therapies: Toward Clinical Success. *Stem Cells Transl. Med.* 2019, *8*, 75–81.
89. Ciavardelli, D.; Rossi, C.; Barcaroli, D.; Volpe, S.; Consalvo, A.; Zucchelli, M.; De Cola, A.; Scavo, E.; Carollo, R.; D'Agostino, D.; et al. Breast cancer stem cells rely on fermentative glycolysis and are sensitive to 2-deoxyglucose treatment. *Cell Death Dis.* **2014**, *5*.
90. Palorini, R.; Votta, G.; Balestrieri, C.; Monestiroli, A.; Olivieri, S.; Vento, R.; Chiaradonna, F. Energy metabolism characterization of a novel cancer stem cell-like line 3AB-OS. *J. Cell. Biochem.* **2014**, *115*, 368–379.
91. Zhou, Y.; Zhou, Y.; Shingu, T.; Feng, L.; Chen, Z.; Ogasawara, M.; Keating, M.J.; Kondo, S.; Huang, P. Metabolic alterations in highly tumorigenic glioblastoma cells: Preference for hypoxia and high dependency on glycolysis. *J. Biol. Chem.* **2011**, *286*, 32843–32853.
92. De Luca, A.; Fiorillo, M.; Peiris-Pagès, M.; Ozsvari, B.; Smith, D.L.; Sanchez-Alvarez, R.; Martinez-Outschoorn, U.E.; Cappello, A.R.; Pezzi, V.; Lisanti, M.P.; et al. Mitochondrial biogenesis is required for the anchorage-independent survival and propagation of stem-like cancer cells. *Oncotarget* **2015**, *6*, 14777–14795.
93. Lagadinou, E.D.; Sach, A.; Callahan, K.; Rossi, R.M.; Neering, S.J.; Minhajuddin, M.; Ashton, J.M.; Pei, S.; Grose, V.; O'Dwyer, K.M.; et al. BCL-2 inhibition targets oxidative phosphorylation and selectively eradicates quiescent human leukemia stem cells. *Cell Stem Cell* **2013**, *12*, 329–341.
94. Pastò, A.; Bellio, C.; Pilotto, G.; Ciminale, V.; Silic-Benussi, M.; Guzzo, G.; Rasola, A.; Frasson, C.; Nardo, G.; Zulato, E.; et al. Cancer stem cells from epithelial ovarian cancer patients privilege oxidative phosphorylation, and resist glucose deprivation. *Oncotarget* **2014**, *5*, 4305–4319.
95. Sancho, P.; Burgos-Ramos, E.; Tavera, A.; Bou Kheir, T.; Jagust, P.; Schoenhals, M.; Barneda, D.; Sellers, K.; Campos-Olivas, R.; Graña, O.; et al. MYC/PGC-1 α Balance Determines the Metabolic Phenotype and Plasticity of Pancreatic Cancer Stem Cells. *Cell Metab.* **2015**, *22*, 590–605.
96. Gammon, L.; Biddle, A.; Heywood, H.K.; Johannessen, A.C.; Mackenzie, I.C. Subsets of Cancer Stem Cells Differ Intrinsically in Their Patterns of Oxygen Metabolism. *PLoS One* **2013**, *8*, 62493.
97. Cheong, J.H.; Park, E.S.; Liang, J.; Dennison, J.B.; Tsavachidou, D.; Nguyen-Charles, C.; Cheng, K.W.; Hall, H.; Zhang, D.; Lu, Y.; et al. Dual inhibition of tumor energy pathway by 2-deoxyglucose and metformin is effective against a

- broad spectrum of preclinical cancer models. *Mol. Cancer Ther.* **2011**, *10*, 2350–2362.
98. Nabi, K.; Le, A. The intratumoral heterogeneity of cancer metabolism. In *Advances in Experimental Medicine and Biology*; Springer, Cham, 2018; Vol. 1063, pp. 131–145.
 99. Damiani, C.; Gaglio, D.; Sacco, E.; Alberghina, L.; Vanoni, M. Systems metabolomics: from metabolomic snapshots to design principles. *Curr. Opin. Biotechnol.* **2020**, *63*, 190–199.
 100. Franchi-Mendes, T.; Eduardo, R.; Domenici, G.; Brito, C. 3D cancer models: Depicting cellular crosstalk within the tumour microenvironment. *Cancers (Basel)*. **2021**, *13*.
 101. Rodrigues, J.; Heinrich, M.A.; Teixeira, L.M.; Prakash, J. 3D In Vitro Model (R)evolution: Unveiling Tumor–Stroma Interactions. *Trends in Cancer* **2021**, *7*, 249–264.
 102. Klemm, F.; Joyce, J.A. Microenvironmental regulation of therapeutic response in cancer. *Trends Cell Biol.* **2015**, *25*, 198–213.
 103. Guo, S.; Deng, C.X. Effect of stromal cells in tumor microenvironment on metastasis initiation. *Int. J. Biol. Sci.* **2018**, *14*, 2083–2093.
 104. Boedtker, E.; Pedersen, S.F. The Acidic Tumor Microenvironment as a Driver of Cancer. *Annu. Rev. Physiol.* **2020**, *82*, 103–126.
 105. Li, Z.; Sun, C.; Qin, Z. Metabolic reprogramming of cancer-associated fibroblasts and its effect on cancer cell reprogramming. *Theranostics* **2021**, *11*, 8322–8336.
 106. Chen, D.; Zhang, X.; Li, Z.; Zhu, B. Metabolic regulatory crosstalk between tumor microenvironment and tumor-associated macrophages. *Theranostics* **2020**, *11*, 1016–1030.
 107. Mantovani, A.; Sozzani, S.; Locati, M.; Allavena, P.; Sica, A. Macrophage polarization: Tumor-associated macrophages as a paradigm for polarized M2 mononuclear phagocytes. *Trends Immunol.* **2002**, *23*, 549–555.
 108. Quail, D.F.; Joyce, J.A. Microenvironmental regulation of tumor progression and metastasis. *Nat. Med.* **2013**, *19*, 1423–1437.
 109. Xing, F.; Saidou, J.; Watabe, K. Cancer associated fibroblasts (CAFs) in tumor microenvironment. *Front. Biosci.* **2010**, *15*, 166–179.
 110. Pavlides, S.; Whitaker-Menezes, D.; Castello-Cros, R.; Flomenberg, N.; Witkiewicz, A.K.; Frank, P.G.; Casimiro, M.C.; Wang, C.; Fortina, P.; Addya, S.; et al. The reverse Warburg effect: Aerobic glycolysis in cancer associated fibroblasts and the tumor stroma. *Cell Cycle* **2009**, *8*, 3984–4001.

111. Zhang, Z.; Gao, Z.; Rajthala, S.; Sapkota, D.; Dongre, H.; Parajuli, H.; Suliman, S.; Das, R.; Li, L.; Bindoff, L.A.; et al. Metabolic reprogramming of normal oral fibroblasts correlated with increased glycolytic metabolism of oral squamous cell carcinoma and precedes their activation into carcinoma associated fibroblasts. *Cell. Mol. Life Sci.* **2020**, *77*, 1115–1133.
112. Ippolito, L.; Morandi, A.; Taddei, M.L.; Parri, M.; Comito, G.; Iscaro, A.; Raspollini, M.R.; Magherini, F.; Rapizzi, E.; Masquelier, J.; et al. Cancer-associated fibroblasts promote prostate cancer malignancy via metabolic rewiring and mitochondrial transfer. *Oncogene* **2019**, *38*, 5339–5355.
113. Bizzarri, M.; Cucina, A. Tumor and the microenvironment: A chance to reframe the paradigm of carcinogenesis? *Biomed Res. Int.* **2014**, *2014*.
114. Junttila, M.R.; De Sauvage, F.J. Influence of tumour micro-environment heterogeneity on therapeutic response. *Nature* **2013**, *501*, 346–354.
115. Nakasone, E.S.; Askautrud, H.A.; Kees, T.; Park, J.H.; Plaks, V.; Ewald, A.J.; Fein, M.; Rasch, M.G.; Tan, Y.X.; Qiu, J.; et al. Imaging Tumor-Stroma Interactions during Chemotherapy Reveals Contributions of the Microenvironment to Resistance. *Cancer Cell* **2012**, *21*, 488–503.
116. Jain, R.K.; Duda, D.G.; Clark, J.W.; Loeffler, J.S. Lessons from phase III clinical trials on anti-VEGF therapy for cancer. *Nat. Clin. Pract. Oncol.* **2006**, *3*, 24–40.
117. Pardoll, D.M. The blockade of immune checkpoints in cancer immunotherapy. *Nat. Rev. Cancer* **2012**, *12*, 252–264.
118. Han, S.J.; Kwon, S.; Kim, K.S. Challenges of applying multicellular tumor spheroids in preclinical phase. *Cancer Cell Int.* **2021**, *21*, 1–19.
119. Mittler, F.; Obeid, P.; Rulina, A. V.; Haguët, V.; Gidrol, X.; Balakirev, M.Y. High-content monitoring of drug effects in a 3D spheroid model. *Front. Oncol.* **2017**, *7*.
120. Jensen, C.; Teng, Y. Is It Time to Start Transitioning From 2D to 3D Cell Culture? *Front. Mol. Biosci.* **2020**, *7*, 33.
121. Costa, E.C.; Moreira, A.F.; de Melo-Diogo, D.; Gaspar, V.M.; Carvalho, M.P.; Correia, I.J. 3D tumor spheroids: an overview on the tools and techniques used for their analysis. *Biotechnol. Adv.* **2016**, *34*, 1427–1441.
122. Langhans, S.A. Three-dimensional in vitro cell culture models in drug discovery and drug repositioning. *Front. Pharmacol.* **2018**, *9*, 1–14.
123. Metzger, W.; Sossong, D.; Bächle, A.; Pütz, N.; Wennemuth, G.; Pohlemann, T.; Oberringer, M. The liquid overlay technique is the key to formation of co-culture spheroids consisting of primary osteoblasts, fibroblasts and endothelial cells. *Cytotherapy* **2011**, *13*, 1000–1012.

124. Costa, E.C.; Gaspar, V.M.; Coutinho, P.; Correia, I.J. Optimization of Liquid Overlay Technique to Formulate Heterogenic 3D Co-Cultures Models. *Biotechnol. Bioeng* **2014**, *111*, 1672–1685.
125. Carlsson, J.; Yuhas, J.M. Liquid-overlay culture of cellular spheroids. *Recent Results Cancer Res.* 1984, *95*, 1–23.
126. Long, T.J.; Sprenger, C.C.; Plymate, S.R.; Ratner, B.D. Prostate cancer xenografts engineered from 3D precision-porous poly(2-hydroxyethyl methacrylate) hydrogels as models for tumorigenesis and dormancy escape. *Biomaterials* **2014**, *35*, 8164–8174.
127. Andersen, T.; Auk-Emblem, P.; Dornish, M. 3D Cell Culture in Alginate Hydrogels. *Microarrays* **2015**, *4*, 133–161.
128. Hume, R.D.; Pensa, S.; Brown, E.J.; Kreuzaler, P.A.; Hitchcock, J.; Husmann, A.; Campbell, J.J.; Lloyd-Thomas, A.O.; Cameron, R.E.; Watson, C.J. Tumour cell invasiveness and response to chemotherapeutics in adipocyte invested 3D engineered anisotropic collagen scaffolds. *Sci. Rep.* **2018**, *8*, 12658.
129. Ferreira, L.P.; Gaspar, V.M.; Mano, J.F. Decellularized Extracellular Matrix for Bioengineering Physiomimetic 3D in Vitro Tumor Models. *Trends Biotechnol.* 2020, *38*, 1397–1414.
130. Drost, J.; Clevers, H. Organoids in cancer research. *Nat. Rev. Cancer* **2018**, *18*, 407–418.
131. Bhatia, S.N.; Ingber, D.E. Microfluidic organs-on-chips. *Nat. Biotechnol.* 2014, *32*, 760–772.
132. Gilardi, M.; Bersini, S.; Valtorta, S.; Proietto, M.; Crippa, M.; Boussohier-Calleja, A.; Labelle, M.; Moresco, R.M.; Vanoni, M.; Kamm, R.D.; et al. The driving role of the Cdk5/Tln1/FAK5732 axis in cancer cell extravasation dissected by human vascularized microfluidic models. *Biomaterials* **2021**, *276*, 120975.
133. Korving, J.; Moll, J.; Voest, E.E.; Weeber, F.; de Ligt, J.; Rottenberg, S.; Bounova, G.; Boj, S.F.; Kopper, O.; Vries, R.G.J.; et al. A Living Biobank of Breast Cancer Organoids Captures Disease Heterogeneity. *Cell* **2017**, *172*, 373-386.e10.
134. Clevers, H. Modeling Development and Disease with Organoids. *Cell* **2016**, *165*, 1586–1597.
135. Sutherland, R.M. Cell and environment interactions in tumor microregions: The multicell spheroid model. *Science (80-.)*. 1988, *240*, 177–184.
136. Sutherland, R.M.; Sordat, B.; Bamat, J.; Gabbert, H.; Bourrat, B.; Mueller-Klieser, W. Oxygenation and Differentiation in Multicellular Spheroids of Human Colon Carcinoma. *Cancer Res.* **1986**, *46*, 5320–5329.

137. Chaicharoenaudomrung, N.; Kunhorm, P.; Noisa, P. Three-dimensional cell culture systems as an in vitro platform for cancer and stem cell modeling. *World J. Stem Cells* **2019**, *11*, 1065–1083.
138. Nederman, T.; Glimelius, B.; Norling, B.; Carlsson, J.; Brunk, U. Demonstration of an Extracellular Matrix in Multicellular Tumor Spheroids. *Cancer Res.* **1984**, *44*, 3090–3097.
139. Ivascu, A.; Kubbies, M. Diversity of cell-mediated adhesions in breast cancer spheroids. *Int. J. Oncol.* **2007**, *31*, 1403–1413.
140. Tesei, A.; Sarnelli, A.; Arienti, C.; Menghi, E.; Medri, L.; Gabucci, E.; Pignatta, S.; Falconi, M.; Silvestrini, R.; Zoli, W.; et al. In vitro irradiation system for radiobiological experiments. *Radiat. Oncol.* **2013**, *8*, 257.
141. Minchinton, A.I.; Tannock, I.F. Drug penetration in solid tumours. *Nat. Rev. Cancer* **2006**, *6*, 583–592.
142. Trédan, O.; Galmarini, C.M.; Patel, K.; Tannock, I.F. Drug resistance and the solid tumor microenvironment. *J. Natl. Cancer Inst.* **2007**, *99*, 1441–1454.
143. Wigerup, C.; Pålman, S.; Bexell, D. Therapeutic targeting of hypoxia and hypoxia-inducible factors in cancer. *Pharmacol. Ther.* **2016**, *164*, 152–169.
144. Franco, S.S.; Szczesna, K.; Iliou, M.S.; Al-Qahtani, M.; Mobasher, A.; Kobolák, J.; Dinnyés, A. In vitro models of cancer stem cells and clinical applications. *BMC Cancer* **2016**, *16*.
145. Mcmillin, D.W.; Negri, J.M.; Mitsiades, C.S. The role of tumour-stromal interactions in modifying drug response: Challenges and opportunities. *Nat. Rev. Drug Discov.* **2013**, *12*, 217–228.
146. Majety, M.; Pradel, L.P.; Gies, M.; Ries, C.H. Fibroblasts influence survival and therapeutic response in a 3D co-culture model. *PLoS One* **2015**, *10*.
147. Hoffmann, O.I.; Ilmberger, C.; Magosch, S.; Joka, M.; Jauch, K.W.; Mayer, B. Impact of the spheroid model complexity on drug response. *J. Biotechnol.* **2015**, *205*, 14–23.
148. OpenStax College *Anatomy and Physiology Volume 3 of 3*; 2013; Vol. 2; ISBN 978-1-304-84331-9.
149. Overview of the Breast - Breast Pathology | Johns Hopkins Pathology Available online: <https://pathology.jhu.edu/breast/overview> (accessed on Jan 10, 2022).
150. Frederic H. Martini, Michael J. Timmons, R.B.T. *Human Anatomy*; Seventh ed.; Pearson, 2012; ISBN 0471326429.
151. Veronesi, U.; Goldhirsch, A.; Veronesi, P.; Gentilini, O.D.; Leonardi, M.C. *Breast cancer: Innovations in research and management*; 2017; ISBN 9783319488486.

152. Polyak, K. Breast cancer: Origins and evolution. *J. Clin. Invest.* 2007, *117*, 3155–3163.
153. Allred, D.C.; Mohsin, S.K.; Fuqua, S.A.W. Histological and biological evolution of human premalignant breast disease. In Proceedings of the Endocrine-Related Cancer; 2001; Vol. 8, pp. 47–61.
154. Rojas, K.; Stuckey, A. Breast Cancer Epidemiology and Risk Factors. *Clin. Obstet. Gynecol.* **2016**, *59*, 651–672.
155. Santen, R.; Cavalieri, E.; Rogan, E.; Russo, J.; Guttenplan, J.; Ingle, J.; Yue, W. Estrogen mediation of breast tumor formation involves estrogen receptor-dependent, as well as independent, genotoxic effects. In Proceedings of the Annals of the New York Academy of Sciences; Blackwell Publishing Inc., 2009; Vol. 1155, pp. 132–140.
156. Hamajima, N.; Hirose, K.; Tajima, K.; Rohan, T.; Friedenreich, C.M.; Calle, E.E.; Gapstur, S.M.; Patel, A. V.; Coates, R.J.; Liff, J.M.; et al. Menarche, menopause, and breast cancer risk: Individual participant meta-analysis, including 118 964 women with breast cancer from 117 epidemiological studies. *Lancet Oncol.* **2012**, *13*, 1141–1151.
157. Press, D.J.; Sullivan-Halley, J.; Ursin, G.; Deapen, D.; McDonald, J.A.; Strom, B.L.; Norman, S.A.; Simon, M.S.; Marchbanks, P.A.; Folger, S.G.; et al. Breast cancer risk and ovariectomy, hysterectomy, and tubal sterilization in the women’s contraceptive and reproductive experiences study. *Am. J. Epidemiol.* **2011**, *173*, 38–47.
158. Ewertz, M.; Duffy, S.W.; Adami, H. -O; Kvåle, G.; Lund, E.; Meirik, O.; Møller, A.; Soini, I.; Tulinus, H. Age at first birth, parity and risk of breast cancer: A meta-analysis of 8 studies from the nordic countries. *Int. J. Cancer* **1990**, *46*, 597–603.
159. Beral, V.; Bull, D.; Doll, R.; Peto, R.; Reeves, G. Breast cancer and breastfeeding: Collaborative reanalysis of individual data from 47 epidemiological studies in 30 countries, including 50 302 women with breast cancer and 96 973 women without the disease. *Lancet* **2002**, *360*, 187–195.
160. Beaver, E.F.; Buist, D.S.M.; Barlow, W.E.; Malone, K.E.; Reed, S.D.; Li, C.I. Recent oral contraceptive use by formulation and breast cancer risk among women 20 to 49 years of age. *Cancer Res.* **2014**, *74*, 4078–4089.
161. Rossouw, J.E.; Anderson, G.L.; Prentice, R.L.; LaCroix, A.Z.; Kooperberg, C.; Stefanick, M.L.; Jackson, R.D.; Beresford, S.A.A.; Howard, B. V.; Johnson, K.C.; et al. Risks and benefits of estrogen plus progestin in healthy postmenopausal women: Principal results from the women’s health initiative randomized controlled trial. *J. Am. Med. Assoc.* **2002**, *288*, 321–333.

162. Renehan, A.G.; Egger, M.; Zwahlen, M. Body Mass Index and Cancer Risk: The Evidence for Causal Association. *Open Obes. J.* **2014**, *2*, 12–22.
163. Aicr; WCRF Diet, nutrition, physical activity and breast cancer.
164. Hamajima, N.; Hirose, K.; Tajima, K.; Rohan, T.; Calle, E.E.; Heath, C.W.; Coates, R.J.; Liff, J.M.; Talamini, R.; Chantarakul, N.; et al. Alcohol, tobacco and breast cancer - Collaborative reanalysis of individual data from 53 epidemiological studies, including 58 515 women with breast cancer and 95 067 women without the disease. *Br. J. Cancer* **2002**, *87*, 1234–1245.
165. Goss, P.E.; Sierra, S. Current perspectives on radiation-induced breast cancer. *J. Clin. Oncol.* 1998, *16*, 338–347.
166. Lalloo, F.; Evans, D.G. Familial Breast Cancer. *Clin. Genet.* 2012, *82*, 105–114.
167. Larsen, M.J.; Thomassen, M.; Gerdes, A.M.; Kruse, T.A. Hereditary breast cancer: Clinical, Pathological and molecular characteristics. *Breast Cancer Basic Clin. Res.* **2014**, *8*, 145–155.
168. Mavaddat, N.; Barrowdale, D.; Andrulis, I.L.; Domchek, S.M.; Eccles, D.; Nevanlinna, H.; Ramus, S.J.; Spurdle, A.; Robson, M.; Sherman, M.; et al. Pathology of breast and ovarian cancers among BRCA1 and BRCA2 mutation carriers: Results from the consortium of investigators of modifiers of BRCA1/2 (CIMBA). *Cancer Epidemiol. Biomarkers Prev.* **2012**, *21*, 134–147.
169. DeSantis, C.E.; Ma, J.; Gaudet, M.M.; Newman, L.A.; Miller, K.D.; Goding Sauer, A.; Jemal, A.; Siegel, R.L. Breast cancer statistics, 2019. *CA. Cancer J. Clin.* **2019**, *69*, 438–451.
170. DeSantis, C.E.; Bray, F.; Ferlay, J.; Lortet-Tieulent, J.; Anderson, B.O.; Jemal, A. International variation in female breast cancer incidence and mortality rates. *Cancer Epidemiol. Biomarkers Prev.* **2015**, *24*, 1495–1506.
171. Azamjah, N.; Soltan-Zadeh, Y.; Zayeri, F. Global trend of breast cancer mortality rate: A 25-year study. *Asian Pacific J. Cancer Prev.* **2019**, *20*, 2015–2020.
172. NCI Cancer Statistics Review, 1975-2017 - SEER Statistics Available online: https://seer.cancer.gov/archive/csr/1975_2016/ (accessed on Jan 9, 2022).
173. Heer, E.; Harper, A.; Escandor, N.; Sung, H.; McCormack, V.; Fidler-Benaoudia, M.M. Global burden and trends in premenopausal and postmenopausal breast cancer: a population-based study. *Lancet Glob. Heal.* **2020**, *8*, e1027–e1037.
174. Tsang, J.Y.S.; Tse, G.M. Molecular Classification of Breast Cancer. *Adv. Anat. Pathol.* **2020**, *27*, 27–35.
175. Pathology Outlines - WHO classification Available online: <https://www.pathologyoutlines.com/topic/breastmalignantwhoclassification.html> (accessed on Jan 11, 2022).

176. Malhotra, G.K.; Zhao, X.; Band, H.; Band, V. Histological, molecular and functional subtypes of breast cancers. *Cancer Biol. Ther.* 2010, *10*, 955–960.
177. Harbeck, N.; Penault-Llorca, F.; Cortes, J.; Gnant, M.; Houssami, N.; Poortmans, P.; Ruddy, K.; Tsang, J.; Cardoso, F. Breast cancer. *Nat. Rev. Dis. Prim.* **2019**, *5*, 1–31.
178. Acheampong, T.; Kehm, R.D.; Terry, M.B.; Argov, E.L.; Tehranifar, P. Incidence Trends of Breast Cancer Molecular Subtypes by Age and Race/Ethnicity in the US From 2010 to 2016. *JAMA Netw. open* **2020**, *3*, e2013226.
179. PDQ Adult Treatment Editorial Board *Breast Cancer Treatment During Pregnancy (PDQ®): Patient Version*; National Cancer Institute (US), 2002;
180. Mariotto, A.B.; Etzioni, R.; Hurlbert, M.; Penberthy, L.; Mayer, M. Estimation of the number of women living with metastatic breast cancer in the United States. *Cancer Epidemiol. Biomarkers Prev.* **2017**, *26*, 809–815.
181. Buonomo, O.C.; Caredda, E.; Portarena, I.; Vanni, G.; Orlandi, A.; Bagni, C.; Petrella, G.; Palombi, L.; Orsaria, P. New insights into the metastatic behavior after breast cancer surgery, according to well-established clinicopathological variables and molecular subtypes. *PLoS One* **2017**, *12*.
182. Wong, E.; Robello, J. Breast cancer pathogenesis and histologic vs. molecular subtypes | McMaster Pathophysiology Review Available online: <http://www.pathophys.org/breast-cancer/breastcancer-copy/> (accessed on Jan 12, 2022).
183. Waks, A.G.; Winer, E.P. Breast Cancer Treatment: A Review. *JAMA - J. Am. Med. Assoc.* **2019**, *321*, 288–300.
184. Tchou, J.; Sonnad, S.S.; Bergey, M.R.; Basu, S.; Tomaszewski, J.; Alavi, A.; Schnall, M. Degree of tumor FDG uptake correlates with proliferation index in triple negative breast cancer. *Mol. Imaging Biol.* **2010**, *12*, 657–662.
185. Choi, J.; Kim, D.H.; Jung, W.H.; Koo, J.S. Metabolic interaction between cancer cells and stromal cells according to breast cancer molecular subtype. *Breast Cancer Res.* **2013**, *15*, R78.
186. Jeon, H.M.; Kim, D.H.; Jung, W.H.; Koo, J.S. Expression of cell metabolism-related genes in different molecular subtypes of triple-negative breast cancer. *Tumori* **2013**, *99*, 555–564.
187. Santidrian, A.F.; Matsuno-Yagi, A.; Ritland, M.; Seo, B.B.; LeBoeuf, S.E.; Gay, L.J.; Yagi, T.; Felding-Habermann, B. Mitochondrial complex I activity and NAD⁺/NADH balance regulate breast cancer progression. *J. Clin. Invest.* **2013**, *123*, 1068–1081.
188. Antalis, C.J.; Arnold, T.; Rasool, T.; Lee, B.; Buhman, K.K.; Siddiqui, R.A. High

- ACAT1 expression in estrogen receptor negative basal-like breast cancer cells is associated with LDL-induced proliferation. *Breast Cancer Res. Treat.* **2010**, *122*, 661–670.
189. Kung, H.N.; Marks, J.R.; Chi, J.T. Glutamine synthetase is a genetic determinant of cell type-specific glutamine independence in breast epithelia. *PLoS Genet.* **2011**, *7*, 1002229.
 190. Sotgia, F.; Martinez-Outschoorn, U.E.; Pavlides, S.; Howell, A.; Pestell, R.G.; Lisanti, M.P. Understanding the Warburg effect and the prognostic value of stromal caveolin-1 as a marker of a lethal tumor microenvironment. *Breast Cancer Res.* **2011**, *13*, 213.
 191. Martinez-Outschoorn, U.E.; Pavlides, S.; Whitaker-Menezes, D.; Daumer, K.M.; Milliman, J.N.; Chiavarina, B.; Migneco, G.; Witkiewicz, A.K.; Martinez-Cantarin, M.P.; Flomenberg, N.; et al. Tumor cells induce the cancer associated fibroblast phenotype via caveolin-1 degradation: Implications for breast cancer and DCIS therapy with autophagy inhibitors. *Cell Cycle* **2010**, *9*, 2423–2433.
 192. Ilaria Elia, Roberta Schmieder, S.C.& S.-M.F.; Elia, I.; Schmieder, R.; Christen, S.; Fendt, S.M. Organ specific cancer metabolism and its potential for therapy. In *Handbook of Experimental Pharmacology*; Springer, Cham, 2015; Vol. 233, pp. 321–353.
 193. Mostofi, F.K.; Sobin, L.H.; Torloni, H.; Organization, W.H. Histological typing of urinary bladder tumours. **1973**.
 194. Epstein, J.I.; Amin, M.B.; Reuter, V.R.; Mostofi, F.K.; Algaba, F.; Allsbrook, W.C.; Ayala, A.G.; Becich, M.J.; Beltrán, A.L.; Boccon-Gibód, L.; et al. The World Health Organization/International Society of Urological Pathology consensus classification of urothelial (transitional cell) neoplasms of the urinary bladder. *Am. J. Surg. Pathol.* **1998**, *22*, 1435–1448.
 195. PubMed Health. A service of the National Library of Medicine, N.I. of H. Bladder Cancer Treatment (PDQ®). *PubMed Heal.* **2021**.
 196. Humphrey, P.A.; Moch, H.; Cubilla, A.L.; Ulbright, T.M.; Reuter, V.E. The 2016 WHO Classification of Tumours of the Urinary System and Male Genital Organs—Part B: Prostate and Bladder Tumours. *Eur. Urol.* **2016**, *70*, 106–119.
 197. Babjuk, M.; Burger, M.; Compérat, E.M.; Gontero, P.; Mostafid, A.H.; Palou, J.; van Rhijn, B.W.G.; Rouprêt, M.; Shariat, S.F.; Sylvester, R.; et al. European Association of Urology Guidelines on Non-muscle-invasive Bladder Cancer (TaT1 and Carcinoma In Situ) - 2019 Update. *Eur. Urol.* **2019**, *76*, 639–657.
 198. Sanli, O.; Dobruch, J.; Knowles, M.A.; Burger, M.; Alemozaffar, M.; Nielsen, M.E.; Lotan, Y. Bladder cancer. *Nat. Rev. Dis. Prim.* **2017**, *3*, 17022.
 199. Sjö Dahl, G.; Lauss, M.; Lövgren, K.; Chebil, G.; Gudjonsson, S.; Veerla, S.;

- Patschan, O.; Aine, M.; Fernö, M.; Ringnér, M.; et al. A molecular taxonomy for urothelial carcinoma. *Clin. Cancer Res.* **2012**, *18*, 3377–3386.
200. Hedegaard, J.; Lamy, P.; Nordentoft, I.; Algaba, F.; Høyer, S.; Ulhøi, B.P.; Vang, S.; Reinert, T.; Hermann, G.G.; Mogensen, K.; et al. Comprehensive Transcriptional Analysis of Early-Stage Urothelial Carcinoma. *Cancer Cell* **2016**, *30*, 27–42.
201. Damrauer, J.S.; Hoadley, K.A.; Chism, D.D.; Fan, C.; Tiganelli, C.J.; Wobker, S.E.; Yeh, J.J.; Milowsky, M.I.; Iyer, G.; Parker, J.S.; et al. Intrinsic subtypes of high-grade bladder cancer reflect the hallmarks of breast cancer biology. *Proc. Natl. Acad. Sci. U. S. A.* **2014**, *111*, 3110–3115.
202. Choi, W.; Porten, S.; Kim, S.; Willis, D.; Plimack, E.R.; Hoffman-Censits, J.; Roth, B.; Cheng, T.; Tran, M.; Lee, I.L.; et al. Identification of Distinct Basal and Luminal Subtypes of Muscle-Invasive Bladder Cancer with Different Sensitivities to Frontline Chemotherapy. *Cancer Cell* **2014**, *25*, 152–165.
203. Antoni, S.; Ferlay, J.; Soerjomataram, I.; Znaor, A.; Jemal, A.; Bray, F. Bladder Cancer Incidence and Mortality: A Global Overview and Recent Trends. *Eur. Urol.* **2017**, *71*, 96–108.
204. Van Oers, J.M.M.; Adam, C.; Denzinger, S.; Stoehr, R.; Bertz, S.; Zaak, D.; Stief, C.; Hofstaedter, F.; Zwarthoff, E.C.; Van Der Kwast, T.H.; et al. Chromosome 9 deletions are more frequent than FGFR3 mutations in flat urothelial hyperplasias of the bladder. *Int. J. Cancer* **2006**, *119*, 1212–1215.
205. McKenney, J.K.; Desai, S.; Cohen, C.; Amin, M.B. Discriminatory immunohistochemical staining of urothelial carcinoma in situ and non-neoplastic urothelium: An analysis of cytokeratin 20, p53, and CD44 antigens. *Am. J. Surg. Pathol.* **2001**, *25*, 1074–1078.
206. Sfakianos, J.P.; Lin Gellert, L.; Maschino, A.; Gotto, G.T.; Kim, P.H.; Al-Ahmadie, H.; Bochner, B.H. The role of PTEN tumor suppressor pathway staining in carcinoma in situ of the bladder. *Urol. Oncol. Semin. Orig. Investig.* **2014**, *32*, 657–662.
207. American Cancer Society Bladder Cancer Signs and Symptoms Available online: <https://www.cancer.org/cancer/bladder-cancer/detection-diagnosis-staging/signs-and-symptoms.html> (accessed on Jan 16, 2022).
208. Society, A.C. Tests for Bladder Cancer Available online: <https://www.cancer.org/cancer/bladder-cancer/detection-diagnosis-staging/how-diagnosed.html> (accessed on Jan 16, 2022).
209. Chang, S.S.; Boorjian, S.A.; Chou, R.; Clark, P.E.; Daneshmand, S.; Konety, B.R.; Pruthi, R.; Quale, D.Z.; Ritch, C.R.; Seigne, J.D.; et al. Diagnosis and Treatment of Non-Muscle Invasive Bladder Cancer: AUA/SUO Guideline. *J. Urol.* **2016**, *196*,

1021–1029.

210. Massari, F.; Ciccamese, C.; Santoni, M.; Iacovelli, R.; Mazzucchelli, R.; Piva, F.; Scarpelli, M.; Berardi, R.; Tortora, G.; Lopez-Beltran, A.; et al. Metabolic phenotype of bladder cancer. *Cancer Treat. Rev.* 2016, *45*, 46–57.
211. Von Rundstedt, F.C.; Rajapakshe, K.; Ma, J.; Arnold, J.M.; Gohlke, J.; Putluri, V.; Krishnapuram, R.; Piyarathna, D.B.; Lotan, Y.; Gödde, D.; et al. Integrative Pathway Analysis of Metabolic Signature in Bladder Cancer: A Linkage to the Cancer Genome Atlas Project and Prediction of Survival. *J. Urol.* **2016**, *195*, 1911–1919.
212. Conde, V.R.; Oliveira, P.F.; Nunes, A.R.; Rocha, C.S.; Ramalhosa, E.; Pereira, J.A.; Alves, M.G.; Silva, B.M. The progression from a lower to a higher invasive stage of bladder cancer is associated with severe alterations in glucose and pyruvate metabolism. *Exp. Cell Res.* **2015**, *335*, 91–98.
213. Jebar, A.H.; Hurst, C.D.; Tomlinson, D.C.; Johnston, C.; Taylor, C.F.; Knowles, M.A. FGFR3 and Ras gene mutations are mutually exclusive genetic events in urothelial cell carcinoma. *Oncogene* **2005**, *24*, 5218–5225.
214. Wang, X.; Wu, G.; Cao, G.; Yang, L.; Xu, H.; Huang, J.; Hou, J. Zoledronic acid inhibits the pentose phosphate pathway through attenuating the Ras-TAp73-G6PD axis in bladder cancer cells. *Mol. Med. Rep.* **2015**, *12*, 4620–4625.
215. Jiang, B.; Li, E.H.; Lu, Y.Y.; Jiang, Q.; Cui, D.; Jing, Y.F.; Xia, S.J. Inhibition of fatty-acid synthase suppresses p-akt and induces apoptosis in bladder cancer. *Urology* **2012**, *80*, 484.e9-484.e15.
216. Kennecke, H.; Yerushalmi, R.; Woods, R.; Cheang, M.C.U.; Voduc, D.; Speers, C.H.; Nielsen, T.O.; Gelmon, K. Metastatic behavior of breast cancer subtypes. *J. Clin. Oncol.* **2010**, *28*, 3271–3277.
217. Foulkes, W.D.; Smith, I.E.; Reis-Filho, J.S. Triple-Negative Breast Cancer. *N. Engl. J. Med.* **2010**, *363*, 1938–1948.
218. Bareche, Y.; Venet, D.; Ignatiadis, M.; Aftimos, P.; Piccart, M.; Rothe, F.; Sotiriou, C. Unravelling triple-negative breast cancer molecular heterogeneity using an integrative multiomic analysis. *Ann. Oncol.* **2018**, *29*, 895–902.
219. Lanning, N.J.; Castle, J.P.; Singh, S.J.; Leon, A.N.; Tovar, E.A.; Sanghera, A.; MacKeigan, J.P.; Filipp, F. V; Graveel, C.R. Metabolic profiling of triple-negative breast cancer cells reveals metabolic vulnerabilities. *Cancer Metab.* **2017**, *5*.
220. Arundhati, J.R.D.; Mathur, S.R.; Gogia, A.; Deo, S.V.S.; Mohapatra, P.; Prasad, C.P. Metabolic changes in triple negative breast cancer-focus on aerobic glycolysis. *Mol. Biol. Rep.* 2021, *48*, 4733–4745.
221. Lovitt, C.J.; Shelper, T.B.; Avery, V.M. Advanced cell culture techniques for

- cancer drug discovery. *Biology (Basel)*. 2014, **3**, 345–367.
222. Westhouse, R.A. Safety assessment considerations and strategies for targeted small molecule cancer therapeutics in drug discovery. *Toxicol. Pathol.* 2010, **38**, 165–168.
223. Gomez-Roman, N.; Stevenson, K.; Gilmour, L.; Hamilton, G.; Chalmers, A.J. A novel 3D human glioblastoma cell culture system for modeling drug and radiation responses. *Neuro. Oncol.* **2017**, **19**, 229–241.
224. Weigelt, B.; Ghajar, C.M.; Bissell, M.J. The need for complex 3D culture models to unravel novel pathways and identify accurate biomarkers in breast cancer. *Adv. Drug Deliv. Rev.* 2014, **69–70**, 42–51.
225. Campioni, G.; Pasquale, V.; Busti, S.; Ducci, G.; Sacco, E.; Vanoni, M. An Optimized Workflow for the Analysis of Metabolic Fluxes in Cancer Spheroids Using Seahorse Technology. *Cells* **2022**, **11**, 866.
226. Jong, B.K. Three-dimensional tissue culture models in cancer biology. *Semin. Cancer Biol.* 2005, **15**, 365–377.
227. Yip, D.; Cho, C.H. A multicellular 3D heterospheroid model of liver tumor and stromal cells in collagen gel for anti-cancer drug testing. *Biochem. Biophys. Res. Commun.* **2013**, **433**, 327–332.
228. Wise, D.R.; Thompson, C.B. Glutamine addiction: a new therapeutic target in cancer. *Trends Biochem. Sci.* 2010, **35**, 427–433.
229. Pelicano, H.; Zhang, W.; Liu, J.; Hammoudi, N.; Dai, J.; Xu, R.H.; Puztai, L.; Huang, P. Mitochondrial dysfunction in some triple-negative breast cancer cell lines: Role of mTOR pathway and therapeutic potential. *Breast Cancer Res.* **2014**, **16**.
230. Yao, C.H.; Liu, G.Y.; Wang, R.; Moon, S.H.; Gross, R.W.; Patti, G.J. Identifying off-target effects of etomoxir reveals that carnitine palmitoyltransferase i is essential for cancer cell proliferation independent of β -oxidation. *PLoS Biol.* **2018**, **16**.
231. Imamura, Y.; Mukohara, T.; Shimono, Y.; Funakoshi, Y.; Chayahara, N.; Toyoda, M.; Kiyota, N.; Takao, S.; Kono, S.; Nakatsura, T.; et al. Comparison of 2D- and 3D-culture models as drug-testing platforms in breast cancer. *Oncol. Rep.* **2015**, **33**, 1837–1843.
232. Compton, S.L.E.; Pyne, E.S.; Liu, L.; Guinan, J.; Shea, A.A.; Grieco, J.P.; Frisard, M.I.; Schmelz, E.M. Adaptation of metabolism to multicellular aggregation, hypoxia and obese stromal cell incorporation as potential measure of survival of ovarian metastases. *Exp. Cell Res.* **2021**, **399**, 112397.
233. Kim, C.; Gao, R.; Sei, E.; Brandt, R.; Hartman, J.; Hatschek, T.; Crosetto, N.;

- Foukakis, T.; Navin, N.E. Chemoresistance Evolution in Triple-Negative Breast Cancer Delineated by Single-Cell Sequencing. *Cell* **2018**, *173*, 879–893.e13.
234. Argüello, R.J.; Combes, A.J.; Char, R.; Gigan, J.P.; Baaziz, A.I.; Bousiquot, E.; Camosseto, V.; Samad, B.; Tsui, J.; Yan, P.; et al. SCENITH: A Flow Cytometry-Based Method to Functionally Profile Energy Metabolism with Single-Cell Resolution. *Cell Metab.* **2020**, *32*, 1063–1075.e7.
235. Kunz-Schughart, L.A.; Heyder, P.; Schroeder, J.; Knuechel, R. A heterologous 3-D coculture model of breast tumor cells and fibroblasts to study tumor-associated fibroblast differentiation. *Exp. Cell Res.* **2001**, *266*, 74–86.
236. Keller, F.; Rudolf, R.; Hafner, M. Towards optimized breast cancer 3D spheroid mono-and co-culture models for pharmacological research and screening. *J. Cell. Biotechnol.* **2019**, *5*, 89–101.
237. Foreman, K.J.; Marquez, N.; Dolgert, A.; Fukutaki, K.; Fullman, N.; McGaughey, M.; Pletcher, M.A.; Smith, A.E.; Tang, K.; Yuan, C.W.; et al. Forecasting life expectancy, years of life lost, and all-cause and cause-specific mortality for 250 causes of death: reference and alternative scenarios for 2016–40 for 195 countries and territories. *Lancet* **2018**, *392*, 2052–2090.
238. Zschenker, O.; Streichert, T.; Hehlhans, S.; Cordes, N. Genome-wide gene expression analysis in cancer cells reveals 3D growth to affect ECM and processes associated with cell adhesion but not DNA repair. *PLoS One* **2012**, *7*.
239. Ravi, M.; Paramesh, V.; Kaviya, S.R.; Anuradha, E.; Paul Solomon, F.D. 3D cell culture systems: Advantages and applications. *J. Cell. Physiol.* **2015**, *230*, 16–26.
240. Costa, E.C.; Silva, D.N.; Moreira, A.F.; Correia, I.J. Optical clearing methods: An overview of the techniques used for the imaging of 3D spheroids. *Biotechnol. Bioeng.* **2019**, *116*, 2742–2763.
241. Nunes, A.S.; Barros, A.S.; Costa, E.C.; Moreira, A.F.; Correia, I.J. 3D tumor spheroids as in vitro models to mimic in vivo human solid tumors resistance to therapeutic drugs. *Biotechnol. Bioeng.* **2019**, *116*, 206–226.
242. Kyere-Yeboah, K.; Denteh, J.; Liu, K.; Ye, P.; Gao, E. Bin Monitoring Nicotinamide Adenine Dinucleotide and its phosphorylated redox metabolism using genetically encoded fluorescent biosensors. *Sens. Bio-Sensing Res.* **2019**, *26*, 100307.
243. Ley-Ngardigal, S.; Bertolin, G. Approaches to monitor ATP levels in living cells: where do we stand? *FEBS J.* **2021**, 1–30.
244. Zhao, Y.; Yang, Y. Real-time and high-throughput analysis of mitochondrial metabolic states in living cells using genetically encoded NAD⁺/NADH sensors. *Free Radic. Biol. Med.* **2016**, *100*, 43–52.

245. Sahu, P.; Mazumder, N. Advances in adaptive optics–based two-photon fluorescence microscopy for brain imaging. *Lasers Med. Sci.* **2020**, *35*, 317–328.
246. Wei, D.; Xu, M.; Wang, Z.; Tong, J. The Development of Single-Cell Metabolism and Its Role in Studying Cancer Emergent Properties. *Front. Oncol.* **2022**, *11*.
247. Damiani, C.; Maspero, D.; Filippo, M. Di; Colombo, R.; Pescini, D.; Graudenzi, A.; Westerhof, H.V.; Alberghina, L.; Vanoni, M.E.; Mauri, G. Integration of single-cell RNA-seq data into metabolic models to characterize tumour cell populations. *bioRxiv* **2018**, 256644.
248. Weeber, F.; Ooft, S.N.; Dijkstra, K.K.; Voest, E.E. Tumor Organoids as a Pre-clinical Cancer Model for Drug Discovery. *Cell Chem. Biol.* **2017**, *24*, 1092–1100.
249. Lee, S.H.; Hu, W.; Matulay, J.T.; Silva, M. V.; Owczarek, T.B.; Kim, K.; Chua, C.W.; Barlow, L.M.J.; Kandoth, C.; Williams, A.B.; et al. Tumor Evolution and Drug Response in Patient-Derived Organoid Models of Bladder Cancer. *Cell* **2018**, *173*, 515-528.e17.
250. Draga, R.O.P.; Grimbergen, M.C.M.; Vijverberg, P.L.M.; Swol, C.F.P.V.; Jonges, T.G.N.; Kummer, J.A.; Ruud Bosch, J.L.H. In vivo bladder cancer diagnosis by high-volume Raman spectroscopy. *Anal. Chem.* **2010**, *82*, 5993–5999.
251. Chen, H.; Li, X.; Broderick, N.; Liu, Y.; Zhou, Y.; Han, J.; Xu, W. Identification and characterization of bladder cancer by low-resolution fiber-optic Raman spectroscopy. *J. Biophotonics* **2018**, *11*.

CONTRIBUTIONS

I contributed to perform and analyze all the experiments presented in Chapter 1 and Chapter 2, except for the Multivariate statistical analysis (Figure 5, S5, S7 of Chapter 2) that were analyzed by my colleague Stefano Busti, PhD. I also contributed to the writing process of both Chapter 1 and Chapter 2, under the supervision of my colleagues and Professor Marco Vanoni. I also contributed to the design of the experiments reported in Chapter 1.

My contribution to the article 'Profiling and Targeting of Energy and Redox Metabolism in Grade 2 Bladder Cancer Cells with Different Invasiveness Properties' (Chapter 3) is more limited, and it does not include the writing of the manuscript. I contributed to perform some of the experiments included in the manuscript, more precisely, Figure 2 b,c,d (flow cytometry analysis of CD133, CD44 and Immunofluorescence staining of SOX-2), Figure 3e (ATP rate assay), Figure 4g (flow cytometry analysis of MitoTracker Red and MitoTracker Green), Figure 5c,f (flow cytometry analysis of DCFDA and MitoSOX) and Figure 6b (Mito Fuel Flex test). Finally, I analyzed the data obtained from ATP rate assay and Mito Fuel Flex test and contributed to set up the protocols and the drug concentrations to perform the experiment presented in Figure 8.

ACKNOWLEDGEMENT

I would like to acknowledge Professor Marco Vanoni for having given me the opportunity to attend the Ph.D. program at his laboratory and for having guided me during this educational course. This experience has allowed me to learn to approach the world of research with a critical mindset and to develop new technical and organizational skills.

I would like to offer my special thanks to the colleagues who shared with me these three years and a half in the lab: Elena, Valentina, and Giacomo. Elena and Valentina have been my guiding lines since the very beginning, always available to give advice when required. Much of what I learned in the laboratory during this journey I owe to their teaching. Giacomo was the first master's degree student (and then Ph.D. student) with whom I shared most of my experience in this group. Giacomo and Valentina have been constant friends and workmates in the lab, with whom I have shared the joy of successful experiments and the frustration of many unsuccessful experiments. I thank you very much for having always supported me in every difficult moment and for having in this way helped me to grow and mature.

A special acknowledgment goes to all the master's degree students who have worked with me during these years, especially those with whom I have worked more closely on the breast cancer project, such as Giusy, Zahia, Anna, and Alessandro, but also the master's students who have worked on other projects, such as Adria, Edoardo, Michela, Stefano, Irene, and Francesca, and the countless bachelor's degree students who have spent some weeks working in our laboratory. I hope I have passed on something good to them, as each of them did to me.

I would like to express my sincere gratitude also to the Gade Laboratory for Pathology at the University of Bergen (Norway) that have hosted me for three months during my period abroad. In particular, I would like to thank Dana for the warm welcome at her laboratory, her kindness, and for everything she taught me about co-cultures. I also

thank Harsh, KC, Stian, Ridhima, Himal, and all of Dana's group for the support and the help they gave me during my stay at their lab.

Finally, I would like to thank my family and especially my husband Denys for accompanying and supporting me throughout this journey of growth and training, even and especially during the most challenging times.